Non-local magnon transconductance in extended magnetic insulating films

Ryuhei Kohno

THÈSE

Pour obtenir le grade de

DOCTEUR DE L'UNIVERSITÉ GRENOBLE ALPES

École doctorale : PHYS - Physique
Spécialité : Physique de la Matière Condensée et du Rayonnement
Unité de recherche : Spintronique et Technologie des Composants

Transconductance non locale des magnons dans couches d'isolants magnétiques étendues

Non-local magnon transconductance in extended magnetic insulating films

Présentée par :

Ryuhei KOHNO

Direction de thèse :

Olivier KLEIN — Directeur de thèse
Ingénieur HDR, CEA centre de Grenoble

Laurent VILA — Co-directeur de thèse
Ingénieur HDR, CEA centre de Grenoble

Rapporteurs :

SEBASTIAN T. B. GOENNENWEIN
Professeur, Universität Konstanz

CATHERINE GOURDON
Directeur de recherche, CNRS DELEGATION PARIS CENTRE

Thèse soutenue publiquement le **15 février 2023**, devant le jury composé de :

SEBASTIAN T. B. GOENNENWEIN Professeur, Universität Konstanz	Rapporteur
CATHERINE GOURDON Directeur de recherche, CNRS DELEGATION PARIS CENTRE	Rapporteure
JEAN-PHILIPPE ATTANE Professeur des Universités, UNIVERSITE GRENOBLE ALPES	Président
ANDRE THIAVILLE Directeur de recherche, CNRS DELEGATION ILE-DE-FRANCE SUD	Examinateur
YOSHICHIKA OTANI Professeur, The University of Tokyo	Examinateur

Résumé

L'insulatronique de spin est un nouveau domaine de recherche, qui vise à exploiter les isolants électriques comme média pour le transport de pur courant de spin, dans le but de développer des composants électroniques plus efficaces sur le plan énergétique. La vision est de remplacer les électrons délocalisés présents dans les matériaux métalliques par des ondes de spin propagatives, qui transportent le spin d'un site atomique à l'autre sans aucune dissipation ohmique. Dans cette thèse, nous étudions les principes fondamentaux de l'excitation et de la propagation des magnons dans des films minces d'isolants magnétiques étendus. Nous concentrons notre étude sur la transconductance des magnons dans les films minces de grenat magnétique excités soit par un gradient de température (effet Seebeck de spin), soit par des effets de transfert de spin (couple de transfert de spin par un fil de Pt adjacent) en utilisant des dispositifs constitués de deux fils de Pt déposés sur des isolants ferromagnétiques étendus agissant respectivement comme émetteur et collecteur de magnons. La génération et la détection électrique des magnons sont rendues possibles grâce à l'effet Hall de spin direct ou inverse.

L'absence de dissipation par effet Joule confère généralement aux matériaux diélectriques un très faible amortissement magnétique, qui est associé à une forte propension des magnons à se comporter de manière non-linéaire. Dans les matériaux à très faible amortissement, une variation de 0,1% par rapport à l'occupation thermique est généralement suffisante pour faire passer la dynamique de magnétisation dans le régime non-linéaire. Cet effet peut être exploité pour des diodes de spin, des amplificateurs de spin ou des redresseurs de spin de signaux micro-ondes. Dans cette thèse, nous analysons l'origine de cet effet de diode de spin qui introduit une asymétrie des propriétés de transport entre le régime d'émission et d'annihilation des magnons. Cette caractéristique trouve son origine dans la variation de la densité d'excitations de spin de basse énergie via un déplacement électrique du potentiel chimique de magnon. Lorsque l'intensité du transfert de spin augmente en polarisation directe (régime d'émission des magnons), les propriétés de transport des magnons à basse énergie passent par trois régimes distincts : *i*) à faible courant, où le courant de spin est une fonction linéaire du courant électrique, le transport de spin est balistique et fixé par l'épaisseur du film : *ii*) pour des amplitudes de l'ordre du seuil de compensation de l'amortissement, il passe à un régime hautement corrélé limité par le processus de relaxation magnon-magnon et marqué par une saturation de la transconductance du magnon. Ici, le biais principal, qui contrôle la densité de magnons, est réglé par les fluctuations thermiques sous l'émetteur. *iii*) Lorsque la température sous l'émetteur approche la température de Curie, la diffusion avec des magnons à hautes énergies domine, ce qui conduit à un transport diffusif. Nous notons qu'une telle séquence de différents régimes de transport est analogue au transport hydrodynamique des électrons dans les milieux ultra-purs prédit par Radii Gurzhi.

Cependant, le transconductance des magnons est portée par une excitation de spin couvrant une large gamme d'énergie. On montrera que cette image peut être simplifiée de façon drastique dans un modèle à deux fluides qui ne prend en compte que les magnons aux deux extrémités du spectre d'énergie : *i*) une grande partie des magnons de haute énergie, proche de l'énergie thermique, avec une longueur caractéristique de propagation dans la gamme sub-micronique, et *ii*) une petite partie des magnons de basse énergie, avec une longueur caractéristique de propagation dans la gamme micronique. Ces caractéristiques de transport distinctes permettent de filtrer les magnons placés à haute énergie et d'exploiter les fonctionnalités spécifiques aux magnons à basse énergie. Ces derniers

peuvent devenir le fluide dominant : *i*) à une grande intensité d'injection pour se trouver dans le régime de l'effet de diode de spin, *ii*) à une grande distance avec l'émetteur, *iii*) à une petite épaisseur de film, ou *iv*) pour un décalage de bande réduit dû au changement de température effective entre la partie du YIG sous l'émetteur et celle sous le volume de propagation.

Sur la base de ces connaissances, nous avons cherché de nouvelles fonctionnalités en contrôlant le transport avec une électrode supplémentaire. Nous avons démontré l'amplification de la part du transport porté par les magnons de basse énergie en chauffant localement le collecteur dans la cas d'un film de YIG dopé au Bi. Ce dernier présente une anisotropie perpendiculaire uniaxiale qui supprime les effets de démagnétisation. Dans ce dernier cas, la conduction peut être améliorée d'un facteur 4 environ en chauffant le collecteur. Les simulations micromagnétiques ont également démontré une augmentation de l'amplitude d'oscillation en réduisant localement l'aimantation pour reproduire la situation du chauffage local. Elles ont révélé la formation d'ondes stationnaires entre les deux fils de Pt, suggérant que le gradient de magnétisation local peut agir comme un miroir pour les magnons de basse énergie.

Dans l'ensemble, nous nous persuadons que ce travail de thèse a contribué à améliorer la compréhension des transports de magnons induits par les effets de transfert de spin dans les géométries étendues. A long terme, cela contribuera au développement de circuits insulatroniques plus réalistes.

Version courte

Dans cette thèse, nous étudions la fonctionnalité donnée par les ondes de spin, ou leurs quanta magnons, pour les dispositifs à base d'isolant. Nous identifions la caractéristique fondamentale de la transconductance des magnons dans les films minces de grenat magnétique excités par les effets de transfert de spin. Nous utilisons des dispositifs composés de deux fils de Pt pour émettre et collecter les magnons. Ils montrent un comportement de conduction asymétrique de type diode qui provient de la population de magnons de basse énergie à l'énergie de GHz. Nous soulignons l'importance de la fluctuation thermique et du processus de relaxation magnon-magnon qui régissent la conduction. De plus, la propagation des magnons peut être considérée comme un transport à deux fluides provenant : i) de magnons de haute énergie à courte portée à l'énergie thermique (THz) et ii) de magnons de basse énergie à longue portée. Enfin, nous avons démontré un contrôle accordable de la transconductance des magnons en chauffant localement le collecteur. Nos résultats pourraient contribuer à la réalisation de circuits à base d'isolant.

Abstract

Spin insulatronics is an emerging field of research, which aims at exploiting electrical insulators as a novel transport medium which can propagate pure spin current with the benefit of developing more energy efficient computers and other electronics. The vision is to replace the delocalized electrons present in metallic materials by propagating spin-waves, which transport the spin from one atomic site to the other without any Joule dissipation. In this thesis, we investigate the fundamentals of magnon excitation and propagation in extended magnetic insulating thin films. We focus our interest on the characteristics of magnon trans-conductance in thin magnetic garnet films excited by either temperature gradient (spin Seebeck effect) or spin transfer effects (spin orbit torques from an adjacent Pt wire) by using devices consisting of two Pt wires deposited on extended ferromagnetic insulators acting as an emitter and a collector of magnons respectively. The electrical generation and detection of magnons are made possible thanks to the direct or inverse spin Hall effect, respectively.

The absence of Joule dissipation usually gifts the dielectric materials with very low magnetic damping, which is associated with a high propensity for magnons to behave nonlinearly. In ultra-low damping materials, a 0.1% variation from the thermal occupation is usually sufficient to drive the magnetization dynamics into the nonlinear regime. This effect could be exploited for spin diodes, spin amplifiers or spin rectifiers of microwave signals. In this thesis, we analyze the origin of the spin diode conduction which introduces an asymmetry of the spin transport properties between the regime of magnon emission and magnon annihilation. The feature is rooted in the variation of the density of low-lying spin excitations via an electrical shift of the magnon chemical potential. As the intensity of the spin transfer increases in the forward direction (regime of magnon emission), the transport properties of low-energy magnon go through 3 distinct regimes: *i*) at low currents, where the spin current is a linear function of the electrical current, the spin transport is ballistic and set by the film thickness: *ii*) for amplitudes of the order of the damping compensation threshold, it switches to a highly correlated regime limited by magnon-magnon relaxation process and marked by a saturation of the magnon transconductance. Here the main bias, that controls the magnon density, is thermal fluctuations beneath the emitter. *iii)* As the temperature under the emitter approaches the Curie temperature, scattering with high-energy magnons dominates, leading to diffusive transport. We note that such a sequence of transport regimes bears an analogy with electron hydrodynamic transport in ultra-pure media predicted by Radii Gurzhi.

The magnon transconductance is carried by spin excitation covering a wide energy range. It will be shown that for all practical purposes this picture can be simplified in a two-fluid model which only takes into account magnons at both ends of the energy spectrum: *i*) a large portion of high-energy magnons at thermal energy, with a characteristic decay length in a sub-micronic range, and *ii*) a small portion of low-energy magnons, with a characteristic decay length in a micronic range. Those distinct transport characteristics provide a way to filter out the high-energy magnons and to exploit the functionality of the low-energy magnons. The latter may become the dominant fluid *(i)* at a large intensity of injection to be in the regime of spin diode effect, *ii*) at a large distance from the emitter, *iii*) at a small film thickness, or *iv*) for a reduced band mismatch due to temperature change between the YIG beneath the emitter and the bulk.

Based on the acquired knowledge, we sought new functionalities by controlling the transport with an additional electrode. We demonstrated the amplification of the trans-

ports of low-energy magnons by locally heating the collector in Bi doped YIG, which has uniaxial perpendicular anisotropy suppressing the demagnetizing effects. The conduction is enhanced by about a factor of 4. Micromagnetic simulations also demonstrated an enhancement of the oscillation amplitude by reducing the magnetization locally to reproduce the situation of the local heating. They revealed a formation of standing waves between the two Pt wires, suggesting that the local magnetization gradient can act as a mirror for the low-energy magnons.

Overall we believe that this thesis work contributed to improving the understanding of magnon transports provided by spin transfer effects in extended geometries. In the long run this will contribute to the development of more realistic insulatronic circuits.

Short version

In this thesis we investigate the functionality given by the spin waves, or their quanta magnons, for insulator-based devices. We identify the fundamental characteristic of the magnon trans-conductance in thin magnetic garnet films excited by the spin transfer effects. We use devices consisting of two Pt wires for emitting and collecting magnons. They show asymmetric diode-like conduction behavior which stems from the population of low-energy magnons at GHz energy. We emphasize the importance of thermal fluctuation and the magnon-magnon relaxation process that govern the conduction. Moreover the magnon propagation can be viewed as a two-fluid transport originating from: i) short range high-energy magnons at thermal energy (THz) and ii) long range low-energy magnons. Finally we demonstrated a tunable control of the magnon trans-conductance by heating up locally the collector. Our results may contribute to the realization of insulator-based circuits.

Contents

Introduction **1**

1 Theoretical backgrounds **5**
1.1 Magnetic Excitation . . . 6
1.1.0.1 Landau Lifshitz equation . . . 7
1.1.0.2 General theory of magnetic excitations . . . 8
1.1.0.3 Confined geometry - spatial texture - eigenvalues and vectors in a disk . . . 12
1.1.0.4 Extended geometry - propagating waves - magnon dispersion relation . . . 14
1.1.1 non-linear effects - saturation effect . . . 16
1.2 Non-local magnon transport experiments . . . 23
1.2.1 Spin transfer effects . . . 24
1.2.2 Magnon excitation by spin transfer effect . . . 26
1.2.3 Confined geometry - auto-oscillation . . . 27
1.2.4 Extended geometries - magnon transport . . . 28
1.2.4.1 Bose statistics . . . 30
1.2.4.2 Low-energy v.s. high-energy magnons . . . 31
1.2.5 Transport of magnons excited by spin transfer effect . . . 32
1.2.5.1 Low-energy magnons in the linear regime . . . 32
1.2.5.2 Low-energy magnons at high power regime . . . 34
1.2.5.3 Self-localization effect . . . 36
1.2.5.4 Lorentz factor enhanced magnon-magnon decay rate . . . 37
1.2.5.5 Current threshold in extended geometries . . . 38
1.2.5.6 High-energy magnons . . . 39
1.2.5.7 Two-fluid model . . . 40
1.2.6 Transport of magnons excited by spin Seebeck effect . . . 42

2 Methods **45**
2.1 Growth of magnetic garnets films . . . 46
2.2 Nano fabrication process . . . 47
2.3 Measurement protocol . . . 48
2.4 Extracting SSE and SOT contribution . . . 49

3 Short range thermal magnon diffusion in magnetic garnets **53**
3.1 Characteristics of YIG and Pt wire, and simulations . . . 55
3.2 Transport characteristics of SSE signals . . . 58
3.3 Modeling of magnon diffusion and fitting of characteristic decay . . . 59
3.4 Conclusions . . . 62

4 Spin diode effect in extended magnetic thin films **63**
4.1 Key findings . . . 65
4.2 Analytical framework . . . 66
4.3 Experiments . . . 66
4.3.1 Sample characterisation . . . 66

4.3.2 Non-local magnon transport . . . 68
4.3.2.1 Measurement of the magnon transconductance . . . 69
4.3.2.2 Spin diode effect . . . 70
4.3.3 Brillouin Light Scatterng . . . 71
4.3.4 Influence of the lattice temperature . . . 74
4.3.5 Mismatch of magnon bands . . . 77
4.3.5.1 Nonlinear frequency shift . . . 77
4.3.5.2 Saturation of the magnon density . . . 79
4.3.6 Linear regime . . . 79
4.4 Conclusion . . . 80

5 Two-fluid behavior for spin transport in extended magnetic thin films 83
5.1 Key findings . . . 85
5.2 Analytical framework . . . 85
5.3 Experiments . . . 85
5.3.1 Magnetic susceptibility of the magnon transmission ratio . . . 86
5.3.2 Spectral signature in non-local measurement. . . . 87
5.3.3 Double decay of the magnon transmission ratio . . . 91
5.3.3.1 Thin films with anisotropic demagnetizing effect . . . 91
5.3.3.2 Thin films with isotropically compensated demagnetizing effect . . . 94
5.3.3.3 Discrepancy between T_c and $T_c^\star$ . . . 96
5.4 Conclusion . . . 97

6 Amplified transport of low-energy magnons in Bi-doped YIG by local heating 99
6.1 Device structures and characteristics . . . 100
6.2 Enhancement of low-energy magnon fluctuation . . . 102
6.3 Simulation by MuMaX^3 . . . 107
6.3.1 Effects of anisotropy . . . 110
6.3.2 Characteristic wavelength . . . 111
6.3.3 Observation of amplification . . . 113
6.4 Conclusions . . . 116

7 Perspectives 117
7.1 Coupling between magnons and phonons . . . 117
7.2 Seeking for magnonic hydrodynamic behavior . . . 123
7.3 Conclusions . . . 125

8 Conclusion 127
8.1 General conclusion . . . 127
8.2 Personal contribution . . . 129
8.3 Acknowledgement . . . 131

Bibliographie 132

Introduction

Thanks to the progress in thin film deposition and nano-scale fabrication techniques, new phenomena appearing in reduced dimensions started to be investigated and exploited. Spintronics has been one of the emergent fields of condensed matter physics. It aims at utilizing the transport properties of spins combined with conventional electronics. The first recognizable discovery is the giant magneto-resistance (GMR) [1, 2], which consequences the Nobel Prize of Physics awarded to Prof. Albert Fert and Prof. Peter Grünberg in 2007. It is observed in devices in which two ferromagnetic metal layers are sandwiching a non magnetic layer spacer and where the resistance changes as a function of the relative orientation of the two ferromagnets. It directly led to industrial applications as to increase the capacity of hard disk drives thanks to more sensitive read heads of hard disk drives [3]. Considering the exponentially increasing demands for the "Internet of Things" [4], one of the important objectives of this field is to realize efficient data writing, storing or computing methods [5, 6] to reduce the consumption of energy and emission of carbon dioxide, and to tackle current issues on global climate changes or natural resource preservation. The community proposed the magnetic random access memory (MRAM), using the so called tunnel magneto-resistance (TMR) where a tunnel barrier is used as the spacer layer to enhance the response and the low and high resistance states define a memory bit [7–10]. The main advantage is the non volatility, avoiding static energy consumption or refreshing the memory unlike the DRAM. However the writing method, to switch the magnetization direction of one layer (called the free layer), was relying on a magnetic field which hampers speed and scalability. Epoch-making discoveries were reported in the late 90s by Slonzewskii and Berger [11, 12] that describe the dynamics of magnetization under the injection of a spin polarized electrical current. One can generate the spin polarized current by injecting a charge current to the fixed layer which will exert a torque on the free layer. Such a torque is called the spin transfer torques (STT) and eventually it switches the free layer due to the conversation of angular momentum. This electrical STT writing method overcomes the scalability difficulties mentioned above, together with the fast dynamics of magnetization switching (GHz) and it has attracted the attention of semiconductor companies worldwide. Other important discoveries were reported in the early 2000s on the generation of pure spin currents in non magnetic materials. It is thanks to the spin orbit coupling and referred to as the spin Hall effect (SHE) [13–17]. A pure spin current means a flow of spin angular momentum without net charge flow. SHE and its inverse effect enable to interconvert charge and spin current in directions transverse to each other. Such spin current can be absorbed by the magnetization, with its polarization direction being orthogonal to that of the applied charge current, and eventually induces magnetization dynamics. Thus it allows the switching of a bit by injecting the charge current underneath (or above) the free layer without passing through the insulator, leading to larger endurance than in the STT method [18]. The torques originating from the SHE are called the spin orbit torques (SOT), as SHE originates from the spin orbit coupling.

Besides the prospects of MRAM application, the STT, SHE and SOT brought innovation to the field of magnonics. Its aim is to utilize collective fluctuations of local magnetic moments, namely spin waves or their quanta magnons, as information carriers. New computing or logic operation methods for beyond CMOS technology can then be foreseen [19–23]. The motivation comes from magnons' tunable operation frequency, wide frequency range from GHz to THz, and their nonlinear nature [24–26], having the potential towards wave-based computation. The phase of oscillation provides further freedom

to be exploited. For example, logic gate operation such as a three terminal transistor [19], XNOR gate [27], majority gate [28] and half adder [29] have been demonstrated using interference effects of spin waves for magnonic Boolean computing. As a new trend, magnonic unconventional computing envisioning much higher performance has also been proposed such as neuromorphic computing [30–32], reservoir computing [33, 34], and an Ising machine [35, 36]. STT, SHE and SOT enable to bridge collective dynamics of spins with electron-based spintronics (and conventional electronics). The classical way to generate and detect magnons was based on inductive microwave techniques which use an oscillating field induced around a microwave antenna. While using high frequency sources or network analyzers is rather complicated, the above mentioned new spintronic discoveries provide new avenues. STT can launch the dynamics of spins by d.c. current application. In a GMR or TMR device, the coherent excitation of dynamics by STT, named spin torque nano oscillator (STNO) has been demonstrated by injecting a charge current across the stack, which expands the range of application of spintronics, such as d.c. - a.c. converters or un-conventional computing [37–42]. Additionally detection of magnons through d.c. voltage has been made possible thanks to the inverse SHE (ISHE) [43] and the spin pumping effect [44, 45], where magnetization precession in a magnetic film generates a spin current in an adjacent non-magnetic heavy metal layer that is eventually converted into a charge current. This leads to the observation of the spin Seebeck effect, where temperature gradient across the magnetic layer generates magnons and eventually pumps spin current to an adjacent heavy metal [46, 47]. This discovery opens up new possibilities of magnonics from the view point of energy harvesting, which may be useful for reusing wasted heat [48].

Indeed, SHE, ISHE and SOT play a crucial role in insulators as well. Especially, SHE enables to inject the spin current to an insulator by simply flowing a charge current in an adjacent conducting layer with large spin orbit coupling. It applies SOT to the magnetization and excites the dynamics [49–53]. Importantly insulating ferromagnets, such as the most known Yttrium Iron Garnet (YIG), bares superiority over metallic ferromagnets. First, there is no mobile electron that dissipates energy due to resistive losses. Second, YIG has the smallest possible magnetic damping thanks to well-established crystal growth techniques, which contributes to a long life time and a long range transport of magnons. Thus magnetic insulators with exceptionally low spin relaxation are excellent platforms for investigating and manipulating the magnons. As a consequence, the coined term *spin insulatronics* has emerged, aiming at exploiting such properties of magnetic insulators to realize dissipation-reduced devices where the magnon transport are spin information carriers. A proto-typical *insulatronic* device has been proposed a couple of years ago [51–53]. It consists of only two narrow Pt wires deposited on a magnetic insulator acting as a magnon emitter and collector with all electrical d.c. operations. Despite its simple device structure, the physics behind is full of complexity. One difficulty is that the properties of generated magnons are largely ambiguous. The frequency, wavelength, and relaxation are not well defined and it complicates the interpretation. Considering that the magnon dispersion extends from GHz (around the ferromagnetic resonance) to THz frequency (thermal energy), the properties at the lowest and highest extrema should be distinct (chapter 5). Luckily or unluckily, the characteristic transport length of magnons in such a device has been found as long as 10 μm regardless of the excitation methods, either thermal or electrical [52]. It is true for the former that it excites magnons around the thermal energy [54, 55], however, does it mean that such magnons are generated for the latter as well? It is to a certain extent questionable to show the long range transport for the thermal case for some reasons, such as for example faster relaxation rates at higher frequencies (chapter 3). It has been reported that the electrically excited magnons show a non-linear increase of the conduction as a function of the input current together with a dependence on the applied magnetic field, especially at high input intensity [56, 57]

(chapter 4). Such behaviors seem more reasonable for magnons around the ferromagnetic resonance frequency, meaning that indeed different types of magnons are taking part in the transport depending on the excitation methods, input current density and so on. Regarding the non-linear behaviors induced by the spin torques, one might consider the above mentioned STNO as its theoretical description is well established [58]. However we have to beware that the pertinent pictures for magnetic excitations are different between confined nano objects such as a STNO and extended geometries playing the role of magnon conduits. For the former, a single-mode picture should be reasonable due to large energy splittings between possible modes due to the geometrical restriction. In this case the lowest energy mode, usually the uniform mode should be the main actor [49]. For the latter, the system is free from the restriction and thus a multi-mode picture sounds appropriate. Our main concern is spin wave propagation phenomena, which are indeed issues on non-uniform modes in extended geometries. Therefore we have to develop different frameworks to better understand the physics behind (chapter 1). Eventually it is crucial to clarify which conditions are advantageous for magnon transports and to show their controllability for further development of the *spin insulatronics* (chapter 6). Our efforts will be devoted to profoundly investigating the above mentioned issues on the transport properties of magnons in such a device.

This manuscript is organized into eight chapters:

- *Chapter 1* describes the basic theoretical backgrounds that are useful to understand the experimental results and their interpretations. The fundamentals of magnetic excitations are introduced while comparing confined or extended geometry cases, followed by the nonlinear saturation effect. The basic concepts of non-local magnon transport experiments are then explained together with spin transfer effects at a YIG|Pt interface. Finally analytical frameworks of the magnon transport are developed.

- *Chapter 2* explains the methods used in this thesis: the device fabrication, measurement protocols and processing of data are introduced.

- *Chapter 3* focuses on the characteristic transport length of the high-energy thermal magnons at the energy around k_BT generated through the spin Seebeck effect. We utilize an Aluminium capping layer that covers the device as a heat sink, to significantly alter the temperature profile. By comparing the spatial decay of non-local signals in the case with and without Al capping, we conclude that the decay length of the high-energy magnons should be no more than a few hundred of nanometers.

- *Chapter 4* investigates the asymmetric non-linear behavior of non-local signal electrically excited by the spin transfer effects with respect to the current applied in the Pt wire, which we are naming *spin diode effect*. This diode-like conduction behavior stems from the low-energy magnetostatic magnons residing close to the Kittel frequency $\hbar\omega_K$ in the dispersion relation in the GHz range. The transport properties of the low-energy magnons go through 3 distinct regimes: i) at low currents, where the conduction is a linear function of the injected electrical current, the transport is ballistic and set by the film thickness; ii) for amplitudes of the order of the damping compensation threshold, it switches to a highly correlated regime limited by magnon-magnon relaxation process and marked by a saturation of the magnon

transconductance. Here the main parameter, that controls the magnon density, is the thermal fluctuations beneath the emitter. iii) As the temperature under the emitter approaches the Curie temperature, the conduction drops down to zero.

- *Chapter 5* experimentally elucidates their spectral nature through the spatial decay of the magnon conduction. While most of the injected magnons remain localized under the emitter, the propagating magnons may be split into two fluids, which we name *two-fluid behavior*: i) a large portion of high-energy magnons, with a characteristic decay length in the sub-micrometer range and ii) a small portion of low-energy magnons, with a characteristic decay length in the micrometer range. Taking advantage of their different physical characteristics, the low-energy magnons may become the dominant fluid i) at a large spin transfer rate for the bias causing the spin diode effect, ii) at a large distance from the emitter, iii) at a small film thickness or iv) for reduced band mismatch between the YIG beneath the emitter and the bulk due to temperature change of the magnon bath.

- *Chapter 6* demonstrates the amplification of the transports of low-energy magnons by locally heating up the collector electrode in Bi doped YIG, which has uniaxial perpendicular anisotropy suppressing the demagnetizing effects. The conduction is enhanced by a factor of 3.4 by 77 K of local heating. The increased dependence on the magnetic field by the local heating proves that the low-energy magnons are subject to the amplification. Systematic variation of injected current and amount of the local heating suggests that the initial large population of such magnons is important. Micromagnetic simulations that describe the dynamics of such magnons governed by standard LLG equation demonstrate the enhancement of the oscillation amplitude by reducing the magnetization locally to reproduce the local heating in experiments.

- *Chapter 7* proposes future perspectives based on the obtained results. One possibility is to exploit the magnon phonon coupling phenomenon that we observed in independent studies in the systems used for non-local transport measurements. The other is to seek hydrodynamic behavior, where the idea stems from the increased magnon-magnon scattering developed in chapter 4. It is an analogy with observed hydrodynamic conduction of electrons in ultra pure systems of graphenes encapsulated with hexagonal boron nitride.

Thereafter, the conclusion of this research will be addressed.

Chapter 1

Theoretical backgrounds

In this chapter, we introduce the theoretical backgrounds which are useful for the understanding of the experimental chapters. This manuscript focuses on the transport of magnetic excitations in magnetic insulator thin films. Thus we will first briefly explain the collective dynamics of spins in a solid, namely spin waves or their quanta magnon, and introduce the basic equations that govern their out-of-equilibrium properties. Next, we will focus on the fundamental principles of emission and detection of magnons in non-local geometries. The magnon transport properties are discussed together with the spin transfer effect, exchange of angular momentum between polarized spins and local magnetization. If we insert this work within the state-of-the-art, the spin transfer effects in confined geometries are rather well understood thanks to their large mode splitting produced by finite size effects. However in extended geometries, the process is still rather elusive due to the overlap between the eigen-modes. We will develop a generic formalism on the magnon transport characteristics to bridge the established knowledge with our measurements presented in the following chapters.

The first part will focus on the derivation of the dynamics of spin. Starting from simple analytical calculations, the fundamental equations that describe the dynamics will be introduced. Comparing confined and extended geometries, localized spin textures derived by solving the eigen-value problem are concerned for the former whereas non-zero wave vector spin waves governed by the magnon dispersion relation are the main actors in the latter. In this context, general formula representing the dispersion relation of magnons will be displayed, which is used many times in the following chapters to understand the observation. Finally, an important non-linear effect of magnons when exposed to high input power, the *saturation effect*, will be introduced. This will be tentatively implemented in our formalism of the magnon transport measurements.

The second part will be dedicated to introducing the spin transfer effect which is particularly important for the generation and detection of itinerant magnon with non-zero wave vector. They rely on the angular momentum transfer between spin current and magnetization, *i.e.*, the *spin pumping* and its reciprocal effect *spin orbit torque* in our measurements. Starting from the spin transfer effects in confined geometries (the auto-oscillation), we will proceed to our main focus, the one in extended geometries. Due to the nature of mode degeneracy in the energy dispersion continuum, it is convenient to use the statistical distribution. This leads to two distinct types of magnons, the *low-energy magnons* around the energy of Kittel frequency and *high-energy magnons* around the thermal energy. To begin with, the Bose-Einstein distribution to describe the number of magnons and the transport characteristics of low-energy magnons will be derived. Consequently a non-linear transport behavior is analytically deduced as will be shown experimentally in chapter 4. Here we add the ingredient of the saturation effects. Finally we will introduce the *two-fluid behavior* to capture the spectral nature of magnon transports.

A part of this chapter is taken from the recently submitted preprints arXiv:2210.08304 and arXiv:2210.08283.

1.1 Magnetic Excitation

This manuscript focuses on the fundamental understanding of the transport phenomenon in the form of magnetic excitations, the spin wave, or their quanta magnons. We start this chapter by introducing analytical frameworks for magnetic excitations. An important remark in the very beginning is that we have to distinguish the pictures for extended geometries, *i.e.*, our measurements, from the ones for confined geometries. One by one we will mention the specific features of both cases. Finally a characteristic non-linear phenomenon that occurs prominently in extended geometries will be introduced to better understand magnon transport phenomenon.

To begin with, we consider the magnetic energy that governs not only the equilibrium configuration but also the dynamics of magnetic moments. Here we list up the different contributions of the energy such that

$$W = \int_V W_{\text{Zeeman}} + W_{\text{anis}} + W_{\text{exchange}} + W_{\text{demag}} + W_{\text{else}} d\boldsymbol{r} \tag{1.1}$$

where the integration is over the whole magnetic volume V. One can get the $\boldsymbol{B}_{\text{eff}}(\boldsymbol{r})$, the effective magnetic field which acts on the local magnetization $\boldsymbol{M} \equiv \boldsymbol{M}(t, \boldsymbol{r})$, by taking the differential of energy with respect to the magnetization,

$$\boldsymbol{B}_{\text{eff}}(\boldsymbol{r}) = -\frac{\partial W(\boldsymbol{r})}{\partial \boldsymbol{M}(\boldsymbol{r})} \tag{1.2}$$

- *Zeeman energy*

  $$W_{\text{Zeeman}} = -\boldsymbol{M} \cdot \boldsymbol{B}_0 \tag{1.3}$$

  This originates from the splitting of the degenerated energy levels spin up and down due to the external magnetic field. The minimized condition is when the magnetization is parallel to the external field $\boldsymbol{B}_0$.

- *Anisotropy energy* Depending on the geometrical shape of materials, elements, or interfacial conditions, the magnetization favors aligning in a certain direction $\hat{\boldsymbol{a}}$ and this is called uniaxial anisotropy. It induces the energy in the system such that

  $$W_{\text{anis}} = K_u \sin^2 \theta_u \tag{1.4}$$

  $$\boldsymbol{B}_{\text{anis}} = \frac{2K_u}{M_s} \cos \theta_u \hat{\boldsymbol{a}} \tag{1.5}$$

  where the θ_u is the angle between $\boldsymbol{M}$ and $\hat{\boldsymbol{a}}$ and $M_s = |\boldsymbol{M}|$ is the saturation magnetization. Thus this energy acts as the correction term against the effective field. This remark is especially important when one deals with thin magnetic film with perpendicular uniaxial anisotropy because it can compensate the below mentioned demagnetizing field.

- *Exchange energy*
  This contribution comes from the mutual interaction between neighboring spins while the previous two act on an individual spin. For such magnetic self interaction contributions, it is convenient to describe in the reciprocal space with the coordinate

of $\boldsymbol{k}$ with a linear tensor self-adjoint operator $\widehat{\boldsymbol{G}}_{\text{exchange}}$

$$W_{\text{exchange}} = \frac{\mu_0}{2}\boldsymbol{M} \cdot \widehat{\boldsymbol{G}}_{\text{exchange}} * \boldsymbol{M} \tag{1.6}$$

$$\widehat{\boldsymbol{G}}_{\text{exchange}} = \lambda^2 k^2 \widehat{\boldsymbol{I}} \tag{1.7}$$

where $\lambda = \sqrt{\frac{2A_{\text{ex}}}{\mu_0 M_s^2}}$ is the exchange length and $A_{\text{ex}} = \frac{dJ\langle S\rangle^2}{a}$ is the exchange stiffness which represents the global sum of the Heisenberg interaction, the factor d depends on the crystalline structure. This energy indeed favors the situation where the parallel alignment of neighboring spins. $\widehat{\boldsymbol{I}}$ is the identity matrix, $*$ denotes the product between a matrix and a vector and $\cdot$ does the product between two vectors.

- *Demagnetizing energy*
  The energy arises from the dipole-dipole magnetostatic interaction between spins, which expresses the dipolar stray field from other positions acting on one position. Especially in a thin film, positive magnetic charges that appear on both surfaces create an internal magnetic field normal to the plane. For this contribution as well, it is useful to describe in the reciprocal space.

$$W_{\text{demag}} = \frac{\mu_0}{2}\boldsymbol{M} \cdot \widehat{\boldsymbol{G}}_{\text{demag}} * \boldsymbol{M} \tag{1.8}$$

$$\widehat{\boldsymbol{G}}_{\text{demag}} = \frac{\boldsymbol{k} \otimes \boldsymbol{k}}{k^2} \tag{1.9}$$

  where $\otimes$ denotes the direct product of vectors.

- *Other types of energy*
  One can consider for example higher order neighbor exchange interactions called RKKY interaction or the anti-symmetric exchange interaction called Dzyaloshinskii-Moriya interaction [59]. Those are not considered in this manuscript.

Finally, the overall magnetic energy can be obtained by

$$W = \int_V \left(-(\boldsymbol{B}_0 - \frac{\boldsymbol{B}_{\text{anis}}}{2}) \cdot \boldsymbol{M} + \frac{\mu_0}{2}\boldsymbol{M} \cdot (\widehat{\boldsymbol{G}}_{\text{exchange}} + \widehat{\boldsymbol{G}}_{\text{demag}}) * \boldsymbol{M} \right) d\boldsymbol{r} \tag{1.10}$$

Consequently, the effective field is then written as follows.

$$\boldsymbol{B}_{\text{eff}} = (\boldsymbol{B}_0 - \boldsymbol{B}_{\text{anis}}) - \frac{\mu_0}{2}(\widehat{\boldsymbol{G}}_{\text{exchange}} + \widehat{\boldsymbol{G}}_{\text{demag}}) * \boldsymbol{M} \tag{1.11}$$

1.1.0.1 Landau Lifshitz equation

Let us start by introducing the Laudau-Lifshitz equation to study the dynamics of magnetization [60], which is analogous to the torque equation of a gyroscope and describes its precessional motion. In the presence of effective magnetic field $\boldsymbol{B}_{\text{eff}}$, $\boldsymbol{M}$ feels the torque $\boldsymbol{\tau}$ as long as it does not completely align to $\boldsymbol{B}_{\text{eff}}$ such that

$$\boldsymbol{\tau} = \boldsymbol{M} \times \boldsymbol{B}_{\text{eff}} \tag{1.12}$$

Recalling the angular momentum $\boldsymbol{J} = -\boldsymbol{S_i}/\gamma$ where the γ is the gyromagnetic ratio, and its time evolution is expressed as $\boldsymbol{\tau} = \partial_t \boldsymbol{J}$, we obtain the following equation,

$$\frac{\partial}{\partial t}\boldsymbol{M} = -\gamma \boldsymbol{M} \times \boldsymbol{B}_{\text{eff}} \tag{1.13}$$

This is the original form of the Landau-Lifshitz equation announced in 1935 and we rely on it to develop the eigen value problems for magnetic excitation in the following subsubsection. Note that it does not consider the magnetic losses and the motion is perpetual. To be more realistic as the magnetic losses are induced due to some relaxation processes, Gilbert introduced the phenomenological friction-like term in Eq. (1.13) and we obtain,

$$\frac{\partial}{\partial t}\boldsymbol{M} = -\gamma \boldsymbol{M} \times \boldsymbol{B}_{\text{eff}} + \alpha \frac{\boldsymbol{M}}{M_s} \times \frac{\partial \boldsymbol{M}}{\partial t} \tag{1.14}$$

where α represents the friction-like dimensionless Gilbert magnetic damping parameter and $M_s = |\boldsymbol{M}|$ is the constant length of the magnetization vector. Eq. (1.14) is called the Landau-Lifshitz-Gilbert equation, which is sometimes abbreviated as LLG equation and is widely used to understand the dynamics of spins including spin wave generation and propagation by solving the equation numerically. A schematic of the vectorial relationship is depicted in Fig. (1).

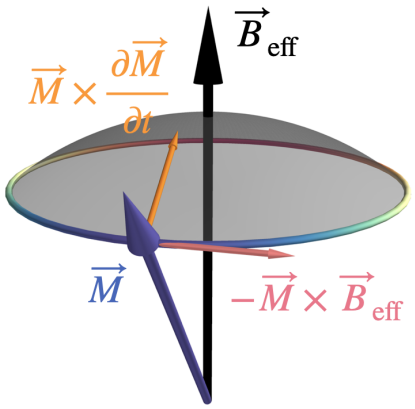

Figure 1: *Schematic of dynamics of magnetization* $\boldsymbol{M}$ *precessing around* $\boldsymbol{H}_{\text{eff}}$ *and corresponding torques.*

1.1.0.2 General theory of magnetic excitations

Let us introduce the general theory of linear magnetic excitations that can be applicable to inhomogeneous parameters as well by considering the premises introduced above. In this subsubsection we will pose and solve an eigen value problem that represents the dynamics derived from the Landau-Lifshits equation. Here we will express more explicitly the effective field and the magnetic damping. This part is based on Appendix A in Ref. [61] contributed by Prof. Vasyl S. Tyberkevych at Oakland University in the U.S.

Here we do not consider the effect of magnetic anisotropy. Let us define the total magnetic self-interaction operator $\widehat{\boldsymbol{G}} \equiv \widehat{\boldsymbol{G}}_{\text{exchange}} + \widehat{\boldsymbol{G}}_{\text{demag}}$. The equilibrium magnetization distribution $\boldsymbol{M}_{\text{eq}}$ can be written as

$$\boldsymbol{M}_{\text{eq}} = M_s \boldsymbol{\mu}\,, \tag{1.15}$$

where $\boldsymbol{\mu}$ is the unit vector in the direction of the equilibrium magnetization. We do not assume that $\boldsymbol{\mu}$ is independent of the spatial coordinates – the presented here formalism is completely general and can be used in spatially inhomogeneous cases.

This leads to defining B the scalar *internal* magnetic field (possibly spatially-inhomogeneous) pointing along $\boldsymbol{\mu}$ in the equilibrium as

$$\boldsymbol{B}_0 - \mu_0 M_s \widehat{\boldsymbol{G}} * \boldsymbol{\mu} = B\boldsymbol{\mu}\,, \tag{1.16}$$

Now the effective field in Eq. (1.11) is re-written such that

$$\boldsymbol{B}_{\text{eff}} = B\boldsymbol{\mu} + \mu_0 \widehat{\boldsymbol{G}} * (\boldsymbol{M} - M_s\boldsymbol{\mu})\,, \tag{1.17}$$

To find the dynamical equations for the small (linear) magnetization excitations, we shall use the following ansatz

$$\boldsymbol{M} = M_s(\boldsymbol{\mu} + \boldsymbol{m}) + O(\boldsymbol{m}^2)\,, \tag{1.18}$$

where $\boldsymbol{m}$ is the small dimensionless deviation of the magnetization from the equilibrium direction $\boldsymbol{\mu}$. Condition of the constant length of the magnetization vector requires orthogonality of $\boldsymbol{\mu}$ and $\boldsymbol{m}$,

$$\boldsymbol{\mu} \cdot \boldsymbol{m} = 0\ . \tag{1.19}$$

Substituting Eq. (1.18) and Eq. (1.17) in Eq. (1.13), keeping only linear in $\boldsymbol{m}$ terms, and using Eqs. (1.16) and (1.19) one obtains the following dynamical equation for $\boldsymbol{m}$:

$$\frac{\partial \boldsymbol{m}}{\partial t} = (\boldsymbol{\mu} \times \widehat{\boldsymbol{\Omega}} * \boldsymbol{m})\,, \tag{1.20}$$

where

$$\widehat{\boldsymbol{\Omega}} = \gamma B \widehat{\boldsymbol{I}} + \mu_0 \gamma M_s \widehat{\boldsymbol{G}}\ . \tag{1.21}$$

It is clear that the tensor operator $\widehat{\boldsymbol{\Omega}}$ has a dimension of frequency and is self-adjoint.

Changes to the magnetic energy due to the excitations $\boldsymbol{m}$ can also be expressed through $\widehat{\boldsymbol{\Omega}}$:

$$\Delta W = \frac{M_s}{2\gamma} \int_V \boldsymbol{m} \cdot \widehat{\boldsymbol{\Omega}} * \boldsymbol{m}\, d\boldsymbol{r}\ . \tag{1.22}$$

Spin wave modes $\boldsymbol{m}_\nu$ are eigen-solutions of Eq. (1.20):

$$-i\omega_\nu \boldsymbol{m}_\nu = (\boldsymbol{\mu} \times \widehat{\boldsymbol{\Omega}} * \boldsymbol{m}_\nu)\ . \tag{1.23}$$

Here ω_ν is the spin wave eigenfrequency and ν is a set of indices used to enumerate different modes.

The main properties of spin wave excitations follow from the eigenvalue problem Eq. (1.23) and the fact that the operator $\widehat{\boldsymbol{\Omega}}$ is self-adjoint and real. To formulate these properties, it would be convenient to introduce the short-hand notation for averaging over the volume of the magnetic body V as

$$\langle f \rangle \equiv \frac{1}{V} \int_V f\, d\boldsymbol{r}\ . \tag{1.24}$$

We shall also use the notation

$$(\boldsymbol{a}, \boldsymbol{b}, \boldsymbol{c}) \equiv \boldsymbol{a} \cdot (\boldsymbol{b} \times \boldsymbol{c}) \tag{1.25}$$

to denote triple scalar product.

From Eq. (1.23) one can easily obtain the following relation:

$$(\omega_\nu^* - \omega_{\nu'}) \left\langle (\boldsymbol{m}_\nu^*, \boldsymbol{\mu}, \boldsymbol{m}_{\nu'}) \right\rangle = 0 \ . \tag{1.26}$$

For $\nu' = \nu$ one gets from this relation $\omega_\nu^* = \omega_\nu$ (unless $\left\langle (\boldsymbol{m}_\nu^*, \boldsymbol{\mu}, \boldsymbol{m}_\nu) \right\rangle = 0$, which, as one can show, is possible only if equilibrium magnetization configuration $\boldsymbol{\mu}$ corresponds to a saddle point of energy W; we shall not consider this case here). Thus, the spin wave spectrum is real.

One can also obtain the orthogonality relation for spin wave modes:

$$\left\langle (\boldsymbol{m}_\nu^*, \boldsymbol{\mu}, \boldsymbol{m}_{\nu'}) \right\rangle = -iC_\nu \delta_{\nu,\nu'} \ . \tag{1.27}$$

Here C_ν are real normalization constants, which depend on the choice of eigen-functions $\boldsymbol{m}_\nu$ and δ is Kronecker's delta. Note, that, in contrast to a usual case, C_ν can be negative (more about it below). If there are several modes having the same frequency ω_ν, orthogonality should be understood as usual, i.e., we can choose a system of degenerate eigenfunctions in such a way that $\boldsymbol{m}_\nu$ satisfy Eq. (1.27).

Another important relation that can be obtained from Eq. (1.23) is the following:

$$\left\langle \boldsymbol{m}_\nu^* \cdot \widehat{\boldsymbol{\Omega}} * \boldsymbol{m}_{\nu'} \right\rangle = \omega_\nu C_\nu \delta_{\nu,\nu'} \ . \tag{1.28}$$

Thus, the eigenfrequency ω_ν can be calculated as

$$\omega_\nu = \frac{1}{C_\nu} \left\langle \boldsymbol{m}_\nu^* \cdot \widehat{\boldsymbol{\Omega}} * \boldsymbol{m}_\nu \right\rangle = \frac{\gamma}{C_\nu} \left\langle \boldsymbol{m}_\nu^* \cdot \left(B\widehat{\boldsymbol{I}} + \mu_0 M_s \widehat{\boldsymbol{G}} \right) * \boldsymbol{m}_\nu \right\rangle \ . \tag{1.29}$$

where the scalar value of the internal field is written such that

$$B = \boldsymbol{\mu} \cdot \boldsymbol{B}_0 - \mu_0 M_s \boldsymbol{\mu} * \widehat{\boldsymbol{G}} * \boldsymbol{\mu} \ . \tag{1.30}$$

The importance of this relation is that the frequency ω_ν, calculated using Eq. (1.29), is variationally stable with respect to perturbations of the mode profile $\boldsymbol{m}_\nu$. Thus, one can use Eq. (1.29) with some reasonable trial profile $\tilde{\boldsymbol{m}}_\nu$ to get an approximate value of ω_ν with high accuracy.

Kalinikos and Slavin solved and calculated Eq. (1.29) for arbitrary $\boldsymbol{k}$ with uniform magnetization across the film thickness in rectangular bodies [26]. The final results of their calculations will be mentioned later on. Let us consider a uniformly magnetized body to give a more concrete example. The contribution from the inhomogeneous exchange interaction to $\widehat{\boldsymbol{G}}$ is null ($k = 0$), thus $\widehat{\boldsymbol{G}} = G_{\text{demag}}$ and the effective field is rewritten in real space expression such that [62]

$$\boldsymbol{B}_{\text{eff}} = \boldsymbol{B}_0 - \mu_0 M_s \int D(\boldsymbol{k}) \widehat{\boldsymbol{G}}_k^{(d)} \exp(i\boldsymbol{k} \cdot \boldsymbol{r}) d^3\boldsymbol{k} = \boldsymbol{B}_0 - \mu_0 \widehat{\boldsymbol{N}} * \boldsymbol{M}_{\text{eq}} \ . \tag{1.31}$$

where $D(\boldsymbol{k})$ is the Fourier transform of the body shape function. $\widehat{\boldsymbol{N}}$ is so called the spatially dependent demagnetization matrix that characterizes the effective field in Eq. (1.11). Spatial average of its tensor components $< N >_{ij}$ in real space expression are calculated as

$$< N >_{ij} = \frac{1}{V} \int |D(\boldsymbol{k})|^2 \frac{k_i k_j}{k^2} \exp(i\boldsymbol{k} \cdot \boldsymbol{r}) d^3\boldsymbol{k} \ . \tag{1.32}$$

For the eigen frequency of the uniform mode ($\boldsymbol{k} = 0$) in a uniformly magnetized body, the spatial distribution is not concerned anymore. Removing the bracket in Eq. (1.29), we obtain

$$\omega_0^2 = \gamma^2 (B + \mu_0 M_s N_{x,x})(B + \mu_0 M_s N_{y,y}) \ . \tag{1.33}$$

Here the product with both $\boldsymbol{x}$ and $\boldsymbol{y}$ is carried out to cancel out the ellipticity of the precession. This represents the well-known *Kittel formula*. Although it is difficult to calculate the value of $< N >_{ij}$ in general, S. Tandon computed $D(\boldsymbol{k})$ and consequent $< N >_{ij}$ for a uniformly magnetized body with arbitrary shape [62], allowing us to calculate eigenmodes of magnetic dynamics in any shape.

Let us mention here the non-conservative torque as initially introduced in Eq. (1.14) that damps the dynamics. The formalism presented above allows us to consider simple linear perturbation for spin waves. Adding a perturbation term to Eq. (1.13), the perturbed Landau-Lifshits equation is given as

$$\frac{\partial \boldsymbol{M}}{\partial t} = \gamma(\boldsymbol{B}_{\text{eff}} \times \boldsymbol{M}) + \gamma(\boldsymbol{b} \times \boldsymbol{M}) \, , \tag{1.34}$$

where $\boldsymbol{b}$ is the effective magnetic field of the perturbations, which may be a function of time and the magnetization distribution $\boldsymbol{M}$. Now Eq. (1.34) allows us to describe non-conservative perturbations. For instance, one can describe the influence of the magnetic damping with $\boldsymbol{b} = -(\alpha/\gamma M_s)\partial \boldsymbol{M}/\partial t$, where α is the Gilbert damping constant.

We can represent the magnetization distribution $\boldsymbol{M}$ as a series over spin-wave eigenmodes for linear processes:

$$\begin{aligned} \boldsymbol{M}(t, \boldsymbol{r}) &= M_s(\boldsymbol{\mu} + \boldsymbol{m}) \\ &= M_s \left[\boldsymbol{\mu}(\boldsymbol{r}) + \sum_\nu (a_\nu(t) \boldsymbol{m}_\nu(\boldsymbol{r}) + \text{c.c.}) \right] \ . \end{aligned} \tag{1.35}$$

Here summation is over the possible $\omega_\nu > 0$, c.c. stands for the complex-conjugated part, and $a_\nu(t)$ are time-dependent spin wave amplitudes. In the case of unperturbed Landau-Lifshits equation $a_\nu(t)$ satisfy trivial equations

$$\frac{da_\nu}{dt} = -i\omega_\nu a_\nu \ . \tag{1.36}$$

In a general case, one can decompose the pertubation $\boldsymbol{b}$ into contributions dependent on or independent of the magnetization configuration $\boldsymbol{m}$:

$$\boldsymbol{b} = \boldsymbol{b}_0 + \widehat{\boldsymbol{R}} * \boldsymbol{m} \, , \tag{1.37}$$

where $\boldsymbol{b}_0$ is the perturbation field in the equilibrium state, and $\widehat{\boldsymbol{R}}$ is a certain linear

operator. For instance, in the case of the Gilbert damping, $\boldsymbol{b}_0 = 0$ and

$$\widehat{\boldsymbol{R}} * \boldsymbol{m} = i\frac{\alpha}{\gamma}\sum_{\nu}\omega_\nu(a_\nu(t)\boldsymbol{m}_\nu(\boldsymbol{r}) - \text{c.c.})\,,$$

where we approximate Eq. (1.36) as zero.

Substituting the series representation Eq. (1.35) and the representation of the perturbation field Eq. (1.37) into Eq. (1.34) and using orthogonality relations Eq. (1.27), one can obtain the following equations for spin wave amplitudes a_ν:

$$\frac{da_\nu}{dt} = -i\omega_\nu a_\nu + i\gamma\sum_{\nu'}\left(S_{\nu,\nu'}a_{\nu'} + \tilde{S}_{\nu,\nu'}a^*_{\nu'}\right) + i\gamma b_\nu\,, \tag{1.38}$$

where

$$S_{\nu,\nu'} = \frac{\left\langle \boldsymbol{m}^*_\nu \cdot \widehat{\boldsymbol{R}} * \boldsymbol{m}_{\nu'}\right\rangle - \langle(\boldsymbol{\mu}\cdot\boldsymbol{b}_0)(\boldsymbol{m}^*_\nu\cdot\boldsymbol{m}_{\nu'})\rangle}{C_\nu}\,, \tag{1.39a}$$

$$\tilde{S}_{\nu,\nu'} = \frac{\left\langle \boldsymbol{m}^*_\nu \cdot \widehat{\boldsymbol{R}} * \boldsymbol{m}^*_{\nu'}\right\rangle - \langle(\boldsymbol{\mu}\cdot\boldsymbol{b}_0)(\boldsymbol{m}^*_\nu\cdot\boldsymbol{m}^*_{\nu'})\rangle}{C_\nu}\,, \tag{1.39b}$$

$$b_\nu = \frac{\langle \boldsymbol{m}^*_\nu\cdot\boldsymbol{b}_0\rangle}{C_\nu}\,. \tag{1.39c}$$

For the case of Gilbert damping the only significant perturbation term is the diagonal term $S_{\nu,\nu} = i\alpha\omega_\nu\langle\boldsymbol{m}^*_\nu\cdot\boldsymbol{m}_\nu\rangle/(\gamma C_\nu)$ (assuming that there are no degenerate modes). Eqs. (1.38) in this case have a simple form

$$\frac{da_\nu}{dt} = -i\omega_\nu a_\nu - \Gamma_\nu a_\nu\,, \tag{1.40}$$

where the spin wave damping rate Γ_ν is given by

$$\Gamma_\nu = \alpha\omega_\nu\frac{\langle\boldsymbol{m}^*_\nu\cdot\boldsymbol{m}_\nu\rangle}{C_\nu}\,. \tag{1.41}$$

1.1.0.3 Confined geometry - spatial texture - eigenvalues and vectors in a disk

Although confined geometries are not directly related to our measurements, it is important to understand some key points of the magnetic excitation specific to this situation, that is, energetically discrete eigenmodes due to its geometrical restriction. We take an example of the perpendicularly magnetized disk reported in Ref. [61]. A specific feature of the disk-shaped geometry is its azimuthal symmetry. Mathematically, this is interpreted that the operator $\boldsymbol{\mu}\times\widehat{\boldsymbol{\Omega}}$ commutes with the operator $\widehat{\boldsymbol{R}}_z(\alpha)$ that describes rotation by the angle α about $\boldsymbol{\mu} = \boldsymbol{z}$ axis. The boundary conditions are invariant under such rotations.

This fact allows us to classify the spin wave modes of an azimuthally magnetized disk according to their behavior under the rotations in the $x-y$ plane. Namely, spin wave

eigenmodes are eigenfunctions of the operator of infinitesimal rotation with respect to $\boldsymbol{z}$ axis corresponding to a certain integer azimuthal number ℓ:

$$\frac{\partial \boldsymbol{m}}{\partial \phi} - \boldsymbol{z} \times \boldsymbol{m} = -i(\ell - 1)\boldsymbol{m} \,. \tag{1.42}$$

Here ϕ is the azimuthal angle of the polar coordinate system. Eq. (1.42) determines the spatial texture of spin wave modes and their dependence on the angle ϕ. Namely, Eq. (1.42) for a fixed ℓ has two classes of solutions:

$$\boldsymbol{m}_\ell^{(1)} = (\boldsymbol{x} + i\boldsymbol{y})e^{-i\ell\phi}\psi_\ell^{(1)}(\rho)\,, \tag{1.43a}$$

and

$$\boldsymbol{m}_\ell^{(2)} = (\boldsymbol{x} - i\boldsymbol{y})e^{-i(\ell-2)\phi}\psi_\ell^{(2)}(\rho)\,, \tag{1.43b}$$

where $\psi_\ell^{(1)}(\rho)$ $\psi_\ell^{(2)}(\rho)$ describe the dependence of spin wave mode on the radial coordinate ρ determined from the dynamical equations of motion. Thus azimuthal symmetry allows one to reduce two-dimensional (ρ and ϕ) vector equations to a one-dimensional (ρ) scalar problem.

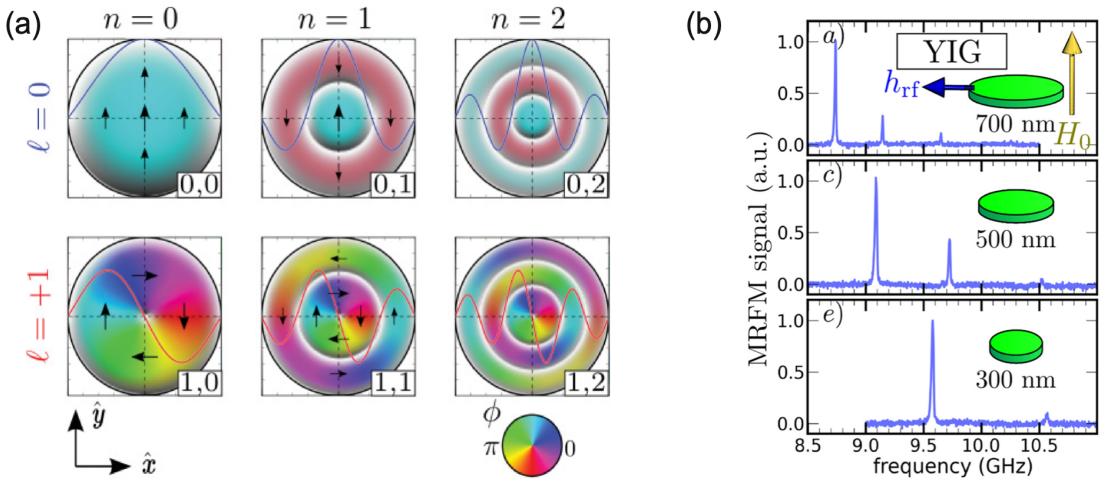

Figure 2: *(a) Example spatial texture of the spin wave eigenmodes in the case of a disk. It corresponds to the color representation of the spatial textures described by the Bessel function for different $\nu = (l, n)$ with the azimuthal mode index l (by row) and radial mode index n (by column). The arrows represent the dynamical component of magnetization and the color represents its phase (direction). The solid line represents the spatial distribution of the amplitude. The figure is taken from Ref. [61]. (b) Experimentally observed spectra with azimuthal index $l = 0$, showing the splitting of frequency between eigenmodes. The top, middle and bottom panels are for a diameter of 700 nm, 500 nm, and 300 nm respectively. The figure is taken from Ref. [63].*

In the following we will drop the superscript (1) in $\boldsymbol{m}_\ell^{(1)}$ and $\psi_\ell^{(1)}$ for simplicity. The spin wave frequencies can be obtained using Eq. (1.29) and appropriate radial functions $\psi_\ell(\rho)$. Here, we can take advantage of the variational stability of Eq. (1.29) and, instead of exact radial profiles $\psi_\ell(\rho)$, use some reasonable set of functions. Let us use radial profiles of the form $\phi_\ell(\rho) = J_\ell(k_{\ell,n}\rho)$, where $J_\ell(x)$ is the Bessel function and $k_{\ell,n}$ are wave numbers determined from the pinning conditions at the disk boundary $\rho = R$. We shall

use $k_{\ell,n} = \kappa_{\ell,n}/R$, where $\kappa_{\ell,n}$ is the n-th root of the Bessel function of the ℓ-th order.

Fig. 2(a) shows example spatial textures of the spin wave eigenmodes in the case of a disk described by the Bessel function for different $\nu = (l, n)$ with the azimuthal mode index l (by row) and radial mode index n (by column). From those magnetization distributions, one can compute the corresponding eigen frequencies by using Eq. (1.29). Panel (b) shows experimentally measured example spectra with azimuthal index $l = 0$, showing the splitting of the frequency between eigenmodes. The different panels show the different diameters of the disk. As the disk reduces the size, the number of peaks decreases because the possible values of wave vector are limited by the lateral size of the sample.

1.1.0.4 Extended geometry - propagating waves - magnon dispersion relation

In the previous subsubsection, we mentioned magnetic dynamics in confined geometries using an example of a disk. Due to the geometrical restriction, possible wave vectors $\boldsymbol{k}$ are discrete due to the pinning condition. It leads to the eigenvalues of magnetic dynamics defined by some indexes. In the case of a magnetic disk, it is radial number index n and azimuthal index l. However in extended geometries on the other hand, possible $\boldsymbol{k}$ are free from the restriction and we have to consider any values. Such eigen modes with $k \neq 0$ represent the propagating spin waves that follow the dispersion relation as shown in Fig. 3(a). Its derivation accompanies very complicated calculations. Fortunately Kalinikos and Slavin solved the problem in 1986 as mentioned previously [26] and needless to say it contributes tremendously to the spintronics community. Here we write down the final results of their calculation. Let us first define $\omega_H = \mu_0\gamma H_0,\ \omega_M = \mu_0\gamma M_s$. One can think of quantized waves in finite size waveguides whose thickness is t. Thus the wave vector becomes now components of in-plane propagation $k_x^2 + k_y^2$ and the integer quantization index m along the thickness.

$$k^2 = k_x^2 + k_y^2 + (\frac{m\pi}{t})^2 \tag{1.44}$$

Assuming that the magnetic field is applied in $\hat{\boldsymbol{x}}$, the dispersion relation is expressed by using the polar angle θ ($\theta = 0$ represents the normal to plane) of magnetization direction and plane angle $\tan\phi = \frac{k_y}{k_x}$ of the propagating direction such that

$$\omega_k^2 = (\omega_H + \lambda^2\omega_M k^2)(\omega_H + \lambda^2\omega_M k^2 + \omega_M F_m) \tag{1.45}$$

$$F_m = P_m + \sin^2\theta\left(1 - P_m(1 + \cos^2\phi) + \frac{\omega_M P_m(1 - P_m)\sin^2\phi}{\omega_H + \lambda^2\omega_M k^2}\right) \tag{1.46}$$

$$P_m = \frac{k_x^2 + k_y^2}{k^2}\left(1 - \frac{k_x^2 + k_y^2}{k^2}\frac{2}{1 + \delta_{0,m}}\frac{1 - (-1)^m e^{-\sqrt{k_x^2+k_y^2}t}}{\sqrt{k_x^2 + k_y^2}t}\right) \tag{1.47}$$

where $\lambda = \sqrt{\frac{2A_{\mathrm{ex}}}{\mu_0 M_s^2}}$ is the exchange length. In this manuscript, we use thin films of magnetic materials and we focus on $m = 0$, which is uniform in thickness, as the energy of higher order modes is much larger. In addition, the in-plane magnetic field is used and in-plane propagating modes are detected in our experiments. If one only considers the spin wave modes in such condition, thus $\theta = \pi/2$, the dispersion relation of $\boldsymbol{k} = k(\cos\phi, \sin\phi, 0)$ is relatively simplified as follows including the effect of uniaxial perpendicular anisotropy

$\omega_{\text{anis}} = \gamma B_{\text{anis}}$ as follows.

$$\omega_k^2 = A_k^2 - B_k^2 \tag{1.48}$$

$$A_k = \omega_H + \lambda^2 \omega_M k^2 + \frac{1}{2}\omega_M \left((\sin^2\phi - 1)(1 - \frac{1 - e^{-kt}}{kt}) + 1 \right) - \frac{1}{2}\omega_{\text{anis}} \tag{1.49}$$

$$B_k = \frac{1}{2}\omega_M \left((\sin^2\phi + 1)(1 - \frac{1 - e^{-kt}}{kt}) - 1 \right) + \frac{1}{2}\omega_{\text{anis}} \tag{1.50}$$

It is worth introducing that at large k, the frequency has an approximated form, which shows quadratic dependence in k.

$$\omega_k \approx \omega_M \lambda^2 k^2 \tag{1.51}$$

Dispersion relations for a spin wave propagating in-plane whose direction is either along ($\hat{\boldsymbol{x}}$) or orthogonal to ($\hat{\boldsymbol{y}}$) the magnetization are useful to interpret the experimental data. The group velocity is obtained by simply doing differential $\partial_k \omega$. Let us consider now $\boldsymbol{k} = k\hat{\boldsymbol{x}}$ or $k\hat{\boldsymbol{y}}$, relevant in our experiments. Corresponding plots for dispersion relations for below listed modes are shown in Fig. (3)(b) using parameters as $\mu_0 H = 0.2$ T, $\mu_0 M_s = 0.17$ T, $A_{\text{ex}} = 4 \times 10^{-12}$ J/m, $\gamma/2\pi = 28.5$ GHz/T, $t = 60$ nm.

- *Magnetostatic surface spin wave (MSSW)* $\boldsymbol{M} \perp \boldsymbol{k}$

$$\omega_k = \sqrt{(\omega_H + \lambda^2 \omega_M k^2 + \omega_M \frac{1 - e^{-kt}}{kt} - \omega_{\text{anis}})(\omega_H + \lambda^2 \omega_M k^2 + \omega_M (1 - \frac{1 - e^{-kt}}{kt}))} \tag{1.52}$$

  It is also called Damon-Eshbach mode. The energy minimum of this mode is $k = 0$, the Kittel mode. Literally the amplitude of precession is localized at the surface and decays in thickness. The specificity of this mode is that the surface where waves propagate can be switched by changing the direction of the magnetic field. In addition previous research achieved the continuous k conversion by an inhomogeneous external magnetic field at a fixed driving frequency and eventually the magnon is converted into a phonon at the cross section of this mode and phonon dispersion [64]. A similar idea is used to convert between the MSSW mode and the below explained BVMSW mode by temperature gradient [65].

- *Backward volume magnetostatic spin wave (BVMSW)* $\boldsymbol{M} /\!/ \boldsymbol{k}$

$$\omega_k = \sqrt{(\omega_H + \lambda^2 \omega_M k^2 + \omega_M \frac{1 - e^{-kt}}{kt} - \omega_{\text{anis}})(\omega_H + \lambda^2 \omega_M k^2)} \tag{1.53}$$

  As named as *volume*, the amplitude is homogeneous in thickness. Due to the self depolarization effect in a thin film, there is the optimal wavelength where the dipolar field of dynamical magnetization is canceled out. Thus there is an energy minimum at a finite k and the negative slope of the dispersion leads to negative group velocity, which implies that the phase and envelope travel in opposite directions. Thanks to such property, the research on magnon Bose-Einstein condensate has been active since the discovery in 2004 by populating all magnons at the energy minimum [66]. Experimentally we mostly detect this mode because of the symmetry of spin charge interconversion, the spin Hall effect.

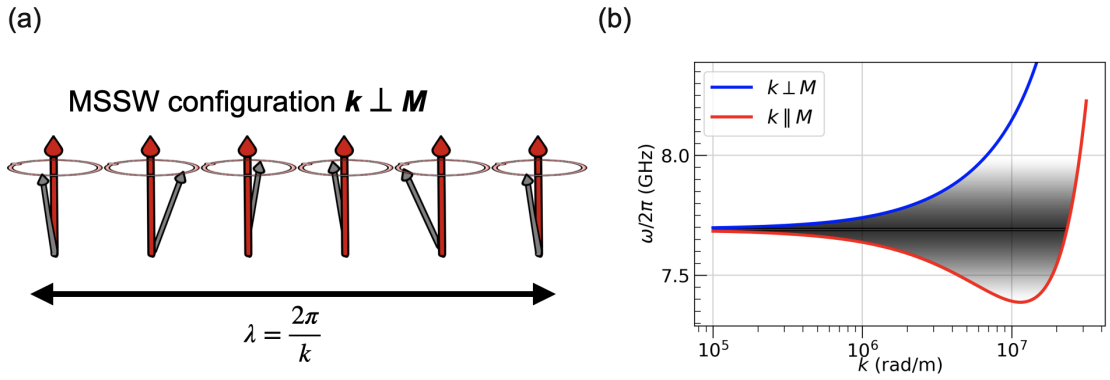

Figure 3: *(a) Schematic of a spin wave propagating in* $\boldsymbol{k} \perp \boldsymbol{M}$ *configuration. (b) Dispersion relation of the BVMSW mode (red) and MSSW (blue).* $\mu_0 H = 0.2$ *T,* $\mu_0 M_s = 0.17$ *mT,* $A_{\mathrm{ex}} = 4 \times 10^{-12}$ *J/m,* $\gamma/2\pi = 28.5$ *GHz/T,* $t = 60$ *nm are used as magnetic parameters.*

In extended geometries, spin waves can propagate any direction in-plane, meaning that there are an infinite number of eigen solutions capped between the BVMSW mode (red) and MSSW (blue). Thus the situation is completely different from the one for the confined geometries with energetically well split eigen solutions. The grey shade in panel (b) emphasizes the degree of the overlap sharing the same frequency and indeed the uniform mode (Kittel mode) with $k = 0$ has the largest degeneracy. In the following subsection, we will introduce a non-linear effect due to such mode degeneracy that consequences the saturation effect.

1.1.1 non-linear effects - saturation effect

Spin waves have rich non-linearity and tunability with applied power together with easy manipulation of resonant frequency by an external field. Such non-linearity has attracted much attention and contributed to opening up new research fields [20]. In this subsection we will introduce an important non-linear effect, the saturation effect occurred when the system is exposed to high input power. This is especially important to understand the experimental results. Let us first consider the time dependence of the magnetization along the equilibrium axis $\hat{\boldsymbol{z}}$ while the other components oscillate in frequency ω_k. It is written under small oscillation limit $\sqrt{m_x^2 + m_y^2} \ll M_s$ as follows.

$$m_z(t) = \sqrt{M_s^2 - m_x^2 \cos^2 \omega_k t - m_y^2 \sin^2 \omega_k t} \approx M_s - \frac{m_x^2 + m_y^2}{4M_s} + \frac{m_x^2 - m_y^2}{4M_s} \cos 2\omega_k t \quad (1.54)$$

The first two terms suggest that due to the oscillation the magnetization is eventually modified as $M_s \to M_s - \frac{m_x^2+m_y^2}{4M_s}$, which leads to the decrease of resonance frequency (red shift) as the precessional cone angle gets larger. The last term suggests that the system has an additional dynamical component along the equilibrium axis oscillating in $2\omega_k$, twice the driving frequency if $m_x^2 - m_y^2 \neq 0$. Considering the in-plane magnetized case in a thin film, the dynamical magnetization points normal to the plane during the precession ($m_x = 0, m_y = 1$), which causes the increase of magnetic charges at the opposite surface of the film and creates demagnetizing field pointing normal to plane. On the contrary, if the phase of precession is shifted by $\pi/2$ ($m_x = 1, m_y = 0$) such additional perpendicular

demagnetizing field is suppressed. This is because the in-plane demagnetizing field is much smaller since the wavelength is mostly much larger than the thickness of the film. In such a way, as shown in Fig. 6(a) magnetic precession causes the elliptic precession oscillating at twice the frequency, whose ellipticity is given by $|m_x/m_y|$. This additional precession effectively creates the oscillating field along the equilibrium axis and it can be a source of excitation of other modes. It is worth mentioning that this process is especially called *parallel pumping* and it causes some non-linear effects [67].

The single mode picture, where magnetization precesses harmonically in a defined frequency, is mainly true in a confined system such as nanopillars thanks to the finite size effect where possible k values are quantized due to the geometrical restriction as shown in Fig. 2. However in unconfined systems such as extended films corresponding to our measurements, the multimode picture should be considered (Fig. 3(b)).

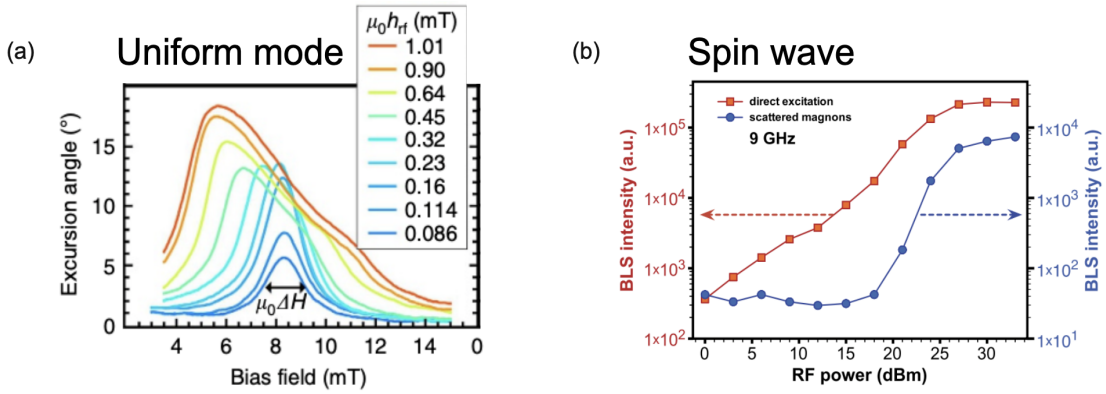

Figure 4: *(a) The power dependence of FMR spectrum showing the saturation of the uniform mode ($k = 0$). The Suhl instability effect can be seen in power dependence measurements of the spectrum. At high power the amplitude saturates, and instead the linewidth broadens. The figure is taken from Ref. [68]. (b) The power dependence of the spin wave amplitude ($k \neq 0$) launched with a microwave antenna detected in Brillouin light scattering measurement, which shows the saturation at high power. It also reveals the saturation of not only the main spin wave modes (red points), but also the coupled spin wave modes due to so called four magnon scattering (blue points). The figure is taken from Ref. [69].*

Now let us discuss the relevant non-linear effects in our measurements. This is the saturation effect. It is well known that when a magnetic system is exposed to a high input power, the precession reaches a saturation, especially in ferromagnetic resonance measurements. This has been explained by H. Suhl in the 1950s by introducing the interaction between the uniform mode (Kittel mode) and propagating modes, which is called Suhl's instability processes [25, 70]. Fig. 4(a) shows the FMR spectrum with different values of input power, showing the saturation of the amplitude of the uniform mode. The saturation effect is indeed observed in spin wave measurements [69, 71, 72]. Panel (b) shows the power dependence of the spin wave amplitude excited by a microwave antenna as a function of the input power. It also reveals the saturation of not only the main spin wave modes (red points), but also the coupled spin wave modes due to so called four magnon scattering (blue points). Even though FMR is not our concern, we will make an analogy with it for spin wave amplitude to understand our experimental results. Thus below we will introduce Suhl's early work that describes the saturation effect of the uniform mode. The following discussion is based on the Ref. [73] page 245. We seek the solution of the

equation of motion in the form

$$\boldsymbol{M} = M_s\hat{\boldsymbol{z}} + \boldsymbol{m}(\boldsymbol{r}, t) \tag{1.55}$$

with $|\boldsymbol{m}| \ll M_s$ a fluctuating component of magnetization. Let us expand it in the Fourier series:

$$\boldsymbol{m}(\boldsymbol{r}, t) = \sum_{\boldsymbol{k}} \boldsymbol{m}_{\boldsymbol{k}}(t) \exp(-i\boldsymbol{k} \cdot \boldsymbol{r}) \tag{1.56}$$

where the summation is over all allowed values of the wave vector $\boldsymbol{k}$. Note here that $k = 0$ corresponds to the uniform precession mode (Kittel mode). Let us introduce the second quantization form of magnetic precession using dimensionless complex conjugates a_k and a^*_{-k}.

$$a_k = \frac{m^k_x + im^k_y}{M_s} \tag{1.57}$$

$$a^*_{-k} = \frac{m^k_x - im^k_y}{M_s} \tag{1.58}$$

$$m_{\boldsymbol{k},z} = \frac{1}{2}M_s \sum_{k'} a'_k a^*_{k'-k} \tag{1.59}$$

The equation of motion of the uniform mode with the driving field $\boldsymbol{h} = (h_x, h_y, 0)$ oscillating orthogonal to the equilibrium axis is then rewritten [74]

$$-i\frac{\partial a_0}{\partial t} = a_0(\omega_0 + i\Gamma_0) + \gamma h \exp i\omega_p t \tag{1.60}$$

$$-i\frac{\partial a_k}{\partial t} = A_k a_k + B_k a_{-k} \tag{1.61}$$

where A_k and B_k are expressed as Eq. (1.49,1.50), h is the external a.c. field oscillating in frequency ω_p, and ω_0 is the eigenfrequnecy of the uniform modes. Γ_0 comes from the imaginary part of the frequency that describes the energy dissipation, thus magnetic damping due to relaxation processes. The ellipticity is then given by

$$\left|\frac{m_x}{m_y}\right| = \left|\frac{A_k + B_k}{A_k - B_k}\right| \tag{1.62}$$

For small k values around the Kittel frequency, B_k is comparable to A_k and the system has strong ellipticity. On the contrary for large k values with thermal energy, the exchange interaction dominates the dynamics and it leads to $B_k \ll A_k$, and then the precession is mostly circular.

Next, let us consider the instability process for spin wave modes which is in frequency degenerate with the uniform mode oscillating in driving frequency ω_p. In that case it is written as follows.

$$a_0 = \frac{\gamma h^+}{\omega_0 - \omega_p + i\Gamma_0} \exp(i\omega_p t) = a^0_0 \exp(i\omega_p t) \tag{1.63}$$

Now, two uniform mode magnons (a_0) scatter into the other two magnons with $\pm k$. The Holstein-Primakoff transformation gives

$$a_k = u_k c_k + v_k c^*_{-k} \tag{1.64}$$

$$a^*_{-k} = v^*_k c_k + u_k c^*_{-k} \tag{1.65}$$

Here c_k represents the coupled dynamics with the steady station solutions $c_k = c^0_k \exp(i\omega_k t)$ and $c^*_{-k} = c^{0*}_{-k} \exp(-i\omega_k t)$. $u_k = \frac{1}{\sqrt{2}}\sqrt{\frac{A_k}{\omega_k}+1}$, $v_k = \frac{1}{\sqrt{2}}\sqrt{\frac{A_k}{\omega_k}-1}\exp 2i\phi_k$ with $\tan\phi_k = k_y/k_x$. Considering the first and the second order in a_0, the equation of motion of the coupled mode c_k is then obtained by inserting Eq. (1.64,1.65) in Eq. (1.61) as

$$-i\frac{\partial c_k}{\partial t} = (\omega_k + i\Gamma_k)c_k + (\rho_k a_0 + \xi_k a_0^2)c^*_{-k} \tag{1.66}$$

$$i\frac{\partial c^*_{-k}}{\partial t} = (\omega_k - i\Gamma_k)c^*_{-k} + (\rho_k a_0 + \xi_k a_0^2)c_k \tag{1.67}$$

$$\rho_k = \rho_{-k} = -\frac{\omega_M}{4\omega_k}(\omega_k + \omega_H + \lambda^2\omega_M k^2)\sin 2\theta_k \exp i\phi_k \tag{1.68}$$

$$\xi_k = \xi_{-k} = \frac{\omega_k + A_k}{4\omega_k}(\omega_M \cos^2\theta_k + \lambda^2\omega_M k^2) \tag{1.69}$$

Here Γ_k is the loss of the coupled spin wave mode c_k and θ_k is the angle between the magnetization and wave vector. The Eq. (1.66,1.67) tells that the coupling between magnons with $\boldsymbol{k}$ and -$\boldsymbol{k}$ emerges from the Kittel mode a_0. Let us consider $\omega_p = \omega_0$ for simplicity. The energy is transferred to coupled oscillators with $\pm k$ from an external drive that excites the uniform mode magnons. In other words, the n uniform mode magnons are annihilated and in return two degenerated magnons $\omega_{\pm k}$ are created such that

$$n\omega_0 \rightarrowtail \omega_k + \omega_{-k} \tag{1.70}$$

At a certain threshold value of the external source, the energy transferred to the oscillators exceeds the losses of coupled modes and their amplitude eventually grows exponentially, *i.e.*, instability is established. The index n refers to the order of instability. For the second order instability $n = 2$, the Eq. (1.66-1.67) is approximated to

$$-i\frac{\partial c_k}{\partial t} = (\omega_k + i\Gamma_k)c_k + \xi_k a_0^2 c^*_{-k} \tag{1.71}$$

$$i\frac{\partial c^*_{-k}}{\partial t} = (\omega_k - i\Gamma_k)c^*_{-k} + \xi_k a_0^2 c_k \tag{1.72}$$

and the steady state solution is given in the form $c_k = c^0_k \exp(i\omega_0 t)$ because we consider the process $2\omega_0 \rightarrowtail \omega_k + \omega_{-k}$, thus $\omega_k = \omega_0$. The above equation tells us that the coupled modes are dominated by the second order of the initially excited uniform magnons $|a_0|^2$ with its prefactor ξ_k. Note that the prefactor ρ_k for the first order term a_0 becomes dominant for the case of $n = 1$, the first order instability which describes the process $\omega_p \rightarrowtail \omega_k + \omega_{-k}$ and thus $\omega_k \approx \omega_p/2$, which is important for the parametric pumping. Inserting the steady state solution in the equation of motion of the coupled modes in Eq. (1.72) gives the threshold amplitude of uniform mode $a^0_{0,\mathrm{th}}$ and corresponding threshold field h_{th} for the

onset of the instability as follows.

$$a^0_{0,\mathrm{th}} \approx \sqrt{\frac{\Gamma_k}{2\xi_k}} \approx \sqrt{\frac{\Gamma_0}{2\xi_k}} \propto \alpha^{1/2} \tag{1.73}$$

$$\gamma h_{\mathrm{th}} \approx \sqrt{\frac{\Gamma_k \Gamma_0^2}{\xi_k}} \approx \sqrt{\frac{\Gamma_0^3}{\xi_k}} \propto \alpha^{3/2} \tag{1.74}$$

Here we recall that Γ_0 describes the energy loss due to the magnetic damping and ξ_k is the order of ω_M. Considering that it can be a source of spin wave emission starting from the uniform mode excitation, the small magnetic damping α is indeed beneficial to have a small threshold for the instability process.

Until now we discussed the instability process that happens intrinsically and does not explain the saturation phenomenon. In fact, inhomogeneity of the magnetic property, which is always present in reality, such as disorders of ions, polycrystallinity, non-uniform stress or surface roughness, can affect the process extrinsically. It is well known that such non-uniformity creates the linewidth broadening or shift of resonance curves, and it is simply the consequence of the difference of the resonance conditions in different regions of the sample. Since the a.c. pumping field excites an entire group of different magnons which have the resonance close to each other, it creates additional relaxation channels for the main uniform mode a_0 or coupled modes c_k by scattering with inhomogeneity-originated modes via the dipole-dipole or the exchange interaction. This relaxation process by the inhomogeneity is called the two-magnon process. While we dealt with the energy and momentum conserving scattering process in Eq. (1.70) with $n = 2$, the two-magnon process allows us to have the *energy conserving* but *momentum non-conserving* scattering such that $\omega_0 \rightarrowtail \omega_k$. This is a linear process that will go on no matter how small the excitation is. Thus the spin waves most prone to instability introduced above are preferentially excited even in the limit of infinitesimal signals, by scattering of the uniform precession at inhomogeneity in the material. Such negative feedback to the uniform mode assures that its amplitude never actually exceeds the threshold value, no matter how large the driving power is. Taking into account the two-magnon process between the uniform mode a_0 or coupled modes c_k and impurity, the equation of motion in Eq. (1.72) is rewritten [70],

$$-i\frac{\partial a_0}{\partial t} = (\omega_0 + i\Gamma_0)a_0 + \sum_k \nu_{0,k} c_k + \gamma h \exp i\omega_0 t \tag{1.75}$$

$$-i\frac{\partial c_k}{\partial t} = (\omega_k + i\Gamma_k)c_k + \nu_{k,0} a_0 + \xi_k a_0^2 c^*_{-k} \tag{1.76}$$

$$i\frac{\partial c^*_{-k}}{\partial t} = (\omega_k - i\Gamma_k)c^*_{-k} + \nu_{k,0} a_0 + \xi_k a_0^2 c_k \tag{1.77}$$

where the rate of change of the uniform precession contains a scattering term to the spin waves, of the form $\sum_k \nu_{0,k} c_k$ with $|\nu_{0,k}|^2$ is the square of the scattering matrix element. Conversely the rates of change of the spin wave amplitudes contain a scattering term $\nu_{k,0} c_0$. Inserting the steady state solution to the above equations gives the amplitude of

the uniform mode at the resonance a_0^0 and corresponding coupled modes c_k^0 such that,

$$a_0^0 = \frac{\gamma h}{\Gamma_0 + \sum_k \frac{|\nu_{0,k}|^2 \Gamma_k}{\Gamma_k^2 - \xi_k^2 (a_0^0)^4}} \tag{1.78}$$

$$c_k^0 = \frac{i\nu_{k0} a_0^0 \left(\Gamma_k - i\xi_k (a_0^0)^2\right)}{\Gamma_k^2 - \xi_k^2 (a_0^0)^4} \tag{1.79}$$

Eq. (1.78) tells as $|a_0^0|$ increases, $\sum_k$ steadily increases as well, so that the right-hand side decreases. It continues until it reaches zero when $|a_0^0|$ attains a certain values $a_{0,c}^0 = \sqrt{\Gamma_k/\xi_k}$ for which the denominator in $\sum_k$ is infinite. To capture it intuitively, a drastic simplification can be proposed by H. Suhl [70], that is, $\Gamma_k, \xi_k, \nu_{k,0}$ and $\nu_{0,k}$ do not vary in the vicinity of the resonance ω_0. Thus for small k we now have $\Gamma_k \to \Gamma$, $\xi_k \to \xi$, $\nu_{0,k} = \nu_{k,0} \to \nu$ and $a_{0,c}^0 \to \sqrt{\Gamma/\xi}$. Also the $\sum_k$ can be converted into the integral $\int d\omega_k$ with a certain density of states $D(\omega_k)$. As a result, Eq. (1.78-1.79) have a simplified form such that

$$a_0^0 \approx \frac{\gamma h}{\Gamma_0 + \frac{\Gamma_0^s}{\sqrt{1 - (a_0^0/a_{0,c}^0)^4}}} \tag{1.80}$$

$$|c_k^0| \approx \frac{a_0^0 \nu}{\Gamma \sqrt{1 - (a_0^0/a_{0,c})^4}} \tag{1.81}$$

where $\Gamma_0^s = |\nu|^2 D(\omega_0)$ is the additional relaxation due to the two-magnon process. One can see from Eq. (1.80) that the effective dissipation parameter of the uniform mode infinitely increases when a_0^0 approaches $a_{0,c}^0$, which prevents the growth of the a_0^0 even at larger h. Fig. 5(a) graphically shows the relationship of the left hand side (black linear line) and right hand side (colored curves with different values of h) of Eq. (1.80). The intersection of the line and a curve gives the solution for a_0^0 at given h. Panel (b) summarizes the behavior of a_0^0 as a function of h, showing the saturation no matter how large the input power is. This effective increase of dissipation due to the Lorentz factor-like denominator $1/\sqrt{1 - (a_0^0/a_{0,c}^0)^4}$ leads to the linewidth broadening of FMR spectrum at high power as shown in Fig. 4(a), which was initially investigated by E. Schlömann in the 1950s [75,76]. It also reveals that the amplitude of the coupled mode, *spin wave*, is affected by the amplitude of the uniform mode. The above explanation started from the microwave excitation of the uniform mode and it is not the case for our measurements using the spin transfer effects. Despite that, we will show some evidence from our experiments and simulations that a large number of localized modes underneath the Pt wire is generated and it is reasonable to consider Suhl's instability process that launches spin waves. To see the saturation of spin wave mode $|c_k^0|$ as observed in Fig. 4(b), we need to implement the energy and momentum conserving four magnon scattering process, such that generated pairs of spin waves flowing oppositely with $\pm k$ scatter each other into another pair of spin waves with $\pm k'$, that is, $\omega_k + \omega_{-k} \rightarrowtail \omega_{k'} + \omega_{-k'}$ [69,72]. To implement the effect of saturation in the following experimental chapters, we pay attention to such an effective increase of the relaxation rate of spin waves. Using the number of magnons (intensity) n instead of the amplitude and its corresponding threshold number N_{sat}, the effective relaxation rate that has the dependence on n in the form of the Lorentz transformation

can be rewritten such that

$$\Gamma \to \frac{\Gamma}{\sqrt{1-(n/N_{\mathrm{sat}})^2}}, \tag{1.82}$$

Here we omit the intrinsic relaxation in the limit of $n \to N_{\mathrm{sat}}$. The Eq. (1.82) will be shown again in the subsection (1.2.5.4) to express the spin wave conductivity exposed to high power. Note that ideally such saturation effects should be suppressed if one wants to populate a certain mode more. Below the importance of the perpendicular uniaxial anisotropy will be mentioned in this context.

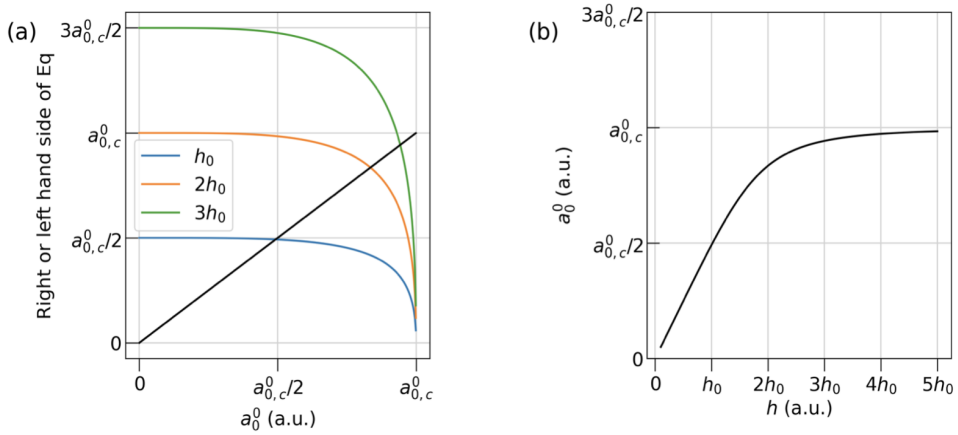

Figure 5: *(a) The left hand side (black linear line) and right hand side (colored in blue, orange, green for different values of h) of Eq. (1.80). The intersection of the linear and a colored curve gives the solutions for a_0^0. (b) a_0^0 as a function of h, showing the saturation. The parameters are arbitrarily chosen.*

Let us put emphasis on the effect of the perpendicular uniaxial anisotropy on the non-linear effects. The ellipticity of the magnetic precession, which induces the coupling between magnons (through the parallel pumping process), is significant for a small k value. In the limit of $k \to 0$ the term B_k in Eq. (1.50) is then becomes $B_k \to \frac{-\omega_M+\omega_{\mathrm{anis}}}{2}$. Thus when the anisotropy is strong enough to have $\mu_0 M_s \approx \mu_0 H_{\mathrm{anis}}$, B_k goes to zero. This leads to the circular precession even for small k values since the ellipticity is 1 as shown in Fig. 6(b). As a result, using the perpendicular uniaxial anisotropy material helps to reduce the non-linear effects. However, the second order instability cannot be canceled out but one can decrease the coefficient for coupled modes ξ_k by reducing the value of $A_k \to \frac{\omega_H+\omega_M-\omega_{\mathrm{anis}}}{2}$. Consequently the value of critical amplitude $a^0_{0,c} = \sqrt{\Gamma_k/\xi_k}$ gets larger, allowing us to populate more magnons in a certain mode before entering the saturation. Another significant contribution by having strong anisotropy is that the Kittel frequency becomes independent of the magnetization as $\omega_K = \sqrt{(\omega_H + \omega_M - \omega_{\mathrm{anis}})}$, which reduces the effect of the non-linear frequency shift when the cone angle gets larger, or the Joule heating which decreases the magnetization. Recently previous studies have shown that a more efficient population of magnons excited by the spin transfer effect is possible by using the material with perpendicular anisotropy [77–79].

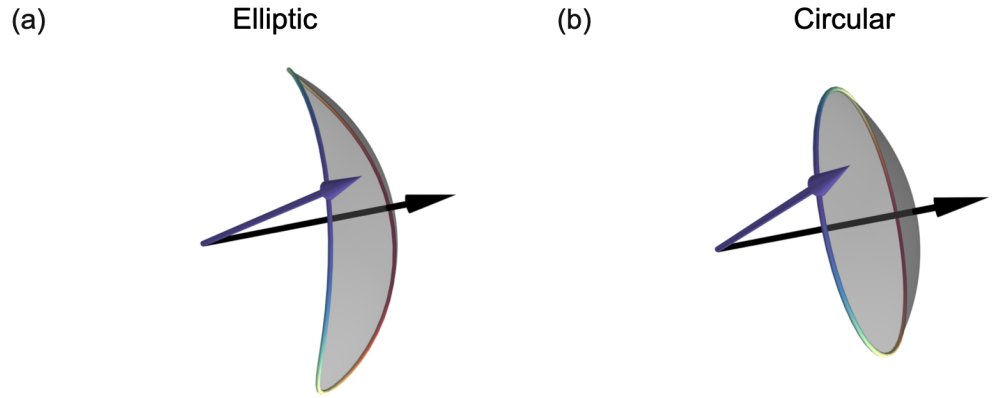

Figure 6: *(a) Schematic of magnetization precession without perpendicular anisotropy (YIG) showing the elliptic behavior. (b) Schematic of magnetization precession with strong enough perpendicular anisotropy (BiYIG) to compensate the effect of demagnetizing field, which shows the complete circular behavior.*

To conclude this section, firstly we briefly explained the eigen value problem in magnetic excitations. Due to the geometrical restriction, confined geometries such as nano-pillar can take discrete values of wave vector and their excitation is basically solved as spatial textures. On the other hand in extended geometries any value of wave vector is allowed and it leads to spin wave emission. We introduced the very important formula of the magnon dispersion relation. Secondly we introduced the non-linear instability process where the uniform mode can couple to other propagating modes through the energy and momentum conserving scattering processes. It leads to the saturation effect on the uniform mode where an effective increase of the relaxation rate in a Lorentz factor-like form appears. This guides us to implement the saturation effects on spin waves in our measurements, which will be explained more in the next section. This picture makes sense for unconfined extended geometries where magnons can take any energetically degenerated modes in dispersion relation around the Kittel frequency. Lastly we mentioned the usefulness of materials with perpendicular uniaxial anisotropy to suppress such non-linear effects.

1.2 Non-local magnon transport experiments

Our focus in this manuscript is to understand and control the transport property of magnons generated either by the spin transfer effect between a ferromagnetic insulator and the adjacent heavy metal layer or temperature gradient, which is eventually detected electrically. This kind of study is sometimes called *non-local magnon transport*. The concept of this field is first proposed and demonstrated by Prof. E. Saitoh's group at Tohoku University (now they moved to Tokyo) in Japan [47, 51]. Then it is further formalized and highly developed by the group of Prof. B. Van Wees's group in Groningen in Netherlands [52] and Prof. S.T.B Goennenwein's group in Munich (now they moved to Dresden and Konstanz) in Germany [53]. Unlike the typical setup of magnonic research, one needs only DC current source and voltmeter. In this section, we will introduce the basic principle of the spin transfer effect between the ferromagnetic insulator and the adjacent heavy metal layer. Then we will show how this effect affects the magnetization dynamics in confined or extended geometries. Especially the latter is our main focus. We develop the analytical framework to describe the characteristics of the magnon transport

electrically excited by the spin transfer effects.

1.2.1 Spin transfer effects

The transfer of spin angular momentum in itinerant electrons in a metal to local spins (or magnetization globally) is possible. This means that a specific current (spin current or spin polarized current) that has large net spin angular momentum can apply torques and indeed modifies the LLG equation, exciting the dynamics. Such formalism of spin transfer torque (STT) is established by Slonczewski [11] and Berger [80] in 1996. This discovery indeed expands the possibility of spintronics which provides ways to manipulate the dynamical properties of spins by electrical current. STT can move local spin textures such as domain walls [81] and skyrmions [82], can switch the magnetization [83] and can induce magnetization dynamics [84]. Also their reciprocal effects are proposed and observed. The movement of magnetic texture leads to spin current generation (spin motive force) [85, 86] and the same things happen in magnetization dynamics [44, 87], which is called spin pumping. Such early discoveries are thanks to the so called spin polarized current, where the electrical current flowing in $3d$ ferromagnetic metals (Fe, Ni, Co) feels unbalance of conductivity between spin up and down because $3d_\uparrow$ and $3d_\downarrow$ are well split in the band structure creating unequal density of state and thus unequal conductivity. Recently new paradigm has emerged thanks to the discovery of the spin Hall effect (SHE) [14, 15, 17, 88], where a non magnetic heavy metal layer acts as spin current source. Such STT application thanks to the spin Hall effect is sometimes called spin orbit torque (SOT). It allows us to inject pure spin current to magnetic insulators as well. Let us briefly explain such phenomena.

Spin current is in general expressed with a 3 by 3 tensor whose column is polarization direction and row is the direction of flow. The relationship between charge current $\boldsymbol{j_c}$ and spin current $\boldsymbol{j_s}$ is obtained by decomposing into the contribution of spin up $\boldsymbol{j}_\uparrow$ and down $\boldsymbol{j}_\downarrow$ such that

$$\boldsymbol{j_c} = \boldsymbol{j}_\uparrow + \boldsymbol{j}_\downarrow, \quad \boldsymbol{j_s} = -\frac{\hbar}{2e}(\boldsymbol{j}_\uparrow - \boldsymbol{j}_\downarrow) \tag{1.83}$$

where $\frac{\hbar}{2e}$ represents the spin angular moment per charge current. One way to generate spin current is to utilize the SHE which occurs in non magnetic heavy metals such as Pt, Ta and W thanks to their large spin orbit coupling. When charge current is applied in such metal, the electrons are deflected in the orthogonal direction to current flow. Unlike the ordinary Hall effect where the Lorentz force is the main drive of deviation, spin direction dependent scattering occurs. Thus spin up electrons go one way and spin down electrons go the other way, creating $\boldsymbol{j_c} = 0$ however $\boldsymbol{j_s} \neq 0$. Such spin to charge conversion process is phenomenologically described as follows.

$$\boldsymbol{j_s} = \frac{\hbar}{2e}\theta_{\mathrm{SHE}}(\boldsymbol{\sigma} \times \boldsymbol{j_c}) \tag{1.84}$$

where θ_{SHE} is the spin Hall angle which represents the efficiency of conversion. Typical values of θ_{SHE} is $0.05 \sim 0.1$ for Pt [89, 90]. In practice, we inject an electrical charge current along the Pt wire axis. Thus the studied device geometry is usually $\boldsymbol{j_c} \parallel \hat{\boldsymbol{x}}$ and effectively we consider only $\boldsymbol{j_s} \parallel \hat{\boldsymbol{z}}$, thus $\boldsymbol{\sigma} \parallel \hat{\boldsymbol{y}}$. Its reciprocal effect, the inverse spin Hall effect (ISHE) is also observed [87] such that the injection of spin current in heavy metal leads to the generation of charge current.

$$\boldsymbol{j_c} = -\frac{2e}{\hbar}\theta_{\mathrm{SHE}}(\boldsymbol{\sigma} \times \boldsymbol{j_s}) \tag{1.85}$$

Measuring the ISHE signal is a powerful way to detect magnetic precession by depositing a heavy metal layer on top of a ferromagnetic layer. The spin current which is injected from the ferromagnetic layer to the heavy metal layer, *i.e.* spin pumping, is expressed as [91].

$$\boldsymbol{j}_{\mathbf{sp}} = -\frac{\hbar g^{\uparrow\downarrow}}{4\pi M_s^2}(\boldsymbol{M} \times \frac{\partial \boldsymbol{M}}{\partial t}) \tag{1.86}$$

where $g^{\uparrow\downarrow}$ is the spin mixing conductance, a characteristic parameter of spin transmission at the interface between a ferromagnet and a heavy metal layer. Combining the above two equations, one can detect the magnetic precession underneath the heavy metal layer as a charge current there. On the other hand this equation effectively has the same symmetry as the damping term of the LLG equation in Eq. (1.14).

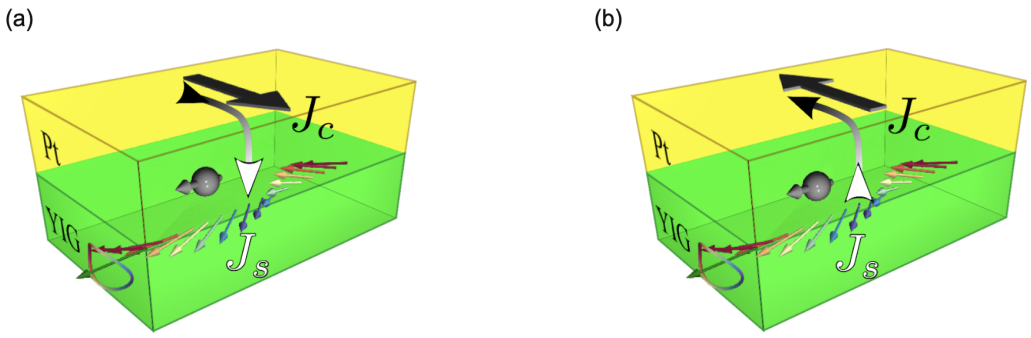

Figure 7: *(a) Schematic of the spin Hall effect and spin orbit torque which appears in YIG/Pt system. (b) Schematic of the spin pumping and inverse spin Hall effect.*

Now let us consider the inverse effect where the injection of spin current from the heavy metal layer into the ferromagnetic layer induces the dynamics of magnetization, *i.e.*, spin torque $\boldsymbol{\tau}_{\mathbf{st}}$.

$$\boldsymbol{\tau}_{\mathbf{st}} = -\frac{\gamma}{M_s^2 t_{\mathrm{FM}}} j_s \left(\boldsymbol{M} \times (\boldsymbol{M} \times \boldsymbol{\sigma})\right) = -\frac{\epsilon\gamma}{2eM_s^2 t_{\mathrm{FM}}} j_c \left(\boldsymbol{M} \times (\boldsymbol{M} \times \boldsymbol{\sigma})\right) \tag{1.87}$$

where ϵ is the spin to charge conversion efficiency accounting for the interface transparency and spin Hall angle. The effect is maximized when $\boldsymbol{M} \perp \boldsymbol{\sigma}$. This equation namely describes the angular momentum transfer between the spin current and magnetization dynamics. Again it has the same form as the damping term of LLG equation, which means that the spin current effectively modulates the magnetic damping. Therefore depending on the direction of the charge current in the heavy metal, one can either enhance or reduce the damping. This kind of spin torque is called *damping like spin torque*. The former and latter situations correspond to the magnon creation and annihilation respectively. Most importantly such spin current from the adjacent heavy metal layer can be injected to the ferromagnetic insulator and it can apply torques to magnetization, which eventually induces the dynamics. Such spin torque application via spin Hall effect is called *spin orbit torque*. Another striking benefit of spin orbit torques is that DC current excites dynamics of magnetization which oscillates in GHz, which can be used to DC to RF converter [40, 84]. Note that one can consider the spin torque with the same symmetry as the 1st term of LLG equation, the conservative torque driven by the effective field. This type of spin torque is called *field like spin torque*. It basically acts as the correction term

for the effective field and does not significantly affect the precessional dynamics. Thus we omit this contribution.

1.2.2 Magnon excitation by spin transfer effect

Let us consider a magnon generation by the damping-like spin orbit torques at the interface between Pt and a ferromagnetic layer. Here one should pay attention that according to the symmetry of spin Hall effect, the direction of flow of spin current is fixed in $\hat{\boldsymbol{z}}$ due to sample stack geometry, thus the spin polarization direction and converted charge current direction have to be inplane and orthogonal to each other. As a result the magnetization direction (or external magnetic field direction) and charge current direction (or Pt wire axis) have to be orthogonal to each other. Considering that the polarization of spin current and charge current should be orthogonal, the relationship of each vectorial parameter is summarized as follows.

$$\boldsymbol{j_s} \parallel \hat{\boldsymbol{z}}, \quad \boldsymbol{\sigma} \parallel \boldsymbol{M} \parallel \hat{\boldsymbol{x}}, \quad \boldsymbol{j_c} \parallel \hat{\boldsymbol{y}} \tag{1.88}$$

Thus naively speaking there should be no spin orbit torque applied to magnetization because $(\boldsymbol{M} \times (\boldsymbol{M} \times \boldsymbol{\sigma})) = 0$. It is in reality true at zero temperature where no thermal fluctuation is induced. However at finite temperature, the magnetization feels stochastic noise and such small perturbation can be subject to the spin orbit torque. Indeed we will conduct measurements at room temperature and later in chapter 4 we will show that the thermal fluctuation is an important parameter that affects the conduction behavior. In short, the spin orbit torque affects the degree of thermal fluctuation and it controls the magnon population, which corresponds to magnon chemical potential μ_M (explained in detail in two subsections after). Fig. 8 depicts the situation. It exerts torque to initially activated thermal fluctuation (grey cone) and it either expands (blue cone with spin direction anti-parallel to magnetization in left panel) or shrinks (red cone with spin direction parallel to magnetization in right panel) the cone, which corresponds to magnon generation and annihilation respectively.

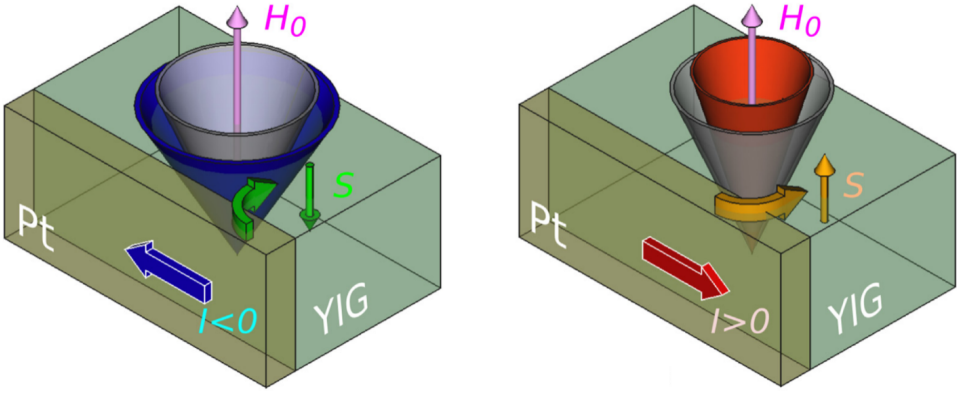

Figure 8: *Schematics of magnon generation and annihilation by spin orbit torques. It exerts torques to initially activated thermal fluctuation (grey cone) and it either expands (blue cone in left panel) or shrinks (red cone in right panel) the cone, which corresponds to magnon generation and annihilation respectively. This figure is taken from Ref. [92].*

1.2.3 Confined geometry - auto-oscillation

As mentioned in the previous subsection, the transfer of angular momentum from spin current to local magnetization is possible, inducing the dynamics. By choosing the direction of spin torque to compensate the magnetic damping, one can achieve lossless dynamics at a certain threshold current. This phenomenon is called auto-oscillation, and a device showing it is sometimes referred to as a spin torque nano oscillator. Theoretical understanding has been well established thanks to the contribution of Prof A. Slavin and Tiberkevich at Oakland University in the U.S [93]. This opens up the new potential of magnonics such as nanoscale microwave emitter excited by DC current, and also artificial neuron device [94], unconventional computing [95] as new trends. An important premise is that the possible modes are well split between each other so that a certain mode (usually the uniform mode with the lowest energy) can be populated dominantly [49]. Thus the arguments of auto-oscillation make sense in confined geometries such as quasi-zero dimensional nanopillars because possible wave numbers are quantized due to the geometrical confinement. The explanation below is for metallic nanopillars in the current to flow perpendicular to plane (CPP) configuration where the system oscillates harmonically with a single mode through the direct spin transfer torque. Thus the spin orbit torque application to extended insulating film is not directly the case. Now the LLG equation Eq. (1.14) has the spin torque term as follows.

$$\frac{\partial}{\partial t}\boldsymbol{M} = -\gamma \boldsymbol{M} \times \boldsymbol{B}_{\text{eff}} + \alpha\gamma \frac{\boldsymbol{M}}{M_s} \times (\boldsymbol{M} \times \boldsymbol{B}_{\text{eff}}) - \frac{\sigma I}{M_s}\gamma \boldsymbol{M} \times (\boldsymbol{M} \times \boldsymbol{\sigma}) \tag{1.89}$$

where $\sigma = \epsilon/2e\mathcal{N}$ is the spin transfer efficiency with ϵ material dependent spin torque parameter and $\mathcal{N} = VM_s/g\mu_B$ is the number of magnetic moments in a device. A schematic of the vectorial relationship is depicted in Fig. (9), showing that the spin torque compensates the magnetic damping. At the threshold current I_{th} for the onset of auto-oscillation, the relaxation rate of the magnetic damping Γ_K for magnons around the Kittel frequency and spin angular momentum transfer rate σI should be equal such that,

$$I_{\text{th}}/e = \frac{\Gamma_K}{\sigma} \approx 2\alpha\omega_k\mathcal{N}/\epsilon \tag{1.90}$$

The decrease of magnetization along the equilibrium axis (external magnetic field) ΔM_z due to cone opening represents the amplitude of magnetic precession such that

$$\frac{\Delta M_z}{2M_s} = \frac{k_B T}{\mathcal{N}\hbar\omega_k} \frac{1}{1 - I/I_{\text{th}}} \tag{1.91}$$

The prefactor represents the noise ratio between the energy of spin wave mode and thermal energy. Thus the amplitude grows rapidly as the current approaches the threshold. As factor $\mathcal{N}$ infers, the auto-oscillation is directly related to the number of spins to compensate by spin transfer, and it is scaled with magnetization thus, as well as with temperature [96].

$$I_{\text{th}}(T) = I_{\text{th}}(T_0) \cdot \frac{M_s(T)}{M_s(T_0)} \tag{1.92}$$

where T_0 and $I_{\text{th}}(T_0)$ is the reference temperature and the threshold current at T_0 respectively. In other words, increased thermal fluctuation at an elevated temperature leads to easier excitation of oscillation and a smaller threshold current. Another important fact is that I_{th} is scaled with the relaxation rate as well. This is simply because the auto-oscillation is caused by competition between the rate of magnetic damping and that of

spin transfer.

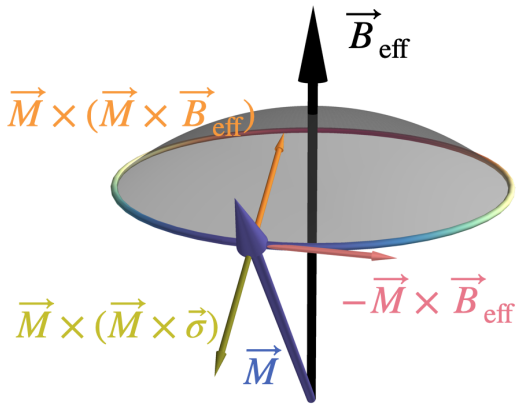

Figure 9: *Schematic of the vectorial relationship in the LLG equation with the spin torque term that counteracts the magnetic damping.*

1.2.4 Extended geometries - magnon transport

From now on, we intensively discuss the spin transfer effects (STE) in extended geometries, that is, our device structures. While the concerned dynamics in confined structures are based on the magnetic texture obtained from the eigenvalue solution, in extended geometries, the spin wave propagation is our main focus[1]. The extension of the zero-dimensional (0D) model [93, 97, 98], to either the one-dimensional (1D) [99–101] or two-dimensional [102–104] (2D) case systems has proven challenging. Experimentally, this extension has been made possible by the discovery of spin transfer mechanisms such as the spin Hall or Rashba effects, which provide the STE while allowing the charge current to flow in-plane (CIP). The nonlocal device used to measure the transconductance by magnons is depicted in Fig. 10(a). It has two contact electrodes deposited on YIG and subject to spin Hall effect (in our case, two Pt stripes $L_{\text{Pt}} = 30$ μm long, $w_{\text{Pt}} = 0.3$ μm wide and $t_{\text{Pt}} = 7$ nm thick). The two stripes are separated by a center to center distance, d. To reach the high power regime, current densities as large as $1 \cdot 10^{12}$ A/m^2 are injected in Pt_1.

To characterize the transport properties, we propose to focus on the dimensionless transmission coefficient $\mathscr{T}_s \equiv I_2/I_1$, which corresponds to the ratio of the emitted and collected spin Hall currents circulating in the two Pt stripes, Pt_1 and Pt_2. The quantity, $\mathscr{T}_s/R_1$, can be loosely associated with the magnon transconductance, where R_1 is the resistance of the emitter. [2].

[1] see the discussion in subsubsection 1.2.5.3 for the arguments on the localized mode in extended geometries which cannot be collected in our measurements.

[2] More precisely, the magnon component requires in addition a renormalization by the product $\epsilon_1 \cdot \epsilon_2$, which factors out of the interfacial efficiencies of the spin to charge interconversion process at both electrodes .

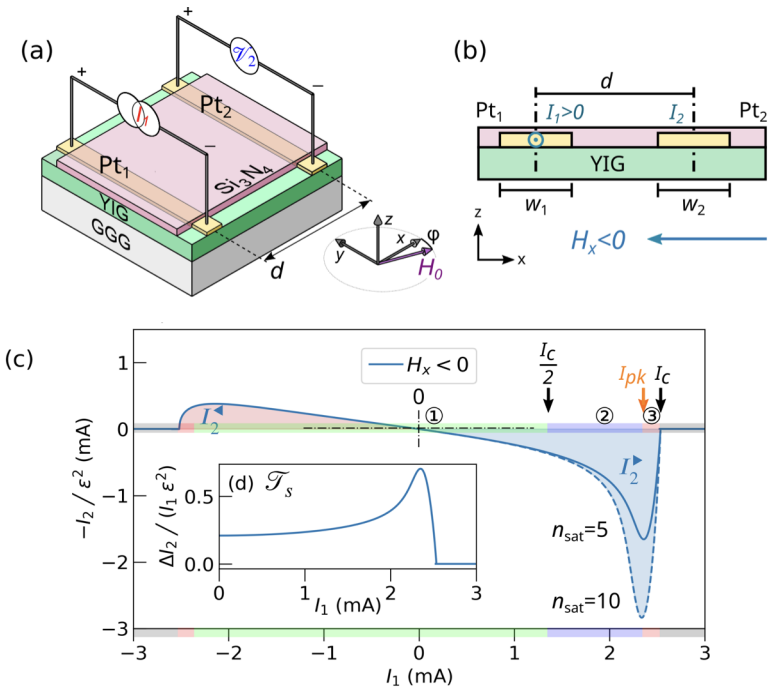

Figure 10: *Spin diode effect in a lateral device. (a) Perspective and (b) cut view of the magnons circuit: an electrical current, I_1, injected in Pt_1 emits or absorbs magnons via the spin transfer effect (STE). The change in density is consequently sensed nonlocally in Pt_2 (collector) through the spin pumping current. $-I_2 = (\mathscr{V}_2 - \overline{\mathscr{V}}_2)/R_2$, where $\overline{\mathscr{V}}_2$ is a background signal produced by magnon migration along thermal gradients. The negative sign in front of I_2 is a reminder that the origin of the spin Hall effect is an electromotive force whose polarity is opposite to Ohmic losses [105]. (c) Change from the nominal thermal occupation of low-energy magnons when $H_x < 0$. We have shaded in blue the deviation in the regime of magnon emission corresponding to the forward bias (▶) and in red the regime of magnon absorption corresponding to the reverse bias (◀). The insert (d) shows the behavior expressed as a transmission ratio $\mathscr{T}_s \equiv \Delta I_2/I_1$, where $\Delta I_2 = (I_2^{\blacktriangleright} - I_2^{\blacktriangleleft})/2$. As shown in (c), an asymmetric nonlinear growth of I_2 occurs in the forward bias, corresponding to the so-called spin diode effect. This growth, however, is capped by n_{sat}, an effective saturation threshold due to the nonlinear coupling between low-energy modes as expressed by Eq. (1.106). The solid and dashed lines show the behavior for two values of the saturation level, n_{sat}. The colored current scale in (c) distinguishes 3 transport regimes, ① (green window): a linear regime, $I_2 \propto I_1$ at low currents, that also encompasses the reverse bias; ② (blue window): a nonlinear asymmetric increase above a forward bias of the order $I_c/2$; and ③ (red window): above I_{pk}, a collapse at I_c of the spin conduction as the temperature of the emitter, $T_1 \to T_c$. When $|I_1| > |I_c|$ all magnons transport vanishes (black window).*

We note that STE being a transverse effect, the different cross section of the spin and charge currents has to be accounted for, resulting in STE efficiency $I_{\mathrm{CIP}} = I_{\mathrm{CPP}} \cdot L_{\mathrm{Pt}}/t_{\mathrm{Pt}}$. Assuming that all the injected spins remain localized underneath the emitter, one can obtain an estimate for the amplitude of the critical current, that compensates Γ_K-damping for this confined mode:

$$\frac{I_{\mathrm{th}}}{e} = 2\,\frac{\Gamma_K}{\epsilon_1}\,\frac{t_{\mathrm{YIG}} \cdot w_1 \cdot t_{\mathrm{Pt}} \cdot M_1}{\gamma\hbar}\,, \tag{1.93}$$

where ϵ_1 is the spin to charge conversion efficiency (at the emitter), M_1 is the magnetization underneath the emitter. A numerical calculation, yields $I_{\rm th} \approx 1.25$ mA for YIG_C films in chapter 4 (see Table.4.1). As will be shown below, the pertinent expression for threshold current in *extended geometries*, $\mathcal{I}_{\rm th}$, differs significantly from the above simplistic estimate. First, the absence of an energy gap between the eigen-modes in higher dimensional geometry permits nonlinear interaction between magnons [106, 106, 107], whose signature is a power dependent magnon-magnon scattering time [68, 69, 71, 108]. Second, the Joule heating and the less efficient thermalization of the emitter lead to a significant rise of the emitter temperature $T_1|_{I_1^2} = T_0 + \kappa R I_1^2$ for large currents. Here the rise is produced relative to T_0, the temperature of the substrate and κ is the efficiency of the device thermalization. This introduces additional complexity due to a significant variation of M_1. These difficulties are a large spectral shift of the magnon dispersion. This creates the energy band mismatch between the regions underneath and outside the emitter, preventing the efficient propagation of magnons. In the following we will present a model that incorporates all these effects and allows to model the magnon transmission ratio [see Fig. 10(c)]. In this model $\mathcal{I}_{\rm th}$ depends on a low-current nominal estimate of $\mathcal{I}_{\rm th,0}$, whose value shall be extracted from a fit of the data. Although the estimate provided by Eq.(1.93) gives the right order of magnitude, the fit value is systematically greater indicating that the affected volume by STE is much larger than just the YIG volume covered by Pt_1 electrode.

1.2.4.1 Bose statistics

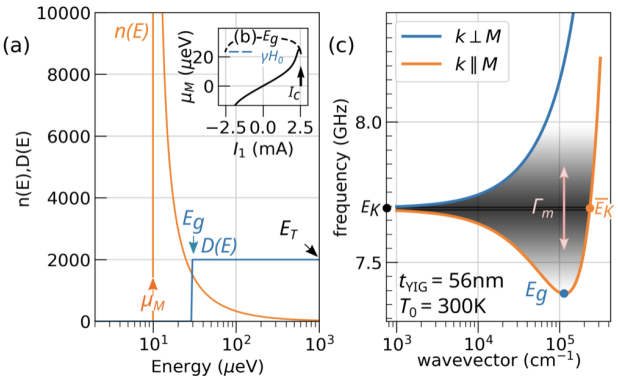

Figure 11: *Magnon transport in extended magnetic thin films. (a) In the magnetostatic energy range, magnons behave as a two-dimensional gas, with a step-like density of states, $D(E)$ (blue). The non-equilibrium magnon distribution, $n(E)$ (orange), can be modulated by shifting μ_M, the magnon chemical potential. (b) In our case, the shift of μ_M is produced by an electrical current, I_1, injected in Pt_1 (emitter). (c) Magnon dispersion for different in-plane propagation directions, θ_k. The plot is shown for the YIG_C film at 300 K. The grey shade emphasizes the degeneracy weight of magnons i.e. their propensity to excite parametrically degenerate modes. The black dot indicates E_K, the energy of the Kittel mode ($k \to 0$), the blue dot indicates E_g, the minimum of the magnons' band, and the orange dot designates $\overline{E}_K$, the mode degenerate with E_K with the highest wavevector. The saturation instability described in Fig. 10(b), produces a sharp enhancement of Γ_m, the nonlinear coupling between degenerate modes in the energy range $E_K \pm (E_K - E_g)$. This constrains μ_M to approach E_g asymptotically at large current as shown in (b).*

On the analytical side, the single mode picture [93] is not pertinent anymore for extended geometry and it should be replaced by a statistical distribution completed by integration over all possible wave-vectors $\int d\mathbf{k}/(2\pi)^3$ [109]. The appropriate framework to describe the out-of-equilibrium regime of the magnon gas is the Bose-Einstein statistics [see Fig. 11(a)]:

$$n(\omega_k) = \frac{1}{\exp\left[(\hbar\omega_k - \mu_M)/(k_B T_1)\right] - 1}, \tag{1.94}$$

with μ_M being the electrically controlled chemical potential, whose value follows the expression [110]:

$$\mu_M = E_g I_1 / \mathcal{I}_{\text{th}}, \tag{1.95}$$

where the analytical expression of $\mathcal{I}_{\text{th}}$ in extended geometries will be defined later in Eq. (1.107). A drastic change of the density of low-energy magnons is expected when μ_M approaches the lowest energy E_g indicated by a blue dot in Fig. 11(c) [111]. This energy level corresponds to spin-wave eigen-mode with the lowest possible energy in the dispersion relation of in-plane magnetized thin films. It occurs for spin-waves propagating along the magnetization direction having wave-vectors $k_g \approx 2\pi \cdot 10^5$ cm^{-1}, or wavelength $\lambda_g \approx 600$ nm. Such wavelength is still very large compared to the film thickness and for all practical purposes, we will assume that the magnons behave as a 2D fluid in the magnetostatic spectral range shown in Fig. 11(c) and thus that the density of states is a step function as shown in Fig. 11(a) [112]. Additionally, in thin films, the splitting between E_g and the energy of the Kittel mode, E_K (black dot), is small, so that $E_g \approx E_K$ can be approximated by the analytical expression of $\hbar\omega_K$. In the following, it will be shown that, in extended thin films, both $\mathcal{I}_{\text{th}}$ and E_g are dependent on I_1, the current bias, for two separate reasons: *i)* as mentioned above the poor thermalization of the electrodes introduces a decrease of M_1 with increasing thermal fluctuation produced by Joule heating ($\propto I_1^2$) and *ii)* the finite degeneracy of the magnon bands allows nonlinear coupling between eigen-modes via the dipolar coupling [see Fig. 11(b)]. As a consequence, Γ_M, the magnon-magnon relaxation rate, which defines $\mathcal{I}_{\text{th}}$, increases for higher density of low-energy magnons.

A drastic simplification can be made by noticing that for boson statistics, there are two ingredients that give rise to a change of the magnon occupation described by Eq. (1.94): one is the chemical potential, μ_M; the second is the temperature of the emitter T_1. The prior dominantly affects the low lying spin excitation, while the latter affects the whole spectrum, mostly weighted by the high-energy part. It is thus natural to simplify the problem as a competing two-fluid problem: loosely of magnetostatic nature at the energy around E_K and a second of thermal nature at the energy around $E_T \sim k_B T_1$. The segregation between the two fluids is precisely the focus of the associated work in chapter 5.

1.2.4.2 Low-energy v.s. high-energy magnons

BVMSW mode has the energy minimum E_g at non zero k. This feature comes from the dipolar-dipolar interaction, in other words, magnetostatic interaction of neighboring dynamical magnetization, where the term ω_H and $\omega_M F_m$ become dominant in Eq. (1.45). Thus they are sensitive to an external magnetic field, thickness and magnetization with a relatively small k vector (or large wavelength) and low frequency close to Kittel mode in GHz range. Magnons in such energy and k vector are called *magnetostatic magnons* or *low-energy magnons* in this manuscript. One can excite magnetostatic magnons by microwave field excitation, and also spin injection from an adjacent layer. In contrast, magnons excited by thermal means have the energy of $k_B T$, where k_B is the Boltzmann

constant and T is the temperature. It means that they have energy in the THz range and eventually have a large k vector and a small wavelength. In this regime, the contribution of k is indeed dominant in Eq. (1.51) and insensitive to ω_H, thus they do not have a strong dependence on an external magnetic field. This type of magnon is called *thermal magnons* or *high-energy magnons* in this manuscript. They are also called *exchange magnons* as the exchange interaction is the dominant factor. One can excite thermal magnons by for example thermal fluctuation or temperature gradient.

The energy landscape of magnetostatic magnons and thermal magnons are completely different, *i.e.*, GHz *vs* THz. Thus their properties are distinct from each other. In this manuscript, we focus on the transport property of the two magnons. The following analytical frameworks will introduce the characteristics of the two as a function of current in the emitter and will discuss how to segregate them utilizing their distinct transport properties.

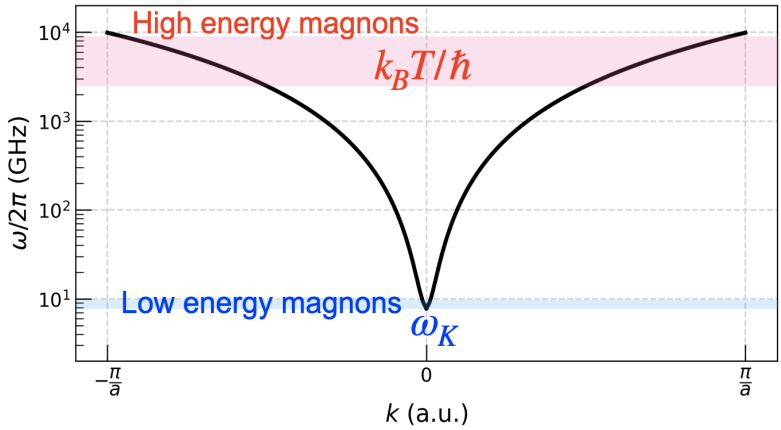

Figure 12: *Magnon dispersion relation ranging from GHz to THz energy.* $\pi/a = 2.55 \times 10^9$ *rad/m is used from* $a = 1.2316$ *nm for YIG.*

1.2.5 Transport of magnons excited by spin transfer effect

1.2.5.1 Low-energy magnons in the linear regime

We now concentrate on deriving an analytical expression for the magnon transmission ratio $\mathscr{T}_K$ in the linear regime ($I_1 \ll I_{\rm th}$). Since we conduct experiments at room temperature using thin film garnets, the approximations $\hbar\omega_K \ll k_BT_1$ and $E_g \approx \hbar\omega_K$ are validated. Starting from Eq. (1.94) and Eq. (1.95), the number of magnons around ω_K as a function of I_1 due to the chemical potential term is approximated as

$$n_K|_{I_1} \approx \frac{k_BT_1}{\hbar\omega_K\left(1-\mu_M/\hbar\omega_K\right)} \approx \frac{k_BT_1}{\hbar\omega_K}\frac{1}{\left(1-I_1/\mathcal{I}_{\rm th}\right)} \tag{1.96}$$

We derive the *linear* variation of low-energy magnons around the Kittel energy, E_K, which is measured through $\Delta n_K = \left|n_K(+I_1) - n_K(-I_1)\right|/2$ where the number of magnons emitted by STE ($I_1 \cdot H_x < 0$) in Fig. 10b) is measured relative to the number of magnons absorbed while reversing the current (or magnetization) direction ($I_1 \cdot H_x > 0$) [96]. In Fig. 10(c), these two biases are symbolically indicated by ▶, for the forward bias (magnon emission) and by ◀, for the reverse bias (magnon absorption). The subtraction allows to discriminate magnons produced electrically ($n(\omega_k)$ being odd in I_1) from magnons

produced by pure Joule heating ($n(\omega_k)$ being even in I_1) [46, 47, 113, 114]. Following the expression of $n(\omega_k)$ in Eq. (1.96), one obtains an analytical expression for the variation of the number of low-energy magnons [96]:

$$\Delta n_K|_{I_1} = |n_K(+I_1) - n_K(-I_1)|/2 \approx \frac{k_B T_1}{\hbar\omega_K} \frac{I_1}{\mathcal{I}_{\rm th}} \frac{1}{1-(I_1/\mathcal{I}_{\rm th})^2} \ , \tag{1.97}$$

where $\mathcal{I}_{\rm th}$ has been introduced in Eq. (1.95). This retains the same expression as the one obtained from the Boltzmann Equation approach [49,96]. The magnon creation stemming from the fluctuation of magnetization produces a relative decrease, which follows the expression

$$\Delta M_1 = \Delta n_K \gamma \hbar / V_1, \tag{1.98}$$

where V_1 is the effective volume of propagation of these magnons. These fluctuations are then sensed nonlocally through the change of spin pumping signal generated in the collector via the ISHE. Let us define the material parameters as $g_{\uparrow\downarrow}$ the spin mixing conductance at the YIG|Pt interface, $\theta_{\rm SHE}$ the spin Hall angle of Pt, $\sigma_{\rm Pt}$ the conductivity, $\lambda_{\rm Pt}$ the spin diffusion length, and θ the cone angle of the precession. The voltage from the ISHE in the emitter $V_{\rm ISHE}$ is written as follows [115, 116].

$$\begin{aligned} V_{\rm ISHE} &\equiv \frac{g_{\uparrow\downarrow}\,\theta_{\rm SHE}}{g_{\uparrow\downarrow} + \sigma_{\rm Pt}/\lambda_{\rm Pt} \dfrac{1-\exp(-2t_{\rm Pt}/\lambda_{\rm Pt})}{1+\exp(-2t_{\rm Pt}/\lambda_{\rm Pt})}} \cdot \frac{\hbar/(2\pi) L_{\rm Pt} \mathscr{E} \omega_K/(2\pi)\sin^2\theta}{2e t_{\rm Pt}} \cdot \frac{(1-\exp(-t_{\rm Pt}/\lambda_{\rm Pt}))^2}{1+\exp(-2t_{\rm Pt}/\lambda_{\rm Pt})} \\ &= \frac{\hbar/(2\pi) L_{\rm Pt} \mathscr{E} \omega_K/(2\pi)\sin^2\theta}{2e t_{\rm Pt}} \cdot \epsilon_2, \end{aligned} \tag{1.99}$$

with $\mathscr{E} \approx 1$ being an ellipticity correction, and

$$\epsilon_2 \equiv \frac{G_{\uparrow\downarrow}\,\theta_{\rm SHE}\,\tanh\left[t_{\rm Pt}/(2\lambda_{\rm Pt})\right]}{G_{\uparrow\downarrow}\coth\left(t_{\rm Pt}/\lambda_{\rm Pt}\right) + \sigma_{\rm Pt}/(G_0\lambda_{\rm Pt})} \ , \tag{1.100}$$

being a dimensionless quantity of the order $\epsilon_2 \approx 3\cdot 10^{-3}$, which represents the overall efficiency of the spin-charge conversion with $G_0 = 2e^2/h$ the quantum of conductance and $G_{\uparrow\downarrow} = g_{\uparrow\downarrow}/G_0$. For the small precession, $\theta \ll 1$, we have approximation such that

$$\sin^2\theta \approx \frac{\Delta M_2}{M_2} \tag{1.101}$$

where the denominator M_2 represents the magnetization underneath the collector and ΔM_2 is the corresponding fluctuation. The generated charge current in the collector $\Delta I_2 = V_{\rm ISHE}/R_{\rm Pt}$ with $R_{\rm Pt}$ the resistance of the collector is rewritten using $R_{\rm Pt} = L_{\rm Pt}/(\sigma_{\rm Pt} w_2 t_{\rm Pt})$ such that

$$\frac{\Delta I_2}{e} \approx \epsilon_2 \frac{\omega_K}{2\pi} \frac{\sigma_{\rm Pt} w_2}{G_0} \frac{\Delta M_2}{M_2}, \tag{1.102}$$

where ΔM_2 is the fluctuated magnetization under the collector, and w_2 is the width of the collector. We further assume that $\Delta M_2 = \zeta\ \Delta M_1/2$, where $\zeta = \mathrm{e}^{-d/\lambda_K} \ll 1$ is the attenuation ratio of the spin signal when magnons propagate from the emitter to the collector with λ_K being the characteristic decay length and the factor $1/2$ taking into

account that an equal flow of magnons propagates undetected in the opposite direction. Thus we obtain

$$\Delta M_2 = \mathrm{e}^{-d/\lambda_K} \Delta n_K \gamma\hbar/2V_1 \tag{1.103}$$

Approximating in the linear regime, $\mathcal{I}_{\mathrm{th},0} \approx I_{\mathrm{th}}$ expressed by Eq.(1.93) and $I_1 \ll I_{\mathrm{th}}$, Δn_K is rewritten such that

$$\Delta n_K|_{I_1} \approx \frac{k_B T_1}{\hbar\omega_K} \frac{I_1}{\mathcal{I}_{\mathrm{th}}} \approx I_1 \cdot \frac{k_B T_1}{\hbar\omega_K} \frac{\epsilon_1 \gamma\hbar}{2\alpha_{\mathrm{LLG}}\omega_K e t_{\mathrm{YIG}} w_1 t_{\mathrm{Pt}} M_1} \tag{1.104}$$

One can derive there an analytical expression for the dimensionless transmission ratio of low-energy magnons $\mathscr{T}_K|_{I_1} \equiv \Delta I_2/I_1$ which simplifies as:

$$\mathscr{T}_K|_{I_1\to 0} \propto \mathrm{e}^{-d/\lambda_K} \cdot \epsilon_1\epsilon_2 \cdot \frac{k_B T_1}{\alpha_{\mathrm{LLG}}\hbar\omega_K} \cdot \frac{\sigma_{\mathrm{Pt}} w_2}{G_0} \cdot \frac{(\gamma\hbar)^2}{M_1 M_2 t_{\mathrm{YIG}} w_1 t_{\mathrm{Pt}} V_1}. \tag{1.105}$$

The numerical application using the material parameters given in table 4.1 in chapter 4 gives $\mathscr{T}_K \approx \mathrm{e}^{-d/\lambda_K} 10^{-7}$, which ensures the consistent order of magnitude as typical experimental values. The above expression gives qualitative agreements. For example it predicts an increase of the magnon transmission ratio with decreasing film thickness $\propto t_{\mathrm{YIG}}^{-1}$, consistent with recent results [117]. This directly follows from the fact that the spin pumping signal, I_2, is proportional to changes of the magnon density. Relating this to an external flow of spins from the interface decaying at a fixed rate, the finding just translates that the concentration is inversely proportional to the magnetic film thickness with all other things being equal. This poses the question of how far the transmission can rise when $t_{\mathrm{YIG}}^{-1} \to 0$. It will be shown below that the answer is disappointing because the nonlocal geometry intrinsically prevents the efficient transport of magnons. The other geometrical influences are confirmed in chapter 4. Note that at large currents the Joule heating increases the temperature of the lattice beneath the emitter as described in Fig. 13(a). The corresponding lateral temperature gradients can further introduce additional dependencies [65, 118], which are not considered in Eq. (1.105).

1.2.5.2 Low-energy magnons at high power regime

Having established the linear response, this section reviews the phenomena that impair the propagation of low-energy magnons in the strongly out-of-equilibrium regime. We distinguish between thermal effects and nonlinear effects within the magnetostatic magnon gas.

The 2D geometry prevents the efficient thermalization of the magnetic material. At high current densities, one should thus expect a significant variation of T_1. We define $T_1 = T_0 + \kappa\, R\, I_1^2$, the temperature elevation of the emitter produced by Joule heating when the substrate is at T_0 and κ is the coefficient that determines the temperature increase per deposited Joule power. Fig. 13(a) shows the typical parabolic increase of T_1 produced by passing large current densities in a thin Pt stripe of 300 nm in width. The collateral damage is a diminution of the saturation magnetization, which decreases with increasing temperature [see Fig. 13(b)], approximately along the analytical form $M_T \approx M_0\sqrt{1-(T/T_c)^{3/2}}$, with M_0 being the saturation magnetization at $T = 0$ K [119]. These changes of temperature introduce a large spectral shift of the magnon dispersion. The relevant energy scale is set here by the difference between $E_K - E_g$, which is less than half a GHz in these thin films as shown in Fig. 11(c). Furthermore, the rise can easily exceed T_c, the Curie temperature even if one tries to use the pulse method as a means to reduce the duty cycle [120]. We define the current I_{c} required to reach $T_c = T_0 + \kappa R I_{\mathrm{c}}^2$.

In this case, one expects that $M_1 = 0$ at I_c as shown by the arrow in Fig13(b).

In turn, the decrease of M_1 should produce a collapse below I_c of any threshold currents at the emitter location. At this stage, we still assume that magnons remain non-interacting. We define $I_{pk} = \mathcal{I}_{th,0} \cdot M_{T_{pk}}/M_{T_0}$ as mentioned in the previous subsection [96], the conjectural threshold current below the emitter, which is heated by Joule effect, while $\mathcal{I}_{th,0}$ is the nominal threshold current estimated from the magnetic characteristics at $I_1 = 0$. In our notation, T_{pk} is the temperature of the emitter at I_{pk}, while T_0 is its temperature at $I_1 = 0$. The position of I_{pk} can be obtained graphically by looking at the intersection point of the dashed curve representing $\mathcal{I}_{th,0} \cdot M_{T_1}/M_{T_0}$ and a straight line of slope 1 crossing the origin shown with dotted points in panel Fig. 13(c). The vertical orange arrow indicates the expected position of auto-oscillation onset assuming that the nominal value is $\mathcal{I}_{th,0} = 5$ mA [3]. It is important to note that the position of I_{pk} is very weakly dependent of the nominal value when $\mathcal{I}_{th,0} \gg I_c$ because of the rapid decrease of M_1 near I_c [see Fig. 13(b)]. We will come back to this observation, when discussing below the relevant bias to renormalize the data. The important conclusion at this stage is that, accounting for Joule heating, the damping compensation should always be reached within the range $[-I_c, I_c]$ independently of the value of $\mathcal{I}_{th,0}$. Thus as long as the single mode picture remains valid, one should always observe a diverging increase of the number of magnons within the current range explored. We shall show below that this is not the case and the culprit is the increased magnon-magnon scattering, which prevents the diverging growth of magnon density.

[3] It corresponds to about a 4 times enhancement from the estimate by Eq.(1.93) for YIG_C

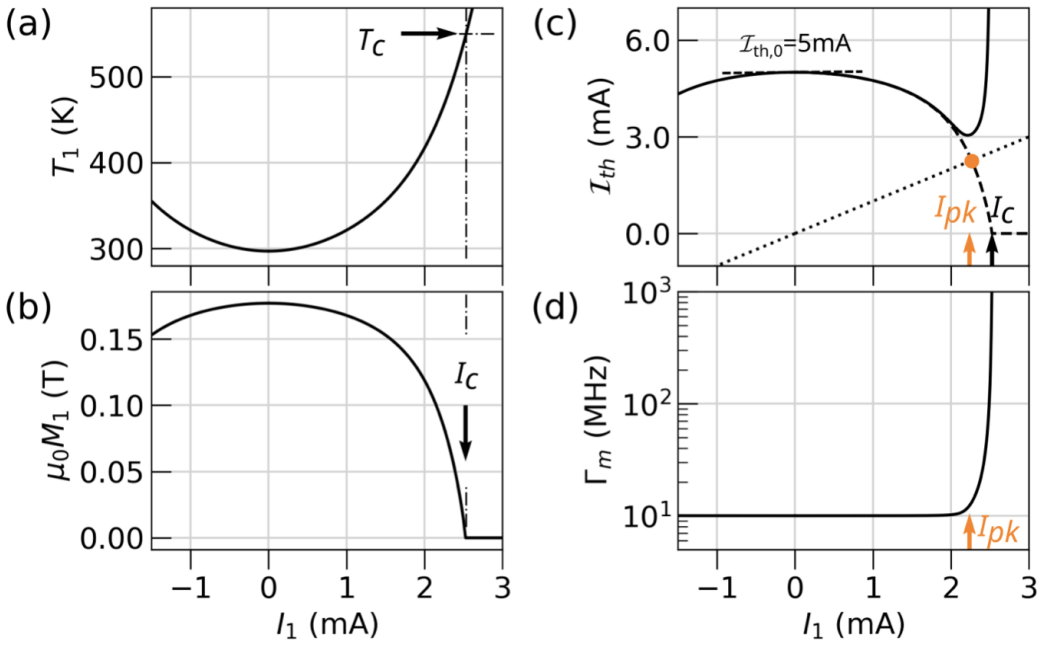

Figure 13: *Electrical variation of the magnetic characteristics at large power. (a) Temperature rise at the emitter due to Joule heating, $T_1|_{I_1^2}$. As shown in (b) it produces a reduction of magnetization beneath the emitter, $M_1|_{T_1}$. We define I_c, the critical current to reach T_c, the Curie temperature. (c) Variation of the conjectural threshold current for damping compensation. The reduction of M_1 produces a collapse below I_c of $I_{pk} = \mathcal{I}_{th,0} M_{T_{pk}}/M_{T_0}$, the expected onset of auto-oscillation for non-interacting magnons. The orange arrow in (c) indicates, I_{pk}, when the nominal threshold $\mathcal{I}_{th,0} = 5$ mA. Due to parametric instability, the occupancy of any eigen-mode is capped at n_{sat} through a sharp enhancement of Γ_m, the nonlinear coupling between degenerate modes as shown in (d). This translates in (c) as a sharp increase of $\mathcal{I}_{th} = \mathcal{I}_{th,0}\Gamma_m/(\alpha_{LLG}\omega_K)$.*

1.2.5.3 Self-localization effect

We emphasize here a trivial observation about the magnon dispersion curve, which concerns nonlocal devices *i.e.* magnon transport outside the volume beneath the Pt|YIG interface. Lateral geometries are *not* appropriate to investigate condensation, that selectively favors the lowest energy lying mode, such as the Bose-Einstein condensate. For in-plane magnetized thin films, the minimum in the dispersion relation, E_g, corresponds to a mode with vanishing group velocity, i.e., a non-propagating mode [121]: cf. blue dot in Fig. 11(c). It means that nonlocal devices are intrinsically insensitive to changes in magnon population that occur in a localized mode. This situation gets even worse when changes in bias or design end up in increasing the magnon concentration, because of the nonlinear redshift of the magnon spectrum. This pushes the whole spectral range of low-lying spin fluctuations at the emitter below the magnons' band gap for outside the emitter. This prevents these magnons to reach the collector and further promotes self-localization [122–124]. The latter gets further amplified by temperature variation produced by Joule heating when large currents are circulated into the emitter. It will be shown in chapter 5, that even if we factor out the product $\epsilon_1 \cdot \epsilon_2 \ll 1$, the transmission ratio still remains well below 50%. This upper bound is actually expected if one considers that less than half of the magnons are propagating in a direction captured by the collec-

tor. We finally add that this difficulty to transmit efficiently affects not only low-energy magnons but also high-energy magnons, which suffer from very short decay lengths (see chapter 5).

As was observed already in numerous studies, it is possible to suppress the nonlinear frequency shift [77,79,103,125]. The first possibility is by tilting the magnetization out-of-plane. There is a peculiar angle where the depolarisation effect vanishes [126]. A second possibility is to use a material whose uniaxial anisotropy, K_u compensates the out-of-plane demagnetization factor $\mu_0 M_s$, leading to a vanishing effective magnetization. In this case, the Kittel frequency just reduces to $\omega_K = \gamma H_0$ and it is independent of the magnetization amplitude or direction. It was already noticed that this eliminates the self-localization effect by the depolarization factor and thus promotes spin propagation outside the emitter area [103].

1.2.5.4 Lorentz factor enhanced magnon-magnon decay rate

We now focus on the inter-magnon nonlinearity that emerges at high power. We mostly consider the saturation effect as introduced in the previous section 1.1.1. One type of instability can be induced for example from the non-isochronous precession of the magnetization (inherent to elliptical trajectories), which radiates at harmonics of the eigen-frequency and hereby allows the parametric excitation of other modes [127]. The other type of instability can be caused by the energy conserving and momentum conserving scattering process among degenerated modes where two magnons with $\pm k$ vector are scattered into other two magnons with $\pm k'$ [70,128]. It is interpreted that the number of magnons that can fill a particular mode is capped by its nonlinear coupling with other magnon modes by introducing a magnon-magnon relaxation time that depends on the mode occupation.

The usual requirement is to find a degenerate eigen-mode within the linewidth. Since this effect depends on the degeneracy level, it becomes dominant in extended geometries due to the increase of mode density. Moreover, the particular shape of the band structure of the magnons at low-energy levels introduces a discrimination between the different frequencies in terms of the number of degenerate modes. It turns out that the energy level with the greatest number of degenerate modes occurs precisely at the Kittel frequency. This is emphasized in Fig. 11(c) by shading in grey the degeneracy weight.

It should be also noted that among all the modes degenerate at E_K, the mode with the highest group velocity, which pointedly also propagates along the normal direction to the wires, is the point $\overline{E}_K$ marked by an orange dot in Fig. 11(c). Interestingly, the wavelength at the orange dot is here of the order of $1/w_1$, the lateral size of the Pt_1 electrode. This suggests that the tranconductance by low-energy magnons is preferentially carried by magnons at this particular position in the dispersion curve. This implication is confirmed by the micromagnetic simulations in chapter 6.

To describe the nonlinear interaction between magnons we introduce a saturation occupancy $\mathcal{N}_{\text{sat}}$, which marks the maximum number of magnons that one can put in one mode before decay to degenerate energy levels starts to kick in. Near this threshold, we assume that the damping rate follows the equation [129]:

$$\Gamma_m|_{I_1} = \frac{\Gamma_K}{\sqrt{1 - \left(\Delta n_K|_{I_1} / \mathcal{N}_{\text{sat}}\right)^2}}, \tag{1.106}$$

with $\Gamma_m - \Gamma_K$ representing the nonlinear enhancement of the relaxation rate caused by magnon-magnon scattering. The dependence of Γ_m on I_1 is plotted in Fig. 13(d). While this instability process has been mainly considered in the ferromagnetic resonance mea-

surements that focus on the uniform mode with $k = 0$, its application to the propagating modes with $k \neq 0$, the ones electrically excited is still elusive. We tentatively implement this idea to understand the characteristic of the magnon transport exposed to a high power of the current to capture our experimental observation.

1.2.5.5 Current threshold in extended geometries

To account for the increase of correlation between magnons discussed above, we replace $I_{\rm th}$ in Eq. (1.93) by

$$\mathcal{I}_{\rm th}|_{I_1} = \mathcal{I}_{\rm th,0}\frac{M_{T_1}}{M_{T_0}}\frac{\Gamma_m|_{I_1}}{\Gamma_K}. \tag{1.107}$$

Introducing this new expression of $\mathcal{I}_{\rm th}$ in Eq. (1.97), it generates a transcendental equation for $\mathcal{I}_{\rm th}$, whose dependence on I_1 is shown in Fig. 13(c). We dare to write the equation to solve as follows.

$$\Delta n_K|_{I_1} \approx \frac{k_B T_1}{\hbar\omega_K}\frac{I_1}{\mathcal{I}_{\rm th,0}\dfrac{M_{T_1}}{M_{T_0}}\dfrac{1}{\sqrt{1-\left(\Delta n_K|_{I_1}/\mathcal{N}_{\rm sat}\right)^2}}}\frac{1}{1-\left(\dfrac{I_1}{\mathcal{I}_{\rm th,0}\dfrac{M_{T_1}}{M_{T_0}}\dfrac{1}{\sqrt{1-\left(\Delta n_K|_{I_1}/\mathcal{N}_{\rm sat}\right)^2}}}\right)^2}, \tag{1.108}$$

We use it to fit the data with only two fitting parameters $\mathcal{I}_{\rm th,0}$ and $\mathcal{N}_{\rm sat}$. As $\Delta n_K(I_1)$ gets close to $\mathcal{N}_{\rm sat}$ by increasing I_1, $\mathcal{I}_{\rm th}$ rises sharply together with the damping $\Gamma_m(I_1)$ as plotted in Fig. 13(d) according to Eq. (1.106,1.107,1.108). The consequence of this rise is that $\mathcal{I}_{\rm th}$ remains unreachable due to a redistribution of the injected spin among an increasing number of degenerate eigen-modes. The consequence on the dependence of μ_M, the magnons' chemical potential, with I_1 is depicted in Fig. 11(b). Near the origin, the linear dependence of μ_M with I_1 is set by the intrinsic damping parameter. As Joule heating starts to decrease the magnetization M_1 beneath the emitter, it skews the curve upward. In the same fashion, the decrease of magnetization pushes E_g to lower energy in accordance with the red-shift nonlinear frequency coefficient. The sharp increase of $\Gamma_m(I_1)$ near I_c stops the rise and μ_M, which eventually approaches asymptotically E_g at high currents.

Fig. 10(c) shows the expected behavior produced on I_2 for two values of $n_{\rm sat} = 5$ (solid line) or 10 (dashed line). Here we use as a parameter $n_{\rm sat} = \mathcal{N}_{\rm sat}/\mathcal{N}_{\rm NL}$ the value expressed relatively to $\mathcal{N}_{\rm NL} = \mathcal{N}\Gamma_K/\omega_M$, which marks the onset when the change of magnetization becomes of the order of the linewidth, with $\omega_M = \gamma\mu_0 M_1 \approx 2\pi \times 4.48$ GHz [73]. We assume in these data that $I_c = 2.5$ mA and $I_{\rm pk} = 2.2$ mA, which amounts to assuming that $\mathcal{I}_{\rm th,0} = 5$ mA [see Fig. 13(c)].

Depending on the current values, we observe 3 regimes of transport: ①: $I_1 \ll I_c$, where we have a linear behavior $I_2 \propto I_1$; ②: $I_1 \in [I_c/2, I_{\rm pk}]$, where we have an asymmetric polynomial increase $I_2 \propto (1 - I_1^2/I_c^2)^{-1}$, the regime for the spin diode effect in an extended film; ③: $I_1 \in [I_{\rm pk}, I_c]$, where we have a drop of $I_2 \propto (1 - I_1^3/I_c^3)^{1/2}$. Note that the result obviously inverts with the inversion of the field direction (not shown).

We conclude this part by accentuating that the susceptibility of low-energy magnons to capture the external flow of angular momentum in a thermally shifting environment predicts a distinctive nonlinear shape for the current dependence of the magnon transmission ratio, which will be corroborated by experimental data in chapter 4.

1.2.5.6 High-energy magnons

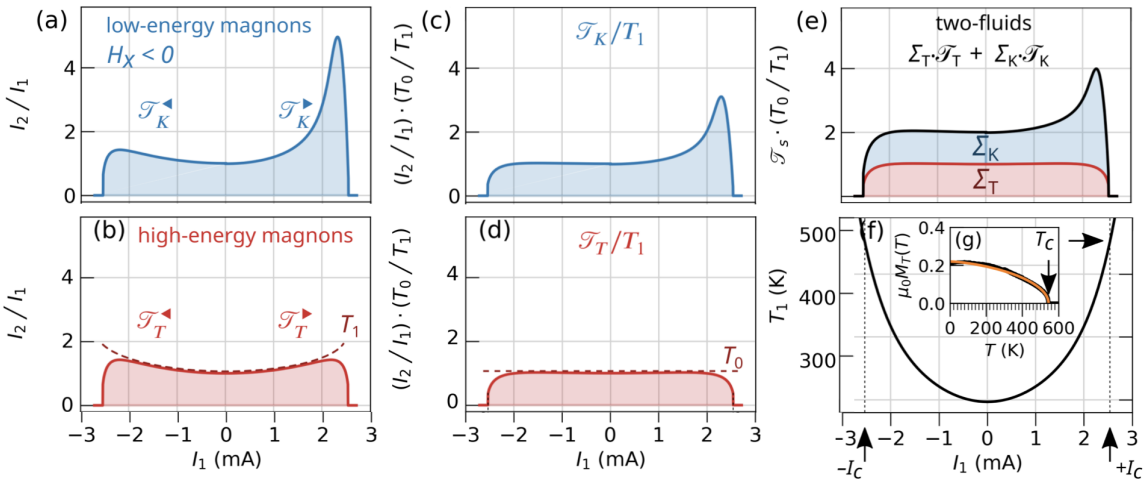

Figure 14: *Dependence of the magnon transconductance on the spectral nature of propagating magnons. Panels (a) and (b) compare the predicted electrical variation of $\mathscr{T}_s$ respectively for low-energy magnons (see Eq. (1.97), top panels), and for high-energy magnons (see Eq. (1.109), bottom panels), when $H_x < 0$. Panel (f) displays the associated variation of $T_1 = T_0 + \kappa R I_1^2$, the lattice temperature under the emitter. The current span exceeds I_c, the current bias that elevates T_1 to T_c, the Curie temperature. Panels (c) and (d) show the behavior when $\mathscr{T}_s$ is renormalized by T_1. Panel (e) shows the two-fluids fitting function: the independent sum of low-energy and high-energy magnon contributions with respective weight Σ_T and Σ_K. The insert (g) shows the temperature dependence of the magnetization M_T as measured by vibrating sample magnetometry (cf Fig. 31), and the solid line is a fit with the analytical expression $M_T \approx M_0\sqrt{1-(T/T_c)^{3/2}}$, with $\mu_0 M_0 = 0.21\ T$ and $T_c = 550\ K$.*

So far we have intensively developed the characteristic of the low-energy magnons. Here we consider the high-energy counterparts. We assume now that the number of high-energy magnons corresponds roughly to the total number of magnons, which is the difference $M_1 - M_0$, where M_0 is the spontaneous magnetization at $T = 0$ K and M_1 is the spontaneous magnetization at $T = T_1$, the temperature of the emitter. We thus express analytically the contribution of high-energy magnons to the magnon transconductance through the equation:

$$\mathscr{T}_T \propto \frac{M_1}{M_2}\cdot\frac{M_0 - M_1}{M_0}\ , \tag{1.109}$$

where the prefactor M_1 represents the level of magnetic polarization available under the emitter. We note that the analytical form expressed by Eq. (1.109) has been proposed previously to describe spin transmission inside paramagnetic materials [130]. As shown in the insert Fig. 14(g) we find that the temperature dependence of M_1 is well described by the analytical $M_1 \approx M_0\sqrt{1-(T_1/T_c)^{3/2}}$. The resulting number of thermally excited magnons that contribute to the nonlocal transport are shown in Fig. 14(b).

Let us here emphasize the influence of T_1. The variation of T_1 has profound consequences both on the level of thermal fluctuations of low-energy magnons as well as the number of high-energy magnons. For the low-energy ones, it enters in the formula of $\mathscr{T}_K$ with I_1 as expressed by Eq.(1.97). The resulting change of the magnon population as

a function of I_1 is re-shown in Fig. 14(a) for the purpose of comparison. To factor out the variation of T_1 produced by Joule heating, which expresses the influence on STE of a varying background of thermal fluctuations, we plot in Fig. 14(c) $\mathscr{T}_K/T_1$. This renormalization is equivalent to looking at nonlinear behavior from the perspective of a thermalized background. The ensuing shape of the curve as a function of I_1 simplifies greatly. In the reverse bias, marked by the symbol ◀, which represents the regime of magnon absorption, the normalized transconductance is constant up to I_c. By contrast, in the forward bias, marked by the symbol ▶, which represents the regime of magnon emission, a peak emerges. This asymmetric peak is coined the spin diode effect. The benefit of the T_1 normalization of the magnon transmission ratio is to make the peak a distinctive feature of the spin diode effect. Repeating the same analysis for high-energy magnons, a more insightful behavior is obtained by renormalizing $\mathscr{T}_T$ with T_1 and the result is shown in Fig. 14(d). In this case the current dependence of $\mathscr{T}_T/T_1$ as a function of I_1 is a constant function until I_c.

1.2.5.7 Two-fluid model

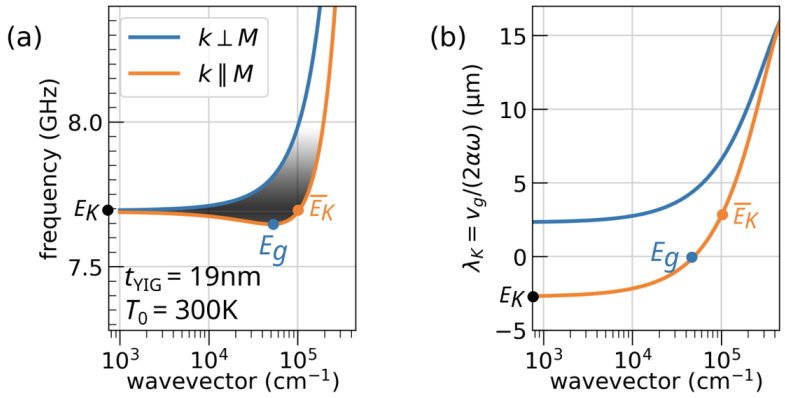

Figure 15: *Decay characteristics of low-energy magnons. (a) Dispersion curves at the bottom of the magnon dispersion of a 19 nm thick YIG film for two values of $\theta_k = 0°$ ($k \parallel M$) and 90° ($k \perp M$), the angle between the wavevector and the applied magnetic field. We mark with dots the Kittel mode (E_K, black dot), the lowest energy mode (E_g, blue dot), and the mode degenerate with the Kittel mode with the highest wavevector ($\overline{E}_K$, orange dot). The curve is calculated for YIG_A thin films. (b) Characteristic decay length calculated from the dispersion curve assuming that magnons follow the phenomenological LLG equation with $\alpha_{LLG} = 4 \cdot 10^{-4}$.*

An advantage specific to nonlocal transport measurements is that the propagation distance, d, offers a potent means to spectrally discriminate different types of magnons, each having their characteristic decay length λ_k along the x-axis [119, 131]. In the following, we will review the expectation for the different extrema of the dispersion curve.

For the high-energy magnons, one can approximate the spin-wave spectrum simply as $\omega_k = \omega_M \lambda_{ex}^2 k^2$, where $\omega_M = \gamma \mu_0 M_s = 2\pi \times 4.48$ GHz and $\lambda_{ex} \approx 15$ nm is the exchange length [132]. High-energy magnons at room temperature ($T_0 = 300$ K) have the frequency $\omega_T = k_B T_0/\hbar = 2\pi \times 6.25$ THz, which corresponds to a wave vector $k_T = 2.5$ nm^{-1}. It is seriously questionable whether an estimate for λ_T from the phenomenological Landau-Lifshitz-Gilbert (LLG) model is applicable to such short-wavelength magnons. Practically *i)* the Gilbert damping is expected to be increased in the THz-range [132] *ii)* the group

velocity is reduced towards the edge of the Brillouin zone [133,134], and *iii)* LLG does not account for the reduction of the characteristic propagation distance due to diffusion processes. Furthermore YIG is a ferrimagnet, higher (antiferromagnetic) spin-wave branches contribute significantly to the magnon transport [134–136]. We believe, that the most reliable estimates have been obtained experimentally by studying the spatial decay of the spin Seebeck signal [46,119] and have found $\lambda_T \approx 0.3$ μm.

Unlike their high-energy counterpart, the LLG framework should provide a good basis to calculate the propagation distance of long-wavelength low-energy magnons. The diopole-dipole interaction confers an anisotropic character to the group velocity of these spin-waves. We re-plot in Fig 15(a) the dispersion curve of magnon propagating either along the x-axis (orange line) or the y-axis (blue line). In the following, we shall focus our attention on the branch $\theta_k = 0°$ (orange line), which corresponds to magnon propagating in the normal direction of the Pt wires. As emphasized in the previous subsections, there are 3 remarkable positions on the curve each marked by a colored dot on Fig 15. The energy minimum, E_g (blue dot) does not contribute to the transport because its group velocity is zero. The longest wavelength spin-waves correspond to the Kittel mode, E_K (black dot). The damping rate, accounting for spin-wave ellipticity, is given by $\Gamma_K = \alpha_{\rm LLG}(\omega_H + \omega_M/2)$, where $\omega_H = \gamma H_0$ [129]. The velocity is equal to $v_K = \partial_k \omega = \omega_H \omega_M t_{\rm YIG}/(4\omega_K)$. The resulting decay length of spin transport carried by $k \to 0$ magnons is $\lambda_K = v_K/(2\Gamma_K) \approx 2.5$ μm for $t_{\rm YIG} = 19$ nm. As will be pointed out in chapter 4, the mode that seems most relevant for long-range magnon transport in nonlocal devices is probably, $\overline{E}_K$, the degenerate mode with the Kittel frequency and having the shortest wavelength. This mode is marked by an orange dot in Fig. 15. For our $t_{\rm YIG} = 19$ nm film, it turns out that its group velocity is of the same order of magnitude as the one at the Kittel mode, hereby giving a similar decay distance. We will evidence later that this estimate is reasonably close to the experimental value. We note, however, that the value of the decay distance at $\overline{E}_K$ increases with increasing film thickness to become independent of $t_{\rm YIG}$ for thickness above 200 nm (not shown). The saturation value is $\lambda_K \approx 20$ μm assuming that $\alpha_{\rm LLG} = 4 \cdot 10^{-4}$.

Since $\lambda_K \approx 10 \times \lambda_T$, changing d allows to tune from spin transport governed by high-energy magnons to spin transport governed by low-energy magnons. One should also add that the current intensity, I_1, also provides a means to tune the ratio between the two-fluid as discussed in the previous chapter.

Learning from the above considerations, we can now put all the contributions together to propose an analytical fit of the data with the two-fluid function:

$$\mathscr{T}_s = \Sigma_{T,0}\ \exp^{-d/\lambda_T}\ \frac{\mathscr{T}_T}{\mathscr{T}_{T,I_1\to 0}} + \Sigma_{K,0}\ \exp^{-d/\lambda_K}\ \frac{\mathscr{T}_K}{\mathscr{T}_{K,I_1\to 0}}\ , \tag{1.110}$$

combining two independent magnon contributions: one at thermal energy and the second at magnetostatic energy. We assume here that both magnon kinds follow an exponential decay. To ease the notation, we shall refer below at $(\mathscr{T}_T)^\star \equiv \mathscr{T}_T/\mathscr{T}_{T,I_1\to 0}$ as the normalized quantity by low current value. We define $\Sigma_K|_d = \Sigma_{K,0}\ \exp^{-d/\lambda_K}$ and $\Sigma_T|_d = \Sigma_{T,0}\ \exp^{-d/\lambda_T}$, where the index 0 represents the extrapolated value at the emitter position ($d = 0$): see Fig. 10(b). Thus the parameter $\Sigma_K/(\Sigma_K + \Sigma_T)|_d$ represents the variation with the distance of the proportion of low-energy propagating magnons over the total number of propagating magnons. An exemplary solution for $d = 0$ and identical high-energy and low-energy contributions is shown in Fig. 14(e).

It is worth emphasizing at this stage that the model proposed by Eq.(1.110), which assigns a fixed decay rate to each magnon category, is certainly over simplistic. One should for example bear in mind that when $M_1 \to 0$ due to Joule heating, this could

have a profound consequence on λ_T by changing the exchange constant. This was already discussed in the context of spin propagation inside paramagnetic materials [130]. We will come back to this issue below in the context of our discussion about the discrepancy in the values of T_c extracted from the transport data in chapter 5.

1.2.6 Transport of magnons excited by spin Seebeck effect

So far we have intensively studied the transport characteristics of magnons excited electrically by the spin transfer effects. To finish this chapter, we mention briefly the magnons excited thermally by the spin Seebeck effects. This is the main focus of chapter 3.

A large current density is applied to a heavy metal layer and consequently Joule heating is induced. It creates a vertical temperature gradient along the stack. Such temperature gradient generates an electric voltage across the heavy metal originating from magnon generation, the spin pumping and the ISHE. This phenomenon is called *spin Seebeck effect* (SSE) which was first observed by Prof. Saitoh's group at Keio University, Japan [46,47,137]. If one prepares the Pt/YIG sample stack and applies the temperature gradient along $\hat{\boldsymbol{z}}$, one can detect inverse spin Hall voltage if the magnetization direction and charge current direction are orthogonal to each other. Considering the symmetry of ISHE, the detected charge current due to pumped spins generated by SSE is expressed as follows.

$$\boldsymbol{j_c} = S_{\mathrm{SSE}} \boldsymbol{\nabla} T \times \frac{\boldsymbol{M}}{M_s} \tag{1.111}$$

where S_{SSE} is the spin Seebeck coefficient. The origin of this spin thermometric conversion was elusive for years since the first observation. However now it has been understood as the generation of thermally excited magnons concluded by studying the YIG thickness dependence and observing the increase and saturation of signals, indicating finite decay length behavior [138]. Indeed the generated magnons have an energy range of $k_B T$ and they can be categorized as high-energy magnons. When it comes to non-local magnon transport experiments, the detected voltage from magnon propagation is a mixture of the two contributions, the STE and SSE. SSE is induced simply by the Joule heating effect, so one can use the symmetry with respect to current, *i.e.*, strictly even in current as shown in Fig. 16(a) that does not depend on the direction of the current and always expands the cone (blue or red) with respect to the initially activated thermal fluctuation (grey cone). The generated magnons originated from SSE eventually diffuse away though and a part of them is pumped towards the heavy metal layer. The diffusive nature of thermal magnons is confirmed in previous studies [139–142] as depicted in Fig.16(b). Let us define temperature T and chemical potential μ of the diffusive gas of high-energy magnons described by a set of transport coefficients [143]. The measured SSE signal is proportional to the magnon chemical potential at the interface between YIG and Pt [144]. The continuity equation for magnon current density J_s in the steady state is

$$-\boldsymbol{\nabla} \cdot \boldsymbol{J_s} = g\mu, \tag{1.112}$$

where g is the magnon relaxation coefficient. In linear response, the transport equation is

$$\boldsymbol{J_s} = -\sigma(\boldsymbol{\nabla}\mu + \varsigma \boldsymbol{\nabla} T), \tag{1.113}$$

where σ is the magnon conductivity and ς is the bulk spin Seebeck coefficient. The two equations are combined and lead to

$$\frac{\mu}{\lambda^2} = \boldsymbol{\nabla}^2 \mu + \varsigma \boldsymbol{\nabla}^2 T, \tag{1.114}$$

where $\lambda = \sqrt{\sigma/g}$ is the thermal magnon diffusion length. We will use this to study the characteristic decay of such the SSE signals in chapter 3 which allows us to extract a picture of the high-energy magnons.

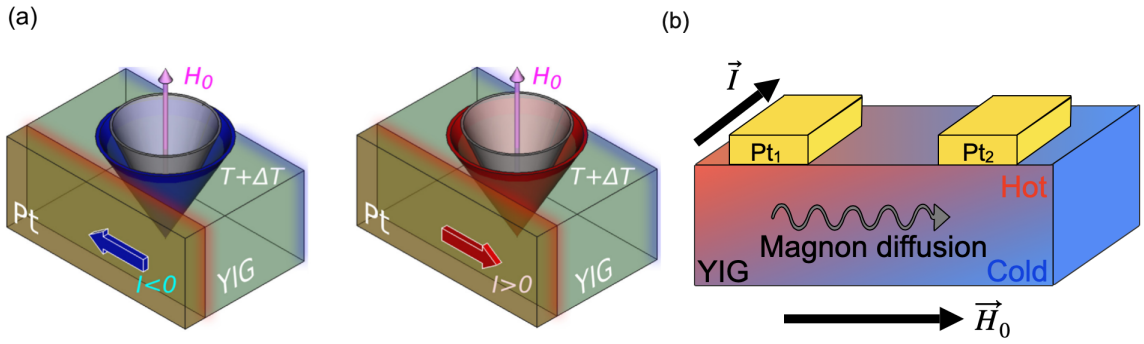

Figure 16: *(a) Schematic of magnon generation by spin Seebeck effect. The Joule heating induced by charge current application in Pt produces a temperature gradient along the thickness, which leads to magnon generation by the spin Seebeck effect. Since the direction of the spin current does not change the direction of the temperature gradient, it always generates magnons unlike the STE case (increase the cone angle with respect to initial fluctuation in grey regardless of the direction of current). This figure is taken from Ref. [92]. (b) Schematic of magnon diffusion from Pt_1 to Pt_2 and induced local temperature gradient.*

To conclude this section, we introduced the fundamentals of our measurement scheme, the spin transfer effects. The spin polarized current can affect the magnetic dynamics and vice versa. After briefly mentioning the spin transfer effect in confined geometry, namely auto-oscillation, our formalism of magnon transport has been derived. An important premise is that the excited magnons are mostly incoherent energetically spread from GHz (Kittel frequency) to THz (thermal energy) and we will show experimentally that one can conveniently simplify the picture by separating the magnons in two fluids representing both ends of the dispersion curve. We started from the Bose-Einstein statistics to consider the low-energy magnons, where the chemical potential is subject to the spin transfer effects. We developed a dimensional analysis of the conductivity that depends on many parameters such as temperature or thickness. Then we implemented the saturation effects introduced in the previous section 1.1.1 to explain the high power regime, which shows the non-linear rise and eventual drop of the conductivity. Lastly we mentioned the spin Seebeck effect, another source of magnon transport that is triggered by the temperature gradient.

Chapter 2

Methods

Magnetic damping parameter α is a barometer to evaluate the quality of magnetic films. To have a small α provides us quite a few interesting benefits, such as a smaller threshold for non-linear effects like auto-oscillation or instability processes, and coupling with other quasi particles such as photons or phonons [145]. Needless to say, for non-local magnon transport devices as well, smaller α is ideal to realize long distance transport. We relied on our collaborators to grow high quality YIG and Bismuth doped YIG (BiYIG) films. The former is fabricated by the group of Dr. Jamal Ben Youssef at Université de Bretagne Occidentale in Brest, France by the liquid phase epitaxy and the latter by the group of Dr. Abdelmadjid Anane at Unité Mixte Physique CNRS Thales in Palaiseau, France by the pulsed laser deposition. BiYIG is of particular interest in the community because it realizes the circular precession, suppressing non-linear effects. In the end it contributes to efficiently populating magnons in a certain mode. Since I have not participated in the growth part, I will only introduce the basic principle of those techniques. Then the nanofabrication process to construct the Pt nanowires on YIG films is briefly explained. Next we detail the measurement protocol to collect the data of non-local magnon transport signals and how to extract the Joule heating contribution (spin Seebeck effect, SSE) and the electrical contribution (spin transfer effect, *i.e.*, spin orbit torque, SOT).

2.1 Growth of magnetic garnets films

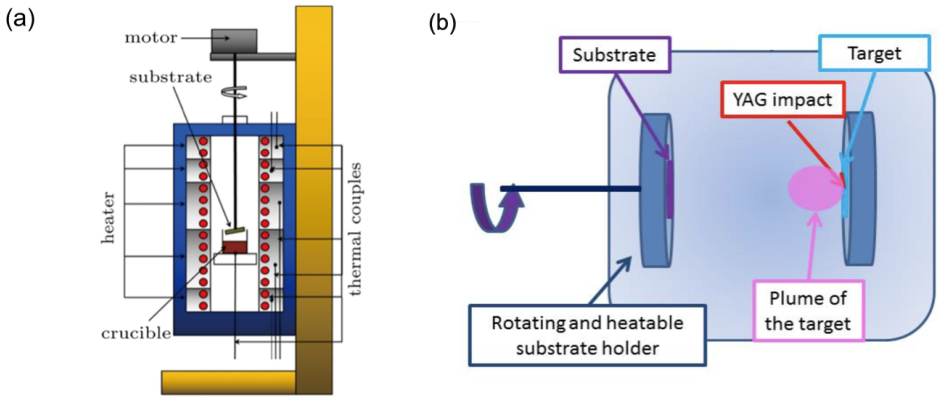

Figure 17: *Schematics of deposition techniques. (a) represents the liquid phase epitaxy technique. The image is taken from Ref. [146]. (b) represent the pulsed laser deposition. The image is by the courtesy of Dr. Lucile Soumah [147].*

Yttrium Iron Garnet (YIG) is widely used when it comes to studying the property of magnons simply thanks to its very small magnetic damping. YIG can be grown by several techniques such as sputtering, atomic layer deposition [148], molecular beam epitaxy and liquid phase epitaxy. In this thesis, we used films made with these last two techniques.

- *Liquid phase epitaxy (LPE)* This technique is commonly used because it ensures the epitaxial growth of a single crystalline film by using Gadolinium Gallium Garnet (GGG) substrate with almost the same lattice parameter as YIG. As named *liquid*, the basic idea is to dip the substrate into the liquid at room pressure. It is composed of rare earth oxides Fe_2O_3 and $YFeO_3$ melt in a platinum crucible placed on a furnace. The GGG substrate is connected to a rotation rod and dipped in the liquid, the rotation ensures good homogeneity of the thickness of the deposit. A schematic of the technique is shown in Fig. 17(a). The samples of YIG are provided by the group of Dr. Jamal Ben Youssef at the Université de Bretagne Occidentale in Brest, France. This technique ensures excellent crystallinity at the local scale (μm scale), however sometimes it creates inhomogeneity at the global scale (mm scale) in nanometer thick samples, with some spatial variation of the magnetic anisotropy. Fortunately, non-local transport device is at the μm scale and this does not give any problem.

- *Pulsed laser deposition (PLD)* This technique is widely used not only for garnets but also for other materials like oxides. In ultra high vacuum, the target is exposed to a high power laser which forms a beam of the evaporated elements that deposits on a facing substrate. In our case, YAG laser ($\lambda = 355$ nm) with about 45 mJ is irradiated on a polycrystalline BiYIG target at 400 degrees under O_2 pressure. The high temperature is needed to give kinetic energy to atoms allowing them to form a better crystalline structure. Schematic of the technique is shown in Fig. 17(b). Bi substituted YIG has perpendicular uniaxial anisotropy, mainly due to a small lattice mismatch and induced strain [125, 149]. This technique brings more precise control of thickness than the LPE thanks to the slow deposition rate. In addition it allows more homogeneity at larger scale than the LPE, but at the local scale LPE deposition is still better properties. The samples of BiYIG are provided by

the group of Dr. Abdelmadjid Anane at Unité Mixte Physique CNRS Thales in Palaiseau, France.

2.2 Nano fabrication process

The nanofabrication is conducted to construct 300 nm width Pt wires on top of the garnets. The clean room facility of PTA (Platforme Technologique Amont) in CEA Grenoble is used. We perform electron beam (EB) lithography to pattern the structures. EB lithography on insulating materials is slightly tricky because electric charges from the beam accumulating on the surface prevent a reliable drawing. To overcome this issue, a 20 nm Aluminium layer is deposited before EB lithography to let the charge diffuse. At the time of the development of the lithography, we conduct chemical etching to remove the Aluminium layer with a basic solution. Below several remarks are listed.

1. *Resist coating*
   The resist for EB lithography PMMA with 4 % dilution is spin coated with 4000 rpm for 1 minute followed by 1-2 minute baking at 180 degrees. 20 nm Aluminium metallic mask is deposited with PLASSYS electron beam evaporator afterward.

2. *EB lithography*
   After the preparation above, the JOEL EB 100 keV lithography is used to pattern the nanometric wires. The open source software *KLayout* is used to draw the patterns as shown in Fig. 18. The control of position is done by mounting the sample on a motorized stage and an electric field is used to deflect the beam. The position of the stage is monitored by a laser interferometer system to allow precise (1nm) position control. The positioning of the devices on the substrate relies on alignment marks, which are constructed at a first lithography step, as shown in Fig. 18(a). The detection of these alignement marks allows positioning of the patterns to be drawn at an accuracy of 20-30 nm. The beam is focused through several lenses forming a spot of 7 nm that is exposed to the resist. The used beam current is usually 1 nA.

3. *Resist development*
   Before developing the resist, the Al layer is removed by chemical etching in a basic solution and the sample is rinsed with pure water for 1 minute. Next, it is dipped into MIBK(1):IPA(3) developer for 30 seconds, then rinsed with pure IPA (iso-propanol) solvent for 30 seconds.

4. *Electrode deposition*
   The sample cleaning is conducted before metal deposition by using a SENTECH plasma cleaner and etched with low power 70 W oxygen plasma for 30 seconds. The sample is then placed in the deposition chamber (sputtering for main Pt wires or electron beam evaporation for guide electrodes and contact pads) and the metal is deposited after in-situ Ar ion etching with 250 V of acceleration voltage for 1 minute for a further cleaning purpose. Finally the sample is dipped into acetone for the lift-off process.

5. *Optical lithography*
   It is convenient to use photolithography to pattern relatively large size structures, namely the contact pad on whole sample surfaces. The AZ5214E photo resist is used with 4000 rpm spin coating for 1 minute. The baking is 120 degrees for 2 minutes. MJB4 mask aligner is used for alignment and exposure whose time is 30 seconds.

The whole sample preparation process consists of three EB lithography steps and one optical lithography step. The procedures are following: alignment markers Ti(20 nm)/Pt(70 nm) → main Pt wires whose width, length and thickness is 300 nm, 30 μm and 7 nm respectively → guiding electrodes Ti(20 nm)/Pt(30 nm) → contact pads Ti(20 nm)/Au(80 nm). The drawing of those structured is shown in Fig. 18(b). As the YIG samples are quite precious, we optimized the device packing to allow as much as possible of the YIG surface to be covered by devices (usually 300 devices on a 1 cm^2 surface).

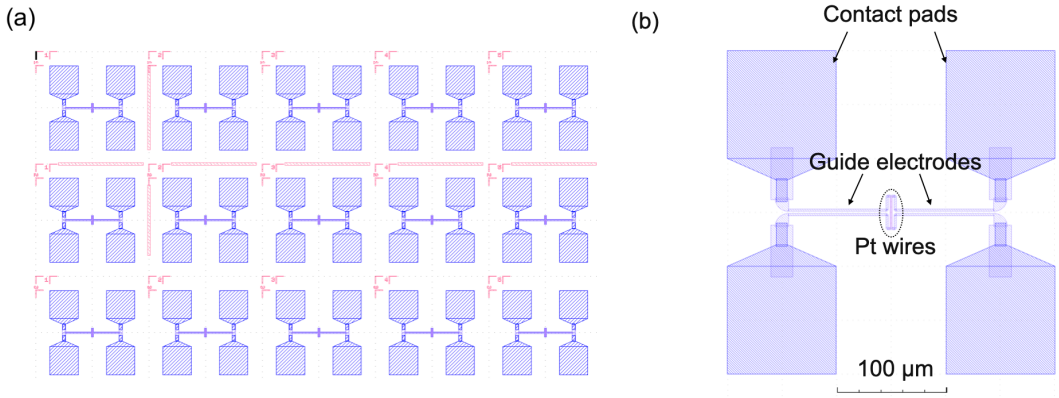

Figure 18: *Design of patterning. (a) Array of devices with alignment marks. (b) Zoom on 1 device, which consists of two main Pt wires, guide electrodes and contact pads.*

2.3 Measurement protocol

One of the main advantages of the non-local magnon transport device is the simplicity of the circuits. A DC current source connected to one Pt wire and a voltmeter connected to the other Pt wire under an in-plane magnetic field are basic elements of the measurement protocol. The sample is glued on a sample holder with contact pads placed on a rotation rod. The device is electrically connected to the cable by wire bonding between the device contact pads and the sample carrier. Through the cable, the Pt wires are connected to the Keithley 6221 current source for the emitter electrode or the Keithley 2181a nano-voltmeter for the collector electrode. The voltage of the collector electrode is monitored while electrical current pulses are applied in the emitter electrode, under an in-plane magnetic field. We use the *Pulse delta method* which is functional when a Keithley 6221 current source and a Keithley 2181a nano-voltmeter are connected via a RS232 cable. This method is based on a 3-point average reading of the voltage, comparing current off and on states. It is useful to reduce noise and to remove the thermal baseline that is induced for example by the normal Seebeck effect. The clock in the system is set by the power line cycle (PLC) with is 20 ms. The duration of the current pulse is chosen to be 10 ms with 100 ms of interval between pulses corresponding to 10 % duty cycle. The voltage of the collector is read after a delay time of 500 μs to wait for the voltage to be stable after the transient regime. The measured voltage is the average of 200 Pulses and readings to increase the signal to noise ratio. Through this method, a low noise (a few tens of nanovolt) and large current application (2×10^{12} A/m^2) can be realized. We measure the voltage with positive and negative polarity of current for each data point to extract the contributions explained below. A more detailed characterization of this method can be found in Ref. [105].

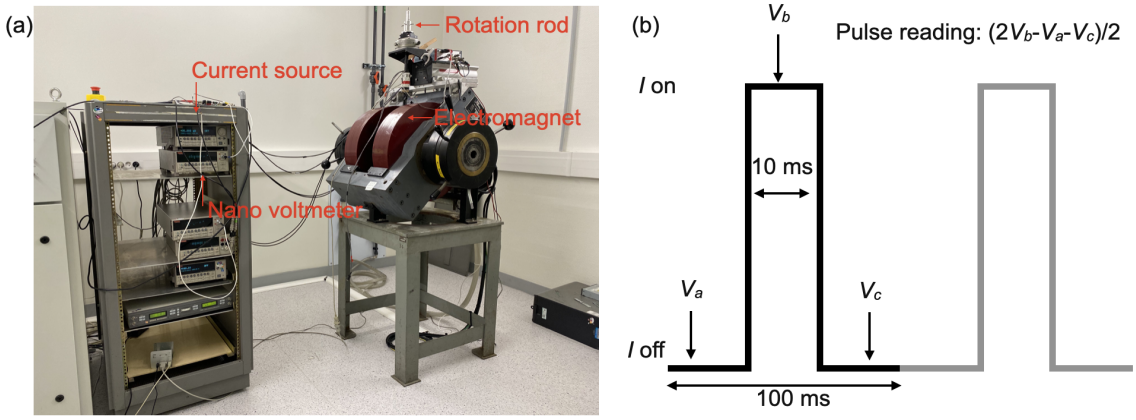

Figure 19: *(a) Picture of the experimental setup used in this manuscript. The main components are an electromagnet, current source and a nano voltmeter. (b) Schematics of the Pulse delta method. The horizontal and vertical axis corresponds to time and voltage, respectively.* V_a *and* V_c *are the voltage read before and after the current application, and* V_b *is the voltage when the current is applied. The final output is the* $\frac{2V_b - V_a - V_c}{2}$ *to reduce the effect of thermal drifting.*

2.4 Extracting SSE and SOT contribution

We measure the voltage at the collector while the current is applied in the emitter. The obtained voltage is a mixture of several contributions. One is from spurious electrical conduction, others are from magnon conduction by SSE or SOT. Here we list up the procedure to extract these contributions. However the non-linear asymmetric behavior of the magnon conduction complexifies the decomposition. In chapter 4 and 5, we will refine this process.

1. *Spurious electrical conduction*
   The first one comes from the spurious electrical conduction in the insulator. It is reported that at a high temperature the electrical conductivity of YIG increases. We attribute impurities incorporated in YIG during the fabrication process such as Pb ion to being responsible for conduction channels. The detailed discussion is found in Ref. [105, 150]. This effect can be subtracted by comparing the voltages $V_{2,\perp}$ and $V_{2,\parallel}$ at the Pt_2 collector when the magnetic field is either orthogonal to or along Pt wires (along x or y in Fig. 10) respectively. Due to the symmetry of the spin Hall effect, the voltage from the magnon propagation cannot be sensed when the magnetic field is along the Pt wire. Thus in this configuration, only the contribution of spurious electrical conduction is detected. The signals related to magnon conduction $\mathscr{V}_2$ are then obtained as follows.

$$\mathscr{V}_2 = V_{2,\perp} - V_{2,\parallel} \tag{2.1}$$

   Let's call $\overline{\mathscr{V}_2}$ and $-R_2 I_2$ the contribution from SSE and SOT respectively, R_2 and I_2 are the resistance and the collected current of Pt_2, respectively. The overline for SSE represents that it is naively expressed as the averaging of the voltages for positive and negative current applications. The minus sign in the SOT contribution accounts for the fact that the spin-charge conversion is an electromotive force and the current flows opposite to the voltage drop. Thus, the voltage subtracted from

the spurious electrical contribution is further decomposed into two elements :

$$\mathscr{V}_2 = \overline{\mathscr{V}_2} - R_2 I_2 \tag{2.2}$$

2. *Simple current symmetry operation for low current*
At a low current application, where the conduction of magnons behaves linearly, the contribution of SOT and SSE can be extracted by doing a simple current symmetry operation. The SSE contribution comes purely from Joule heating as the temperature gradient is the main source. Thus the SSE is even in current. On the other hand, the SOT contribution comes from the spin transfer effect, thus the magnon annihilation or creation occurs depending on the relative direction of spin polarization and magnetization. In the end the SOT contribution is odd in current. Regarding the symmetry of the angle and field, they mostly follow the symmetry of the spin Hall effect. The spin charge interconversion occurs 1 time for SSE only at the collector, thus the angular dependence is $\cos\phi$. If the magnetic field is flipped in the opposite direction, the SSE signal also changes the sign. In contrast, for the SOT contribution both the generation and detection rely on the interconversion process, which leads to the angular symmetry of $\cos^2\phi$. Thus the sign of SOT signal does not change when the magnetic field is flipped. In conclusion, the SOT contribution V_{SOT} and the SSE contribution V_{SSE} can be obtained by changing the polarity of current I_1 such that

$$\overline{\mathscr{V}_2} == \frac{\mathscr{V}_2(+I_1) + \mathscr{V}_2(-I_1)}{2} \tag{2.3}$$

$$-R_2 I_2 = \mathscr{V}_2 - \overline{\mathscr{V}_2} \tag{2.4}$$

3. *Non-linear behavior for high current*
The magnon conduction shows non-linear behavior at large density of spin current injection. Especially for low-energy magnetostatic magnons, diode-like conduction, that is, the asymmetry between the forward and reverse direction of current appears. It means that the simple symmetry operation introduced above underestimates the SOT contribution as soon as the system exceeds the linear response. We introduce a tentative way to estimate separately the magnon annihilation and creation process for SOT contribution. The first important observation is the continuity at the origin regardless of the polarity of the current, that is, $-R_2 I_2(+I_1) = -(-R_2 I_2(-I_1))$ [52, 151], with I_1 the current in the Pt_1 emitter. This is supported by the analytical expression of Eq. (1.96). Thus, we assume that the annihilation process can be interpreted as a linear deviation of the number of magnons with respect to the magnon population activated by thermal fluctuation. Thus for the reversed bias, the conductivity is assumed to have a constant behavior if we divide it by I_1. The magnon creation process in the forward polarity is recovered by subtracting the annihilated contribution from the anti-symmetric part of the signals. Indeed the SSE contribution can be deduced from the residual signal of $\mathscr{V}_2$ as introduced just above.

Fig. 20 shows exemplary data of our field dependence measurements, using the BiYIG 20 nm sample discussed mainly in chapter 6. The distance between the emitter and collector and the injected current are fixed to be $d = 3.3$ μm and $I_1 = 1.5$ mA. Panel (a) shows the obtained raw signal without any processing. The blue and red curves correspond to the negative and positive polarity of the current. The grey curve represents the contribution from the spurious electrical current conduction. The finite difference

between $\pm I_1$ represents the contribution from SOT. The switching of the signal at a low field comes from the magnetization reversal, which flips the sign of the SSE contribution. A slope appears in only one particular polarity of current, ($-I_1$ for $H > 0$ and $+I_1$ for $H < 0$). This is the signature of low-energy magnetostatic magnons that are sensitive to the magnetic field. Panel (b) presents the extracted SSE contribution and shows the expected sign reversal of the signal, with odd symmetry in field. Panel (c) shows the extracted SOT contribution. The field dependence now reveals the sole signature of the excitation of the low-energy magnons. The switching of the sign does not occur, which shows even symmetry in the magnetic field. BiYIG has perpendicular uniaxial anisotropy but the magnetic field is applied in-plane and about 40 mT (corresponding to the anisotropy field) is needed to saturate the magnetization along the field. This effect can be seen when one pays attention to the data points near the zero field. Fig. 21 is exemplary data of angular dependence measurement. Panel (a) shows the obtained raw signal where the blue and red curves correspond to the negative and positive polarity of the current. Indeed the finite difference between $\pm I_1$ represents the contribution from SOT. (b) and (c) represent the extracted SSE and SOT contribution with $\cos\phi$ and $\cos^2\phi$ fitting as a dashed curve respectively, which is expected from the symmetry of the spin Hall effect.

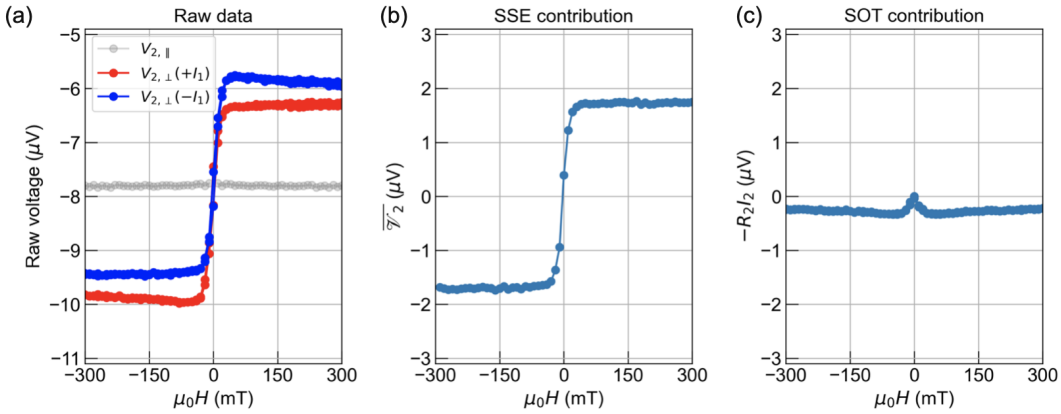

Figure 20: *Example of field dependence measurements. (a) Shows the obtained raw signal without any processing. The blue and red curves correspond to the negative and positive polarity of the current and the grey curve represents the contribution from the spurious electrical current conduction. The finite difference between $\pm I_1$ represents the contribution from SOT. The switching of the sign of the signal is due to the magnetization reversal and SSE contribution. The slope appears in only one particular polarity of current, ($-I_1$ for $H > 0$ and $+I_1$ for $H < 0$), which is the signature of the low-energy magnons. (b) Extracted SSE contribution. (c) Extracted SOT contribution.*

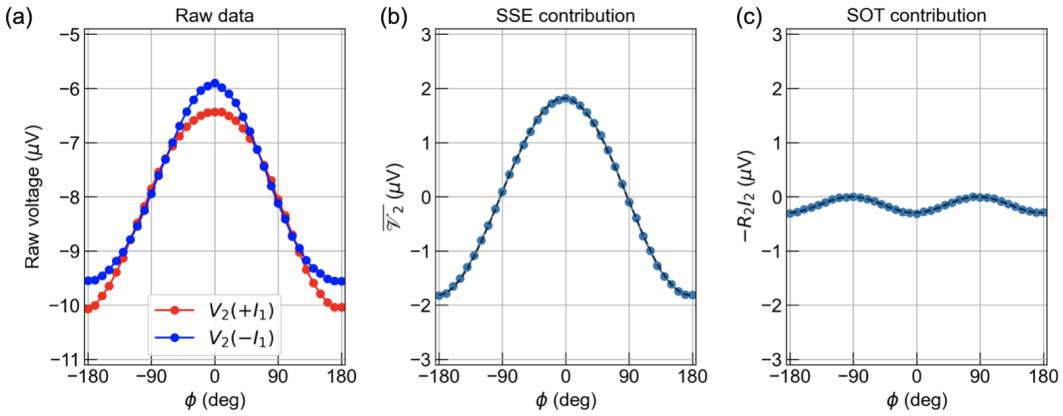

Figure 21: *Example of angular dependence measurement. (a) Shows the obtained raw signal. The blue and red curves correspond to the negative and positive polarity of the current. (b) Extracted SSE contribution with* $\cos\phi$ *fitting as a dashed curve. (c) Extracted SOT contribution with* $\cos^2\phi$ *fitting as a dashed curve.*

Chapter 3

Short range thermal magnon diffusion in magnetic garnets

We start the chapters on experimental results with the understanding of propagation characteristics of high-energy thermal magnons, which is dominated by λ, the characteristic decay length of the spin information. Previous studies on measuring λ in YIG at room temperature by the spin Seebeck effect (SSE) indicate that for distances larger than $\sim$10 μm (long-range regime), the SSE signal shows an exponential decay of the order of $\lambda_0 \approx 10$ μm [52, 152], which is reprinted in Fig. 22(a). Such a large value is believed to exceed ℓ, the magnon mean free path (energy non-conserving decay length), which is expected to be on the order of a few nanometers [153, 154], suggesting that magnons behave as a diffusive gas [143]. It may seem surprising for high-energy thermal magnons which carry an energy of the order of k_BT. First of all, it is almost identical to the decay length of the magnons excited electrically by spin orbit torques (SOT). It is questionable if similar magnons are generated by the two methods considering that the magnetic field dependence measurements show a clear difference between the two [105]. Quantitatively, if one extends the magnon dispersion up to the THz-range as shown in Fig. 12, the calculated ballistic decay length using the decay rate and group velocity for thermal magnons is $\lambda_{\mathrm{bal}} = \lambda_{\mathrm{ex}}/(2\alpha\sqrt{\omega_T/\omega_M}) = 2$ μm as shown in Fig. 22(b), where $\omega_T = k_BT_0/\hbar = 2\pi \times 6.25$ THz, T_0 is the room temperature, $\lambda_{\mathrm{ex}} \approx 15$ nm is the exchange length in YIG, $\alpha \approx 4\times10^{-4}$ is the Gilbert damping, and $\omega_M = \gamma\mu_0 M(T_0) = 2\pi\times4.48$ GHz, with M being the saturation magnetization. However this estimate λ_{bal}, which is already smaller than λ_0, should be considered as an upper bound because *i)* the magnon lifetime is expected to be reduced in the THz-range [155] *ii)* the group velocity is reduced towards the edge of the Brillouin zone [133, 134], and *iii)* it does not account for the $\sqrt{\ell/\lambda_{\mathrm{bal}}}$ reduction of the characteristic propagation distance due to the diffusion process.

In fact, the distance range of the transport study, *i.e.* the distance between the emitter and collector, is also a straightforward means to select a very specific part of the magnon spectrum. In experiments focusing on the long-range behavior with micron range, one cannot in real sense any short decay magnons. Behind this debate lies a fundamental question of how well magnon transport can be described by a diffusive model forming one gas with a single λ, whose value would govern SSE on all length scales. Submicron lengths have been indicated in several longitudinal SSE measurements in spatial [156, 157] and time domain [158, 159]. In non-local SSE measurements, where two different Pt strips are used for the spin emission and collection, only longer spin decay lengths have been reported. The existence of shorter decay lengths has been difficult to observe because the voltage induced by SSE shows a nontrivial spatial decay as a function of the collector Pt position near the heat source [139, 160]. The complex decay profile can be attributed to the competition between magnons driven by the gradients of temperature and magnon chemical potential [54, 142, 143]. It has been difficult to control these two sources of spin excitation in experiments, which prevents from a correct extraction of a characteristic decay length near the heat source. In addition the appearance of a vertical temperature gradient underneath the collector contributes to the measured signal, which is not indeed

relevant to the characteristics of transport.

Here we develop a way to disambiguate these two contributions after altering the temperature profile. We monitor on the same devices the short-range SSE signal before (case A) and after (case B) by capping it with a non-magnetic metallic aluminum layer. The capping layer allows us to change the vertical thermal gradient without altering the YIG interface. We observe that the sign of SSE voltage inverts twice within a distance of 1 μm from the heat source for case B. The corresponding sign reversal of SSE suggests that the magnons clearly sense the change in the local temperature gradient taking place for case B. With a simple diffusive transport model, the measured SSE decay profile for both cases can be reproduced if one introduces a thermal magnon diffusion length $\lambda \approx 300 \pm 200$ nm. The extracted short λ from our measurement fills the gap between different length scales reported in the longitudinal and nonlocal SSE measurements. This research has been performed in collaboration with Prof. Yaroslav Tserkovnyak group to improve theoretical understandings and has been published in Physical Review B 103, 174432 in 2021 [119]. The former postdoctoral researcher Dr. Kyongmo An in our group led this research and I contributed to the analysis of the data. The part of figures and sentences in this chapter are taken from the Ref. [119].

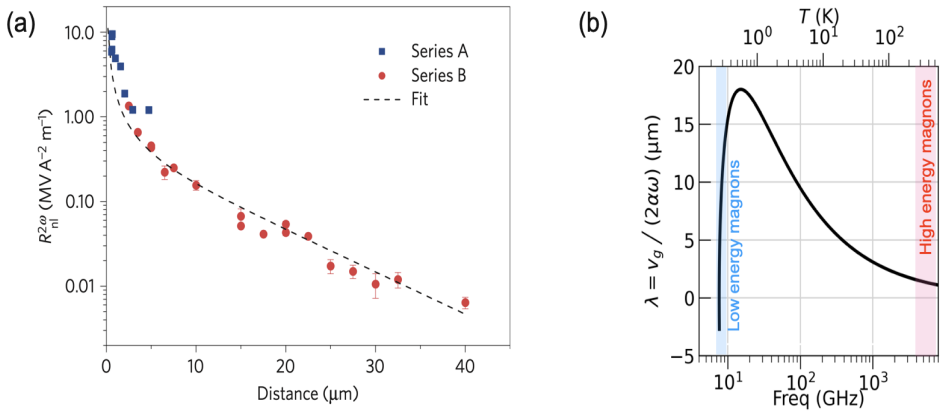

Figure 22: *(a) Decay behavior of initially reported SSE signal. The solid line represents the exponential fit with 9 μ decay length. The figure is taken from Ref. [52], the pioneer paper of this research field. (b) Calculated ballistic magnon relaxation length as a function of frequency. This shows the upper bound of characteristic decay of high-energy thermal magnons as 2 μm. $\alpha = 4 \times 10^{-4}$ is used.*

3.1 Characteristics of YIG and Pt wire, and simulations

We use a 56 nm thick YIG(111) film grown on a 500 μm GGG substrate by liquid phase epitaxy with excellent quality of magnetic damping parameter 2×10^{-4}, which ensures good crystallinity of the YIG film [161]. The sample structure and measurement configuration are shown in Fig. 23. In our notation, subscripts 1 and 2 correspond to the voltages measured by the Pt_1 (emitter) and Pt_2 (collector), respectively. We show the data for both YIG|Pt|Si_3N_4 (case A, red) and YIG|Pt|Si_3N_4|Al (case B, blue), where color conventions will be used consistently throughout the paper. Two Pt strips with width of 300 nm, length of 30 μm and thickness of 7 nm have been deposited directly on top of the YIG film by sputtering. The center-to-center distance d between two Pt strips varies from 0.5 to 6.3 μm. The sample is then covered by a 20 nm thick Si_3N_4 protection film by sputtering. After full characterization of the different devices, a 105 nm thick Aluminum layer with length 30 μm and width 10 μm is deposited on the top of the Si_3N_4 film by electron beam evaporation as illustrated in Fig. 23(b), and the same devices are measured again. The sample is exposed to an external field of $\mu_0 H_0 = 200$ mT rotating within the xy plane, where coordinate is indicated in Fig. 23 (in-plane configuration).

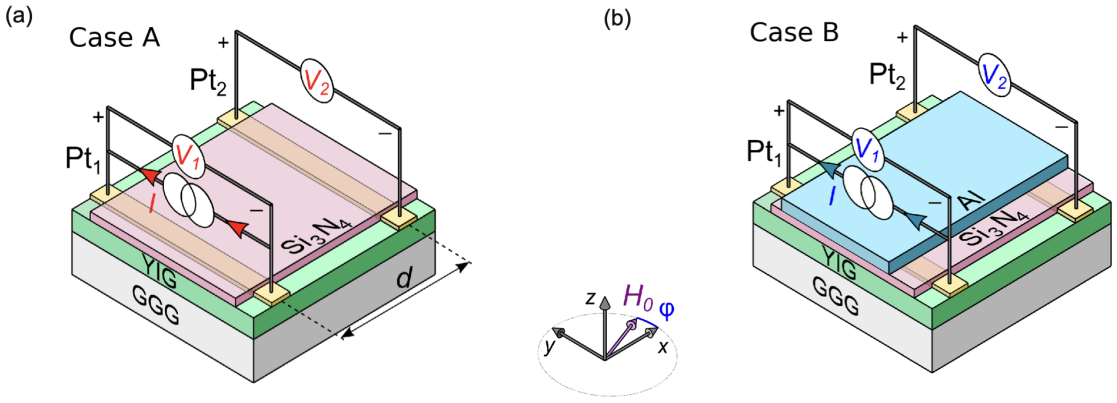

Figure 23: *Schematics of structures of magnon transport devices which consists of two Pt wires deposited on YIG. (a) represents the Case. A without Aluminium capping layer and (b) represents Case. B with the capping layer.*

The magnetometry measurements are conducted using SQUID-VSM technique to determine the temperature response of magnetization and the Curie temperature as shown in Fig. 24(a). The measurement is performed by Dr. Thomas Hauet in Université de Lorraine in Nancy, France. The solid line is the fitting with a phenomenological function $\mu_0 M(T) = \mu_0 M_s (1 - (T/T_c)^a)^b$ and we obtain the saturation magnetization at zero kelvin as $\mu_0 M_s = 0.217$ T, the Curie temperature $T_c = 544$ K, and the exponents $a = 2.0$, $b = 0.6$. Panel (b) represents the $R - I$ characteristics of Pt_1 for both case A and case B. Both a current source and voltmeter are connected to the emitter and the Pulse delta method with 10 % duty cycle is performed. The resistance change ΔR is normalized by $R_0 = 2.8$ kΩ. The increase of resistance while applying current is indeed due to the Joule heating, which can be fitted with a quadratic function. Case B shows a slower increase of resistance by Joule heating, revealing that the Aluminium layer acts as the efficient heat sink. In the inset, the relative increase of the resistance as a function of ambient temperature is plotted, obtaining the temperature coefficient $\zeta = 2.1 \times 10^3$ K^{-1}. Finally

we characterize the temperature rise ΔT due to the Joule heating underneath the emitter for both cases as indicated in the right axis.

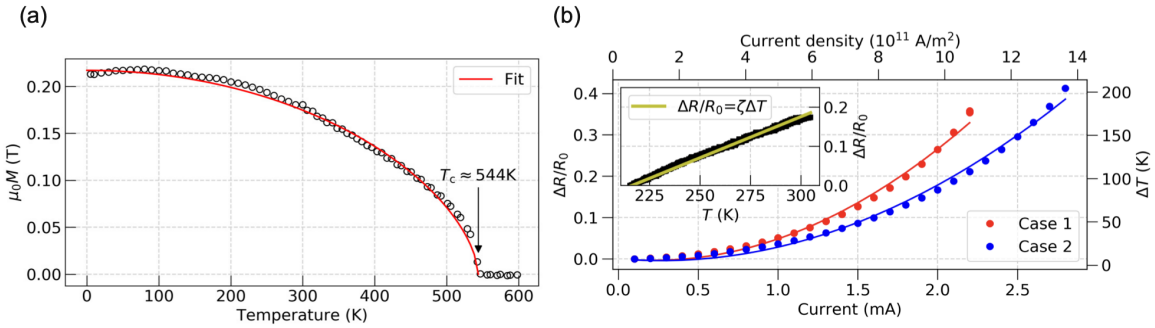

Figure 24: *(a) Magnetization as a function of temperature obtained with SQUID-VSM facility in Université de Lorraine. (b) The relative resistance change as a function injected current for Case A (red) and Case B (blue). The right axis represents the corresponding temperature rise where the temperature coefficient ζ is shown as the inset. The upper scale is the converted current density.*

The finite element simulations are performed to calculate the temperature profile and chemical potential distribution using the commercial software COMSOL. The geometry of simulation cells is two dimensional with a boundary condition that the top and the side surfaces are thermally isolated, and the bottom surface is fixed at room temperature. Additionally we impose that the normal component of the spin current is zero at the boundary. The geometry was chosen to be the same as the actual sample size explained above except for the lateral size and thickness of GGG which is reduced to 30 μm in contrast 500 μm in reality to ease the calculation. The mesh of simulation cells is shown in Fig. 25 The thermal conductivity of GGG [162], YIG [162], Pt [163], Al [164] and Si_3N_4 [165] is set to be 9, 7.4, 29, 220, and 0.5 $Wm^{-1}K^{-1}$.

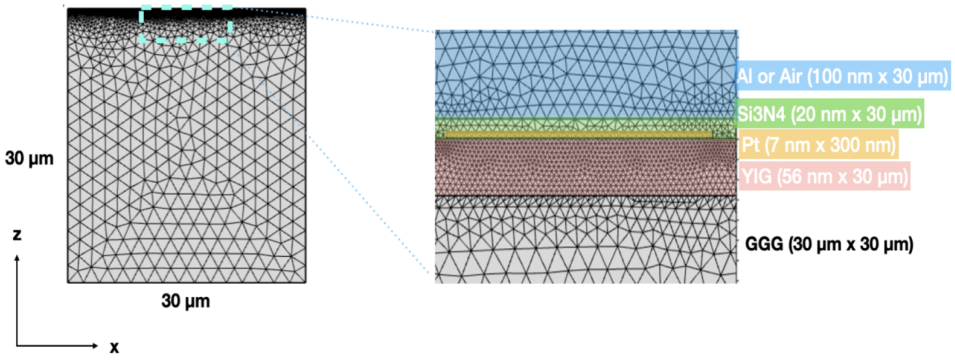

Figure 25: *Mesh of simulation cells used in finite element simulations*

The calculated temperature profiles at the top of YIG surface are shown for the two cases in Fig. 26(a). The temperature difference at d = 0 μm (the center of Pt injector

strip) between the two cases is 37 K, which roughly agrees with the measured temperature difference at 2 mA as shown in Fig. 24. At the same time we obtained the profiles of the vertical temperature gradient, which will be used to calculate the magnon chemical potential as shown in panel (b). To check the validity of the calculated temperature profile, we measured the temperature rise at the position of the detector in case A. Our estimation yields a temperature drop of 46% for the detector placed at d = 0.5 μm away from the injector. This is larger than the simulated temperature drop of 30% over the same distance (red curve in Fig. 26). The discrepancy may arise from (i) the simplification of 2D modeling and (ii) the possible difference in parameters between the simulation and the measurement. Not only the change in the temperature profile, but also the gradient profile shows a drastic change by the metallic heat sink. While in case A the vertical temperature gradient is always directed downwards (into the substrate), in case B, a large thermal gradient directed upwards (into Al) is created half a micron away from the source. The shaded region highlights the effect. Since the vertical thermal gradient drives the SSE, this feature gives rise to an additional signal at Pt_2. In addition, a non-negligible amount of temperature gradient still persists till a few microns away from the heat source, which indeed creates voltages whose sign is reversed.

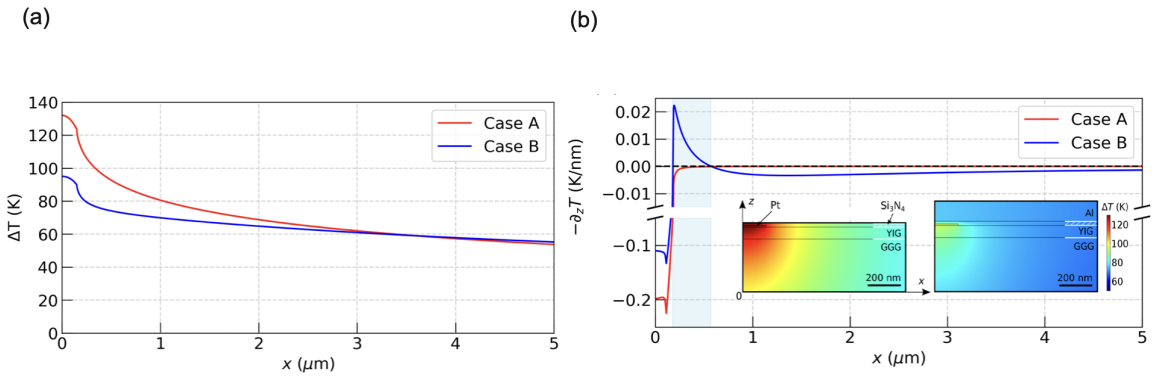

Figure 26: *(a) Spatial profiles of temperature rise near the surface for Case A (red) and Case B (blue) when 2 mA of electrical current is applied in Pt_1. (b) The corresponding profiles of the vertical temperature gradient. The inset shows the density plots of temperature distribution for the two cases.*

In fact, above mentioned spatial profile does not consider the collector electrode that may sink heat. Fig. 27 shows the comparison of the simulated temperature profiles with or without the Pt collector at $d = 1$ μm. It reveals less than 1 K variation of the temperature due to the collector in both cases. It corresponds to less than a 1 % change in the temperature rise. This is because the Pt wire covers only a small area of the YIG surface and its thermal conductivity is estimated to be as low as about 29 $Wm^{-1}K^{-1}$ expected from its high resistance of 3.8 kΩ from the Wiedemann-Franz law. For case B in panel (b), we obtained the same behavior and we conclude that the effect of Pt collector on the thermal profile is negligible.

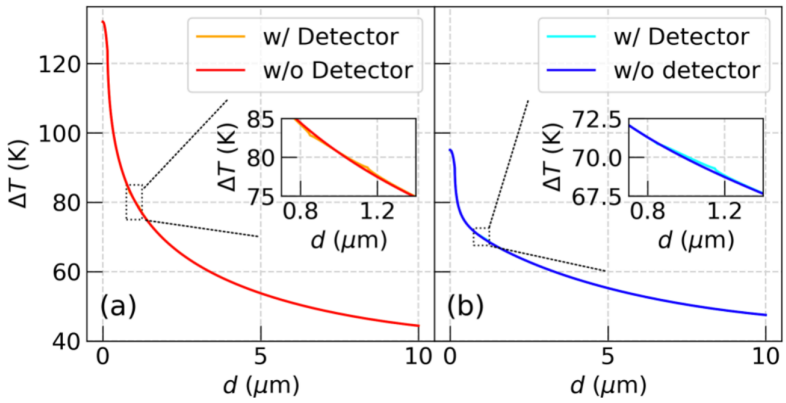

Figure 27: *Comparison of simulated temperature profiles at 2 mA with and without Pt collector placed at $d = 1$ μm for (a) case A and (b) case B.*

3.2 Transport characteristics of SSE signals

Now let us study the behavior of high-energy thermal magnons generated by the spin Seebeck effect (SSE) [46]. We compare the full current dependence of the local SSE signal $\overline{\mathscr{V}_1} = (\mathscr{V}_1(+I_1)+\mathscr{V}_1(-I_1))/2$ for both case A (red) and case B (blue) in Fig. 28(a), where $\mathscr{V}_1$ is the voltage with offset subtraction measured at Pt_1 while electrical current is applied in the same wire ($\mathscr{V}_1 = V_{1,\perp} - V_{1,\parallel}$). It is clearly seen that the voltage is negative for both cases over the whole current range. The parabolic curvature observed at low currents decreases when the Al heat sink is introduced, which agrees with the reduced temperature rise. We observe that $\overline{\mathscr{V}_1}$ reaches a minimum at 2 mA for case A with the minimum shifting to a higher current for case B. We attribute this reversal of the slope as the growing influence of the vanishing YIG magnetization as one approaches T_c=545 K, the Curie temperature of YIG shown in Fig. 24(a). The measured local SSE signal follows the expression as $SL_{\mathrm{Pt}}\langle\partial_z T\rangle$, where S is the spin Seebeck coefficient, $L_{\mathrm{Pt}} = 30$ μm is the length of Pt electrode, and $\langle\partial_z T\rangle$ is the vertical temperature gradient across the YIG thickness. The latter is proportional to the temperature rise of the Pt_1 due to Joule heating, that is, $\langle\partial_z T\rangle = \delta T/l_T$, where l_T is the characteristic decay length of temperature from the top surface. From Fig. 26(b), $\langle\partial_z T\rangle$ =10 K/56 nm for $\Delta T = 130$ K (2 mA), the l_T is estimated as *approx*730 nm. Assuming that S is scaled with $\mu_0 M(T)$ as the number of polarized spins is the dominant factor of the magnon generation process, the expression for local SSE signal $\overline{\mathscr{V}_1}$ as

$$\overline{\mathscr{V}_1} = C\frac{L_{\mathrm{Pt}}}{l_T}\Delta T \mu_0 M(T) \tag{3.1}$$

where $C \equiv S/(\mu_0 M(T))$. Using the result in Fig. 24(a), we successfully fit the $\overline{\mathscr{V}_1}$ for Case A with the single fitting parameter C as a red solid line in Fig. 28(a), yielding $C = 0.43$ $\mu\mathrm{VK}^{-1}\mathrm{T}^{-1}$. Finally the spin Seebeck coefficient at room temperature is deduced as $S \approx 0.08$ $\mu\mathrm{VK}^{-1}$, which agrees with a previous report [166].

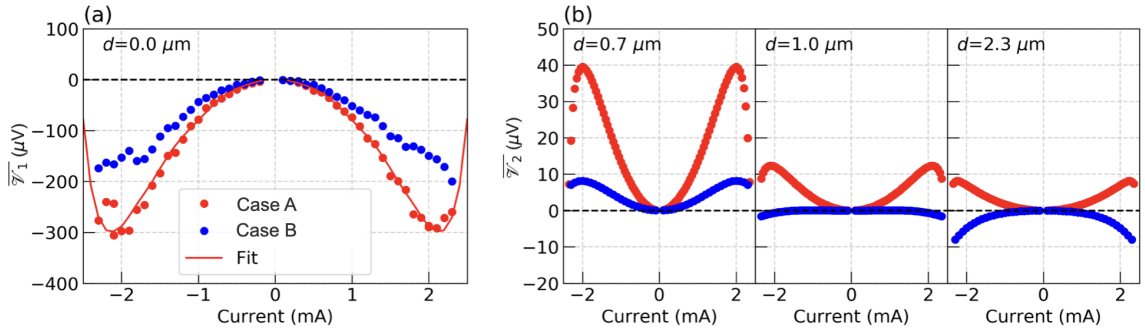

Figure 28: *(a) Current dependence of measured local SSE signal for case A (YIG|Pt|Si_3N_4) and case B (YIG|Pt|Si_3N_4|Al). The red solid line shows that it follows the expected behavior based on the temperature rise with increasing current. (b) Measured current dependence of non-local SSE signal for three different d's for the case A (red) and B (blue).*

While the local voltage $\overline{\mathscr{V}_1}$ is always negative, the non-local voltage $\overline{\mathscr{V}_2} = (\mathscr{V}_2(+I_1) + \mathscr{V}_2(-I_1))/2$ from devices in case A are positive for all the different distances (red curves in Fig. 28(b)). This observation is consistent with the previous works that reported a single sign reversal of the SSE voltage measured as a function of distance from the heat source [139, 167, 168]. It has been reported that the characteristic distance at which the magnon accumulation changes the sign can be tuned by varying the magnetic film thickness [139] or magnon diffusion length [167].

The situation is quite different for case B, as shown with the blue dots in Fig. 28(b). In the vicinity of the injector, the non-local SSE signal $\overline{\mathscr{V}_2}$ is still positive at 0.7 μm but much smaller than case A. The sign of $\overline{\mathscr{V}_2}$ for case B eventually becomes negative when the Pt detectors are positioned at 1 μm and 2.3 μm away from the injector. Our understanding of the sign changes as a function of d is as follows: at $d = 0$, heat drags magnons from Pt_1 down into YIG (negative sign SSE); at larger d, magnons can transfer spin from the YIG bulk into Pt_2 (positive sign); adding Al creates a region of inverted heat flow over a short range (positive sign within 0.2 and 0.5 μm) and significant heat flow down into YIG over a longer range (negative sign). The fact that we see a negative signal after the second crossing signifies that the positive SSE driven by the magnon diffusion already becomes diminished and the local temperature driven SSE dominates, as indicated in Fig. 26(b) that for Case B the vertical temperature gradient remains active even at a large distance. In this perspective the second crossing point (the distance at the second sign change of the gradient), which is defined as d_2 from now on, may put an upper bound on the estimate of λ.

3.3 Modeling of magnon diffusion and fitting of characteristic decay

To model our experiment, let us recall the formalism introduced in chapter 1 subsection 1.2.6. we consider the magnons in YIG as a diffusive gas with temperature T and chemical potential μ described by a set of transport coefficients [143]. The measured $\overline{\mathscr{V}_{1,2}}$ signal is proportional to the magnon chemical potential at the interface between YIG and Pt [144].

The continuity equation for spin current density J_s in the steady state is

$$-\boldsymbol{\nabla} \cdot \boldsymbol{J_s} = g\mu, \tag{3.2}$$

where g is spin relaxation coefficient. In linear response, the transport equation is

$$\boldsymbol{J_s} = -\sigma(\boldsymbol{\nabla}\mu + \varsigma\boldsymbol{\nabla}T), \tag{3.3}$$

where σ is the spin conductivity and ς is the bulk spin Seebeck coefficient. The two equations are combined and lead to

$$\frac{\mu}{\lambda^2} = \boldsymbol{\nabla}^2\mu + \varsigma\boldsymbol{\nabla}^2 T, \tag{3.4}$$

where $\lambda = \sqrt{\sigma/g}$ is the thermal magnon diffusion length.

We use again the finite element method, COMSOL to calculate the magnon chemical potential μ using the profile of the vertical temperature gradient shown in Fig. 26(b). The calculated spatial profiles of μ for three different values of λ are compared with the experimental data at 1 mA or 2 mA of injection as shown in Fig. 29(a) and (b) after normalization to the measured values at $d = 0$ μm. The second crossing point d_2 observed in case B, as indicated in Fig. 29(b), is an important feature that reveals the inverted heat flow near the heat source as shown in Fig. 26(b). We find that the second sign reversal at d_2 can be reproduced by simulations with a short $\lambda = 100$ nm. Increasing it to 0.5 or 1 μm, however, no longer reproduces the second crossing in case B (compare solid line with dashed and dotted lines in Fig. 29(b)). In addition the data with 1 mA agrees better with the behavior of the theoretical model with $\lambda = 100$ nm for both cases. This suggests that at high current, the non-negligible contribution of low-energy magnetostatic magnons can be contained in the $\overline{\mathscr{V}_2}$, where simply symmetry operation cannot exclude.

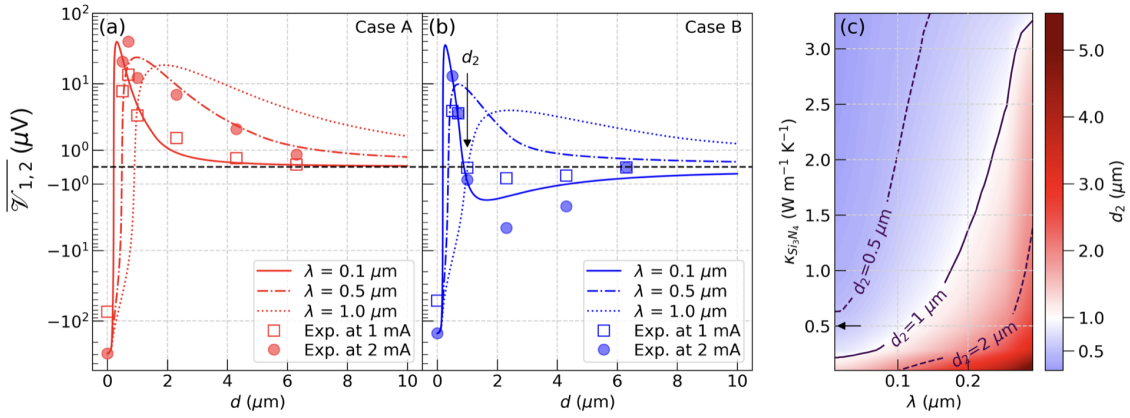

Figure 29: *Comparison of the experimentally measured $\mathscr{V}_1$ and $\mathscr{V}_2$ at 1 and 2 mA with the numerically calculated chemical potential profile for (a) case A and (b) case B on a symmetric log scale. The result with $\lambda = 0.1$ μm reproduces the measured double crossing as shown in (b). The second crossing does not appear anymore when increasing λ to 0.5 or 1 μm. (c) Contour plot of the second crossing position d_2 as a function of λ and thermal conductivity of Si_3N_4. The black lines represent the iso-lines for different d_2's. The arrow points to the value of $\kappa_{Si_3N_4}$ used in panels (a) and (b).*

The fit value of λ depends on other parameters in the model. The second crossing

point, d_2, can be affected by the temperature profile at the interface, which is sensitive for example to the thermal conductivity of Si_3N_4. We show a contour plot for d_2 as a function of $\kappa_{Si_3N_4}$ and λ in Fig. 29(c). The measured second crossing constraints the parameter space to the line along $d_2 = 1$ μm. The second crossing is not observed for $\lambda > 500$ nm regardless of $\kappa_{Si_3N_4}$. These considerations can be further modified by the interfacial SSE due to the magnon-phonon temperature difference at the interface [169, 170]. Enhanced local temperature driven contribution to the measured signal can increase λ for a given d_2. To have *quantitative* agreement with the data, we also get an upper bound of $\lambda \sim 500$ nm, although it is worth mentioning that in the limit of large temperature mismatch between the YIG and the Pt one can *qualitatively* reproduce the single crossing in case A and double crossing in case B for much larger λ. The Kapitza resistance, which creates a temperature discontinuity, δT across the YIG|Pt interface can be a source of spin currents [170, 171]. One can assume that δT is proportional to the temperature gradient at the interface, $\partial_z T$. We recall that z is the direction normal to the film. The measured SSE voltage including the interfacial contribution can be written as

$$V_{SSE} = C_1(\mu - C_2 k_B \partial_z T) \tag{3.5}$$

where μ is the magnon chemical potential obtained by solving Eq. (3.4). C_1 is a constant, which normalizes the simulation results to the experimental data at $d = 0$ μm. C_2 is a parameter proportional to the Kapitza length, which represents the contribution of the interfacial term. The negative sign implies that the heat flow is along the opposite direction of the temperature gradient. One can assume that C_2 is the same for both case A and case B for fixed d because the Al layer does not touch either the YIG or Pt directly. Fig. 30 shows the effect of adding a finite C_2 for different values of λ. For $C_2 = 0.5$ μm, the calculation can reproduce the observed double crossing in case B for all four values of λ. However, $\lambda = 1$ μm case does not predict well either the observed first crossing in case A or the second crossing in case B. It is important to also point out that V_{SSE} eventually follows the temperature gradient profile in Fig. 26 when the C_2 term becomes more dominant (see reduced dependence on λ when $C_2 = 0.5$ μm). Thus in the limit of very large C_2, the observation of a double SSE sign crossing in case B is not anymore conspicuous of a short decay length of thermal magnons. Another consequence of assuming that the interfacial effects are dominant is to reduce strongly (more than three orders of magnitude) the amplitude of the signal after the first crossing in case A. The fact that we observe experimentally only an order of magnitude reduction of the SSE signal for case A thus points to a small value of $C_2 \ll 0.5$ μm. Experimentally, we have performed an estimation of the Kapitza resistance by comparing the increase of the Pt temperature inferred from the variation of its resistance and the temperature increase of YIG inferred from the decrease of the Kittel frequency due to a change of $M_s(T)$, whose slope is about 0.4 mT/K at room temperature [56]. We have found no temperature difference between the Pt and the YIG underneath within the uncertainty of 2 K when the increase of temperature is 70 K. From this we estimate an upper bound of Kapitza length of about 20 nm.

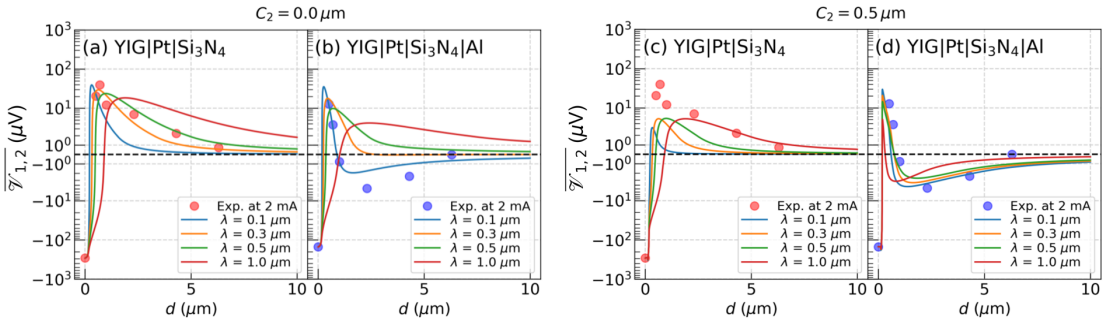

Figure 30: *The calculated spatial profile of μ after normalization to the measured values at $d = 0$ μm. The results are compared to the experiments with varying λ for (a,c) case A and (b,d) case B with $C_2 = 0, 0.5$ μm. Only $\lambda = 100$ and 300 μm show qualitative agreements for case B with $C_2 = 0$. With an increased $C_2 = 0.5$ μm, $\lambda = 500$ nm can roughly fit for both cases (panel c,d).*

Although our proposed fit with a diffusive equation parametrized by $\lambda \in [100, 500] \approx 300 \pm 200$ nm captures well the short-range behavior in both cases A and B, we emphasize that this does not contradict earlier works [52, 140]. The data observed for case A are similar to the one already observed in other YIG devices, where the fit of the long-range decay behavior has led to the larger $\lambda_0 \approx 30 \times \lambda$. We note that the magnon diffusion equation is constructed under the assumption of a long range behavior, where all the magnons are equilibrated to a common chemical potential. It is not surprising, however, to have a significant departure in the spin transport behavior at short distances, where magnons are not yet internally equilibrated or thermally equilibrated with the surrounding phonons [157]. In certain special cases, this may be modeled by introducing effective length scales, which is illustrated in our analysis. Specifically we suggest a possibility that a subset of out-of-equilibrium magnons, from the thermal energy range, is locally decaying on a shorter length scale (λ) than the asymptotic long-distance decay (λ_0). Our extracted λ is close to the value for the magnon diffusion length predicted in a previous work [172], while λ_0 is comparable to the upper bound estimated in Ref. [173]. The previously reported energy relaxation length of magnons [156–159] is also seen to be similar to λ, which may stem from the multi-scale issue of magnon transports.

3.4 Conclusions

In conclusion, we studied the spatial distribution of thermally generated magnons in a thin YIG film. We modulated the temperature profile across the YIG film with an Aluminum capping layer. This induces the non-equilibrium thermal magnon profile to deviate from an exponential decay and shows a double sign reversal. We use a linear response magnon transport theory to obtain the short-range thermal magnon diffusion length being in the submicron range, which is about two orders of magnitude smaller than the value found in previous reports focused on long range measurements. Our results suggest that the local effect of heating is to produce magnons which decay on a short range near the source. The experimental approach using a heat sink to reveal a short magnons diffusion length may find applications to other systems, especially when the length scale of the diffusion and temperature gradient are comparable.

Chapter 4

Spin diode effect in extended magnetic thin films

While the previous chapter 3 focused on the property of the high-energy magnons excited by the spin Seebeck effect. In this chapter, we will study the transport characteristics of magnons excited by the spin transfer effects, especially that of low-energy magnons. This chapter and next chapter are based on the preprint manuscripts published on ArXiv (arXiv:2210.08304 and arXiv:2210.08283).

Diodes are key components in the art of electronics [174]. Their common function is to produce asymmetric electrical conductance, which facilitates the transport in the forward direction, while blocking it in the reverse. This asymmetry is exploited in rectification or clipping devices. Control of the forward threshold voltage forms the basis of the bipolar junction transistor. A few of these diodes additionally offer the uncommon feature of negative differential resistance, which is exploited in oscillators and active filters [175,176]. Until recently, it was believed that the only possible realization of solid state diodes was with semiconductor materials. Their gapped band structure allows strong modulation of the carrier density by an electric shift of the chemical potential between the valence and conduction bands.

Recent advances in the field of spintronics have shown that one could design new types of nonlinear devices, which rely instead on the transport of the spin of the electron rather than on its charge [20, 177–179]. In this new paradigm, electrical insulators are good spin conductors by allowing the spin to propagate between localized magnetic moments via spin-waves (or their quanta magnons) to transmit spin information inside the crystal lattice without any Joule dissipation [102,113,180,181]. The absence of Joule dissipation usually gifts the dielectric materials with very low magnetic damping, which is associated to a high propensity for magnons to behave nonlinearly. In ultra-low damping materials, a 0.1% variation from the thermal occupation is usually sufficient to drive the magnetization dynamics into the nonlinear regime [182]. These effects could be exploited for spin diodes [102, 183], spin amplifier [109, 184, 185] or spin rectifier of microwave signals [22, 38, 186–188].

A key milestone in this nascent offshoot of spintronics using electric insulators, coined insulatronics [92], has been the discovery of the interconversion process between the spin and charge degrees of freedom (*e.g.* through the spin Hall effect [16,17,88,189–192]), which enables the electrical control of μ_M, the magnon chemical potential, via the spin transfer effects (STE) from an adjacent metal electrode [109,110,193,194]. The anticipated benefit is the realization of a new form of solid state spin diode (see Fig. 10) obtained by shifting μ_M relative to E_g, the energy gap in the magnons' band diagram (see Fig. 11). The level-arm is set here by the magnetic damping parameter, α_{LLG} [104,110,195–197]: the smaller is the damping the larger are electrical shifts of μ_M. Therefore, the ferrimagnet yttrium iron garnets (YIG), with the lowest known magnetic damping in nature, is expected to lead to the highest benchmark in asymmetric transport performance [132]. While the spin diode effect in laterally confined geometries is rather well understood [93,198,199], its generalization to extended thin films has so far been largely elusive [200]. The corresponding

difficulty is the collective dynamics that emerges inside the magnons' continuum, when the level splitting between eigen-modes becomes smaller than their linewidth [97, 196]. Considering that magnons behave as bosons, of particular interest is the predicted emergence of new condensed phases at high powers, such as a predicted superfluid phase produced by a Bose-Einstein condensate (BEC) [111, 201–206], which could lead to novel coherent transport phenomena [184, 207–209].

This chapter is organized as follows. After this introduction, we expose in the second section the key findings of our study pertinent to lateral devices deposited on open geometries. In the third section, we present the relevant analytical framework to account for the electrical variation of the magnon transconductance by reminding readers of the subsection 1.2.5 in chapter 1. This framework is based on a two-fluid model introduced in the next chapter 5, which splits the propagating magnons as either low-energy or high-energy magnons. It will be shown that the spin diode characteristics are mostly regulated by the variation in the density of the low-energy component of the two-fluid. In the fourth section, we will show the experimental evidence that supports our interpretation.

4.1 Key findings

The main result presented in this chapter is that the experimental observation of the spin diode in non-local devices can be well understood within a framework which focuses solely on the accumulation of low-energy magnon population, whose growth is limited by a power dependent magnon-magnon scattering rate, which increases sharply as μ_M approaches E_g [110, 200]. This conclusion is drawn from the observation that in open geometries, the regime $\mu_M \geq E_g$ is never reached, despite the use of very large current densities. The current range explored is large enough to bring the magnetization beneath the emitter in the paramagnetic state via Joule heating. It turns out, that, despite the ensuing reduction of the magnetization, which should have reduced any nominal threshold current to zero at the Curie temperature, we do *not* detect *non-locally* any evidence of full damping compensation. We thus conclude that the rise of μ_M by STE is impaired by a rapid increase of the magnon relaxation rate.

We propose a simple analytical model to describe the non-linear interactions between low-energy magnons. In this model, the asymptotic approach of $\mu_M \to E_g$ is governed by a magnon-magnon scattering rate between low-energy magnons, that is enhanced by a Lorentz factor: the analytical form proposed to describe saturation effects of dipolarly coupled spin-waves [70, 106]. This simple model captures well the high power transport regime of any of our non-local devices, where we have varied the aspect ratio of the electrodes, the magnetic characteristics and the film thickness, t_{YIG} (see Table.4.1. The model accounts well the experimental behavior using a very limited set of effective fitting parameters.

Supplementing the transport results with Brillouin Light Scattering (BLS) experiments, we show experimentally that the asymmetric transport behavior, i.e., the spin diode effect, is indeed predominantly caused by low-energy magnons with energies around $E_K = \hbar\omega_K \approx 30$ μeV, where $\omega_K/(2\pi)$ is the Kittel frequency [73]. Thus the picture that emerges from our study on the propagating magnons in YIG films at high power [1] is different from the *frictionless* many-body condensate around the lowest energy mode indicative of a *reduction* of its relaxation rate. Instead, we observe that the enhancement of the magnon density expressing accumulation phenomena, which is limited instead by an *enhancement* of magnon-magnon relaxation rate, which caps the occupation of each mode below a saturation threshold [70, 106]. In other words, the reported non-local transport signal hints at coupled dynamics between numerous modes rather than the BEC picture of a single dominant mode [111, 201–203].

This picture is further confirmed experimentally, by the enhancement of the spin diode effect in materials with isotropically compensated demagnetizing factors, where the uniaxial perpendicular anisotropy, K_u, compensates the out-of-plane demagnetization field. Here, the vanishing small effective magnetization, $M_{\mathrm{eff}} = M_1 - 2K_u/(\mu_0 M_1) \approx 0$, with μ_0 being the vacuum permeability, reduces the limiting nonlinear magnon-magnon interaction and thus enhances the saturation threshold [77].

Finally, we report a collapse of the magnon transconductance when the temperature of the emitter, T_1, approaches the Curie temperature, T_c. In this limit the population of high-energy magnons becomes significantly larger than the number of polarized spins, the spin conduction by low-lying spin excitations becomes impaired by collisions with their high-energy counterpart, leading to a sharp decrease of the transmission ratio.

We study how the enhancement of the magnon density varies with the physical characteristics of the non-local device itself. By systematic variations of the interface transparency of the emitter and collector, as well as the thermal gradient near the emitter, we reveal that the density of low-energy magnons is dominantly governed by thermal fluc-

[1] The situation is different under the Pt electrode [99, 122, 124, 203]

tuation rather than by the effective damping value which remains always finite positive (> 0). The process for the forward polarity (regime of magnon emission), leads to a finding where the density of low-energy magnons seems to be determined by the temperature of the emitter, T_1, with a particle density that increases with increasing temperature. This is opposite to usual (ground state) condensation phenomena, that normally take place upon a decrease of temperature. The behavior of our system resembles that of a free electron gas inside ultra pure 2D materials such as monolayer graphene encapsulated by two layers of hexagonal boron nitride [210, 211]. In the latter, electron transport at high temperatures becomes hydrodynamic and thus can be described by the Navier-Stokes equation [212]. This leads to unusual transport behavior, as first predicted in the 60s by Radii Gurzhi [213]. Our findings thus suggest that very similar processes are at play in ultra pure magnon conductors [214, 215], whose consequence is the emergence of magneto-hydrodynamic regime [214] at high power.

4.2 Analytical framework

We guide readers to refer to subsection 1.2.5 in chapter 1 for a detailed discussion. As introduced in the previous section 4.1, we started from the Bose-Einstein statics including the chemical potential term to describe the current variation of the number of magnons around the Kittel frequency. We derived the theoretical description of the linear regime at low current by using the formula of the inverse spin Hall effect voltage [115]. For the high power regime to capture the non-linear conduction behavior, we phenomenologically implemented the Lorentz factor enhanced magnon-magnon decay rate due to the magnon-magnon scattering responsible for the saturation effects of magnons.

4.3 Experiments

In this section, we present the experimental evidence that supports the physical picture exposed above. We focus on the nonlinear and the asymmetric transport properties, our so-called spin diode effect, and the extraction of the pertinent parameters that govern it.

4.3.1 Sample characterisation

The 4 magnetic garnet films (cf. Table.5.1 in the next chapter) used in this study have been grown by 2 different methods: liquid phase epitaxy in the case of $YIG_{A,C,D}$ and pulsed laser deposition in the case of (Bi-)YIG_B. Their macroscopic magnetic properties have been characterized using a commercial vibrating sample magnetometer where the sample temperature can be controlled by a flux of Argon gas from room temperature to 1200K. Curves of magnetization versus temperature in the range of 300K to 600K are shown in Fig. 31(d-f) . They highlight the value of Curie temperature (T_c) for each sample summarized in Table. 4.1. Similarly the Pt metal for the middle electrode has been deposited by 2 different techniques: e-beam evaporation in the case of YIG_A and YIG_C and sputtering in the case of (Bi-)YIG_B.

In this work, we convert the Joule heating associated with the circulation of an electrical current I_1 in the emitter into a temperature elevation that we plot on the abscissa of Fig. 42, Fig. 45 and Fig. 34, Fig. 35. This is done by calibrating $R_{\mathrm{Pt}}|_{I_1}$: the variation of the Pt_1 resistance with the injected electrical current I_1. We introduce the calibration

factor

$$\kappa_{A,B \text{ or } C} = \kappa_{\mathrm{Pt}} \frac{R_{\mathrm{Pt}}/R_0 - 1}{R_{\mathrm{Pt}} I_1^2} \quad , \tag{4.1}$$

for the conversion coefficient, with $R_0 \equiv R_{\mathrm{Pt}}|_{I_1=0} = \rho_{\mathrm{Pt}} L_{\mathrm{Pt}}/(w_1 t_{\mathrm{Pt}})$ being the nominal value of the Pt wire resistance and the coefficient $\kappa_{\mathrm{Pt}} = R_{\mathrm{Pt}}/\partial_T R_{\mathrm{Pt}}$ is obtained by monitoring the change of the Pt resistance at small current vs. the temperature of the substrate. The obtained values of κ_{Pt} and ρ_{Pt} are indicated in Table. 4.1. Fig. 31(a-c) shows the R-I curves with the corresponding temperature considering Joule heating for each sample.

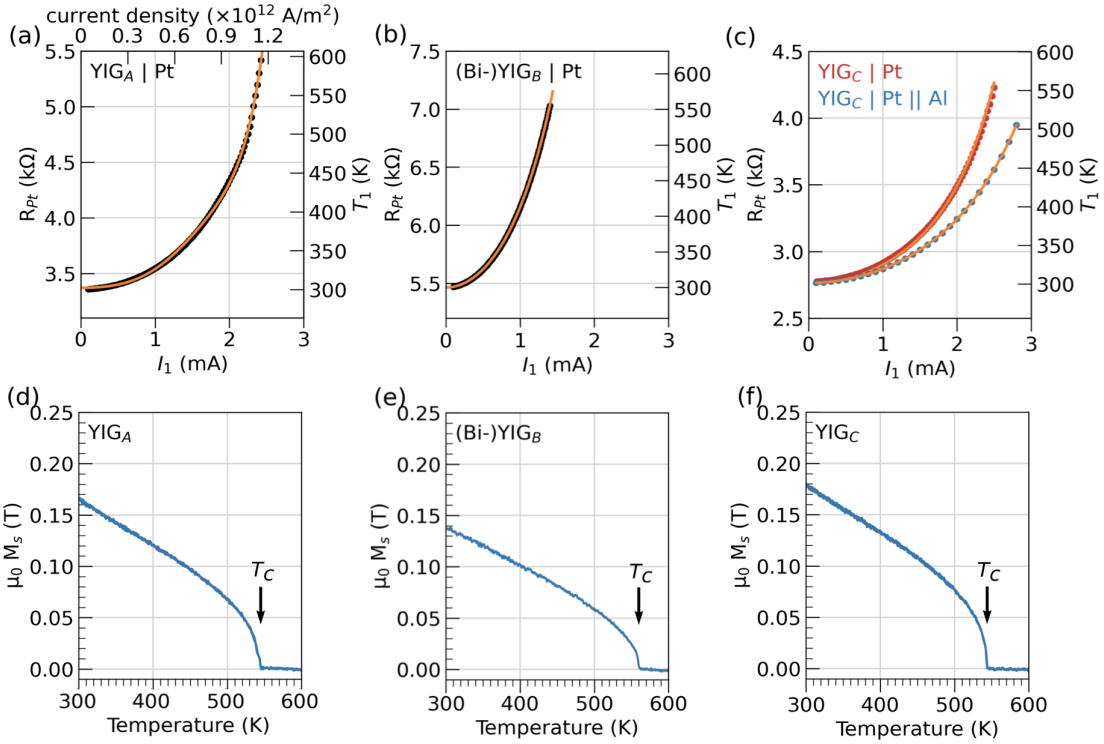

Figure 31: *Garnet thin films characterization. The top row (a,b,c) shows the variation of the Pt resistance as a function of current injected for respectively YIG_A, (Bi-)YIG_B and YIG_C without or with Al coating (see Table. 4.1). The right ordinate axis allows to convert the current bias in a temperature elevation in the [300,600] K range because of Joule heating. The upper abscissa gives the corresponding current density inside Pt. The bottom row (d,e,f) shows the associated variation of the saturation magnetization in the [300,600] K range.*

The charge to spin (or inverted) interconversion is provided by the spin Hall effect. Its efficiency process is determined by the relationship

$$\epsilon \equiv \frac{G_{\uparrow\downarrow}\, \theta_{\mathrm{SHE}}\, \tanh\left[t_{\mathrm{Pt}}/(2\lambda_{\mathrm{Pt}})\right]}{G_{\uparrow\downarrow} \coth\left(t_{\mathrm{Pt}}/\lambda_{\mathrm{Pt}}\right) + \sigma_{\mathrm{Pt}}/(G_0 \lambda_{\mathrm{Pt}})} \quad , \tag{4.2}$$

where θ_{SHE} is the spin Hall angle, $G_{\uparrow\downarrow}$ is the spin mixing conductance, t_{Pt} is the thickness of the Pt layer, $G_0 = 2e^2/h$ is the quantum of conductance and λ_{Pt} is the spin diffusion length inside. To calculate the value of ϵ, we assume that $\lambda_{\mathrm{Pt}} = 3.8$ nm [97] and $\lambda_{\mathrm{Pt}}\theta_{\mathrm{SHE}} =$

Table 4.1: *Physical properties of the magnetic garnet films (values at $T_0 = 300$ K).*

	$t_{\rm YIG}$ (nm)	$\mu_0 M_s$ (T)	H_{Ku} (T)	T_c (K)	$\alpha_{\rm YIG}$ ($\times 10^{-4}$)	$\rho_{\rm Pt}$ ($\mu\Omega$.cm)	$t_{\rm Pt}$ (nm)	$\kappa_{\rm Pt}$ (K)	$G_{\uparrow\downarrow}$ ($\times 10^{18}$ m^{-2})	ϵ ($\times 10^{-3}$)
YIG$_A$	19	0.167	+0.005	545	3.2	27.3	7	480	0.6	2.1
(Bi-)YIG$_B$	25	0.147	+0.174	560	4.2	42.0	6	890	2.4	7.8
YIG$_C$	56	0.178	-0.001	544	2.0	19.5	7	476	○: 0.64 / ●: 1.9	○: 1.3 / ●: 3.6

0.18 nm [216–218]. From Table.4.1, we find that the value of $G_{\uparrow\downarrow} \ll \sigma_{\rm Pt}/(G_0\lambda_{\rm Pt})$ and thus Eq. (4.2) reduces to $\epsilon \approx \theta_{\rm SHE} T$ with a proportionality ratio $T = G_{\uparrow\downarrow} \cdot G_0\lambda_{\rm Pt}/\sigma_{\rm Pt} \approx 0.1$ that is maximized when $t_{\rm Pt} \approx 7$ nm. Numerical evaluations of ϵ are found in Table.4.1. The maximum achieved value is $\epsilon \approx 0.08$ observed in (Bi-)YIG$_B$.

Note that for Pt, $\theta_{\rm SHE} > 0$. This means that the interconversion is governed by the right hand side rule. Using the convention of Fig. 10, a positive current (*i.e.* circulating along $-\hat{y}$) injects spins polarized along $+\hat{x}$, inside an adjacent layer. Thus amplification of spin fluctuations requires that M_s be aligned with $-\hat{x}$ or that $H_x < 0$, as indicated in the figure.

4.3.2 Non-local magnon transport

The experiment is performed here at room temperature, $T_0 = 300$ K, on a 56 nm thick (YIG$_C$) garnet thin film, whose physical properties are summarized in Table.4.1. As explained in the next chapter 5, we purposely select here a device with a large separation between the two Pt electrodes ($d = 2.3$ μm) to allow the low-energy magnons to dominate the transport properties. Injecting an electrical current I_1 in Pt$_1$, we measure a voltage V_2 across Pt$_2$, whose resistance is R_2. To subtract all non-magnetic contributions, we define the magnon signal $\mathscr{V}_2 = (V_{2,\perp} - V_{2,\parallel})$ as the voltage difference between the normal and the parallel configuration of the magnetization with respect to the flow direction of the electrical current in the Pt. Fig. 32(a) shows the measured variation of $\mathscr{V}_2$ for a large span of I_1. The maximum current injected in the device is about 2.5 mA, corresponding to a current density of $1.2 \cdot 10^{12}$ A/m^2. The Joule heating at this intensity is large enough to reach T_c, the Curie temperature. The ensuing voltage $\mathscr{V}_2$ is shown in Fig. 32 for both positive (H_x pointing towards $+x$) and negative (H_x pointing towards $-x$) polarity of the applied field, whose amplitude is $\mu_0 H_0 = 0.2$ T. In Fig. 32(a), the expected inversion symmetry with respect to the field polarity has been folded between the $H_x > 0$ (left ordinate-label in pink) and $H_x < 0$ (right ordinate-label in blue), to directly emphasize the deviation produced by STE between magnon emission and magnon absorption. The measured signal decomposes in two contributions $\mathscr{V}_2 = -R_2\, I_2|_{I_1} + \overline{\mathscr{V}}_2\big|_{I_1^2}$: one is I_2, the electrical signal produced by STE, and the second is $\overline{\mathscr{V}}_2$, a background voltage associated to magnon transport along thermal gradients. The later voltage corresponds to the spin Seebeck effect (SSE). One thus expects $\overline{\mathscr{V}}_2 \approx 0$ in well thermalized devices. We emphasize the minus sign in front of I_2, which accounts for the fact that the spin-charge conversion is an electromotive force thus the current flows opposite to the voltage drop. It is thus a reminder that the ensuing polarity is opposite to Ohmic losses [120], in other words that the voltage drop across the two Pt electrodes should have opposite signs. In the linear regime ($I_1 \to 0$), the electrical signal is even/odd with the polarity of H_x or I_1, while the thermal signal remains always odd/even with H_x or I_1 [102].

4.3.2.1 Measurement of the magnon transconductance

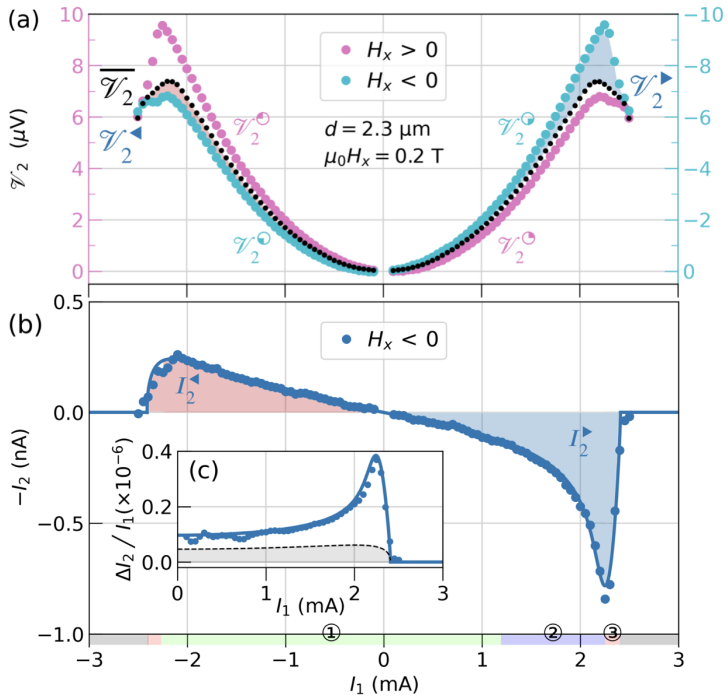

Figure 32: *Experimental observation of the spin diode signal. Panel (a) shows the I_1-dependence of the non-local voltage $\mathscr{V}_2 = (V_{2,\perp} - V_{2,\parallel})$ for both positive (left axis in pink) and negative (right axis in cyan) polarity of the applied magnetic field, H_x. The sign of $\mathscr{V}_2$ is flipped when the field is inverted. The non-local voltage $\mathscr{V}_2 = -R_2 I_2 + \overline{\mathscr{V}}_2$ is decomposed in an electric signal, I_2, and a thermal signal, $\overline{\mathscr{V}}_2$ (black). Panel (b) shows the variation of I_2 at $H_x < 0$ in the forward and reverse bias. The blue and red shaded areas in panels (a) and (b) highlight respectively the regimes of magnon emission and absorption respectively for the forward and reverse bias. Panel (c) plots the magnon transmission ratio $\mathscr{T}_s = \Delta I_2 / I_1$, where $\Delta I_2 \equiv (I_2^{\blacktriangleright} - I_2^{\blacktriangleleft})/2$. The solid line is a fit with Eq. (1.97), (1.106) and (1.107) using $n_{sat} = 4$ and $\mathcal{I}_{th,0} = 6$ mA. The black shaded region shows the assumed background contribution to spin conduction by high-energy magnons, Σ_T. The data are collected on the YIG_C thin film at ambient temperature, $T_0 = 300$ K, using a device operating in the long-range regime ($d = 2.3$ µm).*

Concentrating on the nonlinear behavior observed for $H_x < 0$ configuration (blue data), [2], we flag the forward bias as $\mathscr{V}_2^{\blacktriangleright}$ as the non-local voltage for $I_1 > 0$ and the reverse bias as $\mathscr{V}_2^{\blacktriangleleft}$ as the non-local voltage for $I_1 < 0$. Canceling out Joule effects can be simply obtained by calculating the difference $\mathscr{V}_2^{\blacktriangleleft} - \mathscr{V}_2^{\blacktriangleright}$, which eliminates any contribution that is even in current. The latter quantity represents the number of magnons created by STE relative to the number of magnons absorbed by STE at a given current bias $|I_1|$. The inset (c) of Fig. 32 shows the observed averaged behavior, $\Delta I_2 \equiv (I_2^{\blacktriangleright} - I_2^{\blacktriangleleft})/2 = (\mathscr{V}_2^{\blacktriangleleft} - \mathscr{V}_2^{\blacktriangleright})/(2R_2)$, expressed as a renormalized quantity $\mathscr{T}_s = \Delta I_2 / I_1$, a strictly positive parameter, as suggested by Eq. (1.105). The subtraction operation however does not allow to separate the behavior between the forward and reverse directions. In fact the asymmetry of the electrical signal cannot be obtained from the transport data alone. It requires further

[2] results for the opposite polarity is inferred by mirror symmetry

input information. This shall be provided below by the measurement of the integral intensity of the BLS signal, which monitors directly the low-energy part of the magnons' spectrum. Building on the experimental BLS observation in Fig. 33(e), we expect that the magnon transmission ratio displays continuity across the origin ($I_1 = 0$) and in the reverse bias, it behaves as a step function of amplitude $\mathscr{T}_s^{\blacktriangleleft} \approx \mathscr{T}_s|_{I_1 \to 0} T_1/T_0$ up to I_c. The ratio T_1/T_0 takes into account that the number of thermally excited low-energy magnons in the reverse polarization vary with I_1 due to Joule heating. This introduces a second order distortion, which is discussed in more details in the next section and in the next chapter. We thus construct $\overline{\mathscr{V}}_2 = -\mathscr{V}_2^{\blacktriangleleft} + R_2 \mathscr{T}_s^{\blacktriangleleft} \cdot I_1$ in the reverse bias from the opposite magnetic configuration. We then force $\overline{\mathscr{V}}_2$ to be even in current to get the behavior in the forward bias. The result is shown as black dots in Fig. 32(a). We can then infer $I_2^{\blacktriangleright} = (\overline{\mathscr{V}}_2 - \mathscr{V}_2^{\blacktriangleright})/R_2$ and $I_2^{\blacktriangleleft} = (\overline{\mathscr{V}}_2 - \mathscr{V}_2^{\blacktriangleleft})/R_2$, which is plotted in Fig. 32(b).

We observe in Fig. 32(b) 3 distinct transport regimes as predicted above. We have ① with $I_1 \in [-2, 1]$ mA: the spin conductance is roughly constant; ② with $I_1 \in [1, 2.2]$ mA: the spin conductance increases gradually and saturates quickly; and ③ with $I_1 \in [2.2, 2.5]$ mA: the spin conductance decreases abruptly to vanish at I_c. Only the regime ① is anti-symmetric in current. We emphasize at this stage that the sequence of behavior recalls the 3 regimes predicted in Fig. 10(c). We can also repeat the same analysis to build the data when $H_x > 0$ (see the next chapter 5). The polarity of the asymmetry inverts when one switches the direction of the magnetization, as expected. In all cases, the forward regime only occurs when $I_1 \cdot H_x < 0$, which corresponds to the polarity of damping compensation.

In the next section, we will confirm the above behavior through BLS spectroscopy. We will always discuss from now on the data as shown in Fig. 32(c) in the form of ΔI_2 as a function of $|I_1|$ and properly renormalized by I_1 and T_1 to allow comparison between different devices (see the next chapter 5).

4.3.2.2 Spin diode effect

We now discuss in more details the amplitude of the asymmetric rise of the I_2-signal in Fig. 32(c). A striking feature of Fig. 32(c) is the limited growth of the spin diode signal, which is capped by a meager factor of 3 rise compared to the value at small currents. Such inefficiency is further confirmed in previous reports aiming at modulating the transport by damping compensation with an additional heavy metal electrode placed in between the emitter and collector, which enhances the conduction by at most a factor of 6 [79, 109, 184, 185, 219]. As demonstrated in Fig. 11 this cannot be explained by having a threshold current larger than the current window explored, $[-I_c, +I_c]$, but it rather indicates strong coupling between the magnons, which prevents large growth of the magnon density. The asymmetric contribution is well accounted for by Eq. (1.97). The best fit is obtained by using $T_c^\star = 515$ K, $\mathcal{I}_{\text{th},0} = 6$ mA and $n_{\text{sat}} = 4$ and it is indicated in the plot by the solid line. The contribution from low-energy magnons is added to a background indicated by a dashed line. This background accounts for the competing contribution of high-energy thermal magnons to the electrical transport. Its origin and analytical expression can be found in the next chapter. It represents in our fit a 50% additional contribution $\Sigma_T/(\Sigma_K + \Sigma_T) = 0.5$ in Eq. 1.110. We note also that the value of $T_c^\star$ used for the fit, differs significantly from the Curie temperature of this film (see Fig. 31). This point will be investigated in more detail in the next chapter 5.

4.3.3 Brillouin Light Scatterng

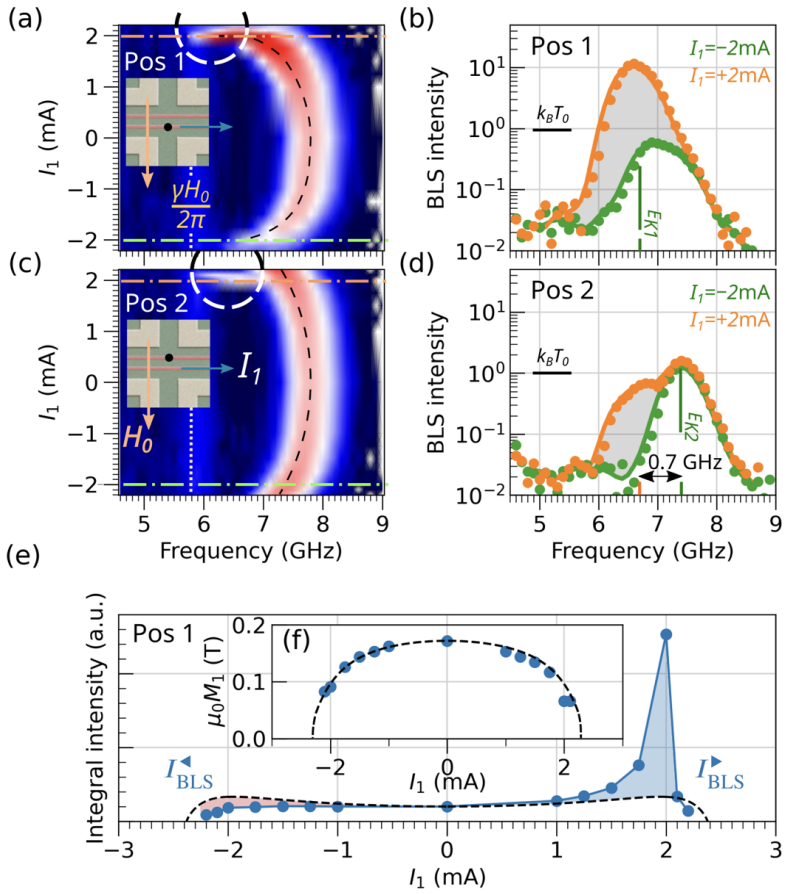

Figure 33: *Experimental evidence that the spin diode effect is mainly governed by low-energy magnons. Panels (a) and (c) show the micro-focus Brillouin Light Scattering (μ-BLS) spectra as a function of I_1 performed under the two Pt electrodes (see black dot on the insert) at Pos1 (emitter) and Pos2 (collector) for $H_x < 0$. Each BLS spectra are renormalized by the amplitude of the Kittel peak at $I_1 = 0$. Panels (b) and (d) show two cuts at fixed current $I_1 = \pm 2$ mA near I_{pk}. The green marker indicates the spectral position of E_K at $I_1 = 2$ mA. The spectral position of self-localized spin fluctuations, E_{K1}, (see circles) at $I_1 = +2$ mA (see orange marker) occur clearly below $E_{g2} \approx E_{K2}$ at Pos2 (see green marker). The shift $E_{K1} - E_{g2}$ is about 0.7 GHz. The paramagnetic limit, $\gamma H_0/(2\pi)$, is indicated by the yellow vertical dotted line at 5.8 GHz. Panel (e) shows the integrated BLS intensity at Pos1 as a function of I_1. The solid blue line is a guide for the eyes. The black dashed line shows the expected variation of thermally activated low-energy magnons produced by Joule heating. In echo with Fig. 32, the blue and red shaded areas highlight the variation of magnon emission and absorption with respect to thermal fluctuation. The inset panel (f) shows the evolution of M_1 induced by Joule heating. The blue dots are inferred from the variation of Kittel frequency (dashed parabola in panel (a)). The dashed lines are inferred from SQUID measurements shown in Fig. 31. The data are collected on the YIG_A thin film at $T_0 = 300$ K using a device with a distance $d = 1.0$ μm between the two Pt electrodes.*

It is useful at this stage to confirm spectroscopically that the spin diode effect reported above indeed arises from an asymmetric modulation of the low-lying energy magnons. BLS is a technique of choice for that purpose since it specifically targets the monitoring of spectral shifts in the magnons' population at GHz energies. Furthermore, its high sensitivity allows to detect fluctuations up to the thermal level. While in the past, we have performed comparative studies of the transport and BLS behavior on the exact same device [102, 120], in this particular case, we shall introduce in the discussion a thinner YIG_A garnet film, whose physical properties are also found in Table 4.1. The change of samples is here not intentional and is purely linked to the chronological context of the experiments. For any practical purpose, the sole relevant difference is a change of the value of I_c from $I_c = 2.5$ mA to 2.1 mA for YIG_C and YIG_A, respectively, arising from differences in the Pt resistivity. We have checked that all other characteristics discussed herein are generic to both samples.

Since we are interested in localized changes of the magnon population we here use micro-focus Brillouin light scattering (μ-BLS) spectroscopy [220]. The probing light with a wavelength of 532 nm and a power of 0.1 mW is produced by a single-frequency laser with spectral linewidth < 10 MHz. It is focused through the sample substrate into a submicrometer-size diffraction-limited spot by using a $100\times$ corrected microscope objective lens with a numerical aperture of 0.85. The scattered light was collected by the same lens and analyzed by a six-pass Fabry–Perot interferometer. The lateral position of the probing spot was controlled by using a high-resolution custom designed optical microscope. The measured signal (the BLS intensity at a given magnon frequency) is proportional to the spectral density of magnons at this frequency and at the position of the spot. By moving the focal spot over the surface of the film, we can obtain information about the spatial variations of the spectral distribution of magnons. Note that only low-frequency, low energy magnons contribute to the BLS intensity as the BLS technique is sensitive only to small wave vectors $< 2.4 \cdot 10^5 \mathrm{cm}^{-1}$. However, since the frequency of low energy magnons depends also on the total number of magnons in the sample, the spectral position of the Kittel peak allows to infer from the BLS data information about the local temperature [221, 222].

Fig. 33 compares the current modulation of the spectral occupation below the emitter and the collector electrodes labeled Pos1 ($x = 0$, emitter) and Pos2 ($x = +d$, collector). The position of the spot is indicated by a black circle in the inset images in Fig. 33. To allow quantitative comparison of the different locations, all curves have been renormalized by the value of thermal fluctuations at $I_1 = 0$, which is assumed constant throughout the thin films. In all these measurements the field is fixed at $\mu_0 H_x = -0.2$ T: a value identical to the one used in the transport measurement shown in Fig. 32.

We start the analysis by concentrating first on panel (a) of Fig. 33, which shows in a density plot the current variation of the magnon spectra at Pos1. The spectral variation of the BLS signal at $I_1 = 0$ leads experimentally to a peak instead of the predicted step function shown in Fig. 11(a) for 2D systems. The attenuation of the spectral sensitivity at high frequency is an experimental artifact linked to the extreme focus of the optical beam, which makes the scattered light insensitive to spin-waves whose wave-vectors are larger than the inverse of the beam waist. The decrease of the signal above the Kittel frequency is thus directly related to the transfer function of the detection scheme, which attenuates short wavelength magnons [104, 223, 224].

The black dashed lines in the plots show the shift of the Kittel frequency as a function of I_1. At low current intensity the shift follows a parabolic behavior as expected for Joule heating. Note that the curvature of the parabola increases when one moves away from the heat source as shown in Pos2, which we associate with the lateral thermal gradient $\partial_x T_1 < 0$ [117, 119]. It is also worth noticing, that for the signal at Pos1 in Fig. 33(c), the local curvature increases dramatically as one approaches I_c, which we ascribed to the

diminution of M_1 as T_1 approaches T_c. Interestingly the effect is more pronounced at $I_1 > 0$ than $I_1 < 0$ suggesting a self-digging effect due to asymmetric excitation of low-energy magnons. Also what is visible in Fig. 33(c) is the extinction of the BLS intensity in region ③ when $I_1 \geq 2.1$ mA. Finally, the BLS signal decays at large currents at Pos1 (below the emitter), while remaining finite at Pos2 (below the collector).

The density plot in Fig. 33(c) furthermore confirms the enhancement / attenuation of spin fluctuation depending on the polarity of the current. Starting from thermal fluctuations at $I_1 = 0$, the signal decreases for $I_1 \cdot H_x > 0$ and increases for $I_1 \cdot H_x < 0$. A more detailed analysis at low current amplitude (not shown) confirms a variation linear in I_1 in region ①. BLS spectra at large currents are displayed in Fig. 33(b), which compares the magnon distribution at $I_1 = 2$ mA for both negative (green dash cut) and positive (orange dash cut) polarity of the current. For $I_1 = -2$ mA, the maximum amplitude at the Kittel mode (green vertical marker at 6.8 GHz) has a normalized amplitude below 1, i.e., a lower amplitude than at $I_1 = 0$. At $I_1 = +2$ mA, the density plot reveals a significant enhancement of the signal, highlighted by the dashed circles. The corresponding amplitude of the signal [orange circles in panel (d)] shows an enhancement by more than one order of magnitude. This enhancement corresponds to the rise of the spin conduction in region ②. Additionally, the BLS data in Fig. 33(c) reveal the self-localization of the asymmetric excitation, due to the red shift that arises for large cone angles [77, 110]. It is important to notice that the induced shift is almost as large as it can be, as the Kittel frequency almost reaches the paramagnetic limit $\omega_H = \gamma H_0$ visible on the plot as a light blue vertical line at around 5.8 GHz [3]. Note that the paramagnetic limit is only reached when $I_1 > 0$ and not for $I_1 < 0$. This suggests that the film is still in its ferromagnetic phase when the signal disappears at $I_c \approx 2.1$ mA. This feature is discussed in the context of the discrepancy between $T_c^\star$ and T_c in the next chapter 5.

The pocket of excitation created under the emitter inside the circle area, also appears as a peak in Fig. 33(d), centered around the orange vertical marker at 6.8 GHz, *i.e.* well below the position of the Kittel mode at this position (green vertical marker at 7.5 GHz). This suggests that one probes magnetic fluctuations that are spectrally located below (about 0.7 GHz) E_g, the energy gap at that position. Although the amplitude of the peak at the orange marker is significantly reduced when one moves from Pos1 to Pos2, which confirms numerous hints that the majority of low-energy magnons stay localized under the emitter electrode (see below), these spectral fluctuations are not fully suppressed. We interpret this apparent contradiction as a sign that the wavelength of the mode excited under the emitter (λ around 0.6μm) remains large compared to the width of the emitter well and the ratio corresponds to the evanescent decay between Pos1 and Pos2. The issue of the spatial decay will be investigated in more detail in the next chapter.

To gain further insight, we plot in Fig. 33(e), the spectral integration of the BLS signal as a function of I_1. The first key feature, that is directly observed in the plot, is the continuity of the signal across the origin for both polarities of the current I_1. This observation is exploited above in the extraction of the asymmetry of the magnon transmission ratio. It will be shown below that the BLS measurement corroborates some other key features that were observed in the transport properties of magnons shown in Fig. 32. The second key feature is the limited growth of the intensity at $I_{\rm pk}$. The size of the peak, however, is larger at Pos1 than at Pos2, underlying here the importance of localized magnons under the emitter. The third key feature is the notion that there are 3 transport regimes. In particular, we observe the collapse of the BLS signal at $I_1 = \pm I_c$.

To highlight the similarity with transport, we tentatively plot in Fig. 33(e) the evolu-

[3] The resonance line at 5.72 GHz in Fig. 33(a,c,d) corresponds probably to the paramagnetic response of the substrate. For the sake of clarity it has been removed from the plot by performing a background subtraction.

tion with I_1 of the number of thermally activated low-energy magnons produced by Joule heating using a dashed line. The behavior follows the curve Δn_{T_1} that is introduced in the chapter 1. The underlying parabolic increase of this background signal is directly visible in the evolution of the maximum BLS intensity along the dashed line in Fig. 33(e). The blue and red shaded areas show the deviation of the BLS intensity from the nominal thermal occupation. They indicate respectively the amount of magnons emitted or absorbed by the STE in the forward or reverse bias and the deviation is analogous to the blue and red shaded area shown in Fig. 32(b). For $|I_1| < I_c/2$ the curves deviate equally from the dashed curve, indicating that equal amounts of magnons are transferred between the metal electrode and the YIG film in the linear regime between the forward and reverse bias. The curvature at the origin should scale as the variation of M_1 with I_1. To that end, we plot in the insert Fig. 33(f) the evolution of M_1 under the emitter. The blue dots are inferred from variation with the current of the spectral position of the Kittel frequency, which is sensitive to temperature. The observed behavior is in agreement with the expected evolution of M_1 with I_1, that one infers from the dependence of T_1 with I_1 as shown in Fig. 31. The result is shown as a dashed line and the agreement ensures the validity of the evolution with I_1 of the thermal background shown in Fig. 33(e). In this data treatment, we do not attempt to correct for the use of different pulse duty cycles, which results in a small discrepancy in the value of I_c.

In conclusion of this section, we interpret the fact that all the distinct transport signatures observed in Fig. 32(b) are present in the BLS intensity displayed in Fig. 33(e) as a strong indication that these are predominantly driven by the change of density of low-energy magnons underneath the emitter. We observe, however, difference in the scaling of the effect that we attribute to the self-localization of these low-energy magnons. This will be the subject of the band mismatch below. A more rigorous quantification of the localization portion is part of the analysis in the next chapter 5.

4.3.4 Influence of the lattice temperature

In this section, we investigate the pertinent parameters that influence the spin diode effect. To that end, we propose to compare in Fig. 34 the asymmetric regime while varying independently either ϵ, the interfacial efficiency of spin to charge conversion, or κ, the efficiency of the device thermalization. It builds on our two recent studies [119] and [216], where more details can be found. The device has been patterned on YIG_C, which is the same film as the one studied in Fig. 32, but twice thicker than YIG_A film studied in Fig. 33 (see Table.4.1). In this batch, local annealing [216] can be used to apparently increase the spin mixing conductance $G_{\uparrow\downarrow}$ of an individual electrode. The term spin mixing conductance should be interpreted here as an effective fitting quantity. As explained by Kohno *et al.* [216], the physics at play in this annealing mechanism does not involve a change of the intrinsic properties but rather a change of the extrinsic properties via an extension of the contact area. We denote $\epsilon_\circ$ and $\epsilon_\bullet$ as the STE efficiency before and after annealing. We have shown that applying local annealing for 60 mins at 560 K can modify $\epsilon_\bullet/\epsilon_\circ \approx 3$ without changing the Pt resistance *i.e.* κ_C [216].

We first investigate changes in the spin transport when alternatively the collector and emitter are annealed using the 4 possible combinatorial configurations possible as summarized in the legend of Fig. 34(a). We find in Fig. 34(c) that the normalized current ratio $(\mathscr{T}_s^{-1})^\star \equiv \mathscr{T}_s|_{I_1\to 0}/\mathscr{T}_s$ of the 4 curves fall on the same parabola. This echoes the behavior reported in Fig. 42 of the next chapter 5, suggesting a drop as $1-(I_1/I_c)^2$ in the regime ②. This already supports that the value of ϵ plays very little in the relative amount of electrically excited low-energy magnons. If the sample would be well thermalized $T_1 \approx T_0$, the zero intercept of the parabolic fit significantly shifts to higher current values

as shown below in Fig. 34(f) suggesting that in this case the extrapolated decay $(\mathscr{T}_s^{-1})^\star$ indicates $\mathcal{I}_{\rm th}$ as suggested by inversion of Eq. (1.97). The intercept value decreases as the influence of Joule heating, or κ_C, increases and it is bounded by I_c as discussed in Fig. 13. We recall that local annealing has not changed the Pt resistance and thus in Fig. 34(a-c) the efficiency of Joule heating κ_C is identical for all 4 cases. These conclusions are also consistent with the behavior of the SSE signal $\overline{\mathscr{V}}_2$ shown in Fig. 34(b). The 4 sets of data exactly separate into two pairs of curves that scale with one another by the ratio of $(\epsilon_\bullet/\epsilon_\circ)$. The difference is solely governed by the value of the efficiency coefficient ϵ_2 at the collector side. As expected for the SSE, changes of the value of ϵ_1 of the emitter are irrelevant.

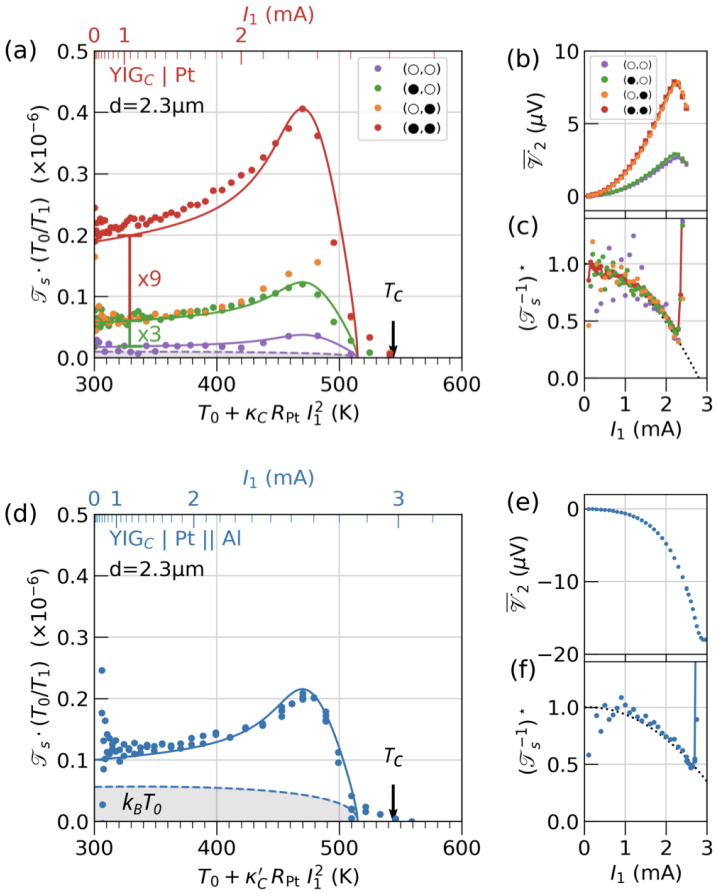

Figure 34: *Experimental evidence that the spin diode effect is mainly governed by thermal fluctuations underneath the emitter. Spin diode effect as a function of the temperature of the emitter elevated by Joule heating, $T_1 = T_0 + \kappa_C R_{Pt} I_1^2$, when either (a) ϵ, the efficiency of spin transfer, or (d) κ_C, the heat dissipation coefficient, are independently altered. The upper scale shows the corresponding current bias, I_1. The legend of panel (a) shows with symbols ○/● which electrode of the pair (emitter, collector) had been subject to local annealing [216] leading to $\epsilon_\bullet/\epsilon_\circ \approx 3$ as shown in Table.4.1. Panel (d) shows the behavior when the annealed device is capped by an Al heat sink, which reduces the efficiency of Joule heating $\kappa'_C < \kappa_C$. In panels (a) and (d) all solid lines have the same shape as in Fig. 32(b) albeit with different scaling factors. The right row shows the associated current dependence of the SSE voltage, $\overline{\mathscr{V}}_2$, in panels (b) and (e) and the normalized inverse transmission coefficient of the spin current $\mathscr{T}_s^{-1} = I_1/I_2$ in panels (c) and (f). The dotted lines are parabolic fit.*

We now plot in Fig. 34(a) the variation of the renormalized STE transmission coefficient $\mathscr{T}_s \cdot T_0/T_1$ as function of $T_1 = \kappa_C R_{\mathrm{Pt}} I_1^2 + T_0$, with $T_0 = 300$ K. The normalization by T_1 allows to view changes in magnon density from the point of view of a well thermalized device as suggested by Eq.(1.105). The upper abscissa scale can be used as an abacus to transform back T_1 into I_1. On all devices, we find that $\mathscr{T}_s \cdot T_0/T_1$ increases nonlinearly above 360 K. Above 460 K the spin transmission reduces with increasing temperature, just as explained in Fig. 32(b). As expected, we find that the amplitude of $\mathscr{T}_s \cdot T_0/T_1$ scales as the product of $\epsilon_1 \cdot \epsilon_2$. This observation confirms that the Pt is weakly coupled to the YIG, i.e., only a small portion of the spin current circulating in the YIG is detected by the collector. If that were not the case, the signal would not depend on the collector efficiency ϵ_2. This is further corroborated by the width dependence of $\mathscr{T}_s$ (see Fig. 36).

The most interesting feature is the superposition of the 2 curves (∘,•) and (•,∘), which consists in inverting the emitter and collector in a device where one electrode is 3 times more efficient to emit magnons. While the amount of spin current circulating between the contact electrodes is proportional to $\epsilon_1 \cdot \epsilon_2$ as Eq. (1.105) explains, the amount of magnons varied inside the YIG only depends on ϵ_1. The superposition of the two curves in Fig. 34(a) indicates that the density of magnons in the YIG (here it is varied by a factor of 3) seems to have no consequence on the shape of $\mathscr{T}_s \cdot T_0/T_1$ and the pertinent parameter that determines its behavior remains the emitter temperature T_1. Additionally, if one would compare in Fig. 43 in the next chapter $\mathscr{T}_s$ versus T_1 (as opposed to as versus I_1) taken on two different YIG thicknesses, it seems that the thickness plays no role in determining the nonlinear behavior between I_2 and I_1^2.

To further support this notion, the coefficient κ_C can be modified while keeping ϵ constant. As explained in [119], one can cover the annealed device with a 105 nm thick Al layer, acting as a heat sink (the heat sink is separated from the Pt electrode by a 20 nm thick protection layer of Si_3N_4). The influence of the heat sink can be seen by comparing the abacus in Fig. 34(a) and Fig. 34(d). The Al layer has diminished the efficiency of Joule heating κ_C by 27 %. The changes are most visible in Fig. 34(e) which shows a completely different nature of the SSE signal compared to Fig. 34(b) (different curvature, different polarity [119]). But despite that, once I_1 is converted into T_1, Fig. 34(d) scales with Fig. 34(a) even though a larger amount of current I_1 are circulated in the former.

This leads to a conclusion that the nonlinearity of the magnon transmission ratio $\mathscr{T}_s \cdot T_0/T_1$ generated by STE appears to be governed predominantly by the lattice temperature. This observation alone seems to contradict our previous conclusion made from the BLS experiment, which attributes the spin diode effect to low-energy magnons. The apparent discrepancy is explained in Fig. 13(c). Knowing that the density of low-energy magnons is also sensitive to temperature, the vanishing of M_1 at I_c due to Joule heating displaces the position of I_{pk} below I_c, which then becomes weakly dependent on the room temperature value of the threshold current, $\mathcal{I}_{\mathrm{th},0}$. The process still requires μ_M to approach E_g by injecting spins, but once in the vicinity and the nonlinear process is fully in place, the change of temperatures is dominant. Thus this artifact is the consequence of the inability to efficiently thermalize the Pt electrode rather than of intrinsic phenomena. Nevertheless, it emphasizes how much thermal fluctuations play an important role in nonlinear phenomena. It underlines that the parametric threshold is also determined by the initial amount of magnon thermal fluctuation in the sample, keeping in mind that all nonlinearities are suppressed at absolute zero temperature.

All the experimental data in Fig. 34(a) and Fig. 34(d) are fitted with the same curve as the one shown in Fig. 32(b). The only varying parameter here is the vertical scaling factor. The fact that all the curves have exactly the same shape also supports the indication that the T_1 determines the nature of $\mathscr{T}_s \cdot T_0/T_1$, where the shaded region shows the background contribution from high-energy thermal magnons $\mathscr{T}_T$, where $\Sigma_T/(\Sigma_T + \Sigma_K) \approx 0.5$ represent the relative weight at this distance.

The Al capping furthermore alters the spatial profile of $T(\mathbf{r})$ that defines the confinement potential of M_T near the emitter as demonstrated in Ref. [119]. Thus the absence of a large discrepancy between Fig. 34(a) and Fig. 34(d) indicates that the depth of the band shift produced by Joule heating is the dominant parameter, while the spatial extent of confinement region defined here by $\partial_x T$ is not significant.

4.3.5 Mismatch of magnon bands

In this section we will further elucidate which nonlinear effects give rise to the suppression of spin propagation in the high power regime.

4.3.5.1 Nonlinear frequency shift

We start this discussion by investigating the issue of nonlinear frequency shift. We recall that this effect comes from the depolarization factor along the film thickness $N_{zz} = -1$, which introduces a correction dependent on M_s to the Kittel frequency. This coefficient corresponds to a redshift, meaning that a decrease of M_T produces a red shift of the Kittel mode and hereby of E_g. The maximum shift that can be induced is $(\omega_K - \gamma H_0)/(2\pi) \approx$ 2 GHz which represents the gap between the Kittel mode and the paramagnetic limit at $\mu_0 H_0 = 0.2$ T. Fig. 33 shows experimental evidence of shifts as large as 0.7 GHz being produced by either Joule heating of the emitter [see dashed line in Fig. 33(a) and (c)] or by the occupancy of the mode (see the dashed circle in Fig. 33). An increase of the precession angle θ produces also a red shift of the resonance due to a decrease of the internal field, which depends on the time averaged magnetization that follows $M_s \cos\theta$ [68, 108]. The latter effect is responsible for the foldover. As shown in the insert of Fig. 35(c), such shift is strong enough to push the whole magnetostatic range of the magnon manifold under the emitter below the energy gap E_g of the collector. This would then suggest that the spinwaves propagate between the two metallic electrodes by tunnel effect, and the propagation length λ_K is the decay length of the evanescent spin waves outside the well. This promotes self-localization effect [122–124] as reported in the analysis of Fig. 43 in the next chapter 5.

We want to compare this behavior with the transport properties in (Bi-)YIG$_B$ thin film (see material parameters in Table.4.1). The peculiarity of our Bi-YIG$_B$ composition is to have a uniaxial anisotropy that matches the saturation magnetization (see Table.4.1), leading to $M_{\text{eff}} \approx 0$. This corresponds to a thin film, which has the isotropically compensated demagnetizing effect. In this case, the Kittel mode becomes isochronous and independent of the precession cone angle. The Kittel frequency simply follows the paramagnetic proportionality relationship $\omega_K = \gamma H_0$ (similar to the response of a sphere). In particular, the value of ω_K is independent of M_T and therefore the nonlinear frequency shift is null [77, 103]. This implies that the conduction band of the magnons between the emitter and collector remains aligned as shown schematically in Fig. 35(d), which then prevents the self-localization effect by the nonlinear frequency shift. The enhancement of the magnon transmission ratio is clearly visible if one compares Fig. 35(c) and Fig. 35(d). Further evidence of the reduction of self-localization in the latter case, is the observation that the variation of the transmission ratio in Fig. 35(d) mimics now the observed variation of low-energy magnons observed under the emitter by BLS as shown in Fig. 33(e). We will come back to this important point in the next chapter while discussing the spatial decay of the magnon transmission ratio.

On the quantitative side, we find that the ratio of initial and maximum values is 15.1 for (Bi-)YIG$_B$ compared to 7.2 for YIG$_C$). Suppression of elliptical precession and temperature dependence of ω_K thanks to the uniaxial anisotropy which compensates the

dipolar field promotes the population of low-energy magnons. The solid line in Fig. 35(c) and (d) is a fit with Eq. (1.97) using $n_{\rm sat}$ as a free parameter. While for the YIG$_C$ sample we find that the best fit is obtained by using $n_{\rm sat} = 4$ as explained above, the value of the saturation threshold increases to $n_{\rm sat} = 11$ in the case of Bi-YIG$_B$. This is a direct experimental evidence that the contribution of low-energy magnons to the spin diode effect concerns a rather narrow spectral window around the Kittel energy, with an upper bound width of about 1 GHz. This broadening should be correlated to the enhanced magnon-magnon scattering time indicated by Γ_m in Fig. 11(c). Another pertinent energy scale is the difference $E_K - E_g$ that varies like $t_{\rm YIG}$. This implies that in ultra-thin films of garnet, this phenomenon of localization of low-energy magnons becomes exalted.

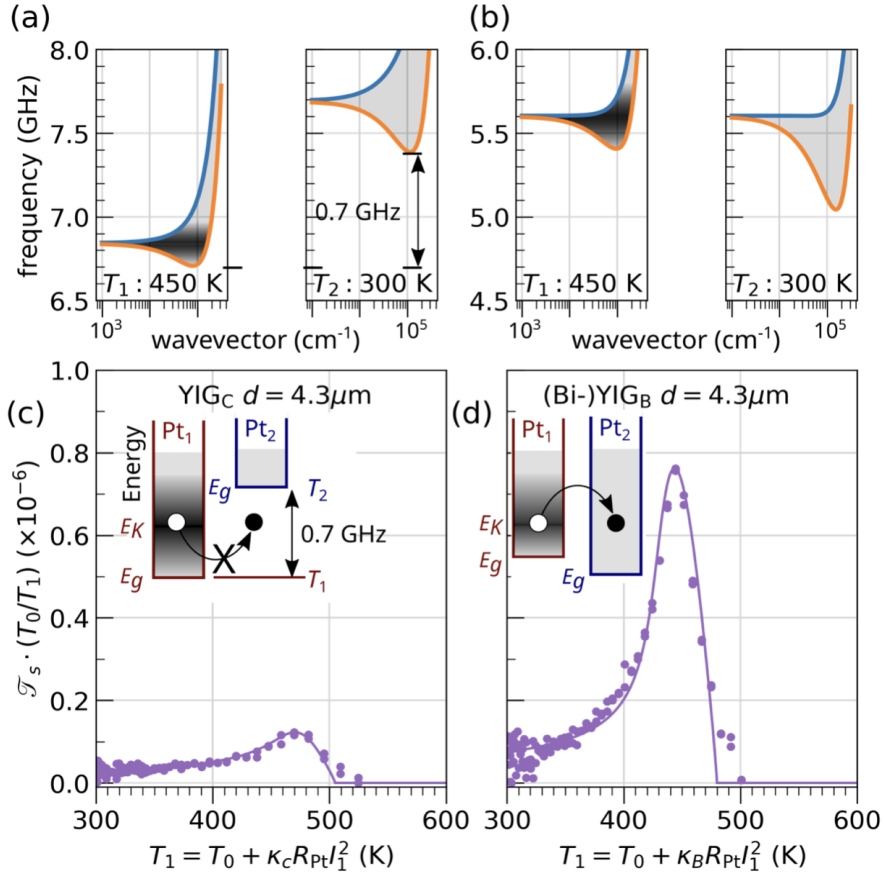

Figure 35: *Experimental evidence that the spin diode effect involves a narrow spectral window of magnons around the Kittel energy. Panels (a) and (b) are an illustration of band mismatch between two regions at different temperatures. It shows the magnon manifold in the GHz energy range in the case of a material, whose nonlinear frequency shift is (a) negative (red-shift) or (b) null ($K_u - \mu_0 M_s \to 0$). When the Kittel mode beneath the emitter is below the gap of the magnon propagation band in the bulk, low-energy magnons produced electrically are prevented to propagate. This promotes self-localization effects and it prevents the growth of a large non-local signal. Comparison of the propensity for low-energy magnons to travel a long distance ($d = 4.3$ μm) between (c) YIG$_C$ and (d) (Bi-)YIG$_B$. We observe a significant increase of the spin diode signal between (c) YIG$_C$ and (d) (Bi-)YIG$_B$. We explain it by the suppression of self-localization effects produced by the nonlinear frequency shift.*

4.3.5.2 Saturation of the magnon density

We emphasize, however, that although the nonlinear frequency shift is zero in the case of (Bi-)YIG$_B$, the system is still subject to the saturation effect. The vanishing nonlinear frequency coefficient only eliminates the ellipticity of the trajectory for the long wavelength magnons, whose wave-vector is smaller than the inverse of the film thickness. It does not eliminate the self-depolarisation effect of the spin-wave. This value depends mostly on θ_k, the angle between the propagation direction and the equilibrium magnetization direction, the latter being the origin of the broadening of the magnon manifold. We note that for the wave-vectors around E_g, this is the dominant origin of ellipticity, since the broadening almost reaches the maximum value of $\gamma\mu_0 M_s$ as shown in Fig. 10(d).

This shows that the tuning of M_{eff}, which allows to remove the non-isochronicity of the long wavelength magnons is responsible for an enhancement of the saturation threshold, which is found to almost triple.

4.3.6 Linear regime

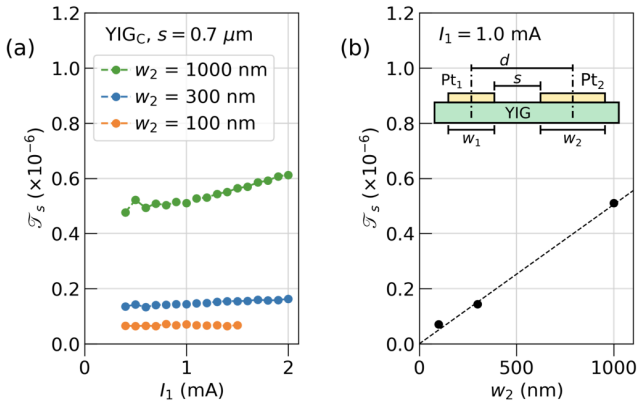

Figure 36: *Influence of the collector width, w_2. Change of w_2 occurs while maintaining constant both the emitter width, $w_1 = 300$ nm, and the edge to edge distance between the two Pt stripes, $s = d - (w_1 + w_2)/2 = 0.7$ μm, with d being the center to center distance. (a) shows $\mathcal{T}_s$ as a function of I_1 for 3 different values of w_2 and (b) shows $\mathcal{T}_s$ at $I_1 = 1$ mA as a function of w_2. The dotted line is a linear fit through the data point. The inset is a schematic side-view of the devices, where the different dimensions used throughout the chapter are defined.*

Finally, it seems relevant to highlight that the data presented above provide some cross-check on the dimensional dependence of the magnon transmission ratio with external parameters as suggested by Eq. (1.105). The dashed line in Fig. 42 in the next chapter shows the proportional dependence of $\mathcal{T}_s$ on T_1. Comparison of the non-local signals using local annealing of the Pt electrode as shown in Fig. 34(a) demonstrates the proportional dependence of $\mathcal{T}_s$ on $\epsilon_1 \cdot \epsilon_2$. The Groeningen group has extensively studied the thickness dependence of the conductivity of electrically excited magnons (low-energy magnons) and they observed the monotonous decrease as the thickness increases, confirming the $1/t_{\text{YIG}}$ behavior [117].

Eq. (1.105) also predicts the linear and inverse linear relationship of magnon transmission ratio with the width of collector w_2 and emitter w_1 respectively. Fig. 36 shows the influence of w_2 on $\mathcal{T}_s$ with different w_2 as a function of I_1 for (a) and of w_2 for (b). Note

that the width of the emitter and the edge to edge distance between the two Pt stripes remain constant as $w_1 = 300$ nm and $s = d - (w_1 + w_2)/2 = 0.7$ μm. Those devices are fabricated at the same time as YIG$_C$ devices and we verify that the spin mixing conductance $G_{\uparrow\downarrow}$ for each w_2 is relatively similar. Taking the value at low current $I_1 = 1.0$ mA to see the behavior of the linear regime, the proportional dependence on w_2 is revealed. This observation suggests that YIG|Pt interface is weakly coupled, meaning that the transfer of angular momentum between YIG and Pt can be considered as ineffective due to the poor transparency at the interface, which leads to only a small fraction of magnons absorbed into the Pt electrodes. It matches the observation in Fig. 34(a) that magnon emission is proportional to ϵ_1.

On the contrary Fig. 37 shows the influence of the emitter width w_1 on (a) $\mathscr{T}_s$ as a function of applied current density $I_1/(w_1 t_{\mathrm{Pt}})$. For the sake of completeness, we show in Fig. 37(b) its influence on $\overline{\mathscr{V}}_2$ voltage as a function of the current density. The behavior illustrates that the thermalization of the Pt$_1$ improves with decreasing width of the injector. Fig. 37(a) qualitatively confirms that the smaller w_1 gives larger conduction of low energy magnons. This enhancement comes from the reduction of the effective number of spins to compensate the damping by spin orbit torques. If one would convert the abscissa of Fig. 37(b) in T_1, one would find that the SSE voltage does not seem to depend largely on the w_1 since the amount of temperature gradient (or Joule heating) matters. The agreement however does not scale as the predicted $1/w_1$. The origin of deviation is still unclear, however one can speculate that the additional increase of magnetic damping α_{LLG} induced at YIG|Pt interface [162, 225] may affect the transport especially for thermal magnons due to its diffusive nature and short decay length of $\lambda_T \approx 0.5$ μm, which is comparable with the variation range of w_1. Further studies are needed to clarify this point.

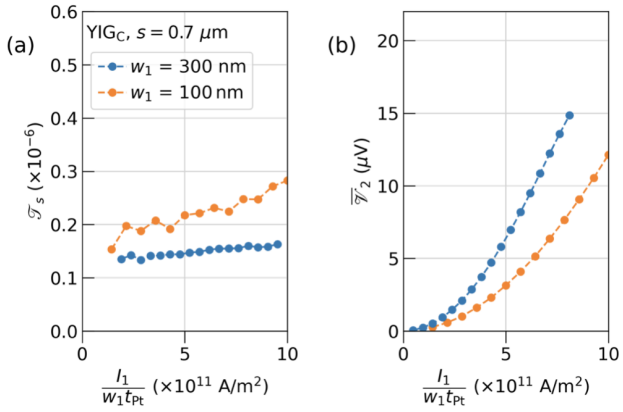

Figure 37: *Influence of the emitter width, w_1. Change of w_1 occurs while maintaining constant both the collector width, $w_2 = 300$ nm, and the edge to edge distance between the two Pt stripes, $s = d - (w_1 + w_2)/2 = 0.7$ μm. (a) shows $\mathscr{T}_s$ as a function of the current density $J_1 = I_1/(w_1 t_{\mathrm{Pt}})$ for 2 different values of w_1 and (b) shows the $\overline{\mathscr{V}}_2$ voltage ($\propto$ SSE) as a function of T_1.*

4.4 Conclusion

In this work, we draw a comprehensive picture of the role of low-energy magnons in the electrical transconductance of extended magnetic thin films. While the spin conduction at low intensity seems to behave mostly as expected, the behavior at large intensities

is distinctively different from what is observed in strongly confined geometries, such as nanopillars.

The principal difference is associated with the propensity of the injected spin to spread between different degenerate eigen-modes. There are thus phenomena related to the two dimensionality that intrinsically prevent a single mode to dominate the others (as is possible in 0D and 1D [203]). In a confined geometry the energy gap produced by confinement between different eigen-modes protects the main fluctuator from relaxation into other modes. In an extended thin film, this barrier is removed and degeneracies arise, leading to an efficient redistribution of energy between degenerate modes. Even admitting that one mode is pumped more efficiently than the others (*e.g.* the mode with wavelength $1/w_1$), non-linear saturation phenomena come into play quickly, so that the critical current can never be reached. This leads to the magnon-magnon relaxation rate becoming power dependent and in particular to increase sharply above a certain mode occupation threshold. We use this to draw a picture of a condensation that seems to have a fluid-like behavior. This picture is supported by a series of different experiments that include non-local transport on different thicknesses of YIG thin films as well as different garnet composition, Brillouin Light spectroscopy, and independent variation of the spin mixing conductance or thermal gradient near the emitter.

We showed that doping with Bi improves the non-local signal. The first reason is that we avoid the non-linear red shift under the emitter, which produces localization being of course detrimental to the non-local geometry. The second reason is that the lateral temperature gradient has no effect on the magnon spectrum because $M_{\text{eff}} \approx 0$ whatever the temperature. So the magnons emitted under the injector have no problem propagating to the detector. And the third reason, is that the precession being quasi-circular, the parametric excitation of other modes of magnons is strongly limited hence allowing n_{sat} to become larger.

We also revealed that the inability to thermalize the emitter electrode plays a crucial role in decreasing M_1 under the emitter. This is a very strong effect in 2D geometry, which, combined with the fact that a single mode cannot be excited and that the critical current goes to infinity, means that we arrive at the Curie temperature before it self-oscillates. Even if this reduction in M_1 may seem favorable for reaching the critical current (which tends towards 0 if $M_1 \to 0$), the non-linear effects mentioned above (coupling between modes, location under the injector, etc.) mean that we never get there.

We did not find any direct signature of BEC in our transport studies on non-local devices. All our experimental data suggest a strong interaction between degenerate modes rather than the fluctuation of a single mode. This problem plagues the non-local geometry, where one only monitors the magnon propagating outside the Pt electrode, which by the way always represents a tiny proportion of the total injected spin. In this regard, our above work does not really address what happens directly beneath the Pt.

Although there is no BEC condensation outside the area beneath the emitter, the analogy with the Gurzhi effect in ultra pure electron conductors seems pertinent. Further studies would be required to exhibit direct evidence of such a magneto-hydrodynamic fluid behavior at high power. The unambiguous signature would be features that can only be ascribed to the Navier-Stokes transport equation [212].

Chapter 5

Two-fluid behavior for spin transport in extended magnetic thin films

As emphasized in the previous chapter 4, one of the original features of the non-local devices depicted in Fig. 38 is to behave as the spin diode at a large current. These devices rely on the spin transfer effect (STE) to electrically modulate the magnon population inside a magnetic thin film. The process changes the amplitude of thermally activated spin fluctuations by transferring, via a stimulated emission process, quanta of $\gamma\hbar$ between an adjacent metallic electrode and the magnetic thin film. In extended geometries, a wide energy range of eigen-modes is available to carry the external flow of angular momentum spanning a frequency window from GHz to THz as indicated schematically in Fig. 38(c), which shows the lower branch of the spin-wave dispersion over the Brillouin zone [134–136]. At high-energy the curve flattens out at around 30 meV, which corresponds to the thermal energy, $E_T \approx k_B T_0$, at ambient temperature, while at low-energy it displays a gap, $E_g \approx \hbar\omega_K \approx 30$ μeV, around the Kittel frequency $\omega_K/(2\pi)$ [73]. Between these two extrema, the spectral identification of the relevant eigen-modes participating in the non-local spin transport has so far remained mostly elusive.

In this chapter, we find that the observed behavior can be well approximated by a two-fluid model as proposed in subsection 1.2.5 in chapter 1, which simplifies the spectral vision as emanating from two independent types of magnons placed at both ends of the magnon manifold. On one side, we have magnons at thermal energies, which shall be referred to as *high-energy* magnons [56], whose distribution follows the temperature of the lattice. On the other side, we have magnons at the bottom of the band near the Kittel frequency, which shall be referred to as *low-energy* magnons, whose electrical modulation at high power is the focus of the previous chapter 4. The response of these two magnon populations to external stimuli varies widely. The high-energy thermal magnons being particles of high wave-vectors are mostly insensitive to any changes in the external conditions of the sample such as shape, anisotropy and magnetic field, instead being defined by the spin-wave exchange stiffness and the large k-value of the magnon [137, 226]. In contrast, low-energy magnetostatic magnons sensitively depend on the extrinsic conditions of the sample. It turns out that non-local devices provide a unique means to study independently each of these two fluids, by comparing the differences in transport behavior as a function of the separation, d, between the 2 circuits and thus benefiting from the spatial filtering associated with the fact that each of these two components decays very differently as a function of the distance as shown schematically in Fig. 38(b).

This chapter will be organized as follows. After an introduction, in the second section, we review the most salient features that support the splitting in two-fluid. In the third section, we describe the analytical framework of a two-fluid model and in particular the expected signature in transport measurement by reminding readers of subsection 1.2.5 in chapter 1. This part builds on the knowledge gathered in the previous chapter 4

around the nonlinear behavior of low-energy magnon. In the fourth section, we will show the experimental evidence that supports such a picture and finally in the fifth section we conclude this work by summarizing the important findings and opening to future perspectives.

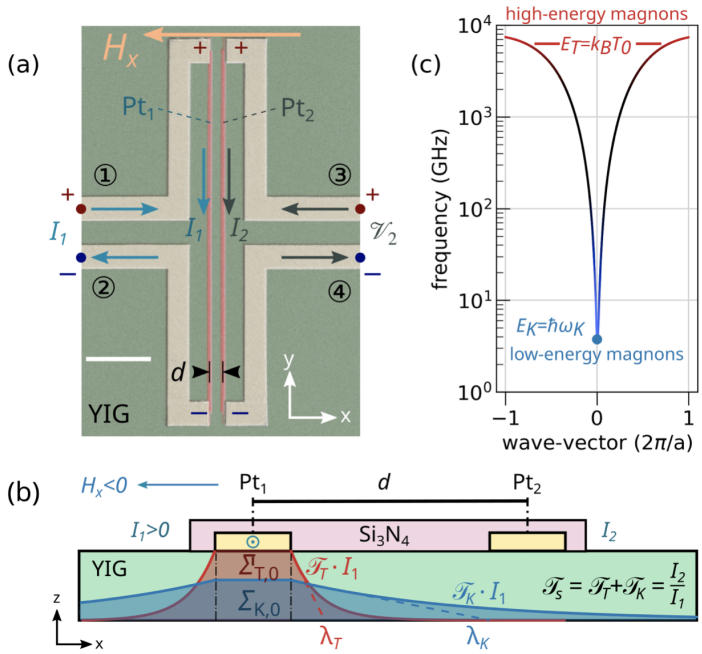

Figure 38: *Lateral measurement of the transconductance by magnon in extended magnetic insulating films. (a) Scanning electron microscope image of a 4-terminal circuit (scale bar is 5 µm), whose 4 poles are connected to two parallel wires, Pt_1 and Pt_2 (shown in pink), deposited on top of an extended YIG thin films. A continuous electrical current, I_1, injected in Pt_1 (emitter), produces an electrical modulation of the magnon population by spin transfer effect (STE). This modulation is consequently sensed laterally by the spin pumping voltage, $-R_2I_2$, via a second electrode Pt_2 (collector), placed at a distance, d, from the emitter. We define the magnon transmission ratio $\mathscr{T}_s = I_2/I_1$ and the transconductance $\mathscr{T}_s/R_1$. Panel (b) is a cut view representing the spatial decay of propagating magnons. (c) Schematic representation of the spin-wave dispersion over the Brillouin zone. We account for the spin transport properties as emanating from two independent fluids placed at both ends of the dispersion curve. Each of the two fluids has a different characteristic decay length respectively λ_T and λ_K as shown in (b).*

5.1 Key findings

The purpose of this chapter is to expose the experimental evidences that support the segregation of magnon transconductance into two components. All this is achieved by measuring the transmission coefficient $\mathscr{T}_s \equiv I_2/I_1$ of magnon emitted and collected via the spin Hall effect between two parallel Pt wires, respectively Pt_1 and Pt_2. It will be shown that a two-fluid model, where $\mathscr{T}_s = \mathscr{T}_T + \mathscr{T}_K$ is the independent sum of a thermal and a magnetostatic magnon contribution, provides a simplified common framework that captures all the observed behavior in non-local devices with different separation between the electrodes, different current bias, different applied magnetic field, different film thickness or magnetic composition, and different temperature of the substrate.

Making a quantitative analysis of the transmission ratio, we find that most of the injected spins remain localized under the emitter or propagate along the magnetization *i.e.* Damon-Eshbach mode (the estimated proportion is about 2/3), making these materials intrinsically *poor* magnon conductors. The remaining propagating magnons split into two distinct categories: first a large portion carried by high-energy magnons, which follow a diffusive transport behavior with a characteristic decay length, λ_T, in the sub-micron range [119, 159]; and second a small portion carried by low-energy magnons, which are responsible for the asymmetric transport behavior, and which follow a ballistic transport with a characteristic decay length, λ_K, in the micrometer range. The different decay behaviors are directly apparent experimentally in the change of nonlinear spin transport behavior with separation, d.

We also study carefully the collapse of the magnon transmission ratio when increasing the temperature of the emitter, T_1, as it approaches the Curie temperature, T_c. Here the number of spin polarized sites under the electrode becomes of the same order as the flow of spin coming from the external Pt electrode. The transition of this regime of magnetization diminution leads to a sharp decrease of the magnon transmission ratio. We report signs of interaction between the low-energy and high-energy parts of the fluid in this highly diffusive regime [227–229]. In addition, the collapse seems to occur actually well before reaching T_c, suggesting that the total number of magnons is significantly underestimated from the one inferred from the sole temperature value of the lattice beneath the emitter. Alternatively this discrepancy might be the indication of a rotation of the equilibrium magnetization under the emitter [122, 230]. Since the discrepancy is actually more pronounced as the magnetic film becomes thinner, this suggests that the culprit is the amount of low-energy magnons.

5.2 Analytical framework

We guide readers to refer to subsection 1.2.5 in chapter 1 for the detailed discussion. We simplify the spectral nature of the magnon transport with the two-fluid model, one with the energy around k_BT and the other with the energy around $\hbar\omega_K$. As they have completely different energy landscapes, the transport characteristic should be distinct from each other. We propose to separate the two contributions in the transport data.

5.3 Experiments

In this section, we present the experimental evidence that supports the two-fluid picture exposed above. To that end, we focus on the evolution of the spin transport with the current, distance, applied magnetic field, temperature of the substrate and effective

magnetization, M_{eff}. This will allow to test the range of validity of our model.

5.3.1 Magnetic susceptibility of the magnon transmission ratio

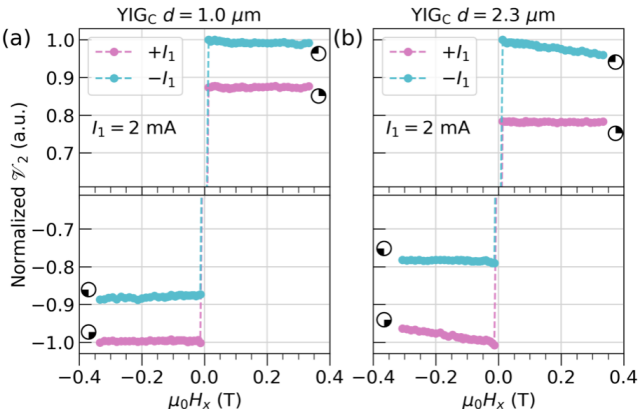

Figure 39: *Dependence of the magnon transmission ratio on an external magnetic field. Comparison of the non-local voltage $\mathscr{V}_2 = (V_{2,\perp} - V_{2,\parallel})$ between (a) short-range device ($d = 1.0$ μm) and (b) long-range device ($d = 2.3$ μm). The panels show zoom at the maximum and minimum of the normalized values. We interpret the detection of a finite susceptibility, $\partial_{H_x}\mathscr{V}_2 < 0$, as indicative of a magnon transmission ratio by low-energy magnons. In contrast, a constant behavior, $\partial_{H_x}\mathscr{V}_2 \approx 0$, is indicative of a magnon transmission ratio by high-energy magnons. Finite susceptibility is uniquely observed in the long-range regime when $I_1 \cdot H_x < 0$, i.e. when i) the number of low-energy magnons is boosted by injecting a current in the forward direction and ii) when the contribution of the rapidly decaying high-energy magnons becomes a minority. The data are collected on the YIG$_C$ thin film driven by a large current amplitude of $\pm I_1 = 2.0$ mA.*

We start this section by first exposing some key experimental evidence supporting the two-fluid picture. A schematic of the 4-terminals device is shown in Fig. 38(a). It circulates pure spin currents between two parallel electrodes subject to the spin Hall effect [17]: in our case, two Pt stripes $L_{\text{Pt}} = 30$ μm long, $w_{\text{Pt}} = 0.3$ μm wide and $t_{\text{Pt}} = 7$ nm thick. The experiment is performed here at room temperature, $T_0 = 300$ K, on a 56 nm thick (YIG$_C$) garnet thin film, whose physical properties are summarized in Table.4.1 in the previous chapter. While injecting an electrical current I_1 in Pt$_1$, we measure a voltage V_2 across Pt$_2$, whose resistance is R_2. To subtract all non-magnetic contributions, we define the spin signal $\mathscr{V}_2 = (V_{2,\perp} - V_{2,\parallel})$ as the voltage difference between the normal and the parallel configuration of the magnetic field with respect to the electrical current direction. Practically, the measurement is simply obtained by recording the change of voltage while rotating an in-plane external magnetic field, H_0, respectively along the $x-$ and the y-direction [the cartesian frame is defined in Fig. 38(a)]. Fig. 39 shows the variation of $\mathscr{V}_2$ as a function of H_x for a large amplitude of $|I_1|$ =2.0 mA, which corresponds to a current density of $1 \cdot 10^{12}$ A/m^2. To reduce the influence of Joule heating and also thermal activation of electrical carriers in YIG [105, 150], we use a pulse method with a 10% duty cycle throughout this study to measure the non-local voltage [56]. In Fig. 39 we compare the magnetic field sensitivity of the (normalized) spin transport at two values of the center to center separation d between emitter and collector for positive and negative polarities of the current. Overall, this leads to 4 possible configurations for the pair

(I_1,H_x) each labeled by the symbols ◔, ◴, ◒, ◕ to conform with the notation of Fig. 40. There a vertical inversion of the marker dissociates scans of opposite H_x-polarity, while a horizontal one dissociates scans of opposite I_1-polarity.

Looking at Fig. 39, we recover the expected inversion symmetry while enhancement of the spin current is clearly visible when $I_1 \cdot H_x < 0$. The signal seems to only depend on the magnetic field for larger distances and $I_1 \cdot H_x < 0$ (forward bias). Taking into account that the two Pt wires are both $w = 0.3$ μm wide, this corresponds to an edge to edge separation $s = d - w$. In one case, the separation $s \approx (2\lambda_T)$, while in the other case $s \approx 4 \cdot (2\lambda_T)$, where $2\lambda_T \approx 0.6\mu$m is the estimated amplitude decay length of magnons at thermal energy. It will be shown below that under the emitter the number of high-energy magnons well exceeds the number of low-energy magnons. Assuming an exponential decay of high-energy magnons, one expects in (a) an attenuation of their contribution by 50%, while in (b) it is decreased by almost 99%. We thus arrive at a situation, where at $d = 1.0$ μm the magnon transport is dominated by the behavior of high-energy magnons while at $d = 2.3$ μm the magnon transport is dominated by the behavior of low-energy magnons (see below). In Fig. 39, we assign the finite susceptibility $\partial_{H_x}\mathscr{V}_2 < 0$, as indicative of a magnon transmission ratio by low-energy magnons. As the energy of these magnons as well as the threshold of damping compensation sensitively depends on the magnetic field [93,195], the low-energy magnons are affected significantly by the amplitude of the magnetic field, H_x [56,79,184]. Such field dependence is explained in Eq. (1.105) in chapter 1. What is observed here is that near the peak bias, $I_{\rm pk} \approx 2.2$ mA (see definition in the previous chapter 4), the device becomes extra sensitive to shift of $\mathcal{I}_{\rm th}$. In our case, the external magnetic field shifts here $\mathcal{I}_{\rm th}$ by shifting the Kittel frequency, $\omega_K = \gamma\mu_0\sqrt{H_0(H_0 + M_s)}$. By contrast, the constant behavior, $\partial_{H_x}\mathscr{V}_2 \approx 0$, is indicative of a magnon transmission ratio by high-energy magnons: because of their short wavelength, their energy is of the order of the exchange energy, and thus independent of the magnetic field strength [47]. Since these 2 plots are measured with the exact same current bias and the only parameter modified is d, it demonstrates that filtering between high-energy and low-energy magnons can be obtained by simply changing the separation range between the emitter and collector. It also directly suggests a double exponential decay as will be discussed later on in Fig. 43.

5.3.2 Spectral signature in non-local measurement.

Fig. 40 compares the variation of $\mathscr{V}_2$ as a function of the emitter current I_1 for two different emitter-collector separations. The maximum current injected in the device is about 2.5 mA, corresponding to a current density of $1.2 \cdot 10^{12}$ A/m^2. The polarity bias for the pair (I_1,H_x) is represented by the symbols ◔,◴,◒,◕, in replicas of the 4 curves pattern. We recover in Fig. 40(a,b) the expected inversion symmetry with $\mathscr{V}_2^{◔} \approx -\mathscr{V}_2^{◒}$ and $\mathscr{V}_2^{◴} \approx -\mathscr{V}_2^{◕}$, while the enhancement of the spin current is visible when $I_1 \cdot H_x < 0$, which represents the forward regime. As explained in the previous chapter, the raw signal $\mathscr{V}_2 = \overline{\mathscr{V}_2} - R_2 I_2$ can be split into *i)* $\overline{\mathscr{V}_2}\big|_{I_1^2}$ a thermal signal produced by the spin Seebeck effect (SSE), which is always odd/even with H_x or I_1 and shown in panels (c,d), and *ii)* $-R_2\, I_2|_{I_1}$, an electrical signal produced by the spin transfer effect (STE), which is in the linear regime even/odd with the polarity of H_x or I_1 and shown in panels (e,f) [1]. This decomposition is obtained by assuming that in the reverse bias $\overline{\mathscr{V}}_2^{◔} = -\mathscr{V}_2^{◒} + R_2\, \mathscr{T}_s|_{I_1\to 0}\ (\mathscr{T}_T)^\star \cdot I_1$ and $\overline{\mathscr{V}}_2^{◒} = -\mathscr{V}_2^{◔} + R_2\, \mathscr{T}_s|_{I_1\to 0}\ (\mathscr{T}_T)^\star \cdot I_1$, which evaluates the number of magnons absorbed as a linear deviation from the number of thermally

[1] The minus sign in front of the electrical contribution accounts for the fact that the spin-charge conversion is an electromotive force and thus the current flows opposite to the voltage drop.

excited low-energy magnons, while assuming C^2 continuity of the magnon transmission ratio across the origin. We recall that in our notation $(\mathscr{T}_T)^\star \equiv \mathscr{T}_T / \mathscr{T}_T|_{I_1 \to 0}$. We then construct $\overline{\mathscr{V}_2^{\textcircled{\scriptsize\bullet}}} = \overline{\mathscr{V}_2^{\textcircled{\scriptsize\bullet}}}$ and $\overline{\mathscr{V}_2^{\textcircled{\scriptsize\bullet}}} = \overline{\mathscr{V}_2^{\textcircled{\scriptsize\bullet}}}$ by enforcing that the signal produced by Joule heating is exactly even in I_1. We observe that in the short-range ($d = 0.5$ μm), we recover $\overline{\mathscr{V}_2^{\textcircled{\scriptsize\bullet}}} \approx (\mathscr{V}_2^{\textcircled{\scriptsize\bullet}} + \mathscr{V}_2^{\textcircled{\scriptsize\bullet}})/2$ and $I_2^{\textcircled{\scriptsize\bullet}} = \text{sign}(I_1)(\mathscr{V}_2^{\textcircled{\scriptsize\bullet}} - \mathscr{V}_2^{\textcircled{\scriptsize\bullet}})/(2R_2)$, which is the expected signature for a symmetric magnons' signal. This equality is not satisfied in the long-range ($d = 2.3$ μm) for $\overline{\mathscr{V}_2}$ due to the asymmetry of the signal between the forward and reverse bias as explained in the previous chapter 4. The consistency of this data manipulation is confirmed below in Fig. 41(a) and (b), by showing small asymmetric enhancement of I_2 at high I_1 by low-energy magnons at a short distance and a distinct enhancement at large distances as discussed in the previous chapter. The fact that a more pronounced enhancement is observed at a large distance is further evidence for the spatial filtering of high-energy magnons.

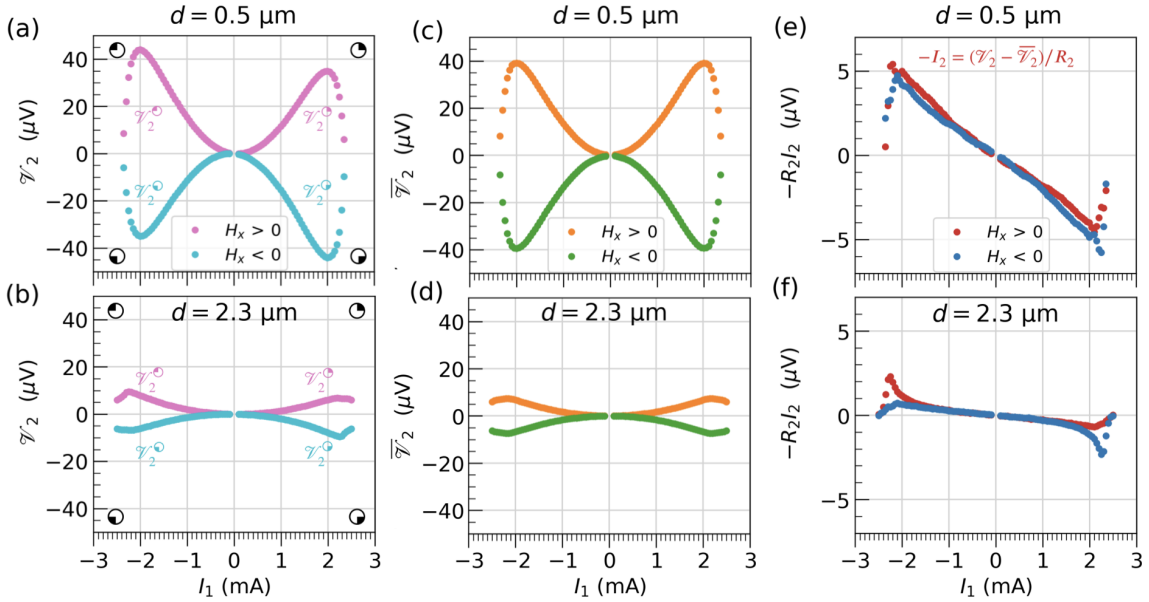

Figure 40: *Dependence of the electric signal, I_2, on I_1. We compare the transport characteristics between two non-local devices: one with a short distance between the emitter and collector in the sub-micron range ($d = 0.5$ μm, top row) and the bottom with a long distance of a couple of microns ($d = 2.3$ μm, right column). The first column (a) and (b) display $\mathscr{V}_2$ at $T_0 = 300$ K as a function of I_1, the injected current, for both positive and negative polarity of H_x, the applied magnetic field. In our symbol notation, the marker position indicates the quadrant in the plot pattern. The raw signal $\mathscr{V}_2 = -R_2 I_2 + \overline{\mathscr{V}_2}$ is decomposed in an electric signal, I_2, and a background thermal signal, $\overline{\mathscr{V}_2}$, as shown respectively in the third column (e,f) or the second column (c,d). The background, $\overline{\mathscr{V}_2}$, represents the background magnon currents along thermal gradients. The measurements are performed on YIG_C thin films.*

It is worth noticing that one can reach a situation where $-R_2 I_2 = 0$ without necessarily having $\overline{\mathscr{V}_2}$ vanishing too as shown in Fig. 40(e) and (f) at $I_1 = 2.5$ mA. This is explained by the establishment of lateral temperature gradients [231]. In other words, the observation

of $M_T = 0$ is a local problem that mostly concerns the region beneath the emitter. It does not imply that $M = 0$ throughout the whole thin film.

As a next step, we demonstrate how the contributions of the high-energy and low-energy magnons can be distinguished using the analytical model in Fig. 41. We will remove the influences of the spurious contribution on the electrical spin transport signal starting from Fig. 40(e,f). First, we normalize the signal by the emitter current to obtain the magnon transmission ratio coefficient $\mathscr{T}_s = I_2/I_1$ as plotted in Fig. 41(a,b). For a small separation we observe that $\mathscr{T}_s$ shows a quadratic behavior that is symmetric in current and consequently we associate it with the device temperature. In contrast, the device with a large separation shows an asymmetric enhancement due to the spin diode effect. The influence of the increase of the emitter temperature T_1 due to Joule heating from I_1 can be removed by normalizing with T_1/T_0. This normalization takes out the symmetric enhancement of the magnon transmission ratio as previous studies report [150, 180, 232, 233], where the justification will be discussed later in Fig. 42 [2]. The obtained traces are shown in Fig. 41(c,d) and can be compared with the theoretical expectation given by Eq. (1.110), which is graphically summarized in Fig. 14(e). The solid lines are fitting curves with our model representing the sum of the contribution by low-energy magnons and the background contributions from high-energy magnons, where the parameters of the fit are found in Table.5.1. The dashed line and shaded area in grey represent the latter $\Sigma_T \Delta n_T$. From the fits we can obtain the ratio $\Sigma_T/(\Sigma_T + \Sigma_K)$ for the two magnon fluids, where the contribution from high-energy magnons drops from 95% at 0.5μm to 50% at 2.3μm, in line with the spatial filtering proposed above.

To illustrate experimentally Eq.(1.109), we have repeated the measurement for different values of the substrate temperature T_0 at small separation. Fig. 42(a) shows the experimental result for five different values of T_0 when I_1 varies on the same $[-2.5, 2.5]$ mA span. Note that data are plotted as a function of $T_1 = T_0 + \kappa_A R_{\mathrm{Pt}} I_1^2$, the temperature of the emitter. The rational for this transformation of the abscissa is apparent in Fig. 42(b) and (c), which show that the nonlinear current dependence of both the SSE and STE signals originate from the enhancement of T_1. In particular, Fig. 42(c) shows the rise of the SSE signal $\overline{\mathscr{V}_2}$ as a function of I_1 for different values of T_0. We find that all the curves almost overlap on the same parabola suggesting an identical thermal gradient of the Pt_1 electrode by I_1 independently of T_0, with small deviation for smaller T_0 due to a decrease of R_{Pt}. Additionally, Fig. 42(d) shows $(1/\mathscr{T}_s)^\star \equiv \mathscr{T}_s|_{I_1 \to 0}/\mathscr{T}_s$, the inverse transmission ratio of the spin current generated by STE normalized by its low current value[3]. The different curves overlap and, similar to the SSE, exhibit a parabolic evolution (see dotted line). This suggests that the primary source of the symmetric nonlinearity between I_2 and I_1 is simply Joule heating. It therefore justifies the transformation of the current abscissa I_1 into a temperature scale T_1 in Fig. 42(a). Focusing now on the remarkable features of Fig. 42(a), one could notice that the low current data taken with $T_0 = 300$ K falls on a straight line intercepting the origin as predicted by Eq. (1.97), which is $I_2/I_1 \propto T_1$. Another remarkable feature, as previously reported [180, 233], is that the transmission ratio reaches a maximum at a high temperature.

[2] The theoretical [232] and experimental studies [180] reported the power law of $T^{3/2}$ at low temperature $T < 300$ K. However the exponent decreases to $T^{1/2}$ as the temperature increases. In the end in our temperature range the exponent 1 well fits the data as shown in Fig. 42 [150].

[3] We shall use consistently this notation of $\star$ to represent normalized quantity by the value at the origin.

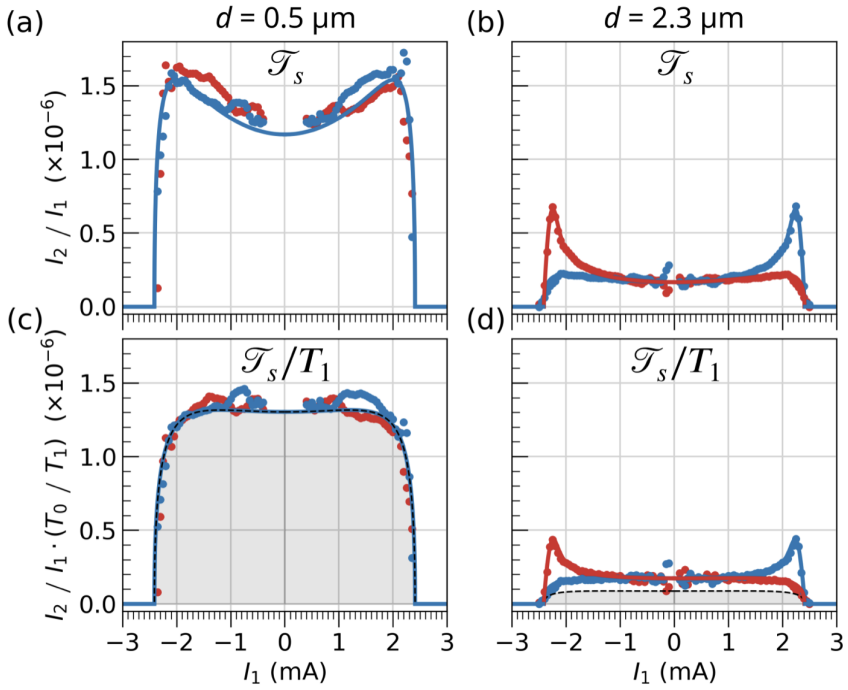

Figure 41: *Dependence of the magnon transmission ratio on distance. Starting from the extraction of I_2 in Fig. 40, the first row compares the variation of the ratio $\mathscr{T}_s = I_2/I_1$ between short-range (left column) and long-range (right column) devices. In the short-range, the behavior shows a symmetric magnon transmission ratio signal with respect to the current polarity I_1, while in the long-range the behavior is asymmetric. We interpret the difference as emanating from two different kinds of magnons: dominantly high-energy magnons in the short-range and dominantly low-energy magnons in the long-range. To eliminate nonlinear distortions produced by Joule heating, $\mathscr{T}_s$ is renormalized by $T_1|_{I_1^2}$, the temperature variation of the emitter produced by Joule heating (see text). The solid lines are fits with Eq. (1.110), where the shaded region shows the background contribution from high-energy magnons $\Sigma_T(\mathscr{T}_T)^\star$, where $\Sigma_T/(\Sigma_T+\Sigma_K)|_d$ represent their relative weight at this distance. In (c) this ratio is about 0.95 while in (d) it drops to about 0.5.*

To support this picture with experimental data, we have plotted in the insert of Fig. 42 the behavior of $M_T(M_0 - M_T)$ suggested by Eq.(1.109). This should represent the magnon transmission ratio by the high-energy portion, namely the number of thermal magnons available multiplied by the amount of spin polarization available in the film. We find that the observed variation of $\mathscr{T}_s$ with T_1 follows the expected behavior inferred from the sole temperature variation of the total magnetization shown in the insert Fig. 42(b). This provides experimental evidence that the short-range behavior is dominated by high-energy magnons and that the change of density follows the analytical expression in Eq. (1.109). Furthermore it confirms that the drop in the magnon transmission ratio above 440 K is associated with a drop of the saturation magnetization as one approaches T_c, which is precisely where thermal magnons reach their largest occupation. The drop suggests that high-energy magnons are actually preventing STE spin transport. This is the nonlinear deviation expected for a diffusive gas: the higher the number of particles the more the transmission is inhibited. What it shows here is that the magnon transconductance is dominated by high-energy magnon around the emitter. This confirms the initial finding of Cornelissen *et al.* [113], who drew this conclusion based on the similarity of the characteristic decay of the SSE and STE as a function of d.

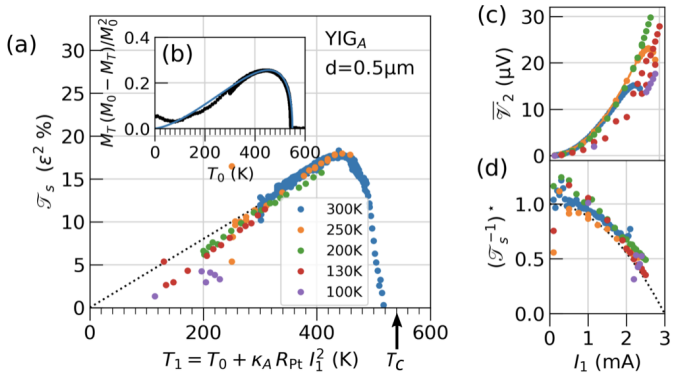

Figure 42: *Dependence of the magnon transmission ratio on the substrate temperature, T_0. Short-range measurement ($d = 0.5$ μm) of the non-local spin transport in YIG_A. (a) Variation of $\mathscr{T}_s$, when the emitter current I_1 is varied in $[-2.5, 2.5]$ mA span at different values of the substrate temperature, T_0. The data are plotted as a function of $T_1 = T_0 + \kappa_A R_{Pt} I_1^2$, the temperature of the emitter. The resulting temperature dependence of $\mathscr{T}_s$ observed in (a) matches the variation $M_T(M_0 - M_T)$ shown in the insert (b), with M_T being the temperature dependence of saturation magnetization. The dots are the experimental points, while the blue solid line is the expected behavior assuming that $M_T \approx M_0\sqrt{1-(T/T_c)^{3/2}}$. This transformation is supported by the observation in (c) and (d), that both the SSE signal, $\overline{\mathscr{V}_2}$ and the normalized inverse transmission ratio $(\mathscr{T}_s^{-1})^\star$ vs. I_1 scales on the same parabolic behavior (dotted line), suggesting that the pertinent bias parameter is T_1.*

5.3.3 Double decay of the magnon transmission ratio

5.3.3.1 Thin films with anisotropic demagnetizing effect

Having established that the spin current is carried by the two fluids and that fitting allows to extract the respective contributions of high-energy and low-energy magnons, we took a series of experimental data of $\mathscr{T}_s \cdot T_0/T_1$ with different separations d ranging from 0.5μm to 6.3μm. The results are shown in Fig. 43. We directly see in Fig. 43 that the decay length of the magnon transmission ratio at small I_1 is much shorter than the decay length of the magnon transmission ratio at large I_1 (spin diode regime). This illustrates experimentally that each of the two fluids has different decay length with $\lambda_T \ll \lambda_K$. These are fitted by varying $\Sigma_K/(\Sigma_K + \Sigma_T)|_d$ while maintaining the other parameters in Eq. (1.97-1.109). The fits are shown as the solid line in Fig. 43(a,c). The fit parameters are set according to the values indicated in Table.5.1.

By means of the analysis, we obtained the amplitude and proportion of high-energy vs. low-energy magnons as a function of d that are summarized in panel (b) and extract the two decay lengths $\lambda_K = 1.5$ μm and $\lambda_T = 0.4$ μm respectively. We thereby confirm the short-range nature of the high-energy magnons and the much longer range of the low-energy magnons. We note that the shortest decay length is of the same order of magnitude as the spatial resolution of standard nanolithography techniques, the regime of magnon conservation could probably never be achieved in lateral devices. Note that there is the discrepancy that the vanishing of I_2 occurs slightly before T_c. We will show that this occurs systematically on all our samples (see subsection *3*). The same analysis applied to the YIG film with the larger thickness (panels (c,d)) reveals an identical behavior of

Table 5.1: *Fitting parameters by Eq. (1.110).*

	t_{YIG} (nm)	n_{sat}	$T_c^\star$ (K)	I_{th} (mA)	λ_K (μm)	λ_T (μm)	$\Sigma_{K,0}^{L\to R}$	$\Sigma_{T,0}^{L\to R}$
YIG_A	19	4	495	8	1.5	0.4	5 %	37 %
(Bi-)YIG_B	25	11	480	3	3.8	0.5	4 %	39 %
YIG_C	56	4	515	8	1.9	0.6	3 %	15 %
YIG_D	65	4	545	8				

the high-energy magnons, whereas the decay of the low-energy magnons is slightly slower with $\lambda_K = 1.9$ μm.

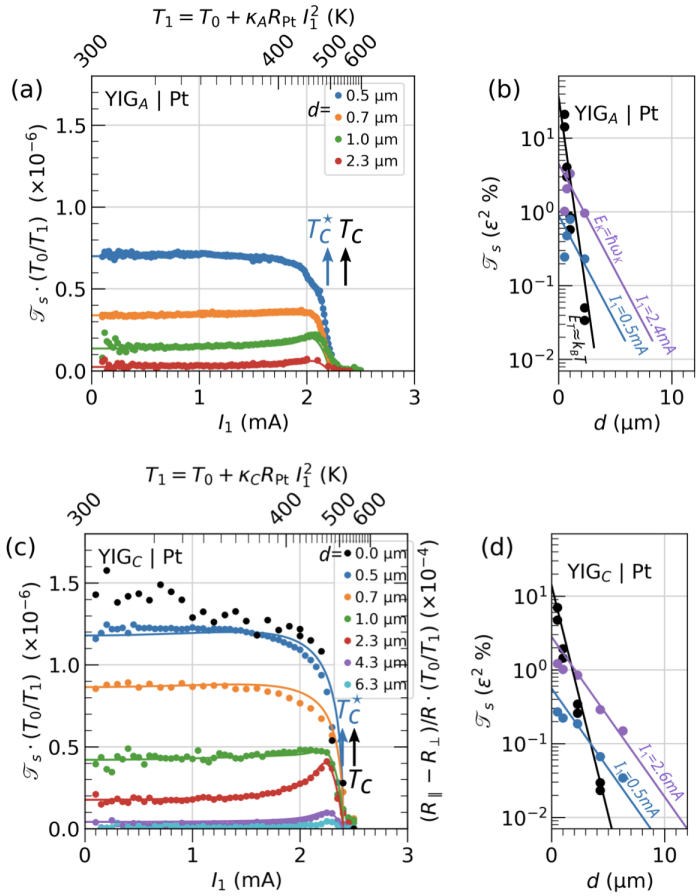

Figure 43: *Double exponential spatial decay of the magnon transmission ratio. (a,c) Current dependence of magnon transmission ratio for (a) the 19 nm thick YIG_A and (c) the 56 nm YIG_C thin films. Solid lines are a fit by Eq. (1.110), with the sole variable parameter the value of $\Sigma_K/(\Sigma_K + \Sigma_T)|_d$. For the YIG_C sample, we have added in panel (c) the variation of the spin magneto-resistance (right axis), which corresponds to the conductivity at $d = 0$. Spatial decay of the magnon transmission ratio for (b) YIG_A and (d) YIG_C,respectively. In both cases the decay of high-energy magnons follows an exponential decay with characteristic length $\lambda_T = 0.4$ μm. The decay of low-energy magnons on the other hand follows for the thinner film (b) an exponential decay with characteristic length $\lambda_K = 1.5$ μm and for the thicker film (d) an exponential decay with characteristic length $\lambda_K = 1.9$ μm.*

We do not see obvious enhanced transmission ratio in thinner film (YIG_A) even though Eq. (1.105) in the previous chapter predicts inverse proportionality as experimentally observed previously [117], which can be attributed to difference in material quality. Despite that, an interesting feature observable when comparing Fig. 43(a) and (c), is that the ratio of low-energy magnons compared to high-energy magnons increases with decreasing film thickness. This can be ascribed to an increase of the cut-off wave-vector where magnons behave bi-dimensional, and thus the spectra extend where the density of state remains constant, which favors the exposure of the growing occupation of low-energy magnons. The higher decay length in the thicker film is further coherent with the longer propagation distance expected for ballistic low-energy magnons, whose propagation range is set by the film thickness. The enhancement however is not in the ratio of the thickness suggesting that some other undefined processes are also at play in this decay.

We stress that the shape of the decay observed in Fig. 43(b) and (d) corresponds to a double exponential decay with two different decay lengths in unprocessed data. This reinterprets the double decay behavior reported in previous non-local transport measurements [113, 117, 131, 234]. The interpretation presented in this work is distinct from the one proposed by Cornelissen *et al.*, where it was associated with the boundary condition of the diffusive problem [113]. We note that while changing the current bias I_1 can affect the proportion between the two fluids but does not alter the decay length as shown in purple lines in panel (b,d). The obtained decay lengths are in rough agreement with the expected decay length of these two populations as discussed in Sect.1.2.4 in chapter 1.

We note that our value of λ_K seems to be dependent on the thickness and anisotropy (see Table.5.1). This contradicts the behavior observed in thicker films ($t_{\mathrm{YIG}} > 200$ nm) where the value was reported independent of the film thickness [117]. The latter observation might be coherent with assigning the dominant low-energy propagating magnons to the mode $\overline{E}_K$ (orange dot in Fig. 15). We believe that the group velocity there is weakly dependent on t_{YIG}, at least for thick films (see discussion above). We should emphasize at this stage, that our report does not cover the same dynamical range as the ones reported in thicker films due to the smaller signal to noise ratio. It may be possible that a third exponential decay could appear at a much lower signal. One possible explanation for the long-range behavior could be that the angular momentum is carried by circularly polarized phonons, which have been found to have a very long characteristic decay length in the GHz range [235, 236].

Finally, it is useful to quantify the spin current emitted by STE as shown in panel (b,d). Renormalizing the transmission ratio coefficient $\mathscr{T}_s$ by the product of spin transfer efficiency at emitter and collector, $\epsilon_1 \cdot \epsilon_2$ (see Table 4.1 in the previous chapter, we observe that only 10% among generated magnon reach a collector placed at $d = 0.2\,\mu$m away. This percentage increases to 15% by extrapolating the decay to $d = 0$, which represents the proportion of *itinerant* magnon among total generated, and there are roughly one order of magnitude ($\times 14$) more high-energy magnons than the low-energy magnons below the emitter. Taking into account the fact that magnons can escape from both sides of the emitter, while we only monitor one side, one can estimate that 70% of generated magnons remain localized. This *localization* is the consequence of three combined effects that impinge principally on the low-energy magnons: *i)* STE favors principally an increase of the density at the bottom of the magnon manifold, which has zero group velocity *ii)* STE, as an interfacial process, couples efficiently to surface magnetostatic modes [237], which are magnons propagating parallel to the wires *iii)* the nonlinear frequency shift associated with the demagnetizing field [77] produces a band mismatch at high power between the region underneath the emitter and outside, which prevents the propagation of magnons (see the previous chapter 4). The spatial localization could be induced either by the thermal profile of Joule heating [119] or by the self-digging bullet modes [104, 122, 124]. This rational affects mainly the magnons, whose wavelengths are shorter than the width

of the Pt electrode.

Further confirmation is the variation of proportion between low-energy magnons and high-energy magnons with the uniaxial anisotropy. When the latter compensates the out-of-plane depolarization field, we observe a suppression of low-energy magnon confinement and the transmitted signal at a large distance (10 μm) fully replicates the variation of low-energy magnons under the emitter.

5.3.3.2 Thin films with isotropically compensated demagnetizing effect

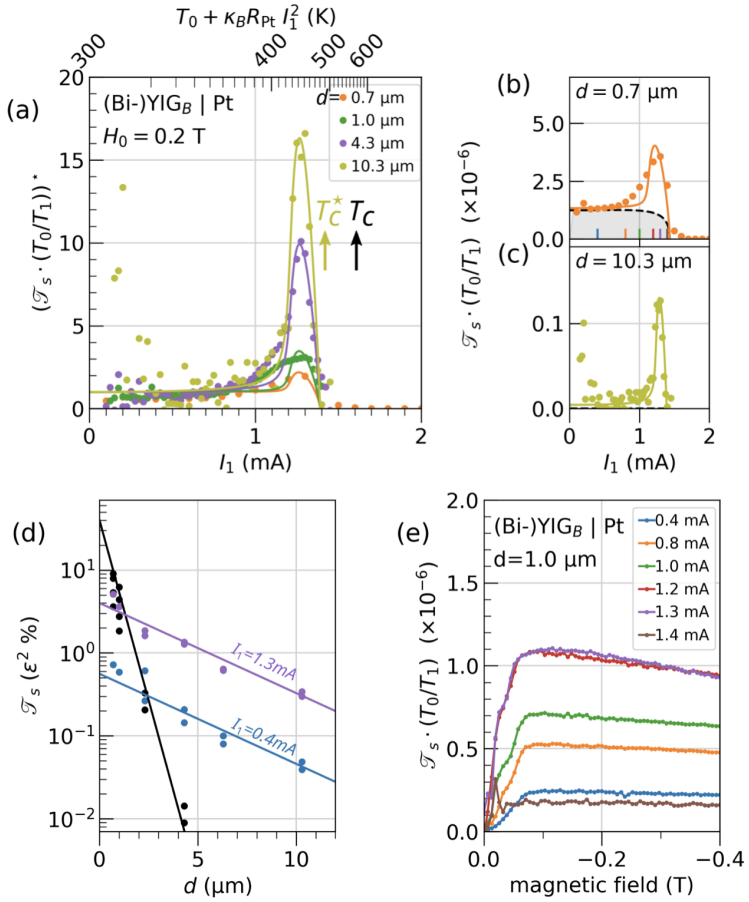

Figure 44: *Two-fluid behavior in thin films with isotropically compensated demagnetizing effect ($M_{eff} = 0$). (a) Variation of the spin diode signal $\mathscr{T}_s$ measured in $BiYIG_B$ for different separation d between emitter and collector. The main panel (a) shows the normalized magnon transmission ratio as a function of T_1, while the side panels on the right show the corresponding current dependence for (b) $d = 0.7$ μm and (c) $d = 10.3$ μm. Solid lines are fits by Eq. (1.110), with the sole variable parameters, Σ_K and Σ_T representing the fraction of low-energy and high-energy magnons. (d) Spatial decay of the two-fluid model separating the high-energy and low-energy magnons contributions. The observed decay can be accounted by a short decay $\lambda_T \approx 0.4$ μm high-energy magnon contribution (k_BT, black line) and a long decay $\lambda_K \approx 4.0$ μm low-energy magnon contribution ($\hbar\omega_K$, magenta and blue lines). The data at $I_1 = 1.3$ mA show the decay behavior in the condensed regime. (e) Magnetic field dependence of the normalized magnon transmission ratio at different currents.*

In this section we will elucidate the influence of self-localization on the saturation threshold n_{sat} that we introduce in our analytical model. To that end, we have repeated the experiment on a Bi-YIG$_B$ sample. This material has a uniaxial anisotropy that matches the saturation magnetization (see Table. 4.1 in the previous chapter). As a consequence, the Kittel frequency follows the paramagnetic proportionality relationship $\omega_K = \gamma H_0$ (similar to the response of a sphere), where the value of ω_K is independent of M_T and cone angle of precession, and therefore it exhibits vanishing nonlinear frequency shift [77,79,103] (see further discussion in the previous chapter 4). We call this as an isotropically compensated material. We emphasize, however, that although the nonlinear frequency shift is zero, the system is still subject to saturation effects [73]. The compensation of the out-of-plane demagnetization factor only eliminates the ellipticity of the trajectory produced by the finite thickness but does not eliminate the self-depolarisation effect of the magnons on itself. The latter depends on the angle between the propagation direction and the equilibrium magnetization direction, being the origin of the broadening of the magnon manifold.

As shown in Fig. 44(a) the nonlinear behavior of $\mathscr{T}_s$ observed in the Bi-YIG$_B$ sample is qualitatively similar to the YIG$_C$. However, quantitatively the size of the spin diode effect is more pronounced in the prior case. This is particularly striking by working at long distances. Comparing Fig. 44(b) ($d = 0.70$ μm) with Fig. 44(c) ($d = 10.3$ μm), for the former the conductivity can be enhanced by an only factor of 3 with respect to its initial value whereas for the latter it can be enhanced by a factor of 15. It is again thanks to filtering out the background from high-energy magnons: in the large distance case the contribution from low-energy magnons is more pronounced. Recalling that in YIG$_C$ the conductivity was enhanced by a factor of 7 by low-energy magnons (see $d > 4.3$ μm data in Fig. 43(c) or Fig. 35 in the previous chapter), here a larger fitting parameter of $n_{\text{sat}} = 11$ is used in Bi-YIG$_B$ whereas $n_{\text{sat}} = 4$ in YIG$_C$, indicating a larger threshold for saturation. This is consistent with the suppression of the nonlinear frequency shift, which affects the long wavelength spin-wave in YIG$_C$ sample. This result suggests that removing the self nonlinearity on the long wavelength magnons improves the ability to generate more propagating magnons. It can also be understood as removal of the self digging process beneath the emitter in pure YIG samples. The fit parameters are listed in Table.5.1. Note that the discrepancy between T_c and $T_c^\star$, which marks the drop of $\mathscr{T}_s$, is even more pronounced in this system. The drop occurs 70 K below T_c. We will come back to this point in the last subsection.

In Fig. 44(d), we plot the spatial decay of $\mathscr{T}_s$ renormalized by ϵ^2 obtained from fits with Eq. (1.110) in percentage for high-energy magnons in black, low-energy magnons at $I_1 = 0.4$ mA ($\mu_m \ll E_g$) in blue and $I_1 = 1.3$ mA ($\mu_m \approx E_g$) in purple. The two decay lengths are $\lambda_T \approx 0.4\mu$m for high-energy magnons, matching with the findings in YIG, as well as a much larger value of $\lambda_K = 4$ μm of low-energy magnons. The latter value is similar to the decay length of magnetostatic magnons observed by BLS in these films [103].

For the sake of completeness, we plot in Fig. 44(e) the magnetic field dependence for different I_1. The drop of the signal at zero field is due to the residual out-of-plane anisotropy, forcing the magnetization to be along the film normal, which leads to no STE applied from Pt. The magnon transmission ratio becomes maximum near 0.05 T, which is the saturation of effective magnetization for BiYIG. The field dependence at a larger field than 0.05 T becomes significant for the current values near the emergence of a peak in (a) at $I_1 = 1.3$ mA, where the conductivity of low-energy magnons reaches the highest. As noted in a previous study [56] the fact that we see a dependence with magnetic fields is direct evidence that we are dealing here with low-energy magnons. Here the extra sensitivity of $\mathscr{T}_s$ to changes in $\mathcal{I}_{\text{th}}$ near I_{pk} as discussed above in the context of describing the behavior of Fig. 39 is here clearly illustrated with the BiYIG sample.

5.3.3.3 Discrepancy between T_c and $T_c^\star$

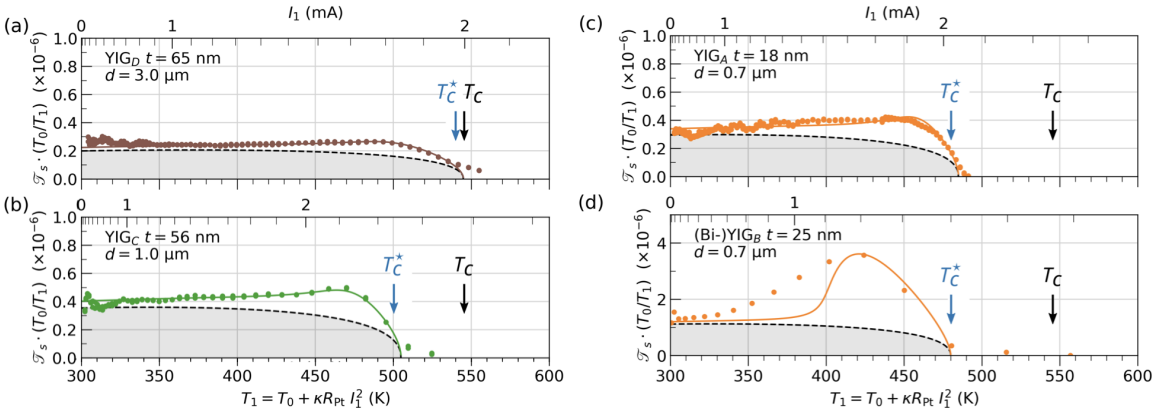

Figure 45: *Dependence of $T_c^\star$ on the thickness of YIG films. Comparing non-local devices with about the same ratio of high-energy magnons to low-energy magnons at $I_1 \to 0$. We observe an increase of $T_c - T_c^\star$ with decreasing film thickness, suggesting an increasing influence of low-energy magnons at high power $I_1 \to I_c$ as the film thickness decreases.*

Finally, we discuss the disappearance of the magnon transmission ratio already at $T_c^\star$ well below the experimentally determined T_c (see Fig. 31). We note in Fig. 43 and Fig. 44 that all curves collapse at the same value independently of d. This clearly points out an issue that concerns exclusively the region under the emitter since there is a lateral temperature gradient. To that end, we summarize the normalized magnon transmission ratio for YIG samples as a function of the emitter temperature T_1 in Fig. 45 with different thicknesses. To avoid any influence of thermal gradients, we have selected devices, whose separation d leads to a similar ratio between Δn_T and Δn_K. This requires to increase d as the film thickness increases, suggesting a decreasing contribution of low-energy magnons. We speculate that collapse can either be caused by the onset of strong electron-magnon scattering as the YIG film becomes conducting [105, 150], or from a reversal of the equilibrium magnetization beneath the emitter that becomes aligned with the injected spin direction [122, 230]. For the latter case, the magnetization below the emitter and collector are opposite, suppressing any spin transport. This process is consistent with assuming that a large portion of the injected spins remains localized. This process is also consistent with the decrease of $\overline{\mathscr{V}_2}$ observed at large I_1, where now the electrical current decreases the effective temperature of the spins system (decrease fluctuations) despite the fact that $I_1 \cdot H_x < 0$.

We review the other hints that support this picture. If one compares the discrepancy between the $T_c^\star$ and T_c between the different samples, one can clearly see on the data in Fig. 45 that the discrepancy increases with decreasing film thickness, as expected for an increased surface effect of STE and reduced volume of polarized spins. Another hint is the fact that the largest discrepancy is observed on films with large uniaxial anisotropy as shown in Fig. 44(a). This is in agreement with the observation made on nano-device on the switching of the magnetization direction by the spin Hall effect [16]. Nevertheless, the discrepancy seems to not scale simply with t_{YIG} in our observation, this suggests that there might be additional phenomena at play, which is responsible for the vanishing magnon transmission ratio at a high temperature, while the system is still in its ferromagnetic phase (see also discussion of Fig. 33 in the previous chapter).

We have tentatively computed I_f, the critical current required to flip the magnetization. We call $n_{\mathrm{sat}} = VM_1/(\gamma\hbar)$ the total number of spins that remain polarized beneath

the emitter. We compare this with the number of injected spins within the spin-lattice relaxation time, which is $I_f\epsilon/(2e\alpha_{\mathrm{LLG}}\omega_K)$. Equalizing the 2 quantities, we find that $I_f = 2.5$ mA for YIG$_A$ samples. According to the upper scale of Fig. 43, T_c is reached when $I = 2.7$ mA. Using Fig. 31, we can compute the difference of temperature produced by Joule heating between these two values, and the result is about 65 K. This is very close to the shift of 50 K observed experimentally on this sample.

While there are indications that a switching occurs, and the number roughly matches the expected figures, the above paragraph is still at this stage rather speculative and a direct proof is still missing. For the sake of completeness, it is worth mentioning that there might be alternative explanations. One possibility is a lowering of T_c in the region below the Pt. The origin of such an effect could be the interdiffusion of Pt atoms inside the YIG at the interface. More thorough systematic studies will be required to clarify this point.

5.4 Conclusion

Through these two chapters 4 and 5, we expose a comprehensive picture of the magnon transport in extended magnetic insulating films that encompasses a wide range of current and magnetic field bias, substrate temperature, as well as non-local geometries with varying propagating distance. The picture of the two-fluid model expressed in the previous chapter completed by a picture of the nonlinear behavior of low-energy magnon expressed in the previous chapter 4 is formulated analytically and it is supported by a series of different experiments that include non-local transport on different thicknesses of YIG thin films with different garnet composition, different interfacial efficiency, as well as different thermalization. While providing a comprehensive study on these materials, our model accounts for almost all the experimental observations within this common framework.

What the analytical model allows to do is:

i) to describe the expected signal in the linear regime [Eq. (1.105)] in the previous chapter 4]

ii) to well fit the non-local transport data on the whole current range and for different separations between the electrodes using very few parameters ($\mathcal{I}_{\mathrm{th},0}$, n_{sat}, $T_c^\star$, λ_T, λ_K, Σ_T and Σ_K)

iii) to incorporate all relevant physical effects: effect of Joule heating on M_1, a divergent form of magnon-magnon relaxation.

What it doesn't do, but could be important:

i) to take into account the propagation properties (propagation angle, group velocity, mode selection by the electrode geometry, spatial variation of these properties due to the temperature gradient) of the magnons excited under the injector to know how they contribute to the signal under the detector.

ii) to take into account nonlinear magnon-localization effects under the injector (for YIG in particular).

iii) to take into account the effects of temperature on damping, exchange constant (and thus group velocity), pumping and detection efficiency.

The fact that these points are not taken into account directly, and that the fits are excellent, means that these effects are effectively deployed in the other ingredients of the

model. In particular, Eq. (1.106) of the relaxation in the previous chapter is very generic and can absorb many different physical effects, hence the effectiveness of the model.

We assume in this chapter that low-energy magnons propagating in the ballistic regime lead to a magnon transconductance that follows an exponential spatial decay in thin film geometries. This argument derives from the experimental finding that in all BLS experiments monitoring the low-energy part of the magnon manifold, the amplitude of the signal follows an exponential decay. Nevertheless, the transport behavior in the clean limit, where the magnon mean free path is greater than the sample boundary is in itself a very interesting research direction.

Another remaining open question concerns the premature collapse of the signal at $T_c^\star$. We have tentatively explained it as a potential switching of the magnetization direction beneath the emitter. However, direct evidence of such a process remains elusive. We think that spin transport in material with low magnetization or close to the paramagnetic phase are both very interesting subjects.

Finally, we summarize the main finding of our two-fluid model, which separates low-energy magnons from high-energy ones. This allows to propose an alternative explanation for the measured variation of the magnon transmission ratio with distance as emanating from a double exponential decay. Each of the fluids has its own transport characteristics which are expressed by two different propagation lengths. This attributes a decay length in the submicron range to the high-energy magnon and a decay length above the micron to the low-energy magnons. This explanation implies that even in the short-range regime, the magnon number is neither a conserved quantity and thus any analogy with electronic transport should take into account this rapid decay. Despite the fact that the model encompasses several parameters, there are still remaining open questions. The similarity of the decay of SSE and STE current with d needs to be reconciled with our finding. The alternative is that low-energy magnons participate in the SSE transport at the long range. Although the amount of quanta carried is in clear disfavor $E_T/E_K \sim 10^3$ of the latter, we should keep in mind that we are looking here at a tiny signal. The role of acoustic phonons [235, 236] in this process is still unclear. Recent experiments have shown that they are strongly coupled to magnetostatic magnons and they also benefit from a very low decay rate. Of particular interest is the contribution of circularly polarized acoustic phonons, which have been shown to be strongly coupled to long wavelength spin-waves while allowing the transmission of angular momentum on large distances.

Chapter 6

Amplified transport of low-energy magnons in Bi-doped YIG by local heating

It has been known for a long time that doping YIG with heavy elements can induce a uniaxial perpendicular magnetic anisotropy [125, 238–240]. The difficulty is to maintain the ultra-low damping. The substitution that achieves both the best is doping with Bismuth. As discussed in the previous chapters, the perpendicular uniaxial anisotropy contributes to the reduction of the demagnetizing field and it promotes circular magnetic precession when the compensation is full. It diminishes the non-linear effects such as the non-linear frequency shifts or parametric instability processes [25, 107], leading to an efficient population of magnons in a given mode [77, 103]. Therefore those materials are of particular interest in the context of magnon transport devices. There have been several attempts to handle the property of the transport by inserting a third electrode between the emitter and the collector to enhance its functionality. For example, previous studies used Py to absorb or pass magnons depending on the direction of its magnetization [241–243], or used Pt to provide additional SOT and to electrically control the effective damping of magnons [79, 109, 114, 184, 219]. In regard to also this point, YIG with a uniaxial anisotropy has been reported to be more advantageous to control the transport [79]. However such additional deposition of metal on the propagation path may absorb magnons, which reduces the detected signals by itself and constitutes a clear drawback to these approaches. In this chapter we demonstrate that using Bi-doped YIG, a significant enhancement of the low-energy magnons emitted by the spin transfer effect is observed by heating up locally the collector electrode. We utilized a heating electrode placed above the collector which is free from contact with the garnet layer. The idea stems from the analytical expression of the transmission ratio for low-energy magnons found in Eq. (1.105) of chapter 1

$$\mathscr{T}_K|_{I_1\to 0} \propto \mathrm{e}^{-d/\lambda_K} \cdot \epsilon_1\epsilon_2 \cdot \frac{k_B T_1}{\alpha_{\mathrm{LLG}}\hbar\omega_K} \cdot \frac{\sigma_{\mathrm{Pt}} w_2}{G_0} \cdot \frac{(\gamma\hbar)^2}{M_1 M_2 t_{\mathrm{YIG}} w_1 t_{\mathrm{Pt}} V_1}. \tag{6.1}$$

One could increase the signal simply by reducing M_2 in the denominator in Eq. (6.1), where M_2 is the magnetization under the collector. Note that this expression comes from the approximation of the precession cone angle $\Delta M/M \approx \sin^2\theta \approx \theta^2$, which appears in the formula of the spin pumping voltage [115]. Thus in the following, we aim at increasing the ISHE voltage by locally increasing the cone angle at the collector when the heater is switched on. Experimentally we observe a 3.4 times amplification of the transmission efficiency by heating the collector to about 380 K.

6.1 Device structures and characteristics

A 21 nm $Bi_1Y_2Fe_5O_{12}$ (BiYIG) film is deposited by pulsed laser deposition on sGGG(111) substrate. The emitter (Pt_1) and collector (Pt_2) electrodes have 300 nm width and 7 nm thick with 3 μm separation patterned by electron beam lithography. The distance is long enough to filter out the contribution of the high-energy magnons. On top of them, a 20 nm of an insulating Si_3N_4 layer is deposited by rf sputtering. After that, we pattern a 400 nm width Ti(5nm)/Pt(30nm) electrode which is placed exactly on top of the collector (Ti/Pt_3). This electrode is in thermal but not in electrical contact with the collector. It will be used to modulate the local temperature of it. The SEM image of the final device is shown in Fig. 46(a). The wires colored in red, yellow, and green correspond to the emitter, collector, and modulator respectively. The inset represents a schematic cut of the device, which emphasizes that the Ti/Pt_3 is electrically isolated from Pt_2 by the Si_3N_4[1]. To begin with, as shown in the inset of Fig.46(b), we measure the temperature dependence of the Pt_2 resistance R_2 in a variable temperature cryostat. This allows to obtain $\zeta = \partial_{T_2} R_2 / R_2^0 = 1.14 \times 10^{-3}$ /K, where R_2^0 is the resistance of the collector Pt_2 at the initial temperature and $\partial_{T_2} R_2$ is the corresponding change of the resistance upon an increase of the local temperature. Then we characterize the Joule heating generated by Ti/Pt_3 electrode. This is achieved by monitoring R_2 while a small bias current (0.1 mA) is injected in Ti/Pt_3. The experiment is performed at room temperature. The value of the relative resistance change $\Delta R_2/R_2^0$ and the corresponding temperature rise ΔT_2 are shown at the left and right axis of Fig.46(b) respectively, showing that $I_3 = 3$ mA gives 77 K of temperature rise at Pt_2 (orange dots). Similarly, the Joule heating generated by applying an electric current I_2 directly in Pt_2 (identical with Pt_1) is studied, showing that $I_2 = 1.5$ mA increases T_2 by 150 K (blue dots). Finally, T_2 as a function of I_2 or I_3 is obtained and is well fitted by simple quadratic expressions (solid lines).

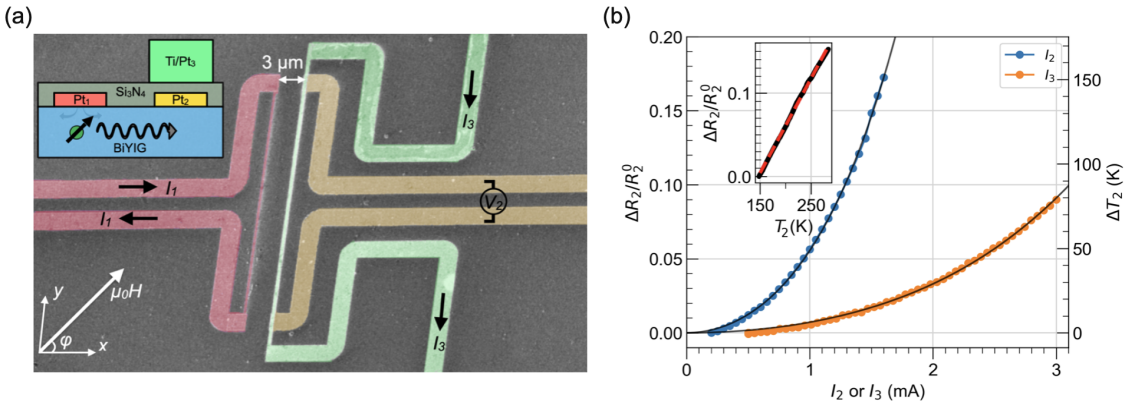

Figure 46: *(a) SEM image of the device. The wires illustrated in red, yellow, and green correspond to the emitter, collector, and temperature modulator respectively. The inset is a schematic cut of the device. (b) Measurement of temperature rise produced by Joule heating in the collector and the modulator. The left axis is the relative change of the resistance of the emitter and the right axis is the corresponding temperature rise whose temperature coefficient is obtained as shown in the inset. The solid lines are fits with a quadratic function.*

To characterize the magnetization of the BiYIG film, we perform SQUID-VSM mea-

[1]To have a better interfacial quality between the BiYIG and Pt, the local Joule annealing is performed by injecting 1.5 mA in Pt_1 and Pt_2 for 1 hour after device fabrication [216].

surements with the help of Dr. Thomas Hauet at Université de Lorraine in Nancy, France. The magnetization as a function of the temperature is plotted in Fig. 47(a), determining the value at room temperature as 0.14 T and the Curie temperature as 560 K. The dashed line is the fit with the power law formula $\mu_0 M(T) = \mu_0 M_s(1-(T/T_c)^a)^b$. The best fit is obtained with $\mu_0 M_s = 0.14$, $a = 6$ and $b = 0.6$[2]. We also performed ferromagnetic resonance measurements to determine the effective magnetization $\mu_0 M_{\text{eff}} = \mu_0(M_s(T) - H_{\text{anis}})$, where $\mu_0 H_{\text{anis}}$ is the anisotropy field. It was obtained by studying either the frequency or angular dependence of the resonance field $\mu_0 H_{\text{FMR}}$. The schematic of the measurement is illustrated in Fig. 47(b), where the sample is placed on a microwave stripline that generates an in-plane radio frequency field. The detection of the resonance is made by measuring the inverse spin Hall effect (ISHE), in the Pt_2. Fig. 47(c) shows the angular dependence of the resonance field at a fixed frequency 4.762 GHz at room temperature. Using the Kittel formula and the gyromagnetic ratio $\gamma = 28.5$ GHz/T, one can calculate $\mu_0 H_{\text{FMR}}$ and can infer the effective magnetization. The value of the fit gives 46 mT. We obtained $\mu_0 H_{\text{anis}} = 94$ mT, which is equivalent to 68% compensation of the $\mu_0 M_s$ value.

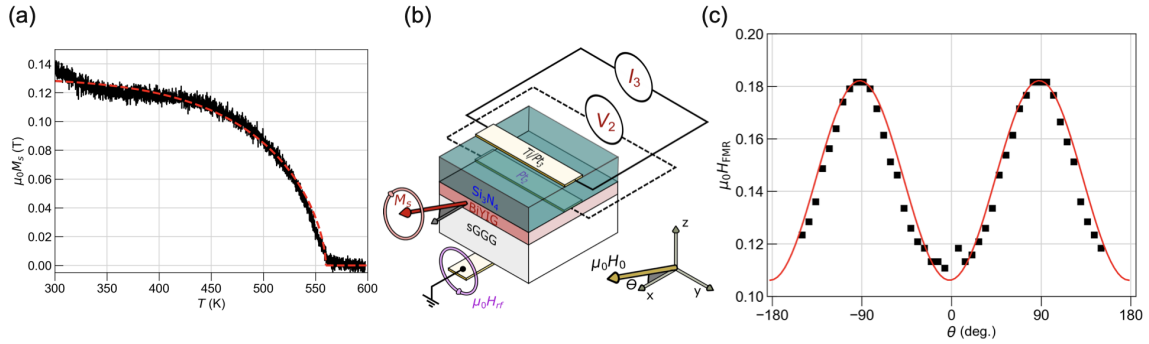

Figure 47: *(a) SQUID-VSM measurement of the magnetic film. From the curve, one can determine determining the magnetization at room temperature (0.14 T) and the Curie temperature (560 K). The dashed red line is a fit with power law* $\mu_0 M(T) = \mu_0 M_s(1-(T/T_c)^a)^b$. *The result of the fit is discussed in the main text. (b) Schematic of spin pumping measurement. The sample is placed on a microwave stripline and the radio frequency field is applied transverse to the static field. The ISHE voltage in* Pt_2 *is monitored while sweeping the magnetic field at a fixed frequency. (c) The polar angle dependence of the ferromagnetic resonance field* $mu_0 H_{\text{FMR}}$ *at 4.762 GHz frequency. The red solid line is a fit with the Kittel formula, giving the effective magnetization.*

Next, we measure the longitudinal spin Seebeck effect (LSSE) [46,47,244] by monitoring the voltage V_2 at Pt_2 generated through ISHE while applying a vertical temperature gradient. It is produced by applying the current I_3 in Ti/Pt_3. In this experiment, an external magnetic field $\mu_0 H_x$ is applied along x. As illustrated in Fig.46(a), the x and y are the in-plane directions perpendicular and parallel to the electrodes axis respectively. Fig.48(a) presents the LSSE signal V_2 as a function of $\mu_0 H_x$ under different values of I_3. The estimated value of the effective magnetization of BiYIG from the saturation field is about 43 mT, which agrees with the result of FMR measurements in Fig.47(c). We confirm the quadratic rise of the LSSE voltage V_2^{SSE} as a function of I_3 due to the Joule heating as shown in Fig.48(c), where the red dashed curve is a fit with a square function.

[2]Here it does not ensure the validity of the parameters at temperatures lower than 300 K.

The amplitude of LSSE voltage shows no difference between $\pm I_3$, however, a slight shift of the curves appears due to the Oersted field $\mu_0 H_{Oe}$ along x. it is calculated from the zero intercept of the hysteresis curves of V_2 vs $\mu_0 H_x$ as shown in the inset of the panel (a). Fig.48(b) shows the extracted $\mu_0 H_{Oe}$ as a function of I_3. A linear fit yields the slope 0.45 mT/mA (see the red dashed line). We notice on offset voltage. This is ascribed to an electrical current leakage from Ti/Pt_3 to Pt_2. This leakage is 5 μV for $I_3 = 1.2$ mA, which corresponds to 1 nA electrical current conduction in Pt_2 whose resistance is 4 kΩ. Later it will be assumed to be small enough to avoid additional spin orbit torque injection to BiYIG layer to modify the magnetic damping.

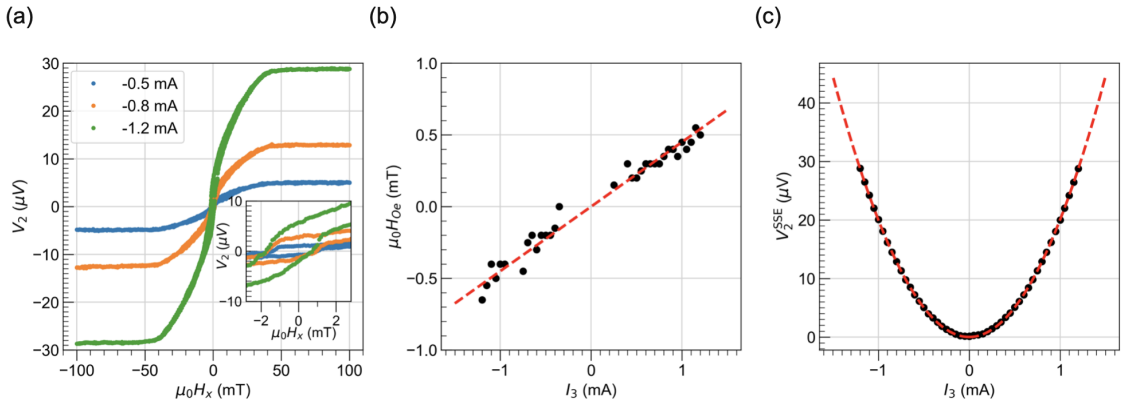

Figure 48: *Measurements of the longitudinal spin Seebeck effect. I_3 is the current in Ti/Pt_3. The corresponding Joule heating generates a vertical temperature gradient, which in turn creates the voltage (V_2) in Pt_2 from the LSSE. (a) V_2 as a function of external magnetic field along x under different values of I_3. The inset is a zoom near zero field, which shows the shift of the magnetic hysteresis curves produced by Oersted field. (b) Estimation of the Oersted field is inferred from the hysteresis shown in the inset of the panel (a). The dashed line in (b) is a linear fitting. Panel (c) shows the LSSE voltage V_2^{SSE} as a function of I_3. It displays the expected quadratic dependence.*

6.2 Enhancement of low-energy magnon fluctuation

We now proceed to the non-local geometry. We investigate the influence of the collector temperature on the magnon transport. Under an in-plane external magnetic field, an electrical current I_1 is applied to Pt_1 and the voltage $\mathscr{V}_2$ of Pt_2 is monitored to generate and detect magnons via the spin transfer effect (STE)[3]. Fig.49(a,b,c) show $\mathscr{V}_2/R_2$ as a function of I_1 under 60 mT external field along x (red), $-x$ (blue) or y (grey) at $\Delta T_2 = 0$ K ($I_3 = 0$ mA) and $\Delta T_2 = 77$ K ($I_3 = \pm 3$ mA) respectively. Here the normalization by the resistance is to integrate the corresponding increase of resistance as a function of temperature. Basically, it shows a parabolic rise with I_1, suggesting that the main signal is produced by the SSE at Pt_1 where generated high-energy magnons diffuse to Pt_2. They have an even symmetry in I_1 due to the origin of the effect which is proportional to

[3]We use the pulse delta method using a Keithley 6221/2182A pair to pick up the contribution from I_1 dominantly. The pulse duration and duty cycle are fixed as 10 ms and 10% respectively. DC continuous current I_3 is kept applied in the modulator Ti/Pt_3 to heat up locally the Pt_2. In this experimental setup, DC background contribution from I_3 such as leakage current or the LSSE is excluded thanks to the three-point reading of the pulse delta method.

Joule heating. Besides that, an asymmetry is present between $\pm I_1$. It is produced by the magnons electrically excited by the STE which has an odd symmetry in I_1. A part of magnons excited by the STE is considered to be low-energy magneto-static magnons which reside close to the bottom of the magnon dispersion relation [97,102,104,110,131,200,245]. The regime of magnon emission and absorption corresponds to $I_1 \cdot H_x < 0$ and $I_1 \cdot H_x > 0$, respectively. Comparing the panel (a) with (b) and (c), it shows that $\mathscr{V}_2/R_2$ for $+H_x$ and $-H_x$ increases when $\Delta T_2 = 77$ K, indicating increased generation of thermal magnons[4]. The offset signal also increases by local heating, which is consistent with the previous observation that the garnet film becomes more conductive at an elevated temperature [105][5].

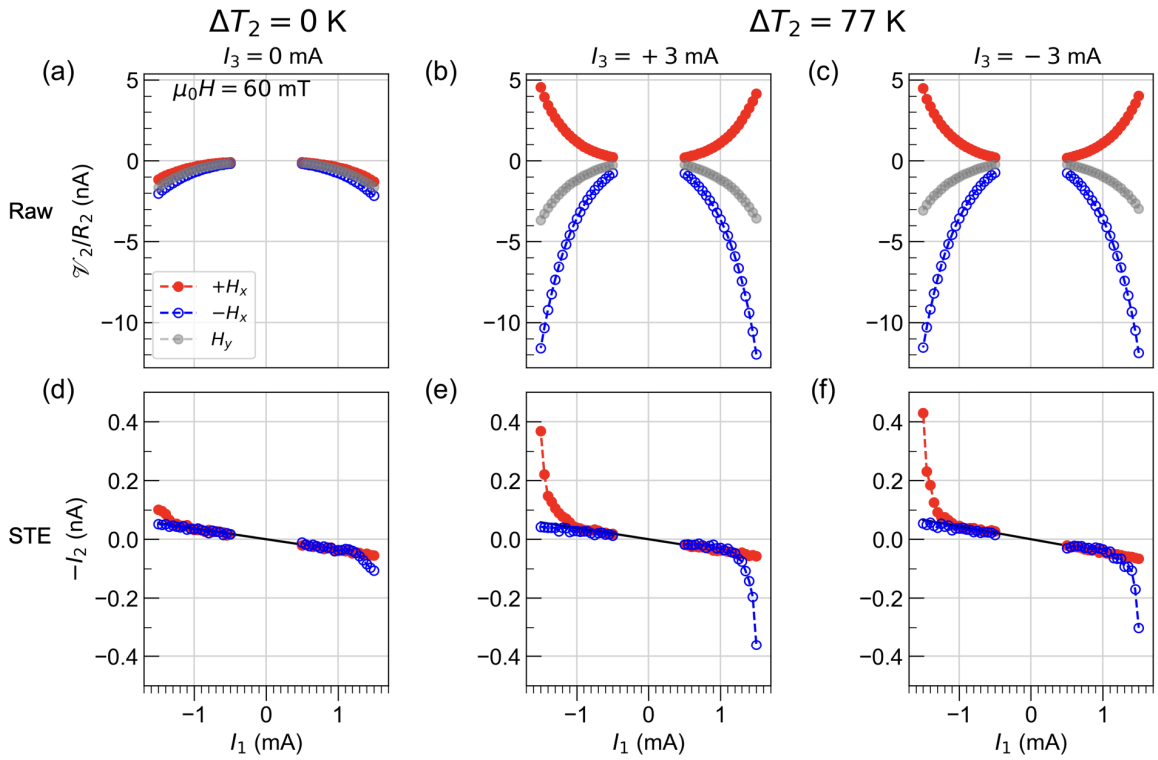

Figure 49: *The effect of local heating on non-local magnon transport. The top row represents the raw data $\mathscr{V}_2/R_2$, the signals normalized by resistance R_2 of Pt_2 under an external magnetic field along $+x$ (red), $-x$ (blue), and y (grey). The bottom row represents $-I_2$, the corresponding contribution from the spin transfer effect. The left column represents the data without local heating $\Delta T_2 = 0$ K. The middle and right columns are data with local heating $\Delta T_2 = 77$ K, where the polarity of the current in the modulator I_3 is positive and negative respectively.*

Fig.49(d,e,f) represent the extracted contribution from spin transfer effect $-I_2$ at $\Delta T_2 = 0$ K ($I_3 = 0$ mA) and $\Delta T_2 = 77$ K ($I_3 = \pm 3$ mA) respectively (For the detailed procedure of the extraction, please refer to chapter 5 section 5.3). Comparing the panel (d) with (e) and (f), an enhancement of the spin diode effect at $|I_1| > 1.2$ mA is

[4]This probably arises due to the increase of non-equilibrium magnons under the emitter which is related to $\mu_0 M_s(T = 0) - \mu_0 M_s(T_2)$. However it is beyond our scope.

[5]The leakage of I_3 to Pt_2 may also be possible as discussed in the previous section, where we do not expect any effects of nA scale current to hamper the magnon conduction.

observed when heating is turned on. The value at the largest $|I_1|$ (1.5 mA) is increased by a factor of 3.4. Most importantly, it is observed regardless of the polarity of I_3 as both panels (e) and (f) show the amplification. We can conclude that the heating rather than the Oersted field or leakage current is the main factor of the modulation[6].

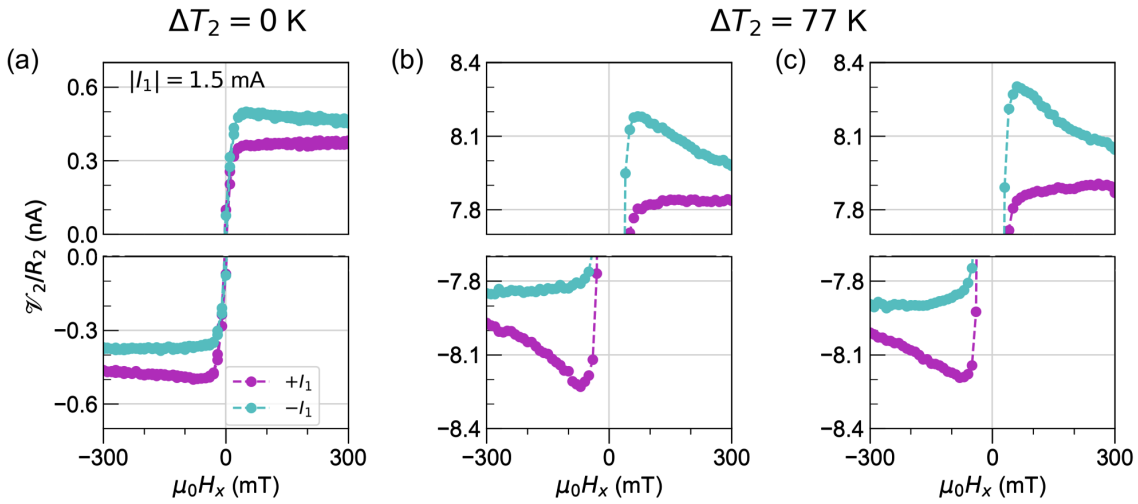

Figure 50: *non-local magnon transport signal without and with local heating as a function of the external magnetic field. (a) Represents data without local heating $\Delta T_2 = 0$ K while (b) and (c) are data with local heating $\Delta T_2 = 77$ K, where the polarity of the current in the modulator I_3 is positive and negative, respectively. Note that the same range of vertical scale is maintained.*

This enhancement concerns low-energy magnons if it shows a field dependence. We have also performed measurements of the variation of V_2/R_2 with the applied magnetic field. Fig.50(a,b,c) show V_2/R_2 as a function of $\mu_0 H_x$ at $\Delta T_2 = 0$ K ($I_3 = 0$ mA) and $\Delta T_2 = 77$ K ($I_3 = \pm 3$ mA) respectively. The intensity of current is $I_1 = \pm 1.5$ mA (magenta and cyan) and we show a zoom near the maximum (top) and minimum (bottom) values for a sake of clarity. The curves show a peak or saturation at around 45 mT revealing the saturation of the magnetization, consistent with Fig.48(a). A finite separation between $+I_1$ and $-I_1$ at $\mu_0|H_x| > 45$ mT is due to magnons produced by the STE and they show dependence on $\mu_0 H_x$ indicated as a slope. It reveals low-energy magnons induced at the forward polarity of I_1 participate in the transport. By heating up the collector in panels (b) and (c), the STE contribution and its field dependence are enhanced regardless of the polarity of I_3. This enhanced field dependence supports the promotion of the itinerant low-energy magnons by the local heating. Application of I_3 shows no large contamination of the signals, confirming the good electrical isolation of Si_3N_4[7].

[6]However in panel (f), one can notice slight asymmetry between the $+H_x$ and $-H_x$ at large I_1 in the forward direction, meaning that the direction of the field is influential. The I_2 is larger when the Oersted field is anti-parallel to the external field. It may be possible that the Oersted field can affect the signal by creating a pocket in the energy landscape (the dispersion curve shifts down when the field is decreased) [246]. Strangely this effect is not observed in the opposite polarity of I_3 (panel (e)), thus this point would not be focused further.

[7]The panel (c) as well shows asymmetry between $+H_x$ and $-H_x$ for the forward direction of I_1 and that the signal is larger when the Oersted field of I_3 is anti-parallel to the external magnetic field.

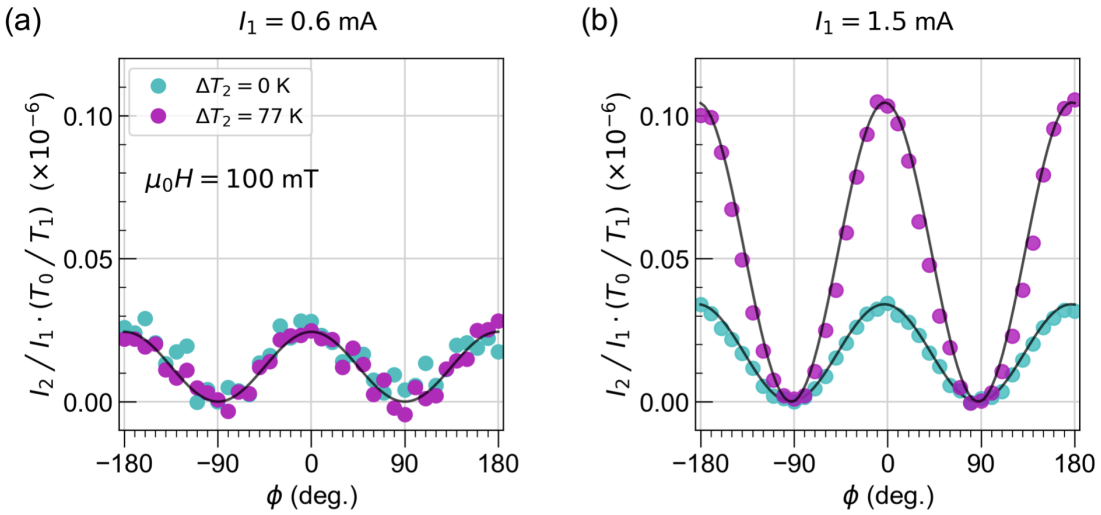

Figure 51: *Measurements of the STE contribution as a function of the angle between the applied external field and the cartesian axis x. They compare without (cyan dots) and with (purple dots) heating. Panel (a) shows the result when I_1 is small. Panel (b) shows the results when I_1 is increased to 1.5 mA. We observe a clear enhancement of the signal when the temperature of the collector is increased in (b).*

Fig.51(a,b) show the angular dependence of the renormalized transmission efficiency I_2/I_1 under 100 mT in-plane magnetic field at $\Delta T_2 = 0$ K (blue) and $\Delta T_2 = 77$ K (orange) for $I_1 = 0.6$ mA (a) and $I_1 = 1.5$ mA (b). The data is renormalized by the ratio T_0/T_1 as explained in chapter 5, where T_0 is the room temperature and T_1 is the temperature at the emitter considering the Joule heating. The solid lines represent the $\cos\phi^2$ fittings, ensuring the valid symmetry for magnons excited by the STE. In (a), it is shown that increasing T_2 does not affect the transmission efficiency for small I_1. However, in (b) for large I_1, almost three times enhancement is revealed by heating up locally the Pt_2. We confirmed that this effect is reversible and repeatable, and that the same enhancement is obtained regardless of the polarity of I_3, supporting again that the enhancement is activated by neither the Oersted field nor the leakage current, but by the heating. Those facts suggest that a large initial population of magnetostatic magnons in the non-linear regime is required to have large amplifications by the local heating.

Next, we plot the amplitude of the $\cos\phi^2$ fit while varying I_1 and ΔT_2. Fig.52(a) shows the transmission efficiency as a function of I_1 at Pt_1 at different ΔT_2 with a field of 60 mT. The efficiency is gradually improved at larger I_1 for all ΔT_2[8]. This effect is more significant when the heater is switched on. At small I_1, it shows more or less a similar value among the 3 different ΔT_2. Then starting from $I_1 = 1.2$ mA, the growth speeds up for $\Delta T_2 = 35$ K (yellow) and $\Delta T_2 = 77$ K (cyan). Finally, at $I_1 = 1.5$ mA, it is 3.4 times larger for $\Delta T_2 = 77$ K than for $\Delta T_2 = 0$ K (magenta). The improvement is more rapid for larger I_1. For $I_1 = 0.6$ mA (blue) , $I_1 = 1.4$ mA (green) and $I_1 = 1.5$ mA (red) at $\Delta T_2 < 40$ K, it more or less follows the dashed line $M_s(T_0)/M_s(T_0 + \Delta T_2)$, the inverse of the normalized magnetization under the collector. However to our surprise, for $I_1 = 1.5$ mA and $\Delta T_2 > 40$ K, it deviates from the dashed line and conduction efficiency reaches 4 times larger values than for $I_1 = 0.6$ mA. One noticeable fact in the high current regime is that a large population of magnons is flowing with a frequency around ω_K and a

[8]Note that the fact that the enhancement is observed for $I_1 = 0.6$ mA here, but not in Fig.51(a) is because magnons produced by STE are more effectively generated under lower external magnetic field even at lower spin injection.

wavelength dominantly in the opposite side of the Kittel mode ($\overline{E_K}$ in Fig.11 in chapter 1). Therefore the flow of magnons has much more monochromatic frequency and wavelength, *i.e.*, much more coherent than in the low current regime. For the coherent transport with quasi-single mode, it efficiently reduces the effective magnetization by the cone angle opening. Considering that the slope in the $M-T$ curve gets steeper at higher temperatures especially near T_c, the effect of local heating to reduce the local magnetization becomes more drastic. Moreover we expect some effects commonly observed in optics, such as formations of standing waves [247].

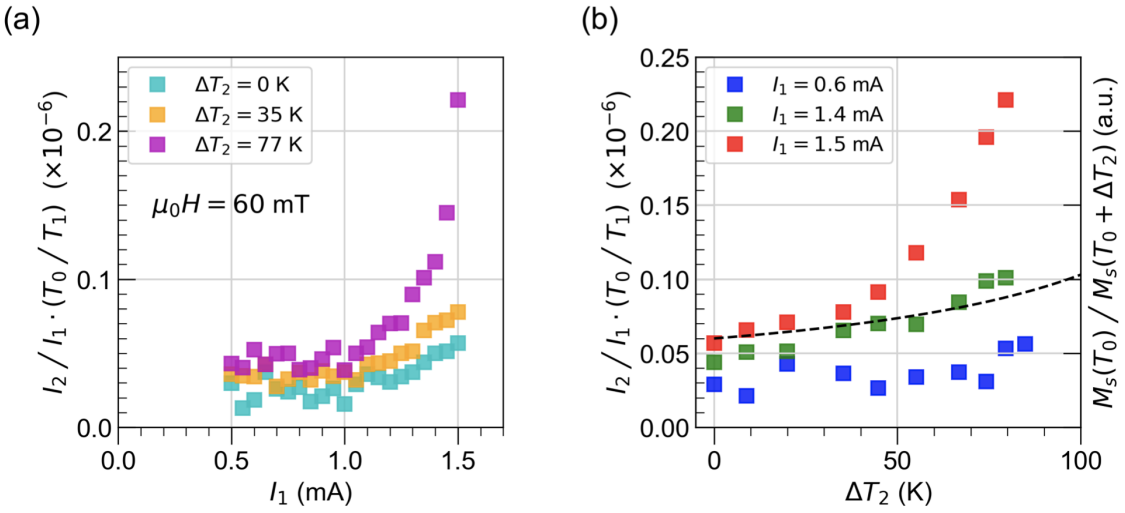

Figure 52: *Evolution of the measured transconductance. Panel (a) is as a function of I_1 for different values of local heating of the collector ΔT_2. Panel (b) shows the variation of the ΔT_2 for different values of I_1. The dashed line in (b) represents the behavior of the normalized magnetization $M_s(T_0)/M_s(T_0 + \Delta T_2)$.*

A related work has been reported where a non-magnetic and non-heavy metal Copper modulator electrode is placed in between the emitter and collector electrodes [248] on YIG (Note that the present experiment differs by the fact that the modulator is not placed on top of the collector). It showed that at a large enough external magnetic field compared to the Oersted field generated by the modulator, the magnon transconductance is not affected by the local heating of the modulator. First of all, this might be simply due to small heat generation (9.9 mJ for our work vs 0.76 mJ for that work) and small spin injection (0.7 TA/m^2 vs 0.1 TA/m^2). Indeed there is barely any effect using small I_3 or I_1 as summarized in Fig.52. Second the position of the modulator should be critical as our intention is to increase the precession cone angle at the collector. Additionally it is possible that the heating generates a localization effect, accumulating the magnons underneath the modulator. On the other hand, the amount of the Oersted field generated by the modulator is almost the same (1.5 mT vs 1.4 mT). It supports our observation that the Oersted field does not play a significant role in the observed amplification[9]. Finally, to

[9]There are several reports showing that inhomogeneous field modulates the dispersion or wave vector of magnons, which leads to the stabilization of Bose-Einstein condensate of parametrically pumped magnons [249] or the interconversion between phonons and surface magneto-static magnons [250]. Indeed the Oersted field with appropriate direction (opposite to static magnetic field) creates a decrease of the local magnetic field and it shifts down the magnon dispersion relation. Thus the propagating magnons may be trapped in the lower energy region, *i.e.* underneath the detector, and it may lead to the accumulation of magnons [246].

compare with the reported technique to modulate the conduction of magnons, the group of Munich in Germany led by Prof. M. Althammer succeeded in enhancing the conduction of magnons by STE by a factor of six [57,79]. Their technique is based on the intermediate spin supply to compensate the damping of itinerant magnons by injecting current in a Pt modulator placed in between the emitter and collector directly on YIG[10]. They reported more efficient modulation by using a material with a perpendicular magnetic anisotropy to facilitate the efficient population of magnons thanks to the favored circular precession, which is consistent with our results. The origin of the enhancement is completely different from their technique and ours. While theirs is asymmetric in I_3, ours is purely based on heating and thus is symmetric in I_3. Our results would propose a new way to control magnon propagation in general.

6.3 Simulation by MuMaX^3

To get insights into the possible origin of the enhancement of low-energy magnon signals observed experimentally, micromagnetic simulations are conducted using the open source software MuMaX^3 [251]. First of all, we study the dispersion curves of a 20 nm film with (BiYIG) or without (YIG) the uniaxial perpendicular anisotropy. Here we express the anisotropy relative to the magnetization, thus if we say "50 % anisotropy" it means $\mu_0 H_{\text{anis}} = 0.5 \times \mu_0 M_s$. Micromagnetic simulations are conducted in 1d chain of 4096 simulation cells along x whose size is 5 nm by 5 nm by t with periodic boundary conditions along y, where x and y are the major and minor axis of the simulation mesh. Here t is the thickness of the magnetic layer and is chosen to be 20 nm. The exchange constant is $A_{ex} = 3.7$ pJ/m^2 [155] and magnetic damping is zero. The $\mu_0 H = 200$ mT external magnetic field is applied along x. The uniform temperature dependent saturation magnetization is considered such that $\mu_0 M_s = \mu_0 M_0 (1 - (\frac{T}{T_c})^a)^b$, where $\mu_0 M_0 = 217$ mT, $T_c = 560$ K, $a = 2.6$ and $b = 0.88$ [119]. We apply a uniform magnetic field $\mu_0 H_x = 200$ mT along x. In addition, on only two cells at the center of the simulation mesh (delta function-like distribution in space), we apply a time dependent perturbation field along y in sinus cardinal function $\sin X/X$ to excite the dynamics. It oscillates in $X = 2\pi f_{cut}(\tau - \tau_0/2)$, where $f_{cut} = 10$ GHz is the cutoff frequency, τ is time and $\tau_0 = 100$ ns is the simulation duration. The reasoning for using those functions is that the Fourier transformation of a delta or a sinus cardinal function gives a constant or a rectangular function. Initially spins are aligned along x with small randomness. We launch the simulation and capture the magnetic configuration of each cell at every $1/(2f_{cut})$. We perform the 2D fast Fourier transformation in time and space domains to obtain the dispersion curves. Finally we compare them with the analytical expression. We remind that the dispersion relation of backward volume mode $\boldsymbol{k} \parallel \boldsymbol{M_s}$ considering the uniaxial perpendicular anisotropy is shown in chapter 1 section 1.1. Fig. 53(a) is the dispersion relation of backward volume mode for the case of $\mu_0 M_{\text{eff}} = \mu_0 M_s$ (YIG). The panel (b) is for the case of $\mu_0 M_{\text{eff}} = 0$, *i.e.* $\mu_0 H_{\text{anis}}/\mu_0 M_s = 100\%$ (BiYIG). The blue or red curve in each panel represents the cases of magnetization at room temperature T_0 or when the temperature is increased to $T_0 + \Delta T$ where $T_0 = 300$ K and $\Delta T = 77$ K. The dots are the results of the micromagnetic simulations and the solid line is based on the analytical expression with 0.05 GHz offset correction, confirming the validity of the simulations. Note that the two panels have the same scale but different offsets. In panel (a) indeed the Kittel frequency ($k = 0$) depends on the magnetization and a larger temperature shifts down the dispersion. On the other hand in panel (b) it does not have a magnetization dependence on the Kittel frequency.

[10]This technique was first proposed by the group of Groningen [109].

However the position of energy minimum and lowest energy varies.

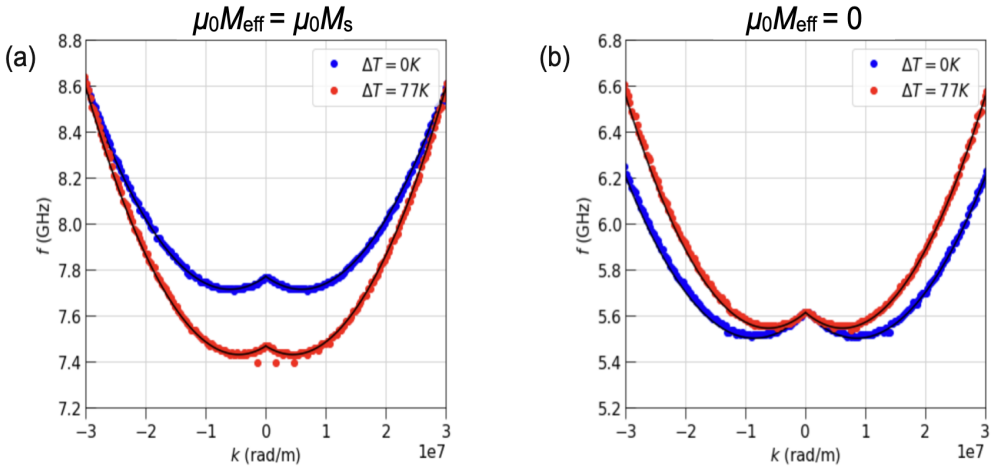

Figure 53: *Simulated (dots) and analytical (solid line) dispersion relation of the backward volume mode for $\mu_0 M_{\text{eff}} = \mu_0 M_s$ (a) or $\mu_0 M_{\text{eff}} = 0$ (b) with uniaxial perpendicular anisotropy $\mu_0 H_{\text{anis}} = \mu_0 M_s$, respectively. Two different values of the magnetization according to the temperature $T = T_0 + \Delta T$ are studied, the blue points are for $\Delta T = 0$ K (room temperature) and red points for $\Delta T = 77$ K (room temperature + Joule heating), where $T_0 = 300$ K.*

Now we use MuMaX^3 to study the magnon propagation excited by the spin transfer effect. The procedure is highly inspired by the previous work by Dr. H. Ulrichs in Göttingen in Germany [122]. In the non-local measurements, we excite magnons by the spin orbit torques from an adjacent Pt layer via the spin Hall effect. In micromagnetic simulations, the Slonczewski spin transfer torque (STT) term takes part in the area of the emitter. The polarization of STT is set anti-parallel to the magnetic field ($-x$), to bias the film in the forward polarity (magnon emission regime). Considering that the applied electrical current density is converted into spin current with the proportionality constant ϵ[11], the actual spin current density which exerts STT is $\epsilon I_1/(w_{\text{emit}} t_{\text{Pt}})$, where w_{emit} is the width of the emitter electrode and t_{Pt} is the thickness of Pt. We fix $I_1 = 0.9$ mA, and the corresponding charge current density is 0.4×10^{12} A/m^2 in the width dependence or anisotropy dependence simulations. The simulation mesh is consist of 4096 by 64 cells with the periodic boundary conditions along the minor axis of the mesh (y). The parameters are basically the same as the previous simulations, however the magnetic damping is set to be $\alpha = 3 \times 10^{-3}$. We impose an absorbing boundary condition that damps dynamics at the edge of the simulation mesh by introducing progressively increasing α towards the edge. We define the area of the emitter where STT is exerted with a width of w_{emit} along x and the length as the whole 64 cells along y. The center of the emitter is fixed as $x_{\text{emit}} = -9.73$ μm. Correspondingly, the width and position of the modulator (identical to the position of the collector) are expressed as w_{modulate} and $x_{\text{modulate}} = x_{\text{emit}} + 3.3$ μm. To consider the effect of Joule heating, we introduce spatially dependent magnetization $\mu_0 M_s\,(T(x))$ following the temperature profile $T(x)$ with exponential decay from the edge of the emitter or modulator. Note that the decay length is arbitrarily chosen to be 70 nm to realize the smooth change of the material parameters while we are limited to 256

[11] $\epsilon = T_r * \theta_{SHE}$ where the spin Hall angle $\theta_{SHE} = 0.11$ and interfacial transparency $T_r = 0.48$

different regions in the simulation meshes for defining different parameters. The local decrease is considered around both the emitter and the modulator.

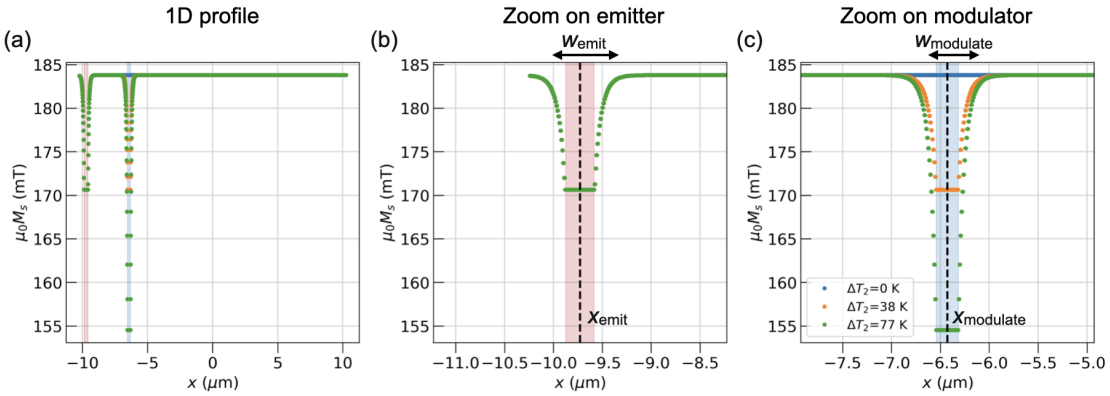

Figure 54: *Example spatial profile of the magnetization. The blue, orange and green dots represent the different values of the local heating under the modulator, where heating is simulated as a reduction of magnetization. The same amount of reduction is introduced under the emitter. Panel (a) represents the global profile and (b) and (c) are the zoom near the emitter and the modulator respectively. The anisotropy also has a similar profile as the magnetization.*

Fig. 54 shows the spatial profile of magnetization in the region nearby the emitter and the modulator. The blue, orange and green dots differentiate the values of the local heating ΔT_2. In this calculation, the Joule heating of the emitter is kept fixed at $\Delta T_1 = 38$ K every ΔT_2. (a) represents the global profile and (b) and (c) represent a zoom near the emitter and the modulator respectively. The colored shaded areas correspond to the region of the emitter and the modulator and the dashed lines are the positions of their center. The anisotropy is assumed to follow the magnetization value accordingly to the analytical formula $K_u(T) = \mu_0 M_s(T) \cdot H_{\mathrm{anis}}/2 \propto M_s^2(T)$, however, it is true that the exponent may vary [252, 253], where a recent report proposed 2.28 [254]. The spins are initially set along x with small randomness. We confirmed that if magnetization is fully aligned with the magnetic field without randomness, no spin wave emission is observed. The STT is exerted on the area of the emitter for 70 ns. Then we take the snapshot of spin configuration and study the spatial profile of $\Delta M_s/M_s = 1 - m_x$, the decreased magnetization along the magnetic field. The quantity is proportional to θ^2, where θ is the cone angle. m_x is the component of normalized spin along x averaged over in y. Note that thermal fluctuations are not implemented in the simulations, *i.e.*, stochastic LLG equation is not considered here [255].

6.3.1 Effects of anisotropy

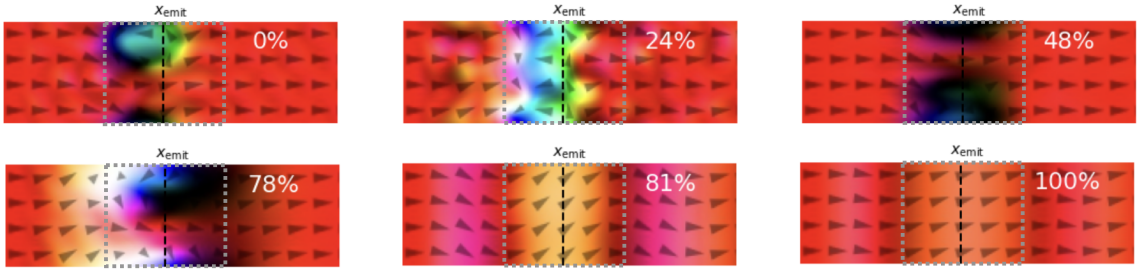

Figure 55: *Snapshots of spin textures near the emitter for different values of anisotropy ratio (see the value in the insert). Other parameters are written in the text. The black dashed line represents the position of the center of the emitter. The grey dashed box represents the region of the emitter. The hue depicts the direction of local spins. The color scaling of red to blue corresponds to in-plane directions (right to left), and that of white to black does to out of plane directions (up to down)*

We now focus our attention on the influence of the anisotropy. As shown in Fig. 53, the uniaxial anisotropy affects the dispersion relation significantly. Especially we recall that the non-linear frequency shift is proportional to $\mu_0 M_{\text{eff}}$ and the Kittel frequency becomes independent of θ when $\mu_0 M_{\text{eff}} = 0$. We show in Fig. 55 the results for different values of $\mu_0 H_{\text{anis}}/\mu_0 M_s$ to see its effect on the excitation and propagation of magnons induced by STT (SOT in real measurements). Here we show the case of $\Delta T_1 = \Delta T_2 = 0$ K. Even for the fixed amount of STT injected, the spatial textures of spins look different as the anisotropy varies. The images in Fig. 55 show the snapshots of the spin texture near the emitter for different values of anisotropy. The black dashed line corresponds to the center of the emitter and the grey dashed box indicates the region of the emitter. The anisotropy ratio $\mu_0 H_{\text{anis}}/\mu_0 M_s$ is written in white as a percentage. When $\mu_0 H_{\text{anis}}/\mu_0 M_s < 78\%$, localized spin wave bullet modes [122, 124] are formed below the emitter. The effect is mainly driven by the band mismatch between inside and outside the emitter as shown in Fig. 53(a) and as discussed in chapter 4 and 5. It happens even without a local decrease of magnetization. This is because the magnetization is effectively decreased when the precession amplitude becomes larger with a cone opening. The excited spin waves inside have lower energy than the energy band outside. Therefore the frequency of such localized magnons and that of the propagating magnons are different, which makes transmission incoherent and inefficient. On the other hand, when $81\% < \mu_0 H_{\text{anis}}/\mu_0 M_s$, coherent spin wave propagation is achieved where the excited spin waves can escape in the energy band in the bulk because there is no mismatch induced by the non-linear frequency shift. Fig. 56 is the normalized spectrum of the averaged fluctuating components of spins (m_y or m_z) inside (red) or outside (blue) the emitter by fast Fourier transformation in the time domain. Panel (a) is for $\mu_0 H_{\text{anis}}/\mu_0 M_s = 0\%$ and panel (b) is for $\mu_0 H_{\text{anis}}/\mu_0 M_s = 100\%$. They confirm that a large enough anisotropy leads to coherent emission of spin waves with a single peak whereas the spectral occupation is broadened when there is no anisotropy. Other simulations reveal that the formation of spin wave bullets depends on the amount of heating under the emitter and thickness. If we implement the local drop of magnetization

considering Joule heating, we observe that spin flip occurs using the same amount of current. This depends also on the anisotropy. As the Joule heating increases, it is easier to have spin flip, for example at $\Delta T_1 = 154$ K, $\mu_0 H_{\rm anis}/\mu_0 M_s = 75\%$ is enough, which implies that smaller magnetization leads to easier switching even for a local perspective. As for the necessary anisotropy to have coherent transmission of spin waves, we confirmed that it basically stays at the similar ratio $\mu_0 H_{\rm anis}/\mu_0 M_s > 81\%$ for $\Delta T_1 = 0, 38, 77, 154$ K at $t = 20$ nm. This ratio is more or less consistent with the case where the Kittel frequency inside the emitter corresponds to the energy minimum of the dispersion curve outside the emitter so that no energy gap is imposed on the generated spin waves. For example for $\Delta T_1 = 77$ K, this specific anisotropy ratio is 76 %.

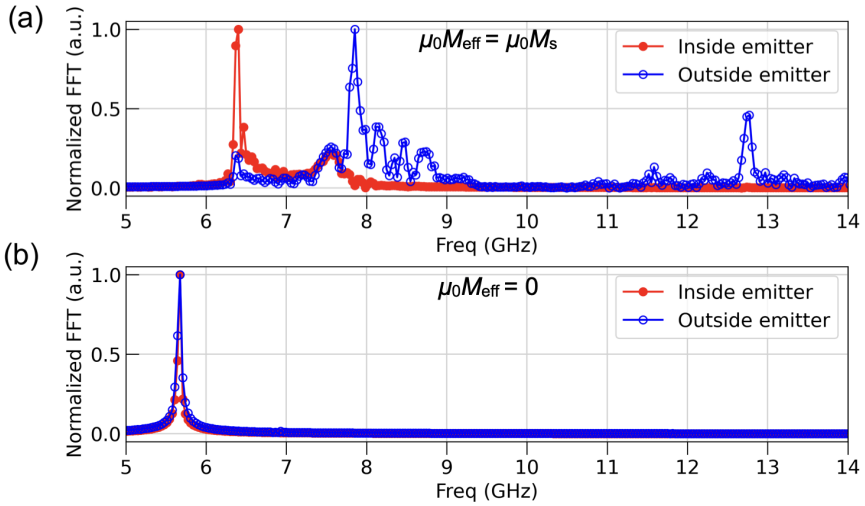

Figure 56: *Comparison of spectral occupation of magnons excited by STE inside (red) and outside (blue) the emitter for (a) $\mu_0 H_{\rm anis}/\mu_0 M_s = 0\%$ and (b) $\mu_0 H_{\rm anis}/\mu_0 M_s = 100\%$ (see Fig. 53 for the dispersion relation of the two cases)*

6.3.2 Characteristic wavelength

One of the great challenges of non-local transport of magnons induced by a d.c. current is to identify the main magnon mode that participates in the transport. We now determine the wavelength of transmitted magnons and study its dependence on the width of the emitter $w_{\rm emit}$ to see if the size of the emitter characterizes the property. Here we use $\mu_0 H_{\rm anis}/\mu_0 M_s = 100\%$, large enough anisotropy to compensate the demagnetizing field which corresponds to the BiYIG case. Note that local heating on the modulator remains fixed at $\Delta T_2 = 0$ K whereas the one under the emitter is considered with $\Delta T_1 = 38$ K. We impose absorbing boundary conditions at the left edge of Fig. 54 whereas the total length of the simulation mesh is four times larger than the characteristic decay length of the spin waves. Fig. 57(a) is the spatial profile of decreased magnetization $1 - m_x$ with different values of $w_{\rm emit}$ while the applied current density is kept the same. It shows its decay-out after traveling 5 μm. First of all, we notice that $w_{\rm emit} > 150$ nm is needed to excite the wave. Second, a larger $w_{\rm emit}$ leads to a larger amplitude of oscillation[12]. Regarding the wavelength, at $w_{\rm emit} = 190$ nm (orange curve), the transmitted wave looks mostly coming from a specific mode, but as the width becomes larger, it looks multi-

[12]This is contrary to our expectation where larger $1/w_{\rm emit}$ gives larger transmission. This discrepancy is still under investigation.

mode. Fig. 57(b) shows the fast Fourier transformation of m_y, the fluctuating component of magnetization, with respect to $x > x_{\text{emit}}$ without apodization. It shows basically two peaks at $k = 1.8 \times 10^7$ rad/m which corresponds to 350 nm wavelength and $k = 3.6 \times 10^7$ rad/m which corresponds to 175 nm wavelength[13]. At $w_{\text{emit}} = 190$ nm (orange curve), the 0th mode (1st peak) has a much larger amplitude than the following modes. However as the width becomes larger, the peak amplitude of 1st harmonics mode becomes larger (red curve). This tendency is confirmed systematically with the other values of w_{emit} (not shown), suggesting that the most coherent single mode emission can be achieved at around $w_{\text{emit}} = 150 - 200$ nm with little contribution from the higher harmonics.

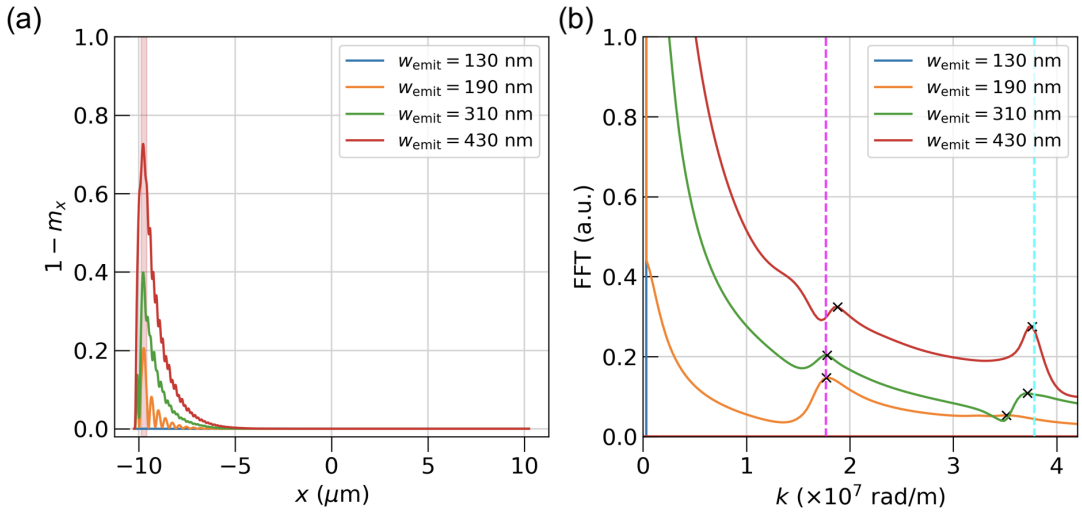

Figure 57: *The dependence of magnon transmission on w_{emit}. (a) Spatial profile of propagating wave with different values of w_{emit} and (b) corresponding fast Fourier transformation spectra, showing two peaks (0th and 1st harmonics). The vertical magenta and cyan dashed lines emphasize their peak positions, whose corresponding values of wavelengths are 350 nm and 175 nm respectively.*

Fig. 58(a) shows the 0th (magenta) and 1st (cyan) harmonics modes wave number k as a function of 150 nm $< w_{\text{emit}} <$ 430 nm, actual range of the device size. The obtained k basically stays the same independently of the injector width for both modes as indicated by the dashed horizontal lines. Panel (b) shows the dispersion relation for inside the emitter ($T_0 + \Delta T_1$) in red and the outside (T_0) in blue obtained from Fig. 53. The grey horizontal line corresponds to the Kittel frequency, then dashed vertical magenta and cyan lines correspond to the obtained 0th and 1st mode wave number calculated in Fig. 57(b). It reveals that the transmitted waves excited by the STT reside in the opposite side of the Kittel mode in the dispersion curve of the region outside the emitter ($\overline{E_K}$ in Fig, 11 in chapter 1) regardless of the width of the excitation site as highlighted with the dashed circle. It is consistent with our previous argument that this mode has the largest group velocity among the degenerated modes around the Kittel frequency which propagate farthest and are collected most efficiently in the measurements . In the next subsections, finally we will investigate the possible origin of the enhancement of the low-energy magnons by local heating observed experimentally by using simulations.

[13]The invert x-axis of the values needs to be multiplied by 2π to convert it into wave length.

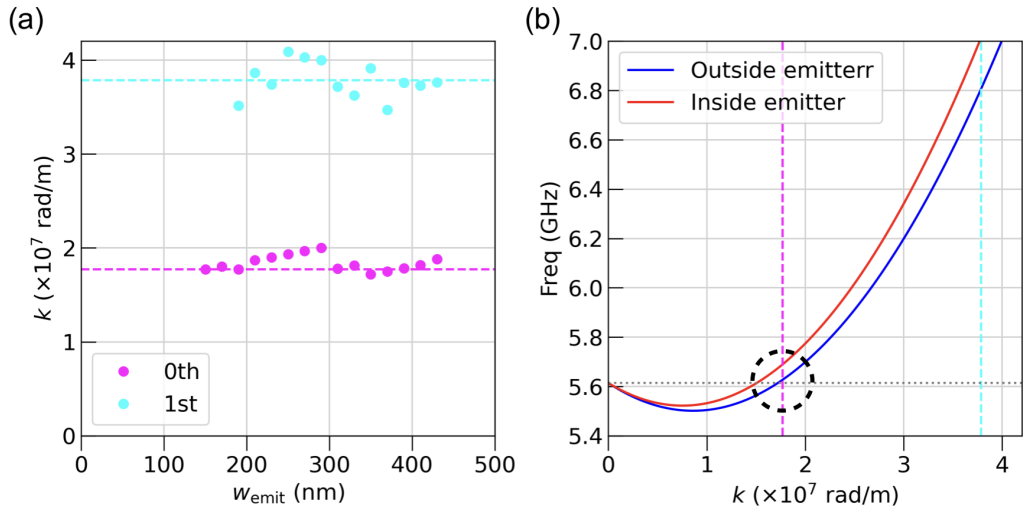

Figure 58: *(a) The dependence of the k values of the 0th and 1st harmonics on* w_{emit}*. (b) Dispersion relation using the parameters inside (underneath) and outside the emitter. The vertical magenta and cyan dashed lines are the extracted wave number of the 0th and 1st harmonics.*

6.3.3 Observation of amplification

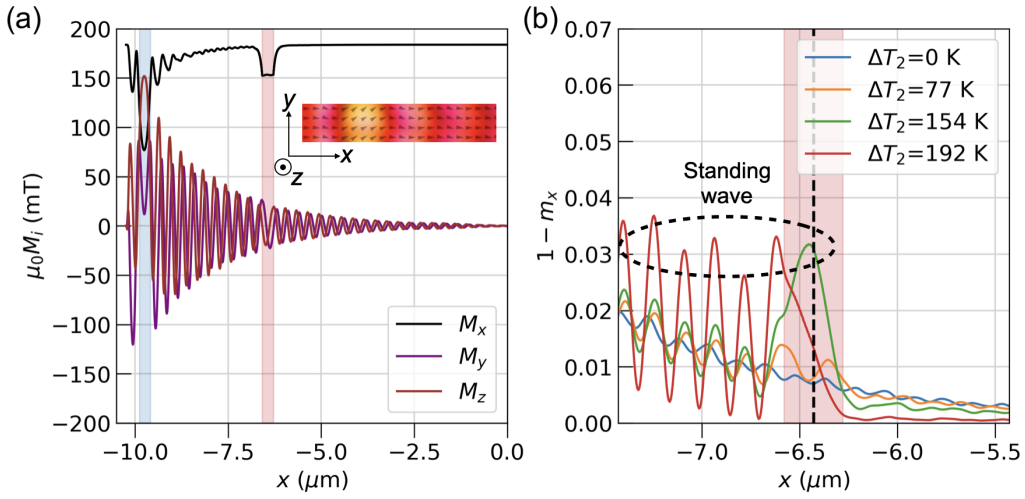

Figure 59: *Effect of a local drop of magnetization on spin wave propagation. (a) Spatial profile of nominal values of magnetization in each component. The inset explains the cartesian axis. (b) Spatial profile of the propagating wave for different values of* ΔT_2 *around the collector.*

Experimentally we observed an amplification of low-energy magnons excited by STE by heating locally the collector. To study this effect we introduced the local drop of the magnetization 3.3 μm away from the center of the injector as expressed in Fig. 54. The local magnetization drop at the injector always corresponds to $\Delta T_1 = 38$ K while the one at the modulator ΔT_2 varies. We choose $w_{\text{emit}} = 300$ nm and $w_{\text{modulate}} = 300$ nm as

well. We simplify our analysis by considering the case of the perfect compensation i.e. $\mu_0 H_{\rm anis}/\mu_0 M_s = 100$ %.

Fig. 59(a) shows the spatial profile of nominal values of magnetization $\mu_0 M_i$ in the unit of mT with $i = x, y, z$. The cartesian axis is as explained in the inset[14]. M_x in black is the component along the magnetic field and M_y in magenta and M_z in brown are the fluctuating components. Importantly, we noticed that M_x shows the local decrease of magnetization at around $x = -6.5$ μm corresponding to 77 K increase of the local temperature, while the fluctuating components do not, revealing a smooth envelope of decay. This ensures that the magnetic fluctuation is continuous and not affected by the local reduction of M_x. Panel (b) shows $1 - m_x$ the normalized spins considering the spatially modulated magnetization zoomed near the modulator. The micromagnetic simulation also reveals the enhancement of the magnetic fluctuation under the modulator by local heating. The heating by 77 K (orange curve) gives a 1.5 times larger amplitude of the dynamics at the modulator than in the case without heating (blue). After passing the region of the modulator ($x > -6.3$ μm), the transmitted wave follows the same trajectory as the blue curve without so much reduction of the amplitude. This enhancement is more spectacular at $\Delta T_2 = 154$ K (green curve). 3 times larger amplification under the modulator is realized. If we take several snapshots to see it as a movie, a contribution from a standing wave localized under the heating area is observed as the dashed circle in panel (b) emphasizes. The amplitude is much larger under the modulator (-6.6 μm $< x < -6.3$ μm) than before (-6.6 μm $> x$) or after ($x > -6.3$ μm). It suggests that the two edges of the magnetization landscape act as magnon mirrors [65, 256], where a part of the incident wave is reflected and travels back in $-x$ direction. This is similar to an optical cavity which is used in a LASER to amplify optical waves by trapping them in between two mirrors. Then at $\Delta T_2 = 192$ K (red curve), most of the incident wave seems to be reflected at the first edge of the magnetization modulation and we can see the signature of the standing wave before the modulator by reflected waves. On the other hand the transmitted wave eventually decays out after the modulator. Fig. 60(a) shows the dependence on ΔT_2 of the amplitude of magnetic fluctuation averaged over the modulator area $\overline{1 - m_x}$. For $\Delta T_2 < 100$ K it progressively increases following the inverse of magnetization $M_s(T_0)/M_s(T_0 + \Delta T_2)$ shown as the red dashed line, where $\Delta T_2 = 100$ K leads to 25% reduction. It confirms the qualitative agreement with the experimental observation as shown in Fig. 52. Then the slope suddenly enhances at $\Delta T_2 = 100$ K. This seems to coincide with the beginning of the formation of a standing wave under the modulator. The reflectance as well as the transmittance of spin waves appear to depend on the local gradient of magnetization. In the end amplification ratio starts to decrease at $\Delta T_2 > 150$ K because a large part of the incident waves is reflected at the first edge of the magnetization gradient. This non-linear increase by the local decrease of magnetization is again qualitatively consistent with experimental observations. However, it kicks in at much larger ΔT_2 than experimental observation (see Fig. 52). Further investigation is needed to solve this discrepancy and we would point out the importance of initial randomness, *i.e.* the thermal fluctuation that governs the non-linear behavior of magnons as discussed in chapter 4[15].

In addition, the change of the wavelength under the modulator is also observed. This is because the dispersion relation depends on the value of magnetization while keeping the value of the Kittel frequency as shown in Fig. 58(b). The spin wave is propagating with the wave number at the opposite side of the Kittel frequency in the dispersion

[14] x is the major axis of the simulation mesh along the magnetic field, y is the minor axis, and z is the out-of-plane direction.

[15] Note that the decrease of the amplification factor due to the reflection at the left edge ($x = -6.6$ μm) of the magnetization modulation cannot be obtained experimentally because of the limitation of the modulator wire to be broken down.

curve and it decreases as the magnetization decreases (or as the temperature increases). Consequently, the wavelength is increased for larger ΔT_2 if we assume that the frequency is kept constant. Fig. 60(b) shows the wavelength under the modulator as a function of ΔT_2 and it shows the monotonous increase until $\Delta T_2 = 130$ K, where the reflection of incident wave starts to be outstanding. The red dashed line is the analytical value obtained from the dispersion relation. The simulation does not agree well with it, which may be due to the small size of the heating area (300 nm) compared to the wavelength.

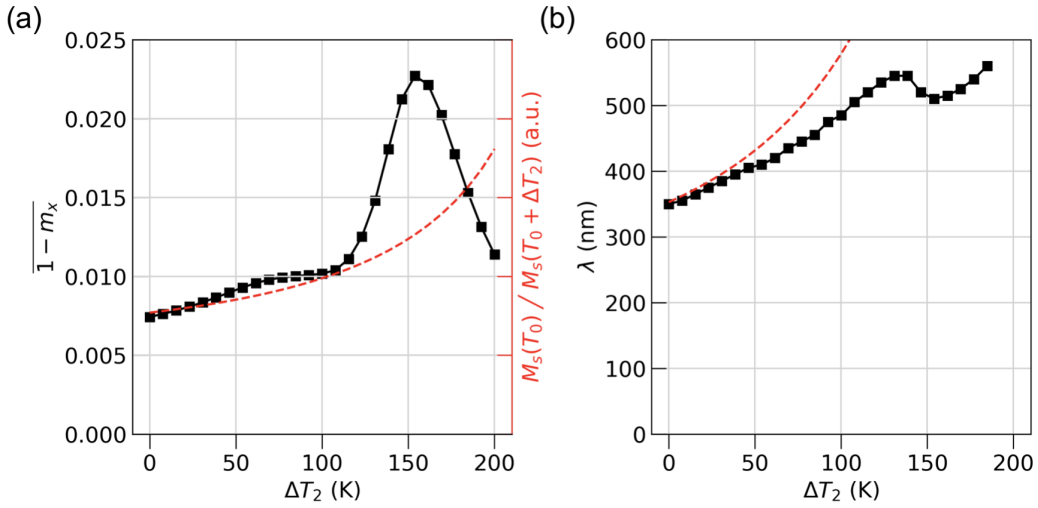

Figure 60: *(a) The amplitude of propagating magnetic fluctuation averaged over the modulator as a function of ΔT_2 (left axis). The red dashed line represents the behavior of $M_s(T_0)/M_s(T_0 + \Delta T_2)$ (right axis). (b) The extracted dominant wavelength of magnetic fluctuation under the modulator as a function of ΔT_2 (black squares) and the analytical value (red dashed line).*

It is worth noticing that the energy of the waves inside $(T_0 + \Delta T_2)$ and outside (T_0) the modulator are identical for $\mu_0 H_{\text{anis}}/\mu_0 M_s = 100$ % as shown in Fig. 53(b). The magnetic fluctuation spectra under the modulator without or with heating is shown in Fig. 60. This confirms the above mentioned statement by revealing the same peak. Thus we do not expect a quantum bound state caused by the potential well. Previous reports on normal YIG explained that magnon reflection and wave vector conversion by the magnetization gradient is caused by the downward shift of the dispersion curve [65, 256]. The band mismatch due to magnetization gradient blocks or converts the coherent spin waves. However in our simulation, there is no band shift because $\mu_0 H_{\text{anis}}/\mu_0 M_s = 100$ %. Thus the origin of observed reflection is still elusive. We point out that the sudden change of the wavelength may affect the propagation. Overall micromagnetic simulations provided us insights into a possible origin of the experimentally observed amplification by local heating. Although the simulations were conducted in the perfectly compensated case $\mu_0 H_{\text{anis}}/\mu_0 M_s = 100$ %, in reality it is $\mu_0 H_{\text{anis}}/\mu_0 M_s = 68$ %. The simulations basically dealt with coherent spin wave propagation, which can be true when we inject a large current density in experiments. The enhancement followed the inverse of the local magnetization at first and eventually boosted up at a larger heating, possibly forming standing waves under the modulator. The large decrease of the magnetization leads to a larger reflectance, however when it is excessive most waves can be reflected at the first edge of the magnetization gradient, which diminishes the amplification. Although we obtained qualitative insight into the experimentally observed amplification, a quantitative

agreement has not yet been reached.

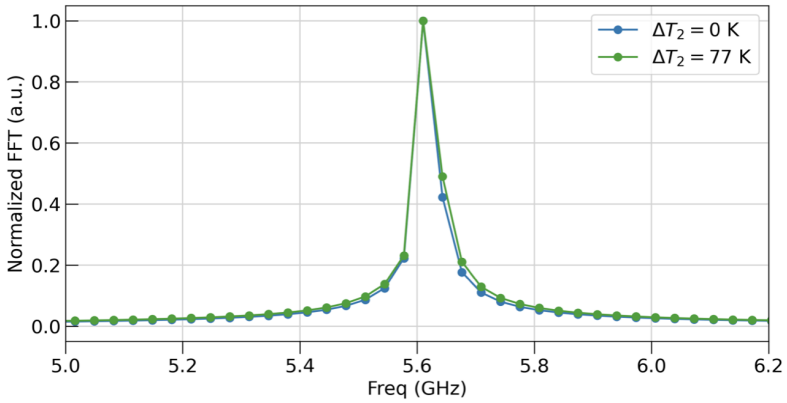

Figure 61: *Magnetic fluctuation spectra underneath the modulator when heated by* $\Delta T_2 = 0$ *K (blue) or* $\Delta T_2 = 77$ *K (green). The spectrum is obtained by FFT of the time evolution of averaged magnetization.*

6.4 Conclusions

We observed the amplification of itinerant low-energy magnons excited by the STE in non-local transport measurements. It is done by locally heating the collector electrode with an additional electrically isolated heating electrode. The magnon transconductance is enhanced by 3.4 times when 77 K of local heating is applied. Further investigation revealed that a large initial emission is needed to observe the enhancement where the transport characteristic is in the non-linear regime. The enhancement followed the inverse of magnetization which increases as the temperature increases, however it boosted up at higher heating. The micromagnetic simulation suggested that the propagating magnons are reflected by the local magnetization drop acting as a mirror, establishing standing waves, although a quantitative agreement has not yet been obtained.

Chapter 7

Perspectives

7.1 Coupling between magnons and phonons

In previous chapters, we demonstrated that one can improve the coherency of transmitted spin waves by using materials with a large uniaxial anisotropy to compensate the demagnetizing field. This already overcomes the drawbacks of electrically excited magnons that their frequency and wavelength are not well defined, that is, incoherent. This opens up a perspective to utilize some useful effects that happen in coherent spin waves. One can consider implementing functional magnonic circuits in a non-local magnon transport device, such as recently demonstrated directional coupler [20, 29, 257]. Here we point out the possibility of coupling between magnons and phonons using the coherent magnons excited by the spin transfer effects in non-local transport devices. GGG|YIG systems have proven to be an excellent platform to study such magnon-phonon coupling because the damping of magnons in YIG is the smallest possible and the damping of phonons in GGG and YIG is also very small (10^{-6}) [258, 259], which is an order of magnitude better than one in quartz. In recent years our group has published several papers on magnon phonon coupling phenomena in such systems (Phys. Rev. B 101, 060407(R)) [235] (Phys. Rev. X 12, 011060) [236] led by Dr. Kyongmo An, where I contributed to device fabrications, data acquisitions, and discussions. Below we introduce briefly our achievements explained precisely in Ref. [92] and how its capability would expand to non-local magnon transports.

In our measurements, the dominant coupling is among the coherent Kittel mode magnon excited by the microwave field and coherent acoustic shear waves. The coupled equation of motion is written as follows.

$$(1 - i\alpha_m)\omega m^+ = \gamma(H_m^+ - D\partial_z^2 m^+ + B\partial_z u^+ - M_s h^+) \tag{7.1}$$

$$-(1 - 2i\alpha_a)\omega^2 \rho u^+ = C_{44}\partial_z^2 u^+ + B/M_s \partial_z m^+ \tag{7.2}$$

where m^+, u^+, h^+ are the circularly polarized oscillating part of the magnetization, lattice displacements, and microwave magnetic field respectively. H is the effective bias magnetic field comprising the externally applied field, the anisotropy, and the demagnetizing field, D is the exchange constant, $B = 7 \times 10^5$ J/m^3 is the effective magneto-elastic coupling constant, $\rho = 5.1$ g/cm ^{3} is the mass density, α_m, α_a are the magnetic and acoustic damping coefficient respectively, and C_{44} is the elastic constant which governs the transverse sound velocity $v = \sqrt{C_{44}/\rho}$. The linearization around the Kittel frequency ω_m with small amplitude of m^+, integration of the coupling over the total crystal thickness, and assumption that the m^+ and h^+ are plane waves, lead to simplified forms of above equations such

that

$$(\omega - \omega_m + i\eta_m)m^+ = \frac{\Omega}{2}u^+ + \kappa h^+ \tag{7.3}$$

$$(\omega - \omega_a + i\eta_a)u^+ = \frac{\Omega}{2}m^+ \tag{7.4}$$

where κ is the inductive coupling to a microwave antenna, $\eta_m = \alpha_m\omega,\ \eta_a = \alpha_a\omega$ are the relaxation rate for the magnon and phonon. Ω is the magneto-elastic overlap integral between the magnons and phonons expressed as [260]

$$\Omega = \frac{B}{\sqrt{2}}\sqrt{\frac{\gamma}{\omega M_s \rho s d}}\left(1 - \cos(\omega\frac{d}{v})\right) \tag{7.5}$$

where s and d are the thickness of the substrate and magnetic layer respectively as illustrated in Fig. 62(b). The coupling strength is thus frequency dependent and since the actual sample size with $s = 0.5$ mm and $d = 200$ nm, the maximum occurs at around 6 GHz. These equations are indeed for two coupled pendulums connected via a spring as depicted in Fig. 62(a), whose Hamiltonian which acts on $\boldsymbol{x} = (m^+, u^+)^\mathsf{T}$ and eigenvalues are expressed as follows.

$$\mathcal{H} = \begin{pmatrix} \omega_m & \Omega/2 \\ \Omega/2 & \omega_a \end{pmatrix} \tag{7.6}$$

$$\omega_\pm = \frac{\omega_m + \omega_a}{2} \pm \sqrt{(\omega_m - \omega_a)^2 + \left(\frac{\Omega}{2}\right)^2} \tag{7.7}$$

Thus when the two resonances match $\omega_m = \omega_a$, those two eigen frequencies do not merge but have finite gap Ω, which is usually called avoided crossing. Fig. 62(c) shows the experimental data on FMR absorption of the Kittel mode in bilayer YIG|GGG at around 5.5 GHz when the static magnetic field is applied normal to the sample, where the precession is precisely circular. A 3.5 MHz periodic structure is revealed in the spectrum when a fine scan of frequency and field is conducted. This comes from standing phonon modes forming in the whole sample stack which has a resonance at every $nv/2(s+d) = n \cdot 3.53$ MHz (n is an integer). The observed evident decoration of the spectrum due to the formation of standing phonons is indeed thanks to the excellent quality of the crystal that allows elastic waves to propagate coherently without losses at interfaces. At the phonon resonance, the avoided crossings of the magnon and phonon dispersion with strength $\Omega/2\pi = 1$ MHz are observed, which proves the strong coupling between the two oscillators. We also show in panels (d-f) the behavior of line shapes at tuned or detuned condition parallel to the FMR resonance indicated by the blue, magenta, and red diagonal cuts in panel (c). The amplitude of the main resonance (blue) dips and the lines broaden at the phonon frequencies. The dip then becomes a dispersive-looking signal (magenta) into peaks (red) sufficiently far from the Kittel resonance as expected from the complex impedance of two detuned resonant circuits. The solid line is the analytical solutions obtained from the above equations. The analysis of the line shape gives the phonon relaxation rate $\eta_a/2\pi = 0.35$ MHz and magnon relaxation rate $\eta_m/2\pi = 0.50$ MHz, where we obtain the cooperative $C = \Omega^2/2\eta_a\eta_m = 3$. Since $C > 1$, magnons and phonons have proven to be strongly coupled with each other in the YIG|GGG system and it shows that magnets can act as source and detector of phononic angular momentum currents, which flow over millimeter distances.

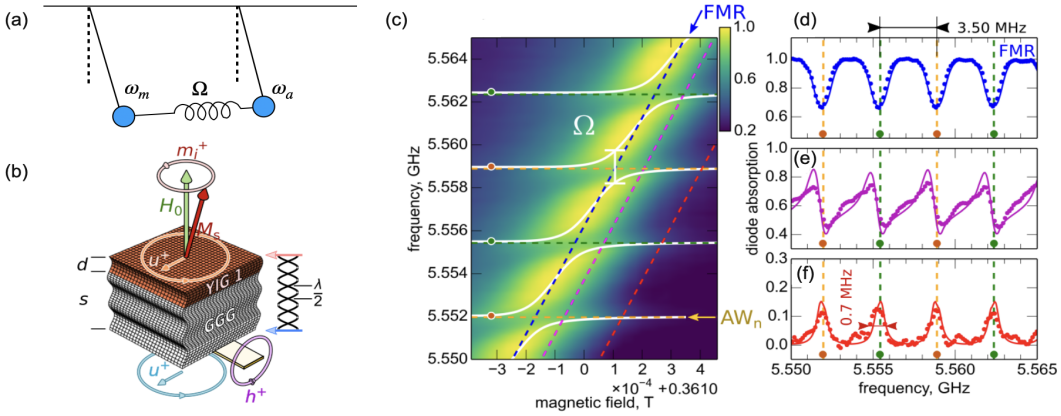

Figure 62: *(a) Schematics of the two coupled pendulums with one oscillating in ω_m (magnon m^+) and the other oscillating in ω_a (phonons u^+) connected through a spring whose constant is Ω. (b) Schematics of the sample structure. An acoustic standing shear wave is formed with circular polarization (u^+) as illustrated as a wavy structure, where the sample thickness $s+d$ matches the integer times half wavelength. A static magnetic field is applied normal to the plane and a microwave field (h^+) excites the magnon (m^+). (c) FMR absorption spectra sweeping the static magnetic field and the microwave frequency. (e-f) the diagonal cut of the spectrum along blue, pink and red dashed lines in (c) respectively, showing the decoration in 3.5 MHz frequency. The figures are by the courtesy of Dr. Kyongmo An.*

Now that we confirmed the excellent phonic quality and the strong coupling between the phonons and magnons. We develop from the above explained results of the two coupled oscillators to three coupled oscillators as depicted in Fig. 63(a). When fabricating YIG on GGG substrate by liquid phase epitaxy technique, YIG is grown on both sides of the GGG substrate in nature, meaning that an as grown stack is YIG|GGG|YIG trilayer. Thus it is a natural direction to investigate the magnon-phonon-magnon tripartite hybridization. The equations of motion is then modified as

$$(\omega - \omega_{m_1} + i\eta_m)m_1^+ = \Omega u_n^+/2 + \kappa_1 h^+ \tag{7.8}$$

$$(\omega - \omega_{m_2} + i\eta_m)m_2^+ = \Omega e^{i\Phi} u_n^+/2 + \kappa_2 h^+ \tag{7.9}$$

$$(\omega - \omega_a + i\eta_a)u_n^+ = \Omega m_1^+/2 + \Omega e^{i\Phi} m_2^+/2 \tag{7.10}$$

where m_2^+ is the Kittel mode of the second YIG layer with circular polarization, $\omega_{m1,2}$ and $\kappa_{1,2}$ are the Kittel frequency of the two magnetic layers and coupling strength to the antenna field for the two layers. Here we label phonons with index n with even or odd integer and Φ is the phonon coupling phase of the second layer with respect to the first layer. $\Phi = 0$ corresponds to n even where both surfaces of the stack oscillate in phase (even phonon) and $\Phi = \pi$ corresponds to n odd where they oscillate in π phase shift as illustrated in Fig. 63(b). The Hamiltonian that acts on $\boldsymbol{x} = (m_1^+, u_n^+, m_2^+)^\mathsf{T}$ is then expressed as follows .

$$\mathcal{H} = \begin{pmatrix} \omega_{m_1} & \Omega/2 & 0 \\ \Omega/2 & \omega_a & \Omega e^{i\Phi}/2 \\ 0 & \Omega e^{i\Phi}/2 & \omega_{m_2} \end{pmatrix} \tag{7.11}$$

Eigenvalues and eigenvectors are analytically solvable and they are plotted in the panel (c) and (g) for $\Phi = \pi$ (odd phonons) and $\Phi = 0$ (even phonons) respectively as a function of detuning $\omega_{m_1} - \omega_{m_2}$ and relative frequency to ω_a. At the degeneracy point ($\omega_{m_1} = \omega_a = \omega_{m_2}$) the eigenfrequencies relative to ω_a and corresponding normalized eigenvectors read:

$$-\frac{\Omega}{\sqrt{2}} : \begin{pmatrix} 1/2 \\ 1/\sqrt{2} \\ \pm 1/2 \end{pmatrix}, 0 : \begin{pmatrix} 1/\sqrt{2} \\ 0 \\ \mp 1/\sqrt{2} \end{pmatrix}, \frac{\Omega}{\sqrt{2}} : \begin{pmatrix} 1/2 \\ -1/\sqrt{2} \\ \pm 1/2 \end{pmatrix}, \tag{7.12}$$

respectively for $\Phi = \pi$ (odd phonons) and $\Phi = 0$ (even phonons) for upper and lower sign. Combining with panels (c) and (g), it is revealed that even and odd phonons correspond to m_2^+ oscillating in π and zero phase shifts with m_1^+, as illustrated in the inset of panel (c) and (g). The line cuts of eigenvalues for odd and even phonons at the degeneracy point are shown in panels (d) and (h). The enhancement and suppression of the m_2^+ are observed for odd and even phonons respectively, which represent the bright and dark states as emphasized as the white or black dot symbols in panels (d) and (h).

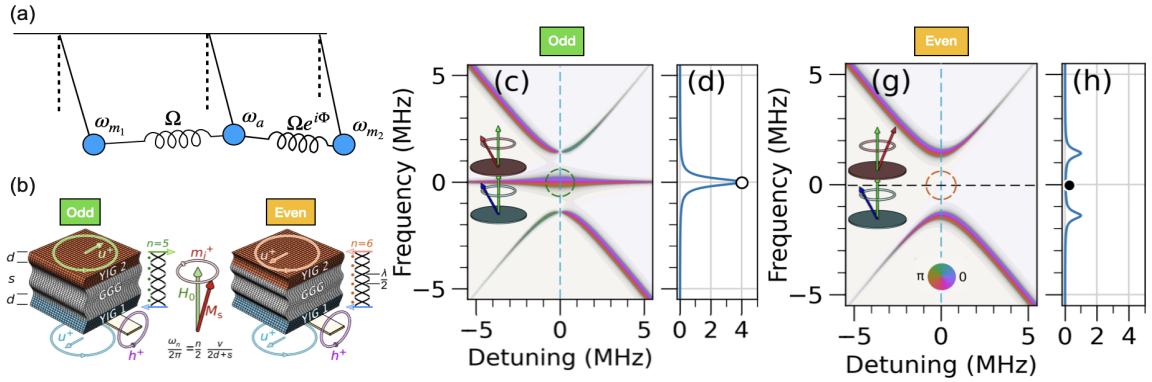

Figure 63: *(a) Schematics of the three coupled oscillators, where the phase shift Φ is introduced between ω_a and $\omega_m 2$. (b) Schematics of the trilayer sample stack and odd (left) and even (right) phonons. (c,g) The solution of the three coupled oscillator model for odd and even phonons respectively. (d,h) The line cuts at their degeneracy points. The figures are by the courtesy of Dr. Kyongmo An.*

We experimentally observed the bright and dark states by matching the Kittel frequency of the two YIG layers considering that phonon resonance spacing of 3.5 MHz is small enough compared to the line width of the Kittel resonance. The slight difference in material characteristics is inevitable even though we designed to grow 200 nm YIG on both surfaces by the liquid phase epitaxy technique. We tune the resonance of the two layers by applying a temperature gradient across the stack that decreases their magnetization of them differently. We apply electrical current in a Pt wire deposited on the top surface (YIG2) while measuring the lock-in voltage synchronized with the microwave application whose antenna touches with the bottom surface (YIG1) giving the diode absorption signal. Fig. 64(a) shows the joule heating dependence of the resonance field of each layer at 15 degree polar angle and 5.11 GHz microwave field. The blue and red data points correspond to the YIG1 and YIG2 respectively, showing the matching of the two resonances at 19 mW of heating. The top axis is the corresponding temperature rise by Joule heating and it indicates that YIG2 layer has two times more efficient heating than YIG1. Now

we slightly modify the frequency to tune the phone resonance. Panels (b,c) show density plots of the ISHE voltage in the Pt contact on YIG2 layer as a function of Joule heating and magnetic field observed at different frequencies to have odd or even phonons at the degeneracy point (triple resonance) respectively. The blue solid lines are the maxima of the spin-pumping signal. The green and orange arrows indicate the positions of odd and even phonon resonances respectively, observable as small cusps in the microwave spectra (blue lines). The circles in (b) and (c) highlight the degeneracy point. the right window compares the line cut measured either at the degeneracy point (magenta vertical dotted line) or at a large detuning (cyan). In (b) at the intersection with an odd mode, the intensity gains a factor of 4, which confirms that the magnetization amplitudes of both YIG1 and YIG2 interfere constructively into a "bright" mode. In (c) at the intersection with an even lattice mode, the peak splits and becomes "dark", forming the destructive interference.

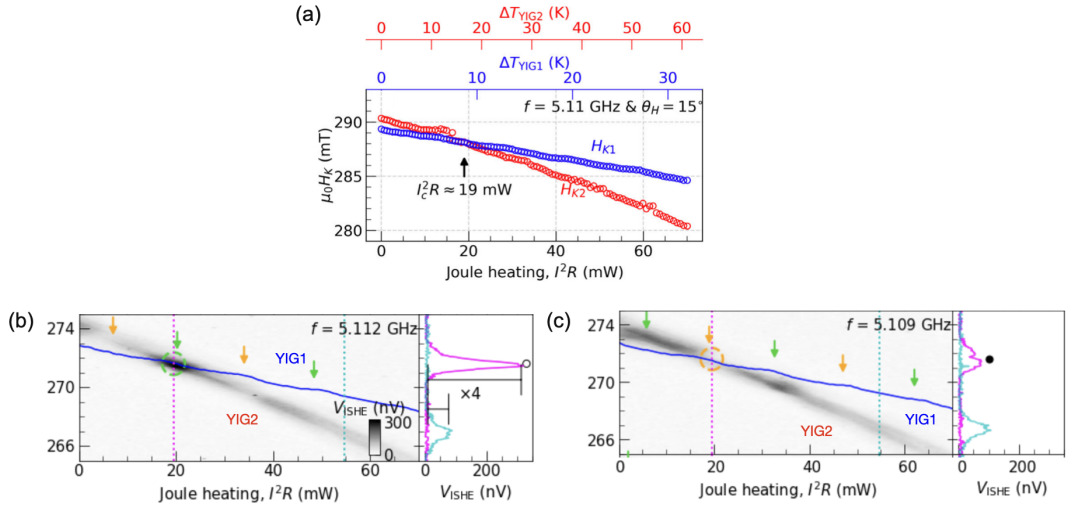

Figure 64: *(a) Joule heating dependence of the resonance field at fixed frequency and angle as indicated for YIG1 by diode detection (blue) and YIG2 by electrical detection through ISHE (red). The top axis represents the corresponding temperature rise at YIG1 (blue) and YIG2 (red). (b,c) Density plots of the ISHE voltage in the Pt contact on YIG2 layer as a function of Joule heating and magnetic field observed at different frequencies to have odd or even phonons at the degeneracy point respectively. The blue solid lines are the maxima of the right and compare the modulation of the spin-pumping signal measured either at the degeneracy point (magenta) or at large detuning (cyan). The green and orange arrows indicate the positions of odd and even phonon resonances, respectively, observable as small cusps in the microwave spectra (blue lines). The figures are by the courtesy of Dr. Kyongmo An.*

The above explained results have been observed when the external magnetic field is applied normal to the sample and we did not have clear evidence of magnon-phonon coupling under an in-plane magnetic field, where the efficiency of spin transfer effects is maximum. Although the reason is still unclear, fortunately, Dr. Kyongmo An recently succeeded in observing the coupling in in-plane configuration with reduced coupling strength as predicted theoretically [261] in the same sample stuck by using the microwave strip line (in preparation for submission and I also contributed to device fabrications and discussion). This excellent news leads to a motivation for long range transfer of spin information from one side of the sample to the other via phonons. For example in

Pt|BiYIG|sGGG|BiYIG|Pt system, coherent magnons can be excited by the spin transfer effects which eventually couple to phonons, carrying the information to the opposite side. Indeed one needs excellent crystal quality for both BiYIG layers which are fairly thin (20 nm) and investigation of magnon phonon coupling in BiYIG [262, 263]. Then for the perspective of non-local magnon transports, we may expect the coupling between magnon backward volume modes and transverse or longitudinal acoustic phonon modes. This has been observed in magnon transports by the spin Seebeck effect. The coupling happens when the dispersion of the magnons and phonons intercept, where the magnon conduction is enhanced [263–265]. Those works focus on the condition where the two dispersion curves have a tangential relationship, however there has been no experimental realization of the coupling at the first interception at GHz frequency. Since excited magnons in compensated BiYIG can have well-defined wave number $k = 1.8 \times 10^7$ rad/m at least demonstrated in simulations, there may be coupling with transverse and longitudinal acoustic phonons at $\mu_0 H = 390$ mT and $\mu_0 H = 730$ mT respectively. In such situations, the magnon transport is mediated by phonons, expecting longer decay length just as observed in microwave antenna excited magnons [266].

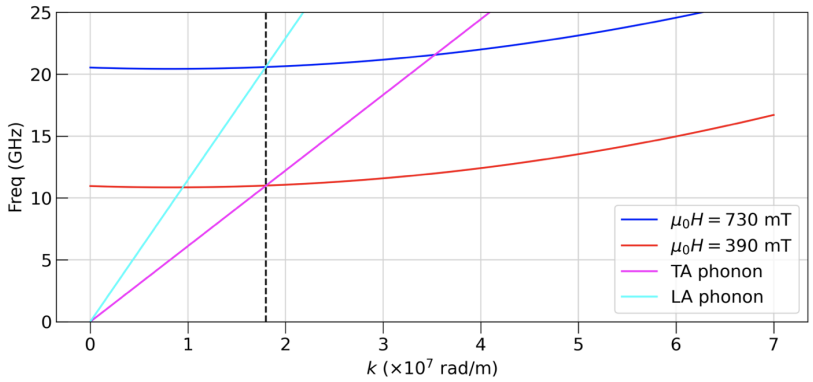

Figure 65: *Magnon and phonon dispersion. The parameters for magnons are the same as the ones in chapter 6 for the fully compensate BiYIG case. The group velocity of longitudinal and transverse phonons is 720 m/s and 384 m/s [64]. The blue and red curves are the magnon dispersion with the two different magnetic fields that cross with the dispersion of longitudinal acoustic phonons (cyan) or transverse acoustic phonons (magenta) at the specific wave number $k = 1.8 \times 10^7$ rad/m. At this wave number the magnons excited by the spin transfer effects are propagating inferred from chapter 6.*

It is worth mentioning theoretical works that propose a possibility to realize the non-local spin information transfer in trilayer YIG|GGG|YIG system mediated by phonons (to be precise, phonon spin current depicted in Fig. 66(a)) even for incoherently excited magnons [267, 268]. Those works are convincing to seek the possibility of a non-local detection of spins excited incoherently by the STE in a vertical fashion where the same samples of our previous works [235,236] can be used. In addition, it may be also interesting to tackle the same idea but in a lateral fashion. Namely two YIG|Pt narrow wires are placed on a GGG substrate as shown in Fig. 66(b). Magnons are excited coherently or incoherently depending on the material by the STE in one YIG|Pt wire, and phonons are excited through the coupling in the GGG, which eventually propagate. Eventually, the phonons are converted back to the magnons in other YIG|Pt wire, realizing the non-local detection of itinerant phonons, which we expect very long range. Related to this, a theoretical paper predicts that one may be able to excite Rayleigh surface acoustic waves

in such lateral devices by coherent excitation of magnons [269], meaning that it may be a new simple platform to launch surface acoustic waves.

Another important remark related to the transport of *phonons* is that such a coupling between magnons and phonons may be an answer for a major issue on the transport length of magnons. As introduced in chapter 0 and 3, the previous study has reported that the thermal and electrical excitation give more or less the same decay length. However we proved the short range behavior of the thermal magnons in chapter 3 and the issue has not yet been answered. Our group found that the generated phonons through the magnon-phonon coupling travel ballistically to the opposite side of the sample. we observed a heat transport mediated by the GHz ballistic phonons by measuring the resistance of a metal layer deposited on the opposite surface to the YIG layer in a YIG|GGG|Pt system. It oscillates in a 3.5 GHz periodicity that matches the standing phonon mode splitting. Now that we experimentally revealed that the phonons can travel as long as 0.5 mm while carrying heat, it motivates us to associate the reported *long range* thermal magnon transport with a phonon-assisted phenomenon. This work is led by Dr. Kyongmo An and I contributed to the sample preparation and data collection, which is in preparation for submission.

For those reasons we believe that seeking the possibility of magnon-phonon coupling phenomenon with electrically excited magnons is a good direction to broaden the potential of the field of the non-local magnon transport.

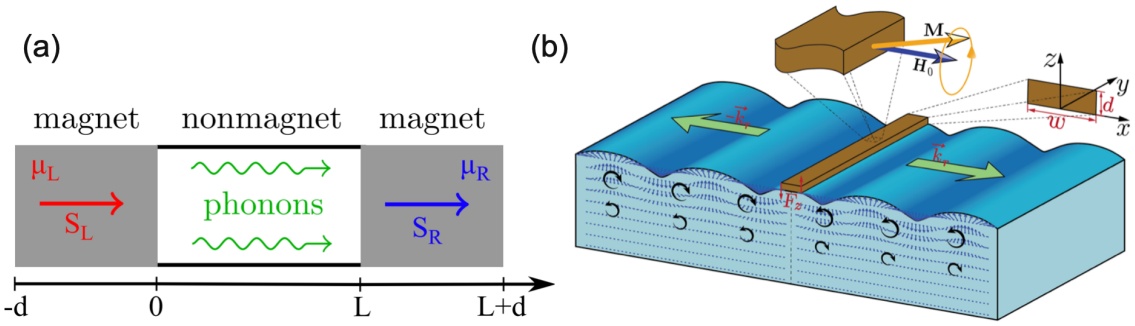

Figure 66: *(a) Schematic of the spin transfer from the left magnet to the right magnet mediated by phonons which is applicable to also incoherent magnon excitation by the spin transfer effects. The figure is taken from Ref. [267]. (b) Schematic of the pumping of surface acoustic waves by one magnetic wire (brown) on top of the phonon conductor (blue). The figure is taken from Ref. [269].*

7.2 Seeking for magnonic hydrodynamic behavior

In recent years, in an extremely clean electric system such as graphene encapsulated with hexagonal boron nitride layers, the hydrodynamic behavior of electron flows has been observed [210, 212]. In such a system where the scattering due to the impurity is significantly reduced, the shortest time (or length) scale is electron-electron scattering. There, the electrons behave as a viscous fluid, which was predicted decades ago. For example, in the 1960s R. Gurzhi stated the decrease of the resistivity (increase of conductivity) at an elevated temperature before entering the regime where electron-phonon scattering is dominant due to thermal fluctuation [213]. This effect, called Gurzhi effect, has been observed

in 2016 and most recently the direct imaging of the Poiseuille flow (Fig. 67(a)) of electrons in a narrow conduction channel with a nitrogen vacancy center microscopy has been realized [270]. In such situations, the conduction is governed by the Navier-Stokes equation. Now let us consider it for magnon transports as well. A prerequisite condition, that is, ultra clean magnonic conductor, may be achievable in GGG|YIG systems known as the smallest magnetic damping and the smallest inhomogeneity material. It allows ballistic propagation of magnons in micron scales without scattering by impurities and incoherent phonons [20, 155]. Theoretical attempts to implement the hydrodynamic equation in the diffusion equation of the magnon transport have been reported [160, 215, 271].

The authors predict that the formation of viscous magnon fluids may be detectable as a sign change of the non-local transport signal, which comes from a swirling of magnon fluids, changing the direction of flow as shown in Fig. 67(b).

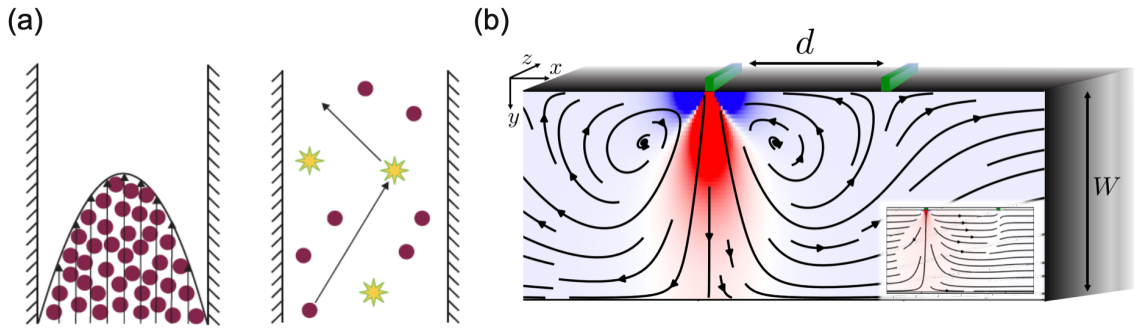

Figure 67: *(a) Schematics of the hydrodynamic (left) and diffusive (right) conduction of particles. The figures are taken from Ref. [212]. (b) Schematics of a hydrodynamic flow of magnons in non-local transport measurements. The inset shows conventional diffusive transport without such effects. The figure is taken from Ref. [160].*

There are several experimental reports who pointed out the possibility of hydrodynamic transport of magnons [272, 273], however, no solid evidence of such phenomenon so far exists. One needs strong enough momentum conserving magnon-magnon interaction. The theoretical papers introduced before pay attention to high-energy magnons at thermal energy. At elevated temperature, the population of such magnons with a large wave number (momentum) is increased and their magnon-magnon interaction is dominated by the exchange interaction, which is typically strong. They estimate the D_ν, the characteristic length of hydrodynamic behavior as 100 nm. We were not able to shorten the separation between the emitter and collector below D_ν, indeed it will be worth spending time to optimize the fabrication process for such a length knowing that high-energy magnons are supposedly dominant contributions in a short distance. On the other hand, we have to emphasize that the low-energy magnons are also influenced by the magnon-magnon scattering, namely the Suhl instability. In previous chapters we have shown that the relaxation rate should be rapidly increased as the population of low-energy magnons are increased by a large intensity of the spin transfer effect, which is the main cause of limited growth of the conduction. It suggests that at this regime the shortest time scale may be the magnon-magnon scattering. Thus it is natural to expect the viscous behavior of low-energy magnons as well, where it is possible to exclude the contribution from high-energy magnons by engineering materials and sample structures. We confirmed the increased magnon conduction triggered by the temperature with interfacial transparency

tuning measurements [216] and the temperature profile tuning measurements [119]. Those two observation leads to an analogy with the Gurzhi effect. Indeed solid theoretical works are needed to consider if the magnon-magnon interaction between low-energy magnons induced by Suhl instability process can be the origin of hydrodynamic behavior. For future studies, we would suggest designing the sample architecture to exploit the hydrodynamic behavior. One straightforward idea is to construct the nano-scale conduction channel, just as the previously reported Gurzhi effects in graphenes with constriction of narrow channels [210]. Direct observation of the Poiseuille flow, or whirlpool created just after the channels by spatially resolved microscopy techniques (NV center, BLS) may be fascinating. We also expect increased conductivity, or velocity in the channel. This is indeed thanks to the Poiseuille flow. The cooperative behavior of magnons may be expected such that the particles organize into streams with spatially distributed velocity with a slow down of flow towards the edge of the channel. It helps to avoid as many contacts as possible with the edge and reduces the loss. There are several ways to construct such nano constructions. The straightforward way is to use the focused ion beam technique to etch out the YIG [20, 274, 275], or the irradiation of high-energy heavy ion beams to turn crystal into amorphous at spotted areas, which deteriorates or vanishes the magnetic property [276]. It may be also possible to directly grow amorphous YIG by pulsed laser deposition on a nano patterned substrate, which is eventually crystallized by annealing [277]. For those reasons we have been convinced that the seeking for the possibility of magnonic hydrodynamic behavior is in a good direction, which may pioneer a new field of magnonics.

7.3 Conclusions

In this chapter, we proposed several perspectives on magnon transport reflecting our obtained results. Firstly we emphasized the prospects of the magnon phonon coupling. Enhanced coherency of emitted spin waves by the spin transfer effects in fully compensated BiYIG is fascinating in various ways including coupling phenomena. We dream of a long range transfer of angular momentum in trilayer BiYIG|sGGG|BiYIG excited and detected fully electrically just the same story as we observed using microwave excitation, or enhanced magnon transport by coupling with longitudinal or transverse acoustic phonons. Secondly, we proposed to investigate possibilities to exploit a hydrodynamic behavior of magnon conduction. To the best of our knowledge, experimental observation has not yet been realized while several pieces of theoretical evidence have been already reported. Rather than concentrating on the high-energy magnons, we would focus on the low-energy magnons, where conventional imaging technique is available. This is because experimentally we observed that the increased magnon-magnon interaction seems to suppress the growth of conduction of low-energy magnons excited by the spin transfer effects. This indicates that magnon-magnon scattering is the most frequent process playing a role in increased viscosity. Recent advances in nano patterning of YIG may be useful to construct nano channels to exploit hydrodynamic characters such as the Poiseuille flows or whirlpools.

Chapter 8

Conclusion

8.1 General conclusion

In this thesis, we have investigated the fundamental characteristic of the magnon transport in thin magnetic garnet films excited by either temperature gradient (spin Seebeck effect) or by the spin transfer effects (spin orbit torque). We used a proto-typical magnonic circuit which consists of two narrow Pt wires deposited on extended garnet films, where electrical generation and detection of itinerant magnons is made possible with direct or inverse spin Hall effect. In particular, we focused on the behavior of low-energy magnons which reside close to the Kittel frequency in the dispersion curve. Especially at large current injection, the $I - V$ characteristic is asymmetric and unipolar, revealing a spin diode effect. Moreover, we aimed at the possibility of controlling the transport with an additional modulator electrode by considering the knowledge acquired. The results shown in this thesis may open up new directions to expand the potential of magnonics.

The first two chapters gathered the basic theoretical concepts and experimental procedures used during this thesis. Chapter 3 was dedicated to deciphering the characteristic decay length of high-energy thermal magnons at the energy around k_BT generated through the spin Seebeck effect. The previously reported 10 μm decay length contradicts the simple estimation of ballistic decay length inferred from the group velocity and relaxation rate, deterioration of the damping at high frequency, coupling with higher branches of dispersion, their diffusive nature, and so on. We studied the characteristic decay length of the non-local spin Seebeck signals in two cases of the temperature profile. One is the usual YIG system capped with a protecting layer, the other one is the exact same sample but this time capped with additionally an Aluminium layer acting as a heat sink. Comparing the two identical YIG|Pt samples with different thermalization to the substrate allows us to disentangle the local contribution that is driven by the gradient of chemical potential. We monitor the number of sign changes of the SSE signals along the separation between the two electrodes as a robust signature of the range of the decay length of the thermal magnons. we found that no more than a few hundred nanometers are needed to fit the two cases.

Chapter 4 focuses on the transport characteristic of the magnons originating from the spin injection from an adjacent Pt wire. Especially we focused on low-energy magnons which reside close to the energy minimum of the magnon dispersion at the energy around the Kittel frequency. The transport is characterized by an asymmetric non-linear increase of the conduction, which we named the *spin diode effect*. While we developed the general formula to describe the amplitude of the conduction analytically at low intensity of the spin transfer effect, the behavior at high intensity is different from what is understood in the case of confined geometry such as nano-pillar. The characteristic behavior observed in confined geometries is the auto-oscillation, which allows the population of a specific mode (uniform mode) because each possible mode is well separated compared to the linewidth due to the finite size effect. However, in an open geometry, namely in our non-

local transport measurements, the excitation affects the continuum of magnons inside the magnon manifold. One consequence is the limited growth of the signal stemming from the non-linear magnon-magnon interaction that prevents the overpopulation of any mode. Instead, the input power is distributed to degenerated modes. This process seems to affect the primary mode around the Kittel frequency propagating in different directions. This is interpreted as the increase of the effective relaxation rate, which directly impacts the threshold current for the magnon chemical potential to reach the energy minimum of the magnon manifold. As a result, as the population of low-energy magnons increase at large intensity, the instability process starts to kick in, increasing the relaxation rate and thus threshold current. Therefore the damping compensation threshold is unreachable in open geometries. The saturation of the magnon population can be improved by using materials with large uniaxial perpendicular anisotropy such as Bi-doped YIG, proposing that a larger concentration of magnons in a given mode is allowed. This is on one side thanks to the suppression of the elliptic precession of small wave-vector magnons, which is one of the main sources of non-linear processes. On the other side, poor thermalization of the film increases the temperature underneath the emitter electrode, shifting down the dispersion relation compared to the region outside the emitter. This prevents the propagation of magnons out of the heated area and instead localization of magnons is promoted. With a large anisotropy comparable to the magnetization, it is possible to reduce the feedback contribution of the magnetization on the Kittel frequency. Indeed experimentally we observed improved growth of the conduction in the measurements. Lastly, we found that the main driving force governing the conduction behavior is the thermal fluctuation underneath the emitter. Through systematic comparison of the same devices in which we either modify the spin to charge conversion efficiency at YIG|Pt interface, or the temperature profile, we found that the results scale on top of each other when renormalized by the temperature below the emitter, and this is independent of the amount of spins being injected. This leads to the conclusion that thermal fluctuations are the main ingredient controlling the asymmetric non-linear conduction regime. In short, the spin injection is not important but the effect of Joule heating on reducing the magnetization rescales every around the emitter temperature.

Linked with the previous chapter, chapter 5 was dedicated to understanding the spectral nature of the magnons emitted by the spin transfer effect. The energy range of the magnons is wide-spread, from $\hbar\omega_K$ (GHz) to k_BT (THz). We showed experimentally the viewpoint as a *two-fluid behavior*, which simplifies the picture as emanating from magnons placed at both ends of the magnon dispersion relation. This explains the different $I-V$ characteristics among devices with different separation d between the emitter and collector. We succeeded in fitting the data sets with different d by considering the contributions from the two fluids with different characteristic decay lengths. It allows us to extract the decay length of the low-energy magnons as about 2 μm and one of the high-energy magnons as about 0.5 μm. Since they decay faster, their ratio decreases as d increases. Considering the nominal spin to charge conversion efficiency obtained from the spin mixing conductance, we estimated that two-thirds of the total generated spins remain localized and do not participate in the conduction. It means that we only sense a small portion of initially injected spins. Finally, we concluded that the low-energy magnons may become the dominant fluid i) at a large spin transfer rate, ii) at a large distance from the emitter d, iii) at small film thickness or iv) for reduced band mismatch between the YIG beneath the emitter and the bulk due to temperature change.

Knowing that we promote the low-energy magnons with large d and uniaxial perpendicular anisotropy, chapter 6 focuses on the observation of the control of such magnons using BiYIG with $d = 3.3$ μm. We observed amplification of the conduction of low-energy

magnons by a factor of 3.4 by heating locally the region beneath the collector electrode. For that purpose, we fabricated a third electrode deposited on top of the collector in thermal contact but electrically isolated by an intercalation layer of Si_3N_4 of 20 nm thickness. The motivation comes from the idea of amplifying $\Delta M_s/M_s$ the oscillation amplitude (cone angle of the precession) by locally reducing the magnetization M_s. The population of low-energy magnons is here controlled by bringing the magnon potential close to the energy gap of magnon manifold at a large current injection. This result demonstrates the reversible control of magnon transports. Previously reported methods were focusing on using a third Pt electrode in between the emitter and collector to provide an additional source of damping compensation, which already deteriorate the signal because Pt itself absorbs magnons. Our method is free from such deterioration with a comparable amplification ratio. Since the low-energy magnons can be described well with the LLG equation, we performed simulations with MuMax^3 to investigate the origin of this amplification. By introducing the local drop of magnetization, we demonstrated the control of the fluctuation amplitude. At first, it is enhanced following the inverse of the magnetization as expected, then the amplification deviates from it and boosts up. Such a sudden increase of enhancement qualitatively agrees with the experiments, but not quantitatively. The associated explanation with the simulations is the formation of the standing waves, suggesting that the magnetization gradient can act as a magnon mirror.

Chapter 7 was dedicated to proposing perspective research directions motivated by our transport results. The motivation was to elucidate the role of phonons in the long range transport properties of angular momentum observed in the transport experiments. The first result was the spectroscopic study on the magnon phonon coupling. In a recent work, we demonstrated the coherent long range coupling between two of the magnons from distant YIG layers separated through the paramagnetic GGG substrate. Knowing that YIG|GGG is a good platform for magnon phonon coupling, its application to non-local magnon transport is promising. The second one was the hydrodynamic behavior of magnon conduction. Although several theoretical investigations have been reported, any experimental evidence has not yet been realized. In chapter 4 we introduced the magnon-magnon interaction when the magnon population is excessive. We expect that the magnon-magnon scattering can be the shortest time (or length) scale. In this situation, hydrodynamic behaviors may emerge, just as observed in ultra clean electronic systems such as graphenes encapsulated with hexagonal boron nitride layers.

8.2 Personal contribution

Through the work of this thesis, I acquired the basic techniques to conduct research, device fabrication, measurements, and data analysis. As for the device fabrication, I contributed to device pattern designing, metal deposition, photolithography, development and lift-off processes, device cleaning, and SEM image acquisition under the supervision of Dr. Laurent Vila. I performed non-local magnon transport measurements and contributed to the automation and optimization of measurement protocols advised by Dr. Vladimir Naletov, Dr. Laurent Vila, and Dr. Olivier Klein. The interpretation and analyses of the obtained data and figure generation have been conducted with the guidance of Dr. Olivier Klein and Dr. Kyongmo An using Python programming. I performed simulations using MuMax^3 greatly stimulated by the previous work [122].

So far several results presented in this manuscript have been published or submitted:

- The works on the characteristic decay length of the high-energy thermal magnons

using an altered temperature profile which reveals their short range nature described in chapter 3 is published in Physical Review B 103, (17) 174432 (2021) entitled *Short range thermal magnon diffusion in magnetic garnet*" [119], where I contributed to the data analysis and discussion as the second author.

- Related to the works in chapter 4, the technical achievements on the enhanced YIG|Pt interfacial quality by injecting large current density is published in Applied Physics Letter 118 (3), 032404 (2021) entitled *"Enhancement of YIG|Pt spin conductance by local Joule annealing"*, where I contributed to the data analysis, discussion, figure generation and manuscript writing as the first author.

- The work on the asymmetric transport behavior of low-energy magnon described in chapter 4 is submitted in Physical Review B and uploaded on ArXiV (arXiv:2210.08304) entitled *"Nonlocal magnon transconductance in extended magnetic insulating films. I: spin diode effect."*, where I contributed to the data analysis, discussion, figure generation, and manuscript writing as the first author.

- The work on the two-fluid behavior of magnon transport by the spin transfer effect described in chapter 5 is submitted in Physical Review B and uploaded on ArXiV (arXiv:2210.08283) entitled *"Nonlocal magnon transconductance in extended magnetic insulating films. II: two-fluid behavior."*, where I contributed to the sample fabrication, data acquisition, data analysis, discussion, figure generation, and manuscript writing as the first author.

Other results that will be submitted soon:

- The work on the amplification of low-energy magnons by local heating described in chapter 6 is in preparation and close to submission entitled *"Amplified magnon transport in Bi-doped YIG by local heating"*, where I contributed to the sample fabrication, data acquisition, data analysis, simulation, discussion, figure generation and manuscript writing as the first author.

- Related to the works in chapter 4 and 5, we are preparing a manuscript focusing on the negative differential conductance of the magnon transport in magnonic devices as entitled "*Negative differential spin conductance in magnetic oxides thin films*", where I contributed to the sample fabrication, data acquisition, data analysis, discussion, figure generation and manuscript writing as the first author.

Works related to the magnon-phonon coupling phenomenon mentioned in chapter 7 led by Dr. Kyongmo An:

- Experimental evidence of strong coupling in YIG|GGG systems and interference effects mediated by phonons in a trilayer YIG|GGG|YIG is published in Physical Review B 101 (6) 060407 as entitled "*Coherent long-range transfer of angular momentum between magnon Kittel modes by phonons*", where I contributed to the data acquisition, data analysis, and discussion as the third author.

- Experimental demonstration of the bright and dark states of magnon-phonon-magnon systems whose resonances are identical using the trilayer YIG|GGG|YIG is published in Physical Review X 12 (1) 011060 entitled "*Bright and dark states of two distant macrospins strongly coupled by phonons*", where I contributed to the sample fabrication, data acquisition, data analysis, discussion, and manuscript writing as the second author.

- Experimental evidence of non-local absorption of heat carried by GHz ballistic phonons in YIG|GGG|Metal systems is in preparation and entitled "*Non-local absorption of ballistic phonons*", where I contributed to the sample fabrication, data acquisition, data analysis, and discussion as the second author.

- Demonstration of evident magnon-phonon coupling measured by the Brillouin light scattering which shows dependence on the magnetic field direction in YIG|GGG systems is in preparation and entitled "*Optical detection of tunable coupling strength in magnon polaron hybrid states*", where I contributed to the sample fabrication, and discussion as a co-author.

8.3 Acknowledgement

I profoundly thank my thesis directors Dr. Olivier Klein and Dr. Laurent Vila, who guided my first deep exposure to science and supported me to be a fledgling scientist. Especially Olivier helps me to advance our understanding of the obtained results which stems from his tremendous amount of knowledge not only on this topic but also on general physics. Through his direction, I learned what the research should be, which is based on complete data set with a step-by-step understanding of physics. I am very lucky to have this opportunity to write a two-volume review on this subject during my thesis, which will be a milestone of my future career path that proves our accomplishments of deep investigation, thinking, and thorough understanding. Laurent, even though he has been very busy with other subjects, has supported me enormously with not only the clean room activities but also the mental support. He often had lunch with us, visited our office, and invited us for drinks or skiing to give us opportunities to casually chat about our daily lives and lab lives. Without him, my stay in France would have been probably difficult. Thanks to their international networks, I had many opportunities to meet world-leading scientists. Especially I had a chance to interact with Prof. Dr. Yoshichika Otani and this led to a precious opportunity to stay in his laboratory at RIKEN in Japan. Subsequently, I had a chance to visit the team of Dr. Jun'ichi Ieda and Dr. Kei Yamamoto at JAEA in Japan during the third year of my thesis. That experience was full of stimulation and they cultivated my perspectives on spintronics and my future career. Dr. Nicolas Thiery, who was a former Ph.D. student in our group, has pioneered our research on magnon transports building the measurement setup and collecting a large amount of data. I feel honored to continue his research and step it further. I also deeply thank Dr. Grégoire de Loubens, Dr. Richard Schlitz, Dr. Vladimir Naletov, and Dr. Kyongmo An who greatly contributed to improving our understanding and manuscript writing. In particular, Kyongmo and Richard gave me chances to casually consult about physics, which I realized how important after they left. My colleagues and friends, Dr. Maxen Cosset-Chéneau, Dr. Sambit Ghosh, Dr. Cécile Grezes, Mr. Salvatore Teresi, Mr. Paolo Sgarro, Mr. Taro Komori, Ms. Aurélie Kandazoglou, Mr. Théo Frottier, Mr. Charles-Ellie Fillion, Mr. Eric Clot, Dr. Michaela Lammel, and all other students in Spintec, they brightened up my daily lives in Grenoble. Finally, I thank Nao Yoshizawa for having made the mountain life in Grenoble so much fun and exciting, and my mother and father and sister for having supported my stay in France for 5.5 years.

Bibliography

[1] M. N. Baibich, J. M. Broto, A. Fert, F. Nguyen Van Dau, F. Petroff, P. Etienne, G. Creuzet, A. Friederich, and J. Chazelas. Giant magnetoresistance of (001)fe/(001)cr magnetic superlattices. *Physical Review Letters*, 61(21):2472–2475, 1988.

[2] G Binasch, P Grünberg, F Saurenbach, and W Zinn. Enhanced magnetoresistance in layered magnetic structures with antiferromagnetic interlayer exchange. *Physical review B*, 39(7):4828, 1989.

[3] Albert Fert. Nobel lecture: Origin, development, and future of spintronics. *Reviews of Modern Physics*, 80(4):1517, 2008.

[4] Anders SG Andrae and Tomas Edler. On global electricity usage of communication technology: trends to 2030. *Challenges*, 6(1):117–157, 2015.

[5] Bernard Dieny, Ioan Lucian Prejbeanu, Kevin Garello, Pietro Gambardella, Paulo Freitas, Ronald Lehndorff, Wolfgang Raberg, Ursula Ebels, Sergej O Demokritov, Johan Akerman, et al. Opportunities and challenges for spintronics in the microelectronics industry. *Nature Electronics*, 3(8):446–459, 2020.

[6] Atsufumi Hirohata, Keisuke Yamada, Yoshinobu Nakatani, Ioan-Lucian Prejbeanu, Bernard Diény, Philipp Pirro, and Burkard Hillebrands. Review on spintronics: Principles and device applications. *Journal of Magnetism and Magnetic Materials*, 509:166711, 2020.

[7] Michel Julliere. Tunneling between ferromagnetic films. *Physics letters A*, 54(3):225–226, 1975.

[8] Jagadeesh Subbaiah Moodera, Lisa R Kinder, Terrilyn M Wong, and R Meservey. Large magnetoresistance at room temperature in ferromagnetic thin film tunnel junctions. *Physical review letters*, 74(16):3273, 1995.

[9] Wei Yuan, Qiong Zhu, Tang Su, Yunyan Yao, Wenyu Xing, Yangyang Chen, Yang Ma, Xi Lin, Jing Shi, Ryuichi Shindou, et al. Experimental signatures of spin superfluid ground state in canted antiferromagnet Cr2O3 via nonlocal spin transport. *Science advances*, 4(4):eaat1098, 2018.

[10] Stuart SP Parkin, Christian Kaiser, Alex Panchula, Philip M Rice, Brian Hughes, Mahesh Samant, and See-Hun Yang. Giant tunnelling magnetoresistance at room temperature with MgO (100) tunnel barriers. *Nature materials*, 3(12):862–867, 2004.

[11] John C Slonczewski. Current-driven excitation of magnetic multilayers. *Journal of Magnetism and Magnetic Materials*, 159(1-2):L1–L7, 1996.

[12] Luc Berger. Emission of spin waves by a magnetic multilayer traversed by a current. *Physical Review B*, 54(13):9353, 1996.

[13] Shuichi Murakami, Naoto Nagaosa, and Shou-Cheng Zhang. Dissipationless quantum spin current at room temperature. *Science*, 301(5638):1348–1351, 2003.

[14] Yuichiro K Kato, Roberto C Myers, Arthur C Gossard, and David D Awschalom. Observation of the spin Hall effect in semiconductors. *science*, 306(5703):1910–1913, 2004.

[15] Sergio O Valenzuela and M Tinkham. Direct electronic measurement of the spin Hall effect. *Nature*, 442(7099):176–179, 2006.

[16] Ioan Mihai Miron, Kevin Garello, Gilles Gaudin, Pierre-Jean Zermatten, Marius V. Costache, Stephane Auffret, Sebastien Bandiera, Bernard Rodmacq, Alain Schuhl, and Pietro Gambardella. Perpendicular switching of a single ferromagnetic layer induced by in-plane current injection. *Nature*, 476(7359):189–193, August 2011.

[17] Jairo Sinova, Sergio O Valenzuela, J Wunderlich, CH Back, and T Jungwirth. Spin Hall effects. *Reviews of Modern Physics*, 87(4):1213, 2015.

[18] Viola Krizakova, Manu Perumkunnil, Sébastien Couet, Pietro Gambardella, and Kevin Garello. Spin-orbit torque switching of magnetic tunnel junctions for memory applications. *Journal of Magnetism and Magnetic Materials*, 562:169692, 2022.

[19] AV Chumak, VI Vasyuchka, AA Serga, and Burkard Hillebrands. Magnon spintronics. *Nature Physics*, 11(6):453, 2015.

[20] AV Chumak, P Kabos, M Wu, C Abert, C Adelmann, AO Adeyeye, J Åkerman, FG Aliev, A Anane, A Awad, et al. Advances in magnetics roadmap on spin-wave computing. *IEEE Transactions on Magnetics*, 58(6):1–72, 2022.

[21] Shaffique Adam, Mikhail L. Polianski, and Piet W. Brouwer. Current-induced transverse spin-wave instability in thin ferromagnets: Beyond linear stability analysis. *Physical Review B (Condensed Matter and Materials Physics)*, 73(2):024425, 2006.

[22] Andrii V Chumak, Alexander A Serga, and Burkard Hillebrands. Magnon transistor for all-magnon data processing. *Nature communications*, 5(1):1–8, 2014.

[23] Philipp Pirro, Vitaliy I Vasyuchka, Alexander A Serga, and Burkard Hillebrands. Advances in coherent magnonics. *Nature Reviews Materials*, 6(12):1114–1135, 2021.

[24] Alexander G Gurevich and Gennadii A Melkov. *Magnetization oscillations and waves*. CRC press, 1996.

[25] H Suhl. The theory of ferromagnetic resonance at high signal powers. *Journal of Physics and Chemistry of Solids*, 1(4):209–227, 1957.

[26] BA Kalinikos and AN Slavin. Theory of dipole-exchange spin wave spectrum for ferromagnetic films with mixed exchange boundary conditions. *Journal of Physics C: Solid State Physics*, 19(35):7013, 1986.

[27] Thomas Schneider, Alexander A Serga, Britta Leven, Burkard Hillebrands, Robert L Stamps, and Mikhail P Kostylev. Realization of spin-wave logic gates. *Applied Physics Letters*, 92(2):022505, 2008.

[28] Stefan Klingler, Philipp Pirro, Thomas Brächer, Britta Leven, Burkard Hillebrands, and Andrii V Chumak. Design of a spin-wave majority gate employing mode selection. *Applied Physics Letters*, 105(15):152410, 2014.

[29] Qi Wang, M Kewenig, M Schneider, Roman Verba, F Kohl, B Heinz, M Geilen, M Mohseni, B Lägel, F Ciubotaru, et al. A magnonic directional coupler for integrated magnonic half-adders. *Nature Electronics*, 3(12):765–774, 2020.

[30] Ádám Papp, Wolfgang Porod, and Gyorgy Csaba. Nanoscale neural network using non-linear spin-wave interference. *Nature communications*, 12(1):1–8, 2021.

[31] Qi Wang, Andrii V Chumak, and Philipp Pirro. Inverse-design magnonic devices. *Nature communications*, 12(1):1–9, 2021.

[32] Aleksandr Vladimirovich Sadovnikov, Andrei Andreevich Grachev, SA Odintsov, AA Martyshkin, Vladislav Andreevich Gubanov, Svetlana Evgen'evna Sheshukova, and Sergei Apollonovich Nikitov. Neuromorphic calculations using lateral arrays of magnetic microstructures with broken translational symmetry. *JETP Letters*, 108(5):312–317, 2018.

[33] Stuart Watt, Mikhail Kostylev, Alexey B Ustinov, and Boris A Kalinikos. Implementing a magnonic reservoir computer model based on time-delay multiplexing. *Physical Review Applied*, 15(6):064060, 2021.

[34] Lukas Körber, Christopher Heins, Tobias Hula, Joo-Von Kim, Helmut Schultheiss, Jürgen Fassbender, and Katrin Schultheiss. Pattern recognition with a magnon-scattering reservoir. *arXiv preprint arXiv:2211.02328*, 2022.

[35] Brooke C McGoldrick, Jonathan Z Sun, and Luqiao Liu. Ising machine based on electrically coupled spin Hall nano-oscillators. *Physical Review Applied*, 17(1):014006, 2022.

[36] Artem Litvinenko, Roman Khymyn, Victor H González, Ahmad A Awad, Vasyl Tyberkevych, Andrei Slavin, and Johan Åkerman. A spinwave ising machine. *arXiv preprint arXiv:2209.04291*, 2022.

[37] M. Tsoi, V. Tsoi, J. Bass, A. G. M. Jansen, and P. Wyder. Current-driven resonances in magnetic multilayers. *Physical Review Letters*, 89(24):246803, 2002.

[38] M. Tsoi, A. G. M. Jansen, J. Bass, W.-C. Chiang, V. Tsoi, and P. Wyder. Generation and detection of phase-coherent current-driven magnons in magnetic multilayers. *Nature*, 406(6791):46–48, July 2000.

[39] N. Locatelli, V. V. Naletov, J. Grollier, G. de Loubens, V. Cros, C. Deranlot, C. Ulysse, G. Faini, O. Klein, and A. Fert. Dynamics of two coupled vortices in a spin valve nanopillar excited by spin transfer torque. *APL*, 98(6):062501, 2011.

[40] D. Houssameddine, U. Ebels, B. Delaët, B. Rodmacq, I. Firastrau, F. Ponthenier, M. Brunet, C. Thirion, J.-P. Michel, L. Prejbeanu-Buda, M.-C. Cyrille, O. Redon, and B. Dieny. Spin-torque oscillator using a perpendicular polarizer and a planar free layer. *Nature materials*, 6:447, 2007.

[41] Tingsu Chen, Randy K Dumas, Anders Eklund, Pranaba K Muduli, Afshin Houshang, Ahmad A Awad, Philipp Dürrenfeld, B Gunnar Malm, Ana Rusu, and Johan Åkerman. Spin-torque and spin-Hall nano-oscillators. *Proceedings of the IEEE*, 104(10):1919–1945, 2016.

[42] Julie Grollier, Damien Querlioz, KY Camsari, Karin Everschor-Sitte, Shunsuke Fukami, and Mark D Stiles. Neuromorphic spintronics. *Nature electronics*, 3(7):360–370, 2020.

[43] E. Saitoh, M. Ueda, H. Miyajima, and G. Tatara. Conversion of spin current into charge current at room temperature: Inverse spin-Hall effect. *Applied Physics Letters*, 88(18):182509, 2006.

[44] Yaroslav Tserkovnyak and Arne Brataas. Current and spin torque in double tunnel barrier ferromagnet-superconductor- ferromagnet systems. *Physical Review B (Condensed Matter and Materials Physics)*, 65(9):094517, 2002.

[45] M. V. Costache, S. M. Watts, M. Sladkov, C. H. van der Wal, and B. J. van Wees. Large cone angle magnetization precession of an individual nanopatterned ferromagnet with dc electrical detection. *Applied Physics Letters*, 89(23):232115, dec 2006.

[46] K Uchida, S Takahashi, K Harii, J Ieda, W Koshibae, Kazuya Ando, S Maekawa, and E Saitoh. Observation of the spin Seebeck effect. *Nature*, 455(7214):778–781, 2008.

[47] K. Uchida, J. Xiao, H. Adachi, J. Ohe, S. Takahashi, J. Ieda, T. Ota, Y. Kajiwara, H. Umezawa, H. Kawai, G. E. W. Bauer, S. Maekawa, and E. Saitoh. Spin Seebeck insulator. *Nature Materials*, 9(11):894–897, NOV 2010.

[48] Gerrit EW Bauer, Eiji Saitoh, and Bart J Van Wees. Spin caloritronics. *Nature materials*, 11(5):391–399, 2012.

[49] Vladislav E Demidov, Sergei Urazhdin, ERJ Edwards, Mark D Stiles, Robert D McMichael, and Sergej O Demokritov. Control of magnetic fluctuations by spin current. *Physical review letters*, 107(10):107204, 2011.

[50] M Madami, S Bonetti, G Consolo, S Tacchi, G Carlotti, G Gubbiotti, FB Mancoff, Mazher Ahmed Yar, and Johan Åkerman. Direct observation of a propagating spin wave induced by spin-transfer torque. *Nature nanotechnology*, 6(10):635–638, 2011.

[51] Y Kajiwara, K Harii, S Takahashi, Jun-ichiro Ohe, K Uchida, M Mizuguchi, H Umezawa, H Kawai, Kazuya Ando, K Takanashi, et al. Transmission of electrical signals by spin-wave interconversion in a magnetic insulator. *Nature*, 464(7286):262, 2010.

[52] LJ Cornelissen, J Liu, RA Duine, J Ben Youssef, and BJ Van Wees. Long-distance transport of magnon spin information in a magnetic insulator at room temperature. *Nature Physics*, 11(12):1022, 2015.

[53] Sebastian TB Goennenwein, Richard Schlitz, Matthias Pernpeintner, Kathrin Ganzhorn, Matthias Althammer, Rudolf Gross, and Hans Huebl. Non-local magnetoresistance in YIG/Pt nanostructures. *Applied Physics Letters*, 107(17):172405, 2015.

[54] Hiroto Adachi, Ken-ichi Uchida, Eiji Saitoh, and Sadamichi Maekawa. Theory of the spin Seebck effect. *Reports on Progress in Physics*, 76(3):036501, 2013.

[55] Sadamichi Maekawa, Hiroto Adachi, Ken ichi Uchida, Jun'ichi Ieda, and Eiji Saitoh. Spin current: Experimental and theoretical aspects. *Journal of the Physical Society of Japan*, 82(10):102002, oct 2013.

[56] Nicolas Thiery, Antoine Draveny, Vladimir V Naletov, Laurent Vila, Jean-Philippe Attané, C Beigné, G de Loubens, M Viret, N Beaulieu, J Ben Youssef, et al. Nonlinear spin conductance of yttrium iron garnet thin films driven by large spin-orbit torque. *Physical Review B*, 97(6):060409, 2018.

[57] Tobias Wimmer, Matthias Althammer, Lukas Liensberger, Nynke Vlietstra, Stephan Geprägs, Mathias Weiler, Rudolf Gross, and Hans Huebl. Spin transport in a magnetic insulator with zero effective damping. *Physical Review Letters*, 123(25):257201, 2019.

[58] Andrei Slavin and Vasil Tiberkevich. Nonlinear auto-oscillator theory of microwave generation by spin-polarized current. *IEEE Transactions on Magnetics*, 45(4):1875–1918, 2009.

[59] Richard Schlitz, Saül Vélez, Akashdeep Kamra, Charles-Henri Lambert, Michaela Lammel, Sebastian TB Goennenwein, and Pietro Gambardella. Control of nonlocal magnon spin transport via magnon drift currents. *Physical Review Letters*, 126(25):257201, 2021.

[60] LD Landau. Über die bewegung der elektronen in kristallgitter. *Phys. Z. Sowjetunion*, 3:644–645, 1933.

[61] V. V. Naletov, G. de Loubens, G. Albuquerque, S. Borlenghi, V. Cros, G. Faini, J. Grollier, H. Hurdequint, N. Locatelli, B. Pigeau, A. N. Slavin, V. S. Tiberkevich, C. Ulysse, T. Valet, and O. Klein. Identification and selection rules of the spin-wave eigenmodes in a normally magnetized nanopillar. *Phys. Rev. B*, 84:224423, Dec 2011.

[62] S. Tandon, M. Beleggia, Y. Zhu, and M. De Graef. On the computation of the demagnetization tensor for uniformly magnetized particles of arbitrary shape. part ii: numerical approach. *Journal Of Magnetism And Magnetic Materials*, 271(1):27–38, April 2004.

[63] C. Hahn, V. V. Naletov, G. de Loubens, O. Klein, O. d'Allivy Kelly, A. Anane, R. Bernard, E. Jacquet, P. Bortolotti, V. Cros, J. L. Prieto, and M. Muñoz. Measurement of the intrinsic damping constant in individual nanodisks of y3fe5o12 and y3fe5o12|pt. *Applied Physics Letters*, 104(15):152410, apr 2014.

[64] J Holanda, DS Maior, A Azevedo, and SM Rezende. Detecting the phonon spin in magnon-phonon conversion experiments. *Nature Physics*, 14:500–506, 2018.

[65] Marc Vogel, Rick Aßmann, Philipp Pirro, Andrii V Chumak, Burkard Hillebrands, and Georg von Freymann. Control of spin-wave propagation using magnetisation gradients. *Scientific reports*, 8(1):1–10, 2018.

[66] S. O. Demokritov, A. A. Serga, A. André, V. E. Demidov, M. P. Kostylev, B. Hillebrands, and A. N. Slavin. Tunneling of dipolar spin waves through a region of inhomogeneous magnetic field. *Physical Review Letters*, 93(4), jul 2004.

[67] Thomas Brächer, Philipp Pirro, and Burkard Hillebrands. Parallel pumping for magnon spintronics: Amplification and manipulation of magnon spin currents on the micron-scale. *Physics Reports*, 699:1–34, 2017.

[68] Hans G. Bauer, Peter Majchrak, Torsten Kachel, Christian H. Back, and Georg Woltersdorf. Nonlinear spin-wave excitations at low magnetic bias fields. *Nature Communications*, 6:8274, sep 2015.

[69] H Schultheiss, K Vogt, and B Hillebrands. Direct observation of nonlinear four-magnon scattering in spin-wave microconduits. *Physical Review B*, 86(5):054414, 2012.

[70] H. Suhl. *J. Appl. Phys.*, 30:1961, 1959.

[71] H Schultheiss, Xavier Janssens, Maarten van Kampen, F Ciubotaru, SJ Hermsdoerfer, B Obry, A Laraoui, AA Serga, Liesbet Lagae, AN Slavin, et al. Direct current control of three magnon scattering processes in spin-valve nanocontacts. *Physical review letters*, 103(15):157202, 2009.

[72] Tobias Hula, Katrin Schultheiss, Aleksandr Buzdakov, Lukas Körber, Mauricio Bejarano, Luis Flacke, Lukas Liensberger, Mathias Weiler, Justin M Shaw, Hans T Nembach, et al. Nonlinear losses in magnon transport due to four-magnon scattering. *Applied physics letters*, 117(4):042404, 2020.

[73] Alexander G Gurevich and Gennadii A Melkov. *Magnetization oscillations and waves*. CRC press, 2020.

[74] OG Vendik, BA Kalinikos, and DN Chartorizhskii. Instability of spin-waves in tangentially magnetized ferromagnetic-films. *FIZIKA TVERDOGO TELA*, 19(2):387–396, 1977.

[75] E. Schlomann. Ferromagnetic resonance at high power levels. Technical report, 1959.

[76] E. Schlömann, J. J. Green, and U. Milano. Recent developments in ferromagnetic resonance at high power levels. *Journal of Applied Physics*, 31(5):S386–S395, 1960.

[77] Boris Divinskiy, Sergei Urazhdin, Sergej O Demokritov, and Vladislav E Demidov. Controlled nonlinear magnetic damping in spin-hall nano-devices. *Nature Communications*, 10(1):1–7, 2019.

[78] M Evelt, L Soumah, AB Rinkevich, SO Demokritov, A Anane, V Cros, Jamal Ben Youssef, G De Loubens, O Klein, P Bortolotti, et al. Emission of coherent propagating magnons by insulator-based spin-orbit-torque oscillators. *Physical Review Applied*, 10(4):041002, 2018.

[79] J Gückelhorn, T Wimmer, M Müller, S Geprägs, H Huebl, R Gross, and M Althammer. Magnon transport in y 3 fe 5 o 12/pt nanostructures with reduced effective magnetization. *Physical Review B*, 104(18):L180410, 2021.

[80] L. Berger. *Phys. Rev. B*, 54:9353, 1996.

[81] André Thiaville and Yoshinobu Nakatani. Domain-wall dynamics in nanowiresand nanostrips. In *Spin dynamics in confined magnetic structures III*, pages 161–205. Springer, 2006.

[82] Albert Fert, Vincent Cros, and Joao Sampaio. Skyrmions on the track. *Nature nanotechnology*, 8(3):152–156, 2013.

[83] J. Grollier, V. Cros, A. Hamzic, J. M. George, H. Jaffres, A. Fert, G. Faini, J. Ben Youssef, and H. Legall. Spin-polarized current induced switching in co/cu/co pillars. *Applied Physics Letters*, 78(23):3663–3665, 2001.

[84] S. I. Kiselev, J. C. Sankey, I. N. Krivorotov, N. C. Emley, M. Rinkoski, C. Perez, R. A. Buhrman, and D. C. Ralph. Current-induced nanomagnet dynamics for magnetic fields perpendicular to the sample plane. *Physical Review Letters*, 93(3):036601, 2004.

[85] Pham Nam Hai, Shinobu Ohya, Masaaki Tanaka, Stewart E Barnes, and Sadamichi Maekawa. Electromotive force and huge magnetoresistance in magnetic tunnel junctions. *Nature*, 458(7237):489–492, 2009.

[86] Masamitsu Hayashi, Jun'ichi Ieda, Yuta Yamane, Jun-ichiro Ohe, Yukiko K Takahashi, Seiji Mitani, and Sadamichi Maekawa. Time-domain observation of the spin-motive force in permalloy nanowires. *Physical review letters*, 108(14):147202, 2012.

[87] E Saitoh, M Ueda, H Miyajima, and G Tatara. Conversion of spin current into charge current at room temperature: Inverse spin-Hall effect. *Applied physics letters*, 88(18):182509, 2006.

[88] Ioan Mihai Miron, Gilles Gaudin, Stéphane Auffret, Bernard Rodmacq, Alain Schuhl, Stefania Pizzini, Jan Vogel, and Pietro Gambardella. Current-driven spin torque induced by the rashba effect in a ferromagnetic metal layer. *Nature materials*, 9(3):230–234, 2010.

[89] JC Rojas Sánchez, Laurent Vila, G Desfonds, S Gambarelli, JP Attané, JM De Teresa, C Magén, and A Fert. Spin-to-charge conversion using rashba coupling at the interface between non-magnetic materials. *Nature communications*, 4:2944, 2013.

[90] J-C Rojas-Sánchez, N Reyren, P Laczkowski, W Savero, J-P Attané, C Deranlot, M Jamet, J-M George, Laurent Vila, and H Jaffrès. Spin pumping and inverse spin Hall effect in platinum: the essential role of spin-memory loss at metallic interfaces. *Physical review letters*, 112(10):106602, 2014.

[91] Yaroslav Tserkovnyak, Arne Brataas, and Gerrit EW Bauer. Spin pumping and magnetization dynamics in metallic multilayers. *Physical Review B*, 66(22):224403, 2002.

[92] Arne Brataas, Bart van Wees, Olivier Klein, Grégoire de Loubens, and Michel Viret. Spin insulatronics. *Physics Reports*, 885:1–27, 2020.

[93] A. N. Slavin and V. Tiberkevich. Nonlinear auto-oscillator theory of microwave generation by spin-polarized current. *IEEE Transactions on Magnetics*, 45(4):1875 –1918, april 2009.

[94] Miguel Romera, Philippe Talatchian, Sumito Tsunegi, Flavio Abreu Araujo, Vincent Cros, Paolo Bortolotti, Juan Trastoy, Kay Yakushiji, Akio Fukushima, Hitoshi Kubota, et al. Vowel recognition with four coupled spin-torque nano-oscillators. *Nature*, 563(7730):230–234, 2018.

[95] Jacob Torrejon, Mathieu Riou, Flavio Abreu Araujo, Sumito Tsunegi, Guru Khalsa, Damien Querlioz, Paolo Bortolotti, Vincent Cros, Kay Yakushiji, Akio Fukushima, et al. Neuromorphic computing with nanoscale spintronic oscillators. *Nature*, 547(7664):428–431, 2017.

[96] IV Borisenko, VE Demidov, S Urazhdin, AB Rinkevich, and SO Demokritov. Relation between unidirectional spin Hall magnetoresistance and spin current-driven magnon generation. *Applied Physics Letters*, 113(6):062403, 2018.

[97] M. Collet, X. de Milly, O. d'Allivy Kelly, V. V. Naletov, R. Bernard, P. Bortolotti, J. Ben Youssef, V. E. Demidov, S. O. Demokritov, J. L. Prieto, M. Munoz, V. Cros, A. Anane, G. de Loubens, and O. Klein. Generation of coherent spin-wave modes

in yttrium iron garnet microdiscs by spin-orbit torque. *Nature Communications*, 7:–, January 2016.

[98] VE Demidov, M Evelt, V Bessonov, SO Demokritov, JL Prieto, M Muñoz, J Ben Youssef, VV Naletov, G De Loubens, Olivier Klein, et al. Direct observation of dynamic modes excited in a magnetic insulator by pure spin current. *Scientific reports*, 6:32781, 2016.

[99] Hugo Merbouche. *Magnonic circuits based on nanostructured ultra-thin YIG for radiofrequency applications*. PhD thesis, 2021. Thèse de doctorat dirigée par Anane, Abdelmadjid et Bortolotti, Paolo Physique université Paris-Saclay 2021.

[100] Kyongmo An, Daniel R Birt, Chi-Feng Pai, Kevin Olsson, Daniel C Ralph, Robert A Buhrman, and Xiaoqin Li. Control of propagating spin waves via spin transfer torque in a metallic bilayer waveguide. *Physical Review B*, 89(14):140405, 2014.

[101] Boris Divinskiy, Vladislav E Demidov, Sergei Urazhdin, Ryan Freeman, Anatoly B Rinkevich, and Sergej O Demokritov. Excitation and amplification of spin waves by spin–orbit torque. *Advanced Materials*, 30(33):1802837, 2018.

[102] N. Thiery, A. Draveny, V. V. Naletov, L. Vila, J. P. Attané, C. Beigné, G. de Loubens, M. Viret, N. Beaulieu, J. Ben Youssef, V. E. Demidov, S. O. Demokritov, A. N. Slavin, V. S. Tiberkevich, A. Anane, P. Bortolotti, V. Cros, and O. Klein. Nonlinear spin conductance of yttrium iron garnet thin films driven by large spin-orbit torque. *Physical Review B*, 97(6), feb 2018.

[103] M. Evelt, L. Soumah, A.B. Rinkevich, S.O. Demokritov, A. Anane, V. Cros, Jamal Ben Youssef, G. de Loubens, O. Klein, P. Bortolotti, and V.E. Demidov. Emission of coherent propagating magnons by insulator-based spin-orbit-torque oscillators. *Physical Review Applied*, 10(4), oct 2018.

[104] Vladislav E. Demidov, Sergei Urazhdin, Henning Ulrichs, Vasyl Tiberkevich, Andrei Slavin, Dietmar Baither, Guido Schmitz, and Sergej O. Demokritov. Magnetic nano-oscillator driven by pure spin current. *Nature Materials*, 11(12):1028–1031, oct 2012.

[105] N Thiery, VV Naletov, L Vila, A Marty, A Brenac, J-F Jacquot, G de Loubens, M Viret, A Anane, V Cros, et al. Electrical properties of epitaxial yttrium iron garnet ultrathin films at high temperatures. *Physical Review B*, 97(6):064422, 2018.

[106] H. Suhl. *J. Phys. Chem. Solids*, 1:209, 1957.

[107] P. W. Anderson and H. Suhl. *Phys. Rev.*, 100:1788, 1955.

[108] I Barsukov, HK Lee, AA Jara, Y-J Chen, AM Gonçalves, C Sha, JA Katine, RE Arias, BA Ivanov, and IN Krivorotov. Giant nonlinear damping in nanoscale ferromagnets. *Science advances*, 5(10):eaav6943, 2019.

[109] LJ Cornelissen, J Liu, BJ Van Wees, and RA Duine. Spin-current-controlled modulation of the magnon spin conductance in a three-terminal magnon transistor. *Physical review letters*, 120(9):097702, 2018.

[110] VE Demidov, S Urazhdin, B Divinskiy, VD Bessonov, AB Rinkevich, VV Ustinov, and SO Demokritov. Chemical potential of quasi-equilibrium magnon gas driven by pure spin current. *Nature communications*, 8(1):1579, 2017.

[111] S. O. Demokritov, V. E. Demidov, O. Dzyapko, G. A. Melkov, A. A. Serga, B. Hillebrands, and A. N. Slavin. Bose–einstein condensation of quasi-equilibrium magnons at room temperature under pumping. *Nature*, 443(7110):430–433, 2006.

[112] Maxime Jonker. Density of states of quasi-equilibrium bose-einstein condensed magnons in yig. B.S. thesis, 2014.

[113] L. J. Cornelissen, J. Liu, R. A. Duine, J. Ben Youssef, and B. J. van Wees. Long-distance transport of magnon spin information in a magnetic insulator at room temperature. *Nature Physics*, 11(12):1022–1026, December 2015.

[114] Janine Gückelhorn, Tobias Wimmer, Stephan Geprägs, Hans Huebl, Rudolf Gross, and Matthias Althammer. Quantitative comparison of magnon transport experiments in three-terminal YIG/Pt nanostructures acquired via dc and ac detection techniques. *Applied Physics Letters*, 117(18):182401, 2020.

[115] Christian Hahn, Grégoire De Loubens, Olivier Klein, Michel Viret, Vladimir V Naletov, and J Ben Youssef. Comparative measurements of inverse spin Hall effects and magnetoresistance in YIG/Pt and YIG/ta. *Physical Review B*, 87(17):174417, 2013.

[116] V. Castel, N. Vlietstra, B. J. van Wees, and J. Ben Youssef. Frequency and power dependence of spin-current emission by spin pumping in a thin-film yig/pt system. *Phys. Rev. B*, 86:134419, Oct 2012.

[117] Juan Shan, Ludo J. Cornelissen, Nynke Vlietstra, Jamal Ben Youssef, Timo Kuschel, Rembert A. Duine, and Bart J. van Wees. Influence of yttrium iron garnet thickness and heater opacity on the nonlocal transport of electrically and thermally excited magnons. *Physical Review B*, 94(17), nov 2016.

[118] P Borys, O Kolokoltsev, N Qureshi, ML Plumer, and TL Monchesky. Unidirectional spin wave propagation due to a saturation magnetization gradient. *Physical Review B*, 103(14):144411, 2021.

[119] Kyongmo An, Ryuhei Kohno, Nicolas Thiery, Derek Reitz, Laurent Vila, Vladimir V Naletov, Nathan Beaulieu, J Ben Youssef, Grégoire de Loubens, Yaroslav Tserkovnyak, et al. Short-range thermal magnon diffusion in magnetic garnet. *Physical Review B*, 103(17):174432, 2021.

[120] N. Thiery, V. V. Naletov, L. Vila, A. Marty, A. Brenac, J.-F. Jacquot, G. de Loubens, M. Viret, A. Anane, V. Cros, J. Ben Youssef, N. Beaulieu, V. E. Demidov, B. Divinskiy, S. O. Demokritov, and O. Klein. Electrical properties of epitaxial yttrium iron garnet ultrathin films at high temperatures. *Physical Review B*, 97(6), feb 2018.

[121] B A Kalinikos and A N Slavin. Theory of dipole-exchange spin wave spectrum for ferromagnetic films with mixed exchange boundary conditions. *Journal of Physics C: Solid State Physics*, 19(35):7013–7033, 1986.

[122] Henning Ulrichs. From chaotic spin dynamics to noncollinear spin textures in yig nanofilms by spin-current injection. *Physical Review B*, 102(17):174428, 2020.

[123] Andrei Slavin and Vasil Tiberkevich. Spin wave mode excited by spin-polarized current in a magnetic nanocontact is a standing self-localized wave bullet. *Physical Review Letters*, 95(23), nov 2005.

[124] Michael Schneider, David Breitbach, Rostyslav O Serha, Qi Wang, Morteza Mohseni, Alexander A Serga, Andrei N Slavin, Vasyl S Tiberkevich, Björn Heinz, Thomas Brächer, et al. Stabilization of a nonlinear magnonic bullet coexisting with a bose-einstein condensate in a rapidly cooled magnonic system driven by spin-orbit torque. *Physical Review B*, 104(14):L140405, 2021.

[125] Lucile Soumah, Nathan Beaulieu, Lilia Qassym, Cécile Carrétéro, Eric Jacquet, Richard Lebourgeois, Jamal Ben Youssef, Paolo Bortolotti, Vincent Cros, and Abdelmadjid Anane. Ultra-low damping insulating magnetic thin films get perpendicular. *Nature Communications*, 9(1), aug 2018.

[126] S. V. Vonsovskii. *Ferromagnetic Resonance*. Elsevier, 1966.

[127] Zheng Duan, Carl T. Boone, Xiao Cheng, Ilya N. Krivorotov, Nathalie Reckers, Sven Stienen, Michael Farle, and Jürgen Lindner. Spin-wave modes in permalloy/platinum wires and tuning of the mode damping by spin Hall current. *Phys. Rev. B*, 90:024427, Jul 2014.

[128] H. Suhl. Proposal for a ferromagnetic amplifier in the microwave range. *Phys. Rev.*, 106:384–385, Apr 1957.

[129] G. de Loubens, V. V. Naletov, and O. Klein. Reduction of the spin-wave damping induced by nonlinear effects. *Physical Review B (Condensed Matter and Materials Physics)*, 71(18):180411, 2005.

[130] Koichi Oyanagi, Saburo Takahashi, Ludo J. Cornelissen, Juan Shan, Shunsuke Daimon, Takashi Kikkawa, Gerrit E. W. Bauer, Bart J. van Wees, and Eiji Saitoh. Spin transport in insulators without exchange stiffness. *Nature Communications*, 10(1), oct 2019.

[131] Juan M Gomez-Perez, Saül Vélez, Luis E Hueso, and Fèlix Casanova. Differences in the magnon diffusion length for electrically and thermally driven magnon currents in y 3 f e 5 o 12. *Physical Review B*, 101(18):184420, 2020.

[132] Vladimir Cherepanov, Igor Kolokolov, and Victor L'vov. The saga of yig: Spectra, thermodynamics, interaction and relaxation of magnons in a complex magnet. *Physics Reports*, 229(3):81 – 144, 1993.

[133] JS Plant. Spinwave dispersion curves for yttrium iron garnet. *Journal of Physics C: Solid State Physics*, 10(23):4805, 1977.

[134] Joseph Barker and Gerrit EW Bauer. Thermal spin dynamics of yttrium iron garnet. *Physical review letters*, 117(21):217201, 2016.

[135] Andrew J Princep, Russell A Ewings, Simon Ward, Sandor Tóth, Carsten Dubs, Dharmalingam Prabhakaran, and Andrew T Boothroyd. The full magnon spectrum of yttrium iron garnet. *npj Quantum Materials*, 2(1):1–5, 2017.

[136] Y Nambu, Joseph Barker, Y Okino, Takashi Kikkawa, Yuki Shiomi, M Enderle, T Weber, B Winn, M Graves-Brook, JM Tranquada, et al. Observation of magnon polarization. *Physical review letters*, 125(2):027201, 2020.

[137] Hiroto Adachi, Ken ichi Uchida, Eiji Saitoh, and Sadamichi Maekawa. Theory of the spin Seebeck effect. *Reports on Progress in Physics*, 76(3):036501, feb 2013.

[138] Andreas Kehlberger, Ulrike Ritzmann, Denise Hinzke, Er-Jia Guo, Joel Cramer, Gerhard Jakob, Mehmet C. Onbasli, Dong Hun Kim, Caroline A. Ross, Matthias B. Jungfleisch, Burkard Hillebrands, Ulrich Nowak, and Mathias Kläui. Length scale of the spin Seebeck effect. *Physical Review Letters*, 115(9), aug 2015.

[139] Juan Shan, Ludo J Cornelissen, Nynke Vlietstra, Jamal Ben Youssef, Timo Kuschel, Rembert A Duine, and Bart J Van Wees. Influence of yttrium iron garnet thickness and heater opacity on the nonlocal transport of electrically and thermally excited magnons. *Physical Review B*, 94(17):174437, 2016.

[140] J Shan, LJ Cornelissen, J Liu, J Ben Youssef, L Liang, and BJ Van Wees. Criteria for accurate determination of the magnon relaxation length from the nonlocal spin Seebeck effect. *Physical Review B*, 96(18):184427, 2017.

[141] Ludo J Cornelissen, J Shan, and BJ Van Wees. Temperature dependence of the magnon spin diffusion length and magnon spin conductivity in the magnetic insulator yttrium iron garnet. *Physical Review B*, 94(18):180402, 2016.

[142] Ludo J Cornelissen, Kevin JH Peters, Gerrit EW Bauer, RA Duine, and Bart J van Wees. Magnon spin transport driven by the magnon chemical potential in a magnetic insulator. *Physical Review B*, 94(1):014412, 2016.

[143] Benedetta Flebus, SA Bender, Yaroslav Tserkovnyak, and RA Duine. Two-fluid theory for spin superfluidity in magnetic insulators. *Physical review letters*, 116(11):117201, 2016.

[144] Vincent Castel, Nynke Vlietstra, J Ben Youssef, and Bart J van Wees. Platinum thickness dependence of the inverse spin-hall voltage from spin pumping in a hybrid yttrium iron garnet/platinum system. *Applied Physics Letters*, 101(13):132414, 2012.

[145] Dany Lachance-Quirion, Samuel Piotr Wolski, Yutaka Tabuchi, Shingo Kono, Koji Usami, and Yasunobu Nakamura. Entanglement-based single-shot detection of a single magnon with a superconducting qubit. *Science*, 367(6476):425–428, jan 2020.

[146] Yi-Heng Rao, Huai-Wu Zhang, Qing-Hui Yang, Dai-Nan Zhang, Li-Chuan Jin, Bo Ma, and Yu-Juan Wu. Liquid phase epitaxy magnetic garnet films and their applications. *Chinese Physics B*, 27(8):086701, 2018.

[147] Lucile Soumah. *Pulsed Laser Deposition of Substituted thin Garnet Films for Magnonic Applications*. PhD thesis, 2019. Thèse de doctorat dirigée par Anane, Abdelmadjid Physique Université Paris-Saclay (ComUE) 2019.

[148] Michaela Lammel, Daniel Scheffler, Darius Pohl, Peter Swekis, Sven Reitzig, S Piontek, H Reichlova, R Schlitz, K Geishendorf, L Siegl, et al. Atomic layer deposition of yttrium iron garnet thin films. *Physical Review Materials*, 6(4):044411, 2022.

[149] Yaning Lin, Lichuan Jin, Huaiwu Zhang, Zhiyong Zhong, Qinghui Yang, Yiheng Rao, and Mingming Li. Bi-yig ferrimagnetic insulator nanometer films with large perpendicular magnetic anisotropy and narrow ferromagnetic resonance linewidth. *Journal of Magnetism and Magnetic Materials*, 496:165886, 2020.

[150] Richard Schlitz, Sergey Granovsky, Darius Pohl, Andy Thomas, Bernd Rellinghaus, and Sebastian TB Goennenwein. Nonlocal magnon-based transport in yttrium-iron-garnet–platinum heterostructures at high temperatures. *Physical Review B*, 103(21):214434, 2021.

[151] Kathrin Ganzhorn, Stefan Klingler, Tobias Wimmer, Stephan Geprägs, Rudolf Gross, Hans Huebl, and Sebastian TB Goennenwein. Magnon-based logic in a multi-terminal YIG/Pt nanostructure. *Applied Physics Letters*, 109(2):022405, 2016.

[152] Brandon L Giles, Zihao Yang, John S Jamison, and Roberto C Myers. Long-range pure magnon spin diffusion observed in a nonlocal spin-seebeck geometry. *Physical Review B*, 92(22):224415, 2015.

[153] Stephen R Boona and Joseph P Heremans. Magnon thermal mean free path in yttrium iron garnet. *Physical Review B*, 90(6):064421, 2014.

[154] Freeman J. Dyson. General theory of spin-wave interactions. *Physical Review*, 102(5):1217–1230, jun 1956.

[155] Vladimir Cherepanov, Igor Kolokolov, and Victor L'vov. The saga of YIG: spectra, thermodynamics, interaction and relaxation of magnons in a complex magnet. *Physics reports*, 229(3):81–144, 1993.

[156] Andreas Kehlberger, Ulrike Ritzmann, Denise Hinzke, Er-Jia Guo, Joel Cramer, Gerhard Jakob, Mehmet C Onbasli, Dong Hun Kim, Caroline A Ross, Matthias B Jungfleisch, et al. Length scale of the spin Seebck effect. *Physical review letters*, 115(9):096602, 2015.

[157] Arati Prakash, Benedetta Flebus, Jack Brangham, Fengyuan Yang, Yaroslav Tserkovnyak, and Joseph P Heremans. Evidence for the role of the magnon energy relaxation length in the spin Seebck effect. *Physical Review B*, 97(2):020408, 2018.

[158] M Agrawal, VI Vasyuchka, AA Serga, A Kirihara, P Pirro, T Langner, MB Jungfleisch, AV Chumak, E Th Papaioannou, and B Hillebrands. Role of bulk-magnon transport in the temporal evolution of the longitudinal spin-seebeck effect. *Physical Review B*, 89(22):224414, 2014.

[159] John S Jamison, Zihao Yang, Brandon L Giles, Jack T Brangham, Guanzhong Wu, P Chris Hammel, Fengyuan Yang, and Roberto C Myers. Long lifetime of thermally excited magnons in bulk yttrium iron garnet. *Physical Review B*, 100(13):134402, 2019.

[160] Camilo Ulloa, A Tomadin, J Shan, M Polini, BJ Van Wees, and RA Duine. Nonlocal spin transport as a probe of viscous magnon fluids. *Physical Review Letters*, 123(11):117203, 2019.

[161] Nathan Beaulieu, Nelly Kervarec, Nicolas Thiery, Olivier Klein, Vladimir Naletov, Hervé Hurdequint, Grégoire De Loubens, Jamal Ben Youssef, and Nicolas Vukadinovic. Temperature dependence of magnetic properties of a ultrathin yttrium-iron garnet film grown by liquid phase epitaxy: Effect of a Pt overlayer. *IEEE Magnetics Letters*, 9:1–5, 2018.

[162] Nathan Beaulieu, Nelly Kervarec, Nicolas Thiery, Olivier Klein, Vladimir Naletov, Herve Hurdequint, Gregoire de Loubens, Jamal Ben Youssef, and Nicolas Vukadinovic. Temperature dependence of magnetic properties of a ultrathin yttrium-iron garnet film grown by liquid phase epitaxy: Effect of a pt overlayer. *IEEE Magnetics Letters*, 9:1–5, 2018.

[163] Xing Zhang, Huaqing Xie, Motoo Fujii, Hiroki Ago, Koji Takahashi, Tatsuya Ikuta, Hidekazu Abe, and Tetsuo Shimizu. Thermal and electrical conductivity of a suspended platinum nanofilm. *Applied Physics Letters*, 86(17):171912, 2005.

[164] Yu A Volkov, LS Palatnik, and AT Pugachev. Investigation of the thermal properties of thin aluminum films. *Zh. Eksp. Teor. Fiz*, 70:2244–2250, 1976.

[165] S-M Lee and David G Cahill. Heat transport in thin dielectric films. *Journal of applied physics*, 81(6):2590–2595, 1997.

[166] Er-Jia Guo, Joel Cramer, Andreas Kehlberger, Ciaran A Ferguson, Donald A MacLaren, Gerhard Jakob, and Mathias Kläui. Influence of thickness and interface on the low-temperature enhancement of the spin Seebck effect in yig films. *Physical Review X*, 6(3):031012, 2016.

[167] Kathrin Ganzhorn, Tobias Wimmer, Joel Cramer, Richard Schlitz, Stephan Geprägs, Gerhard Jakob, Rudolf Gross, Hans Huebl, Mathias Kläui, and Sebastian TB Goennenwein. Temperature dependence of the non-local spin Seebeck effect in YIG/Pt nanostructures. *AIP Advances*, 7(8):085102, 2017.

[168] XJ Zhou, GY Shi, JH Han, QH Yang, YH Rao, HW Zhang, LL Lang, SM Zhou, F Pan, and C Song. Lateral transport properties of thermally excited magnons in yttrium iron garnet films. *Applied Physics Letters*, 110(6):062407, 2017.

[169] Jiang Xiao, Gerrit EW Bauer, Ken-chi Uchida, Eiji Saitoh, Sadamichi Maekawa, et al. Theory of magnon-driven spin Seebeck effect. *Physical Review B*, 81(21):214418, 2010.

[170] Scott A Bender and Yaroslav Tserkovnyak. Interfacial spin and heat transfer between metals and magnetic insulators. *Physical Review B*, 91(14):140402, 2015.

[171] David G Cahill, Wayne K Ford, Kenneth E Goodson, Gerald D Mahan, Arun Majumdar, Humphrey J Maris, Roberto Merlin, and Simon R Phillpot. Nanoscale thermal transport. *Journal of applied physics*, 93(2):793–818, 2003.

[172] Vittorio Basso, Elena Ferraro, Alessandro Magni, Alessandro Sola, Michaela Kuepferling, and Massimo Pasquale. Nonequilibrium thermodynamics of the spin Seebeck and spin peltier effects. *Physical Review B*, 93(18), may 2016.

[173] Silas Hoffman, Koji Sato, and Yaroslav Tserkovnyak. Landau-lifshitz theory of the longitudinal spin Seebeck effect. *Physical Review B*, 88(6):064408, 2013.

[174] Paul Horowitz, Winfield Hill, and Ian Robinson. *The art of electronics*, volume 2. Cambridge university press Cambridge, 1989.

[175] Jo Be Gunn. Microwave oscillations of current in iii–v semiconductors. *Solid State Communications*, 1(4):88–91, 1963.

[176] Dilip Kumar Roy. *Tunnelling and negative resistance phenomena in semiconductors*. Elsevier, 2014.

[177] A. V. Chumak, V. I. Vasyuchka, A. A. Serga, and B. Hillebrands. Magnon spintronics. *Nature Physics*, 11(6):453–461, June 2015.

[178] VE Demidov, S Urazhdin, A Anane, Vincent Cros, and SO Demokritov. Spin–orbit-torque magnonics. *Journal of Applied Physics*, 127(17):170901, 2020.

[179] Anjan Barman, Gianluca Gubbiotti, Sam Ladak, Adekunle Olusola Adeyeye, Maciej Krawczyk, Joachim Gräfe, Christoph Adelmann, Sorin Cotofana, Azad Naeemi, Vitaliy I Vasyuchka, et al. The 2021 magnonics roadmap. *Journal of Physics: Condensed Matter*, 33(41):413001, 2021.

[180] Sebastian T. B. Goennenwein, Richard Schlitz, Matthias Pernpeintner, Kathrin Ganzhorn, Matthias Althammer, Rudolf Gross, and Hans Huebl. Non-local magnetoresistance in YIG/pt nanostructures. *Applied Physics Letters*, 107(17):172405, oct 2015.

[181] Y. Kajiwara, K. Harii, S. Takahashi, J. Ohe, K. Uchida, M. Mizuguchi, H. Umezawa, H. Kawai, K. Ando, K. Takanashi, S. Maekawa, and E. Saitoh. Transmission of electrical signals by spin-wave interconversion in a magnetic insulator. *Nature*, 464(7286):262–U141, MAR 11 2010.

[182] Y. Li, V. V. Naletov, O. Klein, J. L. Prieto, M. Muñoz, V. Cros, P. Bortolotti, A. Anane, C. Serpico, and G. de Loubens. Nutation spectroscopy of a nanomagnet driven into deeply nonlinear ferromagnetic resonance. *Physical Review X*, 9(4), nov 2019.

[183] AS Jenkins, R Lebrun, E Grimaldi, S Tsunegi, P Bortolotti, H Kubota, K Yakushiji, A Fukushima, G De Loubens, O Klein, et al. Spin-torque resonant expulsion of the vortex core for an efficient radiofrequency detection scheme. *Nature nanotechnology*, 11(4):360–364, 2016.

[184] T. Wimmer, M. Althammer, L. Liensberger, N. Vlietstra, S. Geprägs, M. Weiler, R. Gross, and H. Huebl. Spin transport in a magnetic insulator with zero effective damping. *Physical Review Letters*, 123(25), dec 2019.

[185] Matthias Althammer. All-electrical magnon transport experiments in magnetically ordered insulators. *physica status solidi (RRL)–Rapid Research Letters*, 15(8):2100130, 2021.

[186] A. A. Tulapurkar, Y. Suzuki, A. Fukushima, H. Kubota, H. Maehara, K. Tsunekawa, D. D. Djayaprawira, N. Watanabe, and S. Yuasa. Spin-torque diode effect in magnetic tunnel junctions. *Nature*, 438(7066):339–342, November 2005.

[187] J. C. Sankey, P. M. Braganca, A. G. F. Garcia, I. N. Krivorotov, R. A. Buhrman, and D. C. Ralph. Spin-transfer-driven ferromagnetic resonance of individual nanomagnets. *Physical Review Letters*, 96(22):227601, 2006.

[188] Michael Harder, Yongsheng Gui, and Can-Ming Hu. Electrical detection of magnetization dynamics via spin rectification effects. *Physics Reports*, 661:1–59, 2016.

[189] E. Lesne, Yu Fu, S. Oyarzun, J. C. Rojas-Sánchez, D. C. Vaz, H. Naganuma, G. Sicoli, J.-P. Attané, M. Jamet, E. Jacquet, J.-M. George, A. Barthélémy, H. Jaffrès, A. Fert, M. Bibes, and L. Vila. Highly efficient and tunable spin-to-charge conversion through rashba coupling at oxide interfaces. *Nature Materials*, 15(12):1261–1266, aug 2016.

[190] J-Y Chauleau, Margherita Boselli, Stefano Gariglio, R Weil, G De Loubens, J-M Triscone, and Michel Viret. Efficient spin-to-charge conversion in the 2d electron liquid at the lao/sto interface. *EPL (Europhysics Letters)*, 116(1):17006, 2016.

[191] N. Vlietstra, J. Shan, V. Castel, J. Ben Youssef, G. E. W. Bauer, and B. J. van Wees. Exchange magnetic field torques in yig/pt bilayers observed by the spin-hall magnetoresistance. *Applied Physics Letters*, 103(3):032401, 2013.

[192] Cristina Sanz-Fernández, Van Tuong Pham, Edurne Sagasta, Luis E Hueso, Ilya V Tokatly, Fèlix Casanova, and F Sebastián Bergeret. Quantification of interfacial spin-charge conversion in hybrid devices with a metal/insulator interface. *Applied Physics Letters*, 117(14):142405, 2020.

[193] Kevin S Olsson, Kyongmo An, Gregory A Fiete, Jianshi Zhou, Li Shi, and Xiaoqin Li. Pure spin current and magnon chemical potential in a nonequilibrium magnetic insulator. *Physical Review X*, 10(2):021029, 2020.

[194] Chunhui Du, Toeno van der Sar, Tony X. Zhou, Pramey Upadhyaya, Francesco Casola, Huiliang Zhang, Mehmet C. Onbasli, Caroline A. Ross, Ronald L. Walsworth, Yaroslav Tserkovnyak, and et al. Control and local measurement of the spin chemical potential in a magnetic insulator. *Science*, 357(6347):195–198, Jul 2017.

[195] A Hamadeh, G De Loubens, VV Naletov, J Grollier, C Ulysse, V Cros, and O Klein. Autonomous and forced dynamics in a spin-transfer nano-oscillator: Quantitative magnetic-resonance force microscopy. *Physical Review B*, 85(14):140408, 2012.

[196] A Hamadeh, O d'Allivy Kelly, C Hahn, H Meley, R Bernard, AH Molpeceres, VV Naletov, M Viret, A Anane, V Cros, et al. Full control of the spin-wave damping in a magnetic insulator using spin-orbit torque. *Physical review letters*, 113(19):197203, 2014.

[197] VE Demidov, S Urazhdin, G De Loubens, O Klein, V Cros, A Anane, and SO Demokritov. Magnetization oscillations and waves driven by pure spin currents. *Physics Reports*, 673:1–31, 2017.

[198] Petr N Skirdkov and Konstatin A Zvezdin. Spin-torque diodes: From fundamental research to applications. *Annalen der Physik*, 532(6):1900460, 2020.

[199] Giovanni Finocchio, Riccardo Tomasello, Bin Fang, Anna Giordano, Vito Puliafito, Mario Carpentieri, and Zhongming Zeng. Perspectives on spintronic diodes. *Applied Physics Letters*, 118(16):160502, 2021.

[200] V. E. Demidov, S. Urazhdin, E. R. J. Edwards, M. D. Stiles, R. D. McMichael, and S. O. Demokritov. Control of magnetic fluctuations by spin current. *Physical Review Letters*, 107:107204, Sep 2011.

[201] Michael Schneider, Thomas Bracher, David Breitbach, Viktor Lauer, Philipp Pirro, Dmytro A. Bozhko, Halyna Yu. Musiienko-Shmarova, Björn Heinz, Qi Wang, Thomas Meyer, Frank Heussner, Sascha Keller, Evangelos Th. Papaioannou, Bert Lagel, Thomas Löber, Carsten Dubs, Andrei N. Slavin, Vasyl S. Tiberkevich, Alexander A. Serga, Burkard Hillebrands, and Andrii V. Chumak. Bose–einstein condensation of quasiparticles by rapid cooling. *Nature Nanotechnology*, apr 2020.

[202] Michael Schneider, David Breitbach, Rostyslav O Serha, Qi Wang, Alexander A Serga, Andrei N Slavin, Vasyl S Tiberkevich, Björn Heinz, Bert Lägel, Thomas Brächer, et al. Control of the bose-einstein condensation of magnons by the spin Hall effect. *Physical Review Letters*, 127(23):237203, 2021.

[203] B Divinskiy, H Merbouche, VE Demidov, KO Nikolaev, L Soumah, D Gouéré, R Lebrun, V Cros, Jamal Ben Youssef, P Bortolotti, et al. Evidence for spin current driven bose-einstein condensation of magnons. *Nature communications*, 12(1):1–7, 2021.

[204] Yaroslav Tserkovnyak, Scott A. Bender, Rembert A. Duine, and Benedetta Flebus. Bose-einstein condensation of magnons pumped by the bulk spin Seebeck effect. *Physical Review B*, 93(10), mar 2016.

[205] B. Flebus, S. A. Bender, Y. Tserkovnyak, and R. A. Duine. Two-fluid theory for spin superfluidity in magnetic insulators. *Physical Review Letters*, 116(11), mar 2016.

[206] Scott A Bender, Rembert A Duine, and Yaroslav Tserkovnyak. Electronic pumping of quasiequilibrium bose-einstein-condensed magnons. *Physical review letters*, 108(24):246601, 2012.

[207] Dmytro A Bozhko, Alexander A Serga, Peter Clausen, Vitaliy I Vasyuchka, Frank Heussner, Gennadii A Melkov, Anna Pomyalov, Victor S L'vov, and Burkard Hillebrands. Supercurrent in a room-temperature bose–einstein magnon condensate. *Nature Physics*, 12(11):1057–1062, 2016.

[208] Alexander JE Kreil, Dmytro A Bozhko, Halyna Yu Musiienko-Shmarova, Vitaliy I Vasyuchka, Victor S L'vov, Anna Pomyalov, Burkard Hillebrands, and Alexander A Serga. From kinetic instability to bose-einstein condensation and magnon supercurrents. *Physical Review Letters*, 121(7):077203, 2018.

[209] Kouki Nakata, Pascal Simon, and Daniel Loss. Spin currents and magnon dynamics in insulating magnets. *Journal of Physics D: Applied Physics*, 50(11):114004, 2017.

[210] D. A. Bandurin, I. Torre, R. K. Kumar, M. Ben Shalom, A. Tomadin, A. Principi, G. H. Auton, E. Khestanova, K. S. Novoselov, I. V. Grigorieva, L. A. Ponomarenko, A. K. Geim, and M. Polini. Negative local resistance caused by viscous electron backflow in graphene. *Science*, 351(6277):1055–1058, feb 2016.

[211] R. N. Gurzhi, A. N. Kalinenko, and A. I. Kopeliovich. Electron-electron collisions and a new hydrodynamic effect in two-dimensional electron gas. *Physical Review Letters*, 74(19):3872–3875, may 1995.

[212] Marco Polini and Andre K. Geim. Viscous electron fluids. *Physics Today*, 73(6):28–34, jun 2020.

[213] R.N. Gurzhi. Minimum of resistance in impurity-free conductors. *, J. Exp. Theor. Phys.*, 17:521, 1963.

[214] Camilo Ulloa, A. Tomadin, J. Shan, M. Polini, B. J. van Wees, and R. A. Duine. Nonlocal spin transport as a probe of viscous magnon fluids. *Physical Review Letters*, 123(11), sep 2019.

[215] Joaquin F Rodriguez-Nieva, Daniel Podolsky, and Eugene Demler. Probing hydrodynamic sound modes in magnon fluids using spin magnetometers. *Physical Review B*, 105(17):174412, 2022.

[216] Ryuhei Kohno, Nicolas Thiery, Kyongmo An, Paul Noël, Laurent Vila, Vladimir V Naletov, Nathan Beaulieu, J Ben Youssef, Grégoire de Loubens, and Olivier Klein. Enhancement of yig| pt spin conductance by local joule annealing. *Applied Physics Letters*, 118(3):032404, 2021.

[217] J.-C. Rojas-Sánchez, N. Reyren, P. Laczkowski, W. Savero, J.-P. Attané, C. Deranlot, M. Jamet, J.-M. George, L. Vila, and H. Jaffrès. Spin pumping and inverse spin Hall effect in platinum: The essential role of spin-memory loss at metallic interfaces. *Phys. Rev. Lett.*, 112:106602, Mar 2014.

[218] J. C. Rojas Sánchez, L. Vila, G. Desfonds, S. Gambarelli, J. P. Attané, J. M. De Teresa, C. Magén, and A. Fert. Spin-to-charge conversion using rashba coupling at the interface between non-magnetic materials. *Nature Communications*, 4(1), dec 2013.

[219] J Liu, XY Wei, GEW Bauer, J Ben Youssef, and BJ Van Wees. Electrically induced strong modulation of magnon transport in ultrathin magnetic insulator films. *Physical Review B*, 103(21):214425, 2021.

[220] Vladislav E Demidov and Sergej O Demokritov. Magnonic waveguides studied by microfocus brillouin light scattering. *IEEE Transactions on Magnetics*, 51(4):1–15, 2015.

[221] Kyongmo An, Kevin S. Olsson, Annie Weathers, Sean Sullivan, Xi Chen, Xiang Li, Luke G. Marshall, Xin Ma, Nikita Klimovich, Jianshi Zhou, Li Shi, and Xiaoqin Li. Magnons and phonons optically driven out of local equilibrium in a magnetic insulator. *Physical Review Letters*, 117(10), aug 2016.

[222] Daniel R Birt, Kyongmo An, Annie Weathers, Li Shi, Maxim Tsoi, and Xiaoqin Li. Brillouin light scattering spectra as local temperature sensors for thermal magnons and acoustic phonons. *Applied Physics Letters*, 102(8):082401, 2013.

[223] S.O. Demokritov and V.E. Demidov. Micro-brillouin light scattering spectroscopy of magnetic nanostructures. *IEEE Transactions on Magnetics*, 44(1):6–12, jan 2008.

[224] JR Sandercock and W Wettling. Light scattering from surface and bulk thermal magnons in iron and nickel. *Journal of Applied Physics*, 50(B11):7784–7789, 1979.

[225] Iacopo Bertelli, Brecht G Simon, Tao Yu, Jan Aarts, Gerrit EW Bauer, Yaroslav M Blanter, and Toeno van der Sar. Imaging spin-wave damping underneath metals using electron spins in diamond. *Advanced Quantum Technologies*, 4(12):2100094, 2021.

[226] SR Etesami, L Chotorlishvili, and J Berakdar. Spectral characteristics of time resolved magnonic spin Seebeck effect. *Applied Physics Letters*, 107(13):132402, 2015.

[227] Scott A Bender and Yaroslav Tserkovnyak. Thermally driven spin torques in layered magnetic insulators. *Physical Review B*, 93(6):064418, 2016.

[228] Benedetta Flebus, Pramey Upadhyaya, Rembert A Duine, and Yaroslav Tserkovnyak. Local thermomagnonic torques in two-fluid spin dynamics. *Physical Review B*, 94(21):214428, 2016.

[229] H Yu, SD Brechet, P Che, FA Vetro, M Collet, S Tu, YG Zhang, Y Zhang, T Stueckler, L Wang, et al. Thermal spin torques in magnetic insulators. *Physical Review B*, 95(10):104432, 2017.

[230] Can Onur Avci, Andy Quindeau, Chi-Feng Pai, Maxwell Mann, Lucas Caretta, Astera S Tang, Mehmet C Onbasli, Caroline A Ross, and Geoffrey SD Beach. Current-induced switching in a magnetic insulator. *Nature materials*, 16(3):309, 2017.

[231] J. Shan, L. J. Cornelissen, J. Liu, J. Ben Youssef, L. Liang, and B. J. van Wees. Criteria for accurate determination of the magnon relaxation length from the nonlocal spin Seebeck effect. *Physical Review B*, 96(18), nov 2017.

[232] Steven S.-L. Zhang and Shufeng Zhang. Spin convertance at magnetic interfaces. *Physical Review B*, 86(21), dec 2012.

[233] L. J. Cornelissen, J. Shan, and B. J. van Wees. Temperature dependence of the magnon spin diffusion length and magnon spin conductivity in the magnetic insulator yttrium iron garnet. *Physical Review B*, 94(18), November 2016.

[234] LJ Cornelissen and BJ Van Wees. Magnetic field dependence of the magnon spin diffusion length in the magnetic insulator yttrium iron garnet. *Physical Review B*, 93(2):020403, 2016.

[235] K. An, A. N. Litvinenko, R. Kohno, A. A. Fuad, V. V. Naletov, L. Vila, U. Ebels, G. de Loubens, H. Hurdequint, N. Beaulieu, J. Ben Youssef, N. Vukadinovic, G. E. W. Bauer, A. N. Slavin, V. S. Tiberkevich, and O. Klein. Coherent long-range transfer of angular momentum between magnon kittel modes by phonons. *Physical Review B*, 101(6), feb 2020.

[236] Kyongmo An, Ryuhei Kohno, Artem N Litvinenko, Rafael Lopes Seeger, Vladimir V Naletov, Laurent Vila, Gregoire de Loubens, J Ben Youssef, Nicolas Vukadinovic, Gerrit EW Bauer, et al. Bright and dark states of two distant macrospins strongly coupled by phonons. *Physical Review X*, 12(1):011060, 2022.

[237] JR Eshbach and RW Damon. Surface magnetostatic modes and surface spin waves. *Physical Review*, 118(5):1208, 1960.

[238] Lucas Caretta, Se-Hyeok Oh, Takian Fakhrul, Dong-Kyu Lee, Byung Hun Lee, Se Kwon Kim, Caroline A Ross, Kyung-Jin Lee, and Geoffrey SD Beach. Relativistic kinematics of a magnetic soliton. *Science*, 370(6523):1438–1442, 2020.

[239] Lucas Caretta, Ethan Rosenberg, Felix Büttner, Takian Fakhrul, Pierluigi Gargiani, Manuel Valvidares, Zhen Chen, Pooja Reddy, David A Muller, Caroline A Ross, et al. Interfacial dzyaloshinskii-moriya interaction arising from rare-earth orbital magnetism in insulating magnetic oxides. *Nature Communications*, 11(1):1–9, 2020.

[240] Takian Fakhrul, Stana Tazlaru, Lukáš Beran, Yan Zhang, Martin Veis, and Caroline A Ross. Magneto-optical bi: Yig films with high figure of merit for nonreciprocal photonics. *Advanced Optical Materials*, 7(13):1900056, 2019.

[241] KS Das, F Feringa, M Middelkamp, BJ van Wees, and IJ Vera-Marun. Modulation of magnon spin transport in a magnetic gate transistor. *Physical Review B*, 101(5):054436, 2020.

[242] O Alves Santos, F Feringa, KS Das, J Ben Youssef, and BJ van Wees. Efficient modulation of magnon conductivity in y 3 fe 5 o 12 using anomalous spin Hall effect of a permalloy gate electrode. *Physical Review Applied*, 15(1):014038, 2021.

[243] Kumar Sourav Das, Jing Liu, Bart J van Wees, and Ivan J Vera-Marun. Efficient injection and detection of out-of-plane spins via the anomalous spin Hall effect in permalloy nanowires. *Nano letters*, 18(9):5633–5639, 2018.

[244] Ken-ichi Uchida, Hiroto Adachi, Takeru Ota, Hiroyasu Nakayama, Sadamichi Maekawa, and Eiji Saitoh. Observation of longitudinal spin-seebeck effect in magnetic insulators. *Applied Physics Letters*, 97(17):172505, 2010.

[245] L. J. Cornelissen, K. J. H. Peters, G. E. W. Bauer, R. A. Duine, and B. J. van Wees. Magnon spin transport driven by the magnon chemical potential in a magnetic insulator. *Physical Review B*, 94(1), jul 2016.

[246] Huajun Qin, Rasmus B Hollander, Lukás Flajsman, and Sebastiaan van Dijken. Low-loss nanoscopic spin-wave guiding in continuous yttrium iron garnet films. *Nano Letters*, 22(13):5294–5300, 2022.

[247] Johannes Stigloher, Martin Decker, Helmut S Körner, Kenji Tanabe, Takahiro Moriyama, Takuya Taniguchi, Hiroshi Hata, Marco Madami, Gianluca Gubbiotti, Kensuke Kobayashi, et al. Snell's law for spin waves. *Physical review letters*, 117(3):037204, 2016.

[248] Joel Cramer, Lorenzo Baldrati, Andrew Ross, Mehran Vafaee, Romain Lebrun, and Mathias Kläui. Impact of electromagnetic fields and heat on spin transport signals in y 3 fe 5 o 12. *Physical Review B*, 100(9):094439, 2019.

[249] IV Borisenko, B Divinskiy, VE Demidov, G Li, T Nattermann, VL Pokrovsky, and SO Demokritov. Direct evidence of spatial stability of bose-einstein condensate of magnons. *Nature Communications*, 11(1):1–7, 2020.

[250] J. Holanda, D. S. Maior, A. Azevedo, and S. M. Rezende. Detecting the phonon spin in magnon–phonon conversion experiments. *Nature Physics*, apr 2018.

[251] Arne Vansteenkiste, Jonathan Leliaert, Mykola Dvornik, Mathias Helsen, Felipe Garcia-Sanchez, and Bartel Van Waeyenberge. The design and verification of mumax3. *AIP advances*, 4(10):107133, 2014.

[252] Herbert B Callen and Earl Callen. The present status of the temperature dependence of magnetocrystalline anisotropy, and the l (l+ 1) 2 power law. *Journal of Physics and Chemistry of Solids*, 27(8):1271–1285, 1966.

[253] Fatima Ibrahim, Ali Hallal, Alan Kalitsov, Derek Stewart, Bernard Dieny, and Mairbek Chshiev. Unveiling temperature-dependence mechanisms of perpendicular magnetic anisotropy at fe/mg o interfaces. *Physical Review Applied*, 17(5):054041, 2022.

[254] Richard FL Evans, Levente Rózsa, Sarah Jenkins, and Unai Atxitia. Temperature scaling of two-ion anisotropy in pure and mixed anisotropy systems. *Physical Review B*, 102(2):020412, 2020.

[255] Richard Francis L Evans, Denise Hinzke, Unai Atxitia, Ulrich Nowak, Roy W Chantrell, and Oksana Chubykalo-Fesenko. Stochastic form of the landau-lifshitz-bloch equation. *Physical Review B*, 85(1):014433, 2012.

[256] Björn Obry, Vitaliy I Vasyuchka, Andrii V Chumak, Alexander A Serga, and Burkard Hillebrands. Spin-wave propagation and transformation in a thermal gradient. *Applied Physics Letters*, 101(19):192406, 2012.

[257] Qi Wang, Philipp Pirro, Roman Verba, Andrei Slavin, Burkard Hillebrands, and Andrii V Chumak. Reconfigurable nanoscale spin-wave directional coupler. *Science advances*, 4(1):e1701517, 2018.

[258] R.C. LeCraw and R.L. Comstock. Magnetoelastic interactions in ferromagnetic insulators. In *Physical Acoustics vol. 3*, pages 127–199. Elsevier, 1965.

[259] E. G. Spencer, R. T. Denton, and R. P. Chambers. Temperature dependence of microwave acoustic losses in yttrium iron garnet. *Physical Review*, 125(6):1950–1951, mar 1962.

[260] Simon Streib, Hedyeh Keshtgar, and Gerrit EW Bauer. Damping of magnetization dynamics by phonon pumping. *Physical review letters*, 121(2):027202, 2018.

[261] Takuma Sato, Weichao Yu, Simon Streib, Gerrit EW Bauer, et al. Dynamic magnetoelastic boundary conditions and the pumping of phonons. *Physical Review B*, 104(1):014403, 2021.

[262] Steffen Peer Zeuschner, Xi-Guang Wang, Marwan Deb, Elena Popova, Gregory Malinowski, Michel Hehn, Niels Keller, Jamal Berakdar, and Matias Bargheer. Standing spin wave excitation in bi : YIG films via temperature-induced anisotropy changes and magneto-elastic coupling. *Phys. Rev. B*, 106:134401, Oct 2022.

[263] Takashi Kikkawa, Koichi Oyanagi, Tomosato Hioki, Masahiko Ishida, Zhiyong Qiu, Rafael Ramos, Yusuke Hashimoto, and Eiji Saitoh. Composition-tunable magnon-polaron anomalies in spin Seebeck effects in epitaxial bi x y 3- x fe 5 o 12 films. *Physical Review Materials*, 6(10):104402, 2022.

[264] LJ Cornelissen, K Oyanagi, T Kikkawa, Z Qiu, Timo Kuschel, GEW Bauer, BJ van Wees, and E Saitoh. Nonlocal magnon-polaron transport in yttrium iron garnet. *Physical Review B*, 96(10):104441, 2017.

[265] Takashi Kikkawa, Ka Shen, Benedetta Flebus, Rembert A Duine, Ken-ichi Uchida, Zhiyong Qiu, Gerrit EW Bauer, and Eiji Saitoh. Magnon polarons in the spin Seebeck effect. *Physical review letters*, 117(20):207203, 2016.

[266] Jianyu Zhang, Mingfeng Chen, Jilei Chen, Kei Yamamoto, Hanchen Wang, Mohammad Hamdi, Yuanwei Sun, Kai Wagner, Wenqing He, Yu Zhang, et al. Long decay length of magnon-polarons in bifeo3/la0. 67sr0. 33mno3 heterostructures. *Nature communications*, 12(1):1–8, 2021.

[267] Andreas Rückriegel and Rembert A. Duine. Long-range phonon spin transport in ferromagnet–nonmagnetic insulator heterostructures. *Physical Review Letters*, 124(11), mar 2020.

[268] Andreas Rückriegel, Simon Streib, Gerrit E. W. Bauer, and Rembert A. Duine. Angular momentum conservation and phonon spin in magnetic insulators. *Physical Review B*, 101(10), mar 2020.

[269] Xiang Zhang, Gerrit E. W. Bauer, and Tao Yu. Unidirectional pumping of phonons by magnetization dynamics. *Physical Review Letters*, 125(7), aug 2020.

[270] Mark JH Ku, Tony X Zhou, Qing Li, Young J Shin, Jing K Shi, Claire Burch, Laurel E Anderson, Andrew T Pierce, Yonglong Xie, Assaf Hamo, et al. Imaging viscous flow of the dirac fluid in graphene. *Nature*, 583(7817):537–541, 2020.

[271] KH Michel and F Schwabl. Hydrodynamic modes in a gas of magnons. *Physik der kondensierten Materie*, 11(2):144–162, 1970.

[272] N Prasai, BA Trump, GG Marcus, A Akopyan, SX Huang, TM McQueen, and JL Cohn. Ballistic magnon heat conduction and possible poiseuille flow in the helimagnetic insulator cu 2 oseo 3. *Physical Review B*, 95(22):224407, 2017.

[273] V Tiberkevich, IV Borisenko, P Nowik-Boltyk, VE Demidov, AB Rinkevich, SO Demokritov, and AN Slavin. Excitation of coherent second sound waves in a dense magnon gas. *Scientific reports*, 9(1):1–9, 2019.

[274] H Merbouche, B Divinskiy, KO Nikolaev, C Kaspar, WHP Pernice, D Gouéré, R Lebrun, V Cros, J Ben Youssef, P Bortolotti, et al. Giant nonlinear self-phase modulation of large-amplitude spin waves in microscopic YIG waveguides. *Scientific Reports*, 12(1):1–9, 2022.

[275] B Divinskiy, H Merbouche, KO Nikolaev, S Michaelis de Vasconcellos, R Bratschitsch, D Gouéré, R Lebrun, V Cros, J Ben Youssef, P Bortolotti, et al. Dispersionless propagation of ultrashort spin-wave pulses in ultrathin yttrium iron garnet waveguides. *Physical Review Applied*, 16(2):024028, 2021.

[276] Jun'ichi Ieda, Satoru Okayasu, Kazuya Harii, Masaaki Kobata, Kenji Yoshii, Tatsuo Fukuda, Masahiko Ishida, and Eiji Saitoh. The damage analysis for irradiation tolerant spin-driven thermoelectric device based on single-crystalline yfeo/Pt heterostructures. *IEEE Transactions on Magnetics*, 58(8):1–6, 2022.

[277] F Heyroth, C Hauser, P Trempler, P Geyer, F Syrowatka, R Dreyer, SG Ebbinghaus, G Woltersdorf, and G Schmidt. Monocrystalline freestanding three-dimensional yttrium-iron-garnet magnon nanoresonators. *Physical Review Applied*, 12(5):054031, 2019.